Design and Control of a Synchronous Reluctance Machine Drive

Thanaa Sharaf-Eldin
B.Sc., M.Sc.

Thesis submitted for the degree of Doctor of Philosophy

Heriot-Watt University
Department of Computing and Electrical Engineering

April 1999

TABLE OF CONTENTS

ACKNOWLEDGEMENTS

I would like to express my sincere gratitude to my supervisors, Dr. M.W. Dunnigan and Professor B.W. Williams for their professional guidance and support throughout the period of research reported in this thesis. Many thanks to past and present members of the Power Electronics Group for their friendship and assistance during the years of research. Special thanks to past members Dr. Scott Wade, Dr. Mehran Mirkazemi, Dr. A. Karshenas and Mr. N. McNeill. Thanks are also to Dr. S.J. Finney and Mr. A. Houstin.

Finally, I would like to thank all my family for their support and understanding throughout the years of research

Abstract

This thesis investigates the design, performance and control of a synchronous reluctance machine (Synchrel) drive. The Synchrel machine is proposed for variable speed drives because of its advantages over other machines. The rotor has no cage winding, brushes or slip rings. The torque ripple levels are lower in the Synchrel machine than the switched reluctance machine as it operates from a standard sine wave supply. An axially laminated rotor was designed based on finite element analysis, with the aim of producing the same output power as obtained from an induction motor (IM) with a similar stator.

Using vector control, the developed torque is controlled by regulating the stator current vector. Two vector control schemes are used, maximum torque per ampere and constant current in the direct axis. The output torque characteristics of the machine have been confirmed by finite element analysis.

Slotine's approach of sliding mode control is used for position control of the vector controlled synchronous reluctance machine. A comparison is undertaken between the performance of a fixed gain controller with two sliding mode controllers, for both the regulator and servo cases. Invariant performance is obtained using Slotine's sliding mode control approach, unlike with a fixed gain controller. Robustness to parameter variation is an important feature of this technique. This robustness can be achieved through the control law design, assuming parameter variation bounds are known. These improvements are demonstrated for variations in load inertia.

Inductance ripple affects machine performance, for example decreasing output torque and increasing core losses. A state space model for the machine that incorporates this inductance effect, yields drive simulation results that agree with experimental results.

List of Symbols

ζ unsaturated saliency ratio L_d / L_q

i_{ds} stator d-axis current, (A)

i_{qs} stator q-axis current, (A)

i_{dqs} stator current vector

i_{dqm} magnetising current vector

α mmf angle with respect to direct axis

r_s stator resistance, (Ω)

r_c core loss resistance,(Ω)

i_a, i_b, i_c stator phase currents, (A)

θ electrical rotor position, (rad)

θ_r mechanical rotor position, (rad)

ϕ_{dm} magnetizing d-axis flux, (Wb)

ϕ_{qm} magnetizing q-axis flux, (Wb)

ϕ_{dqm} magnetising flux, (Wb)

ω_e electrical rotor speed, (rad/s)

L_{dm} d axis magnetising inductance, (H)

L_{qm} q axis magnetising inductance, (H)

L_s stator leakage inductance, (H)

K_{fill} ratio of lamination thickness to lamination plus insulation thickness

ξ efficiency %

ϕ power factor angle, (rad)

A magnetic vector potential, (Wb/m)

μ permeability, (H/m)

J_c current density, (A/m^2)

B magnetic flux density, (T)

H magnetic field intensity,(A/m)

K_{torque} Torque factor, (H)

V_{dc} dc link voltage, (V)

T_e developed torque, (Nm)

K_T torque factor ,$\frac{3}{2}p(L_{dm}-L_{qm})i_{ds}$, ($Nm/A$)

p number of pole pairs

J moment of inertia, ($kg\ m^2$)

B_1 viscous friction constant, ($Nm/rad\ s^{-1}$)

B_2 coulomb friction constant, (Nm)

B_3 winding friction constant, ($Nm/rad^2\ s^{-2}$)

ϕ boundary layer width, (rad)

λ positive constant (system bandwidth), (rad/s)

η positive constant

s switching variable

b gain margin

θ_d desired rotor position, (rad)

n_{slots} number of slots per pole-pair

L_{do} average d axis inductance, (H)

L_{qo} average q axis inductance, (H)

ΔL_d fundamental d axis self inductance ripple, (H)

ΔL_q fundamental q axis self inductance ripple, (H)

ΔL_{dq} fundamental mutual inductance ripple between d and q axes, (H)

Abbreviations and Acronyms

Synchrel	Synchronous reluctance machine
CCIAC	constant current in the inductive axis control
MTC	maximum torque per ampere control
mmf	magnetomotive force
A/D	analogue to digital converter
D/A	digital to analogue converter

Preface

Scope of Thesis

This thesis considers the design, analysis and control of the synchronous reluctance machine. Finite Element analysis is used for the design and analysis of an axially laminated rotor. Vector control is implemented by regulating the stator current vector. Digital control is used for implementing the control algorithm. Non-linear robust control is applied to a vector controlled synchronous reluctance machine for position control.

The main aim is to show that the synchronous reluctance machine can produce the same output torque as an equivalent size induction motor using the vector control scheme. The thesis presents a comparative study between a linear control technique and a variable structure control technique and shows how sliding mode control is robust against parameter variation and system disturbances. Practical results are presented to validate the robustness of sliding mode control. The effect of inductance ripple is considered and evident in the simulation results.

Structure of Thesis

This thesis is presented in seven chapters. Chapter 1 introduces the literature survey and background theory on rotor types and control methods for the synchronous reluctance machine. The *d-q* circuits and torque equation of the machine are presented. Chapter 2 considers machine design with respect to the magnetic material distribution over the rotor circumference. Saturation effects in the machine are evident and the flux-current relationship for five rotor designs are obtained. Constructional and mechanical details of the finalised rotor design are given. In Chapter 3, the hardware required for the drive system is outlined. It includes information on the main processing element, power stage design and layout and gives the details of operational parameters.

In Chapter 4, vector control is implemented and a mathematical model of the synchronous reluctance machine is presented. Two vector control methods for the control of electromagnetic torque are considered.

Chapter 5 considers Slotine's approach to sliding mode control. This control algorithm is applied to the drive system for position control in both the regulator and servo cases. A practical comparison is made between the sliding mode controller and the fixed gain controller.

The effect of inductance ripple on torque production of the machine is considered in Chapter 6. Direct torque measurement is carried out to determine the first harmonic coefficient of the machine inductance ripple. Drive system simulations accounting for inductance ripple for the fixed gain controller and the sliding mode controller are given in this chapter. The nonlinearity in the mechanical model of the machine is also accounted for the simulations.

The concluding chapter provides a summary of the work reported in this thesis. In chapter 7. The author's contribution is highlighted and areas for further investigation are suggested.

Chapter 1

Introduction

1.1 Introduction

Adjustable speed drives are becoming more common place. This is because they offer many advantages over fixed speed motors, for example, energy saving, speed and position control, and alleviation of transient load effects. Load requirements and other factors dominate the choice of the motor, the electronic converter and the controller. The commonest requirement is for speed control, however position control is of increasing importance, along with fast dynamic response, particularly in robot applications and with actuators, etc.

Prior to 1950, most industrial variable speed drives used commutator motors. This was because adjustable or smoothly varying speed performance could not be obtained from ac drives. Ac motors inherently operated at or near synchronism. However the commutator in a dc machine limits the speed range and some disadvantages arise, such as unsuitability in explosive environments. An ac machine with the same power rating and speed will normally have a lower inertia. This feature offers a faster speed response than a dc machine with the same torque capability. Protection and maintenance of ac machines are much easier than with dc machines. These dc machines disadvantages have forced researchers towards ac machines. Ac drives with suitable control can compete with dc drives in high performance applications such as machine tools, spindle, rolling mill and high speed elevators.

Classical machines (dc, IM, synchronous) account for the lion's share of all markets especially high power applications. The synchronous machine can be operated at unity power factor thereby minimising the kVA requirements. The synchronous machine is more

expensive because of rotor structure and field supply arrangements. In the field of ac drives the induction motor (IM) is widely adopted due to attractive features such as cost, reliability and robust design. However for high precision applications where rated torque at low speeds is required, the low speed rotor losses of the IM make it a sub-optimal choice. The inherent disadvantage of the IM together with the practical availability of vector control for torque control have prompted continual attempts towards the adoption of alternatives, such as the synchronous reluctance (Synchrel) and switched reluctance (SR) machines. The latter has some advantages compared with other motors, for example, simple construction, low rotor losses and a high torque to inertia ratio. However the torque ripple levels and acoustic noise can be high. Unlike the SR machine, the Synchrel machine with a conventional IM stator operates from standard ac sinewave supplies. These two features, along with a proper rotor design enable a uniformly distributed air gap flux to be established. The goal of researchers is to develop rotor structures and control schemes that would make the Synchrel machine a candidate to meet the requirements demanded by high performance drives.

This chapter reviews aspects of the Synchrel machine, in particular rotor design, torque ripple and control methods. It also introduces the *d-q* axes equations and equivalent circuits for the machine in a synchronously rotating reference frame.

1.2 Rotors

Different rotor structures have been proposed as shown in Figure 1.1. The salient pole rotor in Figure 1.1a is part of one of the oldest types of electric motors [1.1] and [1.2]. Though it has a simple construction, machine output torque and power factor are low due to a low saturated saliency ratio ($\zeta=L_d/L_q$). In reference [1.1] a salient pole machine with added flux barriers and cut outs was analysed to obtain expressions for *d* and *q* axis inductances. A

prototype machine was built with a rotor pole arc to pole pitch ratio of 0.5 and a saliency of 3.75. The use of solid steel rotors in reluctance machines was suggested in [1.2]. The machine is self-starting by currents induced in the solid rotor. No cage winding is used for starting purposes. A "second generation" rotor is the segmental rotor, Figure1.1b, with flux guides/barriers, which gives higher values of (L_d/L_q) and offers a more robust construction. Lawrenson [1.3] proposed the segmental type and showed theoretically [1.4] and practically [1.5] that it provides better performance than the salient pole type. Analysis of the segmental design was presented in [1.6] and the issue of quadrature axis channel depth on direct and quadrature axis reactance was addressed. Experimental results on a 4 pole prototype machine confirmed the analysis. Saliency ratios of at least five are obtained from the segmental rotor machines. The axially laminated (AL) design is a later type of rotor structure, Figure 1.1c. It was proposed in 1966 by Cruickshank and Menzies [1.7] in an attempt to obtain better performance than with a segmental rotor, by increasing the saliency ratio. The mmf across the air gap in the q-axis is fairly small at most points on the rotor surface, and the quadrature flux has a large magnetic reluctance. The AL rotor has a d-axis magnetizing inductance, L_d, very close to that of a uniform airgap machine. In [1.8] analysis of the flux distribution and estimation of the direct and quadrature axis reactance of the AL rotor was presented. A comparison has been made between a 3 hp, four pole axially laminated machine, salient pole and induction machine equivalents. Saliency ratios of 4.4 were achieved with cut C-cores occupying 45% of the available pole arc. A maximum power factor of 0.68 and a maximum efficiency of 79.5% were obtained. These Figures fell short of those for the induction machine, but was significantly better than the salient pole rotor used as a comparison. The utilised pole-arc in these designs is limited by the need to incorporate a starting cage which is necessary to on-line start the machine and in minimising the oscillation due to hunting. Though this rotor type gives the highest

saliency ratio it suffers from constructional difficulties, including the inability to skew the rotor.

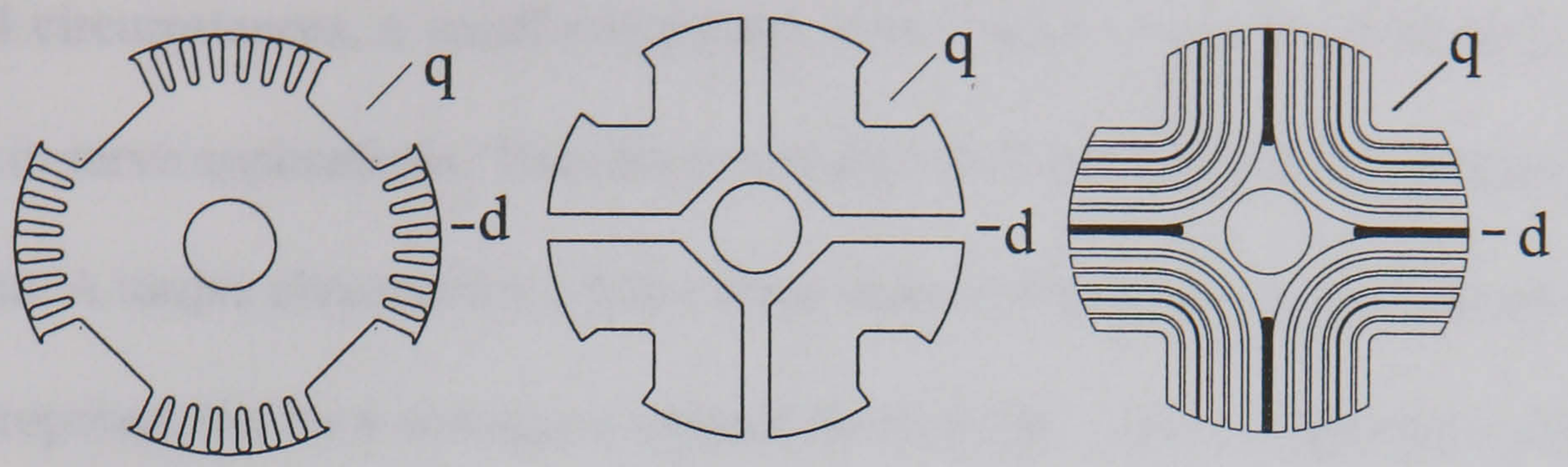

a *b* *c*

Figure 1.1 Rotor types of Synchrel machine
a salient pole b segmental c axially laminated

1.3 Torque ripple

All the considered rotor structures introduce air gap harmonics, which produce torque ripple. The primary reason for the torque ripple is the interaction between rotor segments and stator teeth. Other reasons are related to the control system and factors such as offset current, unbalance of peak current and phase angle, and current lag time. As far as high performance drives are concerned, reduction of the pulsating torque (torque ripple) is essential to achieve smooth torque operation. Therefore both the so called cogging torques (which are due to slotting) and the pulsating torques, due to space and time harmonics, must be reduced. Skewing the rotor by one slot pitch has been a commonly used method to achieve this. A staggered rotor has been suggested in order to remove the long-wavelength torque ripple. This technique is applicable to a non laminated rotor, which is constructed from two sections mounted on the shaft, staggered so that their torques combine almost undiminished but the long-wavelength ripples directly oppose each other, hence cancel. Combining the skew to eliminate slot ripple and stagger to eliminate the long-wavelength ripple might be used for unlaminated rotors. However, any method used for

minimising torque ripple must be evaluated on the basis of manufacturing considerations such as cost, assembly and the equipment required for the manufacturing process. Under normal circumstances, a small percentage of the rated torque is acceptable as cogging torque in servo applications. Various proposals have been suggested to solve this cogging problem. A torque observer for a direct drive motor control system with speed control has been proposed, but for a permanent magnet motor [1.9]. Lower frequency components are compensated, and the 24th component (corresponding to the torque ripple caused by the offset and cogging torque) is reduced by 90%. In [1.10] a design approach to minimise of the torque ripple associated with axially laminated rotors is presented and experimentally verified. In reference [1.11] eight rotor structures were studied and tested, with the aim of increasing torque capability without introducing unwanted ripple. This is achieved with a rotor with two staggered sections, each skewed by one stator slot pitch which is a displacement angle of 32°.

Inductance ripple affects machine performance, for example decreasing output torque and increasing core losses. In reference [1.12] axiallu laminated Synchrel motors with multiple segment rotor structures are considered, and the presence of stator slots, with respect to torque ripple, is considered. A mathematical model accounting for inductance variation was proposed. First harmonic inductance ripple in the machine is determined in [1.13] using direct torque measurement.

Improved rotor design has made the Synchrel machine competitive to the IM in terms of power factor and efficiency. However the Synchrel machines are expensive to manufacture and display torque ripple problem. High performance can be achieved with a suitable control scheme [1.14]-[1.32] .

1.4 Control methods

The development of vector control for ac drives would not have been practical without advances in microprocessors which can realise practically Park's work and others based on the generalised machine theory. The term vector controller is generally used to refer to controllers which control both the amplitude and phase of ac excitation. With a vector control strategy, *d*- and *q*-axis components of the stator current vector are decoupled, so as to give independent control of each component. As with a dc machine, the *d*-axis component represents the field current while the *q*-axis component is the armature current. Specific torque and speed can be obtained by regulating these two components. There are many *d*- and *q*-axis combinations, each defining a particular machine output torque. Maximum torque per ampere control (MTC) is a favourite objective, where the current vector angle is maintained constant and torque is varied by altering the phase current. This method gives the highest steady state efficiency as the flux and current level in the machine are minimum for a given output torque. Copper and iron losses are reduced. Linear magnetic theory assumes that maximum torque per ampere occurs at a current vector angle, α, of $\pi/4$, where α is shown in Figure 1.2. However if saturation is accounted for the angle will be higher. Linear analysis of the Synchrel machine was carried out in [1.14], in which an equation for power factor, cos ϕ, is derived and given by

$$\cos\phi = \frac{\zeta - 1}{\sqrt{2}} \sqrt{\frac{\sin(2\alpha)}{\tan(\alpha) + \zeta^2 \cot(\alpha)}} \tag{1.1}$$

Maximum power factor control (MPFC) can be obtained by differentiating Eq. (1.1) with respect to α to give

$$\alpha_{MPFC} = \arctan\sqrt{\zeta} \qquad rad \tag{1.2}$$

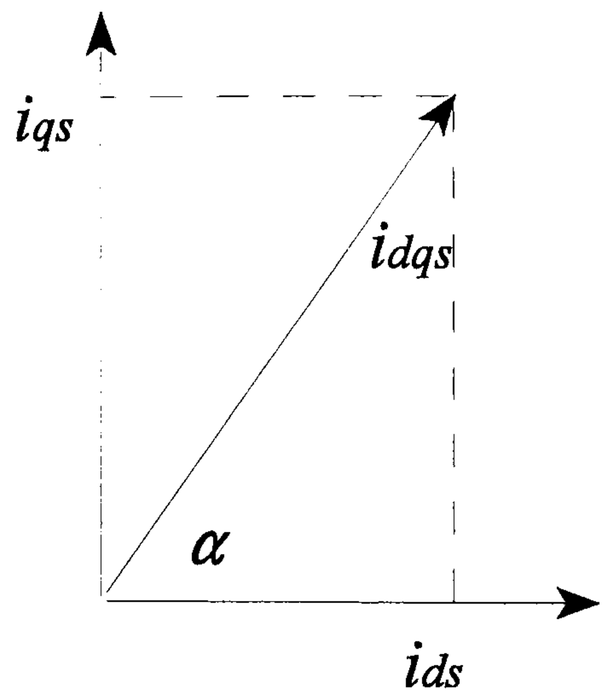

Figure 1.2 Vector diagram of machine currents

A significant reduction in inverter size, for the same output power can be acheived with the MPFC scheme if the Synchrel machine can be designed with $\zeta > 5$. Another commonly used control scheme maintains the machine in a fully fluxed condition with constant field excitation. The torque is regulated by controlling the *q*-axis current. This method offers fast transient response as the torque response is determined by the quadrature axis time constant which is shorter than the direct axis time constant. In addition it is possible to maintain full load torque output. This control method is termed constant current in the inductive axis control (CCIAC). Also in [1.14] a combination of MTC and CCIAC is introduced. The method involves switching from CCIAC to MTC at higher speeds, where the transient response of the former falls off. Therefore the transient torque response can be maximised. However, complication of implementation of transient surface limits its applicability. Torque vector control (TVC) with a hysteretic torque controller has been used in [1.15] and [1.16]. With this technique, the controller uses an optimal voltage vector based on whether the flux and torque should be increased or decreased. This has been adapted for use in a sensorless drive with a base speed range of 400 to 1500 rpm. A good estimate of the stator resistance is essential for efficient use of this scheme. No allowance for the effects of core losses on the flux vector has been made. A modification to the equivalent *d-q* axis circuits

to account for iron losses in the machine was first suggested in [1.17]. The iron losses effectively displace the magnetising current vector, i_{dqm}, from the applied stator current vector, i_{dqs}. The effect is significant at high speeds. This complicates the control schemes as it requires regulation of i_{dqm}, which is not directly measurable. As a continuation of the aforementioned work, [1.18] proposed a modified control scheme using an asymptotic current observer to compensate for the iron losses. The transient equations of the machine are inaccurate in respect to how the stator leakage inductance is included in the model. However this does not seem to affect the results obtained.

In recent years there has been renewed interest in controlling the Synchrel machine so as to achieve optimum efficiency and energy saving. In [1.19] optimum efficiency control is considered. Indirect torque control is implemented on a 0.415 kW axially laminated machine. An on-line controller seeks *d*- and *q*-axis current combinations which provide minimum input power and maximum efficiency. A small amount of perturbation is added to the *d*-axis current reference to search for the minimum input power operating point. The input power of the inverter is calculated from the measured dc link current and voltage. The obtained input power includes machine output power, machine losses and inverter losses. Experimental results are presented, which verify the developed control scheme. Direct torque control of a Synchrel machine based on the stator current vector is proposed in [1.20]. The stator *d*- and *q*- axis voltages which can generate the desired torque, are directly calculated from the machine model. Two models for the machine are proposed, one accounts for the core losses while the second does not. Simulation and experimental results are presented to validate the proposed technique. The test motor is a 3.75 kW axially laminated Synchrel machine. Control implementations based on stationary and synchronous reference frames [1.21] have been considered and relative performance compared. Slightly better results are obtained from the latter. Over load and flux-weakening conditions are

examined, and a strategy for setting the current vector is proposed. Experimental results from a 10 Nm servomotor are presented, which allow a practical evaluation of some second order effects such as lags due to eddy currents and error in measuring the rotor angle. A flux-observer based control scheme which deals with magnetic saturation, core losses and angular measurement error is presented in [1.22]. The proposed controller has been implemented on a prototype 17 Nm, 8000 rpm drive. The control strategy can be used when a large flux weakening range is needed. In [1.23] a fully digital control method, termed incremental torque control, is investigated. A digital simulation is used to verify the proposed technique. Experimental results from a 2 hp, 3600 rpm motor validate the proposed scheme. A descriptive comparison between this technique, sliding mode control and fixed gain control were made. Practical results were presented only for the proposed technique. The design and performance of a 7.5 kW axially laminated Synchrel machine were presented [1.24]. Finite element analysis was used to predict machine parameters. Good performance was demonstrated by both theory and experimentation in both fixed frequency and field weakening modes of operation.

High performance control attracts the efforts of drive researchers, as in [1.25]. The effects of current measurement error classified as offset and scaling error are analysed. It is demonstrated that offset error causes the motor torque to oscillate at the stator electrical frequency while scaling error causes the motor torque to oscillate at twice the stator frequency. These ripple torques deteriorate speed control performance, as they act as load disturbances. A compensation method is proposed to achieve precise torque control and eliminate speed ripple. The simulation and experimental results agree with the presented analysis, and the compensation method improves torque control performance by eliminating torque ripple.

Sensorless control. Rotor position sensing techniques without a rotating shaft sensor have been recently presented [1.26]-[1.29] to simplify and reduce drive costs. In [1.26], position information is provided at the zero crossings of the phase current, giving only six rotor position samples per cycle of a three phase motor. High precision cannot be obtained with this scheme, especially at low speeds. Another position sensing technique [1.27] utilizes the stator phase voltage third harmonic. Effectively six position samples per one electrical cycle result and the method is ineffective at low rotor speeds because it requires extraction of the induced third harmonic voltage whose magnitude is speed dependent. In [1.28] a rotor position detection scheme based on current measurements is investigated. This scheme utilizes the dependence of the machine self and mutual inductances on rotor position. The rate of change of ripple current is detected and converted to a rotor position signal. Good control performance has been obtained at low speed. A sensorless control algorithm [1.29] that implements a maximum torque per ampere control strategy has been proposed, and verified experimentally with a 5.8 kW, axially laminated machine. This algorithm is applicable over the entire speed range of the machine including standstill. However it requires a simple startup procedure to determine rotor initial position before executing the control algorithm.

Sliding mode control. This nonlinear control technique has been proposed to give robust control with invariant performance with changing system conditions. Sliding mode control has been applied to the Synchrel machine previously [1.30],[1.31] and [1.32]. In [1.30] sliding mode with fuzzy control for position and speed control of a Synchrel motor drive is demonstrated. The design and implementation of the control algorithm are presented. Fuzzy control is used to adjust the switching surface in the sliding mode. A new speed loop controller using the proposed technique is tested. The practical results validate the

presented simulations. In [1.31], the above technique is applied to sensorless vector control of the Synchrel machine. The position, speed and acceleration signals are obtained by detecting the voltages and currents of the motor. Practical and simulated results are presented to verify the theoretical analysis. A low-cost robust speed (and position) vector controlled Synchrel machine implementation is investigated in [1.32]. The direct axis current component is kept constant up to the base speed and then reduced gradually above the base speed. A sliding mode speed (and position) controller is used on the q-axis current. A 6-pole experimental Synchrel machine with an axially laminated anisotropic cageless rotor was used in this work. Digital simulation and test results are presented.

None of the aforementioned references use Slotine's approach of sliding mode control, which is reported in this thesis. Also none compare sliding mode control with a fixed-gain control method. This thesis shows that Slotine's approach to sliding mode control for position control of a vector controlled 18 kW Synchrel machine provides robustness to load inertia variation. Indirect torque control is implemented. The machine is maintained fully fluxed with a constant *d*-axis current. Sliding mode control of the *q*-axis current regulates the torque generated. Superior performance is exhibited over a fixed-gain position control method in terms of an invariant regulator response and reduced tracking errors in a servo application. Also Slotine's approach allows torque ripple parameters to be incorporated and ripple reduction is afforded due to the high system gain.

1.5 *D-Q* Equations for the Synchrel Machine

The equations of the generalised machine can be used to evaluate any machine under any operating condition, steady state or transient. Generally the applied voltages are known and it is required to determine the currents, while the torque and speed may be either known or unknown quantities. Park's transformation replaces the voltages and currents in rotating

windings by equivalent axis quantities. The actual phase voltages and currents, v_a, v_b, v_c, i_a, i_b, i_c are converted to fictitious quantities v_{ds}, v_{qs}, v_0, i_d, i_q, i_0, which differ from but are related to the actual quantities. The purpose of this transformation is to simplify the solution of the differential equations that describe machine behaviour, by eliminating time varying coefficients dependent on the rotor position. These dependent coefficients are the self and mutual inductances of the armature coils. The transformation enables ac machines to be analyzed by what is called two axis theory.

The currents i_{ds} and i_{qs} in the fictitious coils are located on quadrature axes and have the number of turns that would set up the same mmf wave as the actual currents i_a, i_b, i_c. To retain invariant power during the transformation a factor of $\sqrt{\frac{2}{3}}$ is introduced [1.33] as follows:

abc to *dq*

$$\begin{pmatrix} i_{ds} \\ i_{qs} \\ i_0 \end{pmatrix} = \sqrt{2/3} \begin{pmatrix} \cos\theta & \cos(\theta-2\pi/3) & \cos(\theta-4\pi/3) \\ \sin\theta & \sin(\theta-2\pi/3) & \sin(\theta-4\pi/3) \\ 1/2 & 1/2 & 1/2 \end{pmatrix} \begin{pmatrix} i_a \\ i_b \\ i_c \end{pmatrix} \tag{1.3}$$

from *dq* to *abc*

$$\begin{pmatrix} i_a \\ i_b \\ i_c \end{pmatrix} = \sqrt{2/3} \begin{pmatrix} \cos\theta & \sin\theta & 1 \\ \cos(\theta-2\pi/3) & \sin(\theta-2\pi/3) & \\ \cos(\theta-4\pi/3) & \sin(\theta-2\pi/3) & 1 \end{pmatrix} \begin{pmatrix} i_d \\ i_q \end{pmatrix} \tag{1.4}$$

Figure 1.3 shows the *d*- and *q*- axis equivalent circuits of the Synchrel machine. The stator winding is sinusoidally distributed and flux harmonics are contributed by rotor saliency. The machine uses an axially laminated rotor structure, and a starting cage would be redundant since the machine can start from rest by proper inverter control. The machine has no field winding. From Park's equations, the behaviour of the Synchrel machine in a synchronously rotating reference frame can be described by the following set of equations,

which ignores the core loss equivalent resistance, r_c:

$$v_{ds} = r_s i_{ds} + \frac{d\phi_{dm}}{dt} - \omega_e \phi_{qm}$$
$$v_{qs} = r_s i_{qs} + \frac{d\phi_{qm}}{dt} + \omega_e \phi_{dm} \qquad (1.5)$$

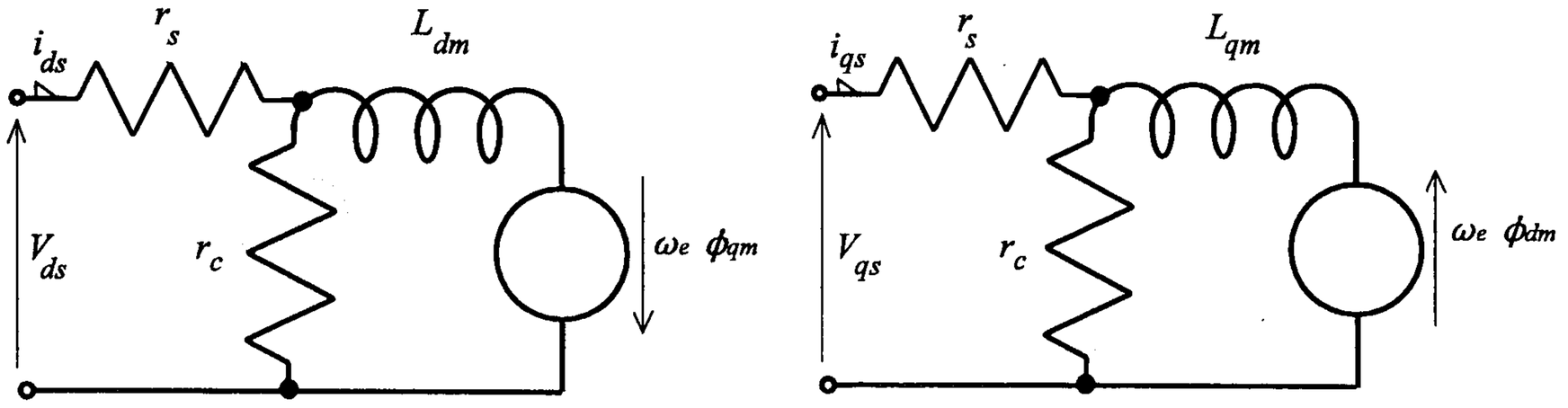

Figure 1.3 Equivalent circuits of the Synchrel machine

The direct and quadrature fluxes ignoring core losses and saturation are:

$$\phi_{dm} = L_{dm} i_{ds} \quad ?$$
$$\phi_{qm} = L_{qm} i_{qs} \quad ? \qquad (1.6)$$

Therefore the torque can be expressed as

$$T_e = \frac{3}{2} p \, i_{ds} \, i_{qs} \, (L_{dm} - L_{qm}) \qquad (1.7)$$

Eq. (1.7) is rewritten as

$$T = K_T \, i_{qs} \qquad (1.8)$$

where $K_T = \frac{3}{2} p (L_{dm} - L_{qm}) i_{ds}$. The torque form in Eq. (1.8) is convenient for sliding mode control implementation, which is considered in chapter 5.

1.6 Summary

This chapter has surveyed publications related to the design and control of the Synchrel machine. An axially laminated rotor design offering the maximum saliency ratio has been chosen, though its construction is complex.

Different control techniques have been proposed with the aim of achieving a high performance drive. The vector control strategy is essential in order to optimise Synchrel machine performance. Sensorless vector control is suggested so as to eliminate the cost of a position sensor. Sliding mode control has been proposed in order to achieve robust control and invariant system performance. Machine equations have been presented based on generalised machine theory and Park's transformation.

References

1.1 Honsinger, V.B.: 'The inductances L_d, L_q of reluctance machine', IEEE, Trans. Power App. and Sys., Vol. 90, No. 1, Jan/Feb 1971, pp. 298-304.

1.2 Chalmers, B.J., and Mulki, A.S.: 'Design and performance of reluctance motors with unlaminated rotors', IEEE, Trans. Power App. and Sys., 1972, pp. 1562-1569.

1.3 Lawerenson, P.J., and Agu, L.A.: 'A new unexcited synchronous machine', Proc. IEE, Vol. 110, No. 7, 1963, pp. 1275.

1.4 Lawerenson, P.J., and Agu, L.A.: 'Theory and performance of polyphase reluctance machines', Proc. IEE, Vol. 111, No. 8, 1964, pp. 1435-1445.

1.5 Lawerenson, P.J., and Agu, L.A.: 'Low-inertia reluctance machines', Proc. IEE, Vol. 111, No. 12, 1964, pp. 2017-2025.

1.6 Lawerenson, P.J., and Gupta, S.K.: 'Developments in the performance and theory of segmental-rotor reluctance motors', Proc. IEE, Vol. 114, No. 5, May 1967, pp. 645-653.

1.7 Cruickshank, A.J.O, Menzies, R.W., Anderson, A.F.: 'Axially laminated anisotropic rotors for reluctance motors', Proc. IEE, Vol. 113, No. 12, 1966, pp. 2058-2060.

1.8 Cruickshank, A.J.O, Anderson, A.F., and Menzies, R.W.: 'Theory and performance of reluctance motors with axially laminated anisotropic rotors', Proc. IEE, Vol. 118, No. 7, July 1971, pp. 887-894.

1.9 Matsui, N., Makino, T., and Satoh, H.: 'Auto compensation of torque ripple of direct drive motor by torque observer', IEEE Trans. Ind. Applicat., Vol. 29, No. 1, Jan. /Feb. 1993, pp. 187-194.

1.10 Vagati, A., Pastorelli, M., and Franceschini, G.: 'Design of low-torque-ripple synchronous reluctance motors', IEEE IAS Ann. Meet., Oct. 1997, pp. 286-293.

1.11 Zuncheng, Z., and Spooner, E.: 'High-speed reluctance machines with mixed-pole windings', IEE Proc. B, Vol. 138, No.5, Sep. 1991, pp 257-263.

1.12 Fratta, A., Troglia, G.P., Vagati, A., and Villata, F.: 'Evaluation of torque-ripple in high performance synchronous reluctance machines', IEEE IAS Ann. Meet., 1993, pp. 163-170.

1.13 Fletcher, J., Williams, B.W., and Green, T.C.: 'Efficiency aspects of vector control applied to synchronous reluctance motors', IEEE IAS Ann. Meet., 1995, pp.294-300

1.14 Betz, R.E.: 'Theoretical aspects of control of synchronous reluctance machines', IEE Proc. B, Vol. 139, No. 4, July 1992, pp. 355-364.

1.15 Boldea, I., Fu, Z.X, and Nassar, S.A.:' Torque vector control (TVC) of axially-laminated anisotropic (ALA) rotor reluctance synchronous motors', Electric machines and Power Systems, Vol. 19, 1991, pp.381-398.

1.16 Lagerquist, R., Boldea, I., and Miller, T.J.:' Sensorless control of the synchronous reluctance motor', IEEE Trans. Ind. Applicat., Vol. 30, No. 2, May /June 1994, pp. 673-681.

1.17 Xu, L., Xu, X., Lipo, A., and Novontny, D.W.: 'Vector control of a synchronous reluctance motor including saturation and iron loss', IEEE IAS Ann. Meet., 1990, pp. 359-364.

1.18 Xu, L., and Yao, J.: 'A compensated vector control scheme of a synchronous motor including saturation and iron loss', IEEE Trans. Ind. Applicat., Vol. 28, No.6, Nov./Dec.1992, pp. 1330-1338.

1.19 Matsuo, T., El-Antably, A., and Lipo, A.: 'A new control strategy for optimum-efficiency operation of a synchronous reluctance motor', IEEE Trans. Ind. Applicat., Vol. 33, No.5, Sep. /Oct. 1997, pp. 1146-1153.

1.20 Kang, S.J, and Sul, S.K.: 'High dynamic torque control of synchronous reluctance motor', IEEE Trans. Power Electronics, Vol. 13, No. 4, July 1998, pp. 793-798.

1.21 Franceschini, G., Fratta, A., Petrache, C., and Vagati, A.: 'Control of high performance synchronous reluctance motors', Intelligent Motion, June 1994, pp. 117-126.

1.22 Vagati, A., Pastorelli, M., and Franceschini, G.: 'High-performance control of synchronous reluctance motors', IEEE Trans. Ind. Applicat., Vol. 33, No. 4, July /Aug.1997, pp.983-991.

1.23 Xiang, Q. Y., and Nassar, S.A.:' A fully digital control strategy for synchronous reluctance motor servo drives', IEEE Trans. Ind. Applicat., Vol. 33, No. 3, May /June 1997, pp.705-713.

1.24 Chalmers, B.J, Musaba, L.: Design and field-weakening performance of a synchronous reluctance motor with axially laminated rotor', IEEE Trans. Ind. Applicat., Vol. 34, No. 5, Sept. /Oct., 1998, pp. 1035-1041.

1.25 Chung, D.W, and Sul, S.K.: 'Analysis and compensation of current measurement error in vector controlled ac motor drives', IEEE Trans. Ind. Applicat., Vol. 34,

No.2, March/April 1998, pp. 340-345.

1.26 Arfeen, M. S, Ehsani, M., and Lipo, A.: 'An analysis of the accuracy of indirect shaft sensor for synchronous reluctance motor', IEEE IAS Ann. Meet., Oct. 1993, pp. 695-700.

1.27 Kreindler, L., Testa, A., and Lipo, A.: 'Position sensorless synchronous reluctance motor drive using the stator phase voltage third harmonic', IEEE IAS Ann. Meet., Oct. 1993, pp. 679-686.

1.28 Matsuo, T., and Lipo, A.: 'Rotor position detection scheme for synchronous reluctance motor based on current measurements', IEEE IAS Ann. Meet., 1994, pp. 627-634.

1.29 Jovanovic', M. G., Betz, R.E., and Platt, D.: 'Sensorless vector controller for a synchronous reluctance motor', IEEE Trans. Ind. Applicat., Vol. 34, No. 2, March/April 1998, pp. 346-354.

1.30 Liu, T. , and Lin, M.: 'A fuzzy sliding-mode controller design for a synchronous reluctance motor drive', IEEE Trans. Aerospace and Electronic Systems, Vol. 32, No. 3, July 1996, pp. 1065-1076.

1.31 Liu, T. , and Lin, M.: 'Sliding-mode with fuzzy controller design for a sensorless synchronous reluctance motor drive', Journal of Control Systems and Technology, Vol.3, No. 2, 1995, pp. 129-136.

1.32 Boldea, I., Muntean, N., and Nassar, S. A.: 'Robust low-cost implementation of vector control for reluctance synchronous machines', IEE Proc.- Elect. Power Appl., Vol. 141, No.1, Jan. 1994, pp. 1-6.

1.33 Hancock, N.N.: 'Matrix analysis of electrical machinery', Second Edition, Pergamon press, Hungary, 1974.

Chapter 2

Machine Design

2.1 Introduction

Electric machine design has been computerised since the early days of computers. From the 1960s, when the experimental physics community created a need for computational magnet design aids, CAD software has grown to occupy an important role in the industrial designer's tool kit. Numerous commercial CAD systems are now available for magnetic design work and electromagnetic field analysis has become an effective tool for optimising machine design. Better material utilisation and geometry optimisation can be achieved with this technique. Design by numerical analysis is capable of dealing with both the geometric complexity and nonlinearities found in electromagnetic devices. Design by numerical analysis therefore inevitably means computer-aided analysis, and increasingly has come to mean full-fledged computer-aided design. The most commonly used methods for analysis are based on finite element techniques. This technique has proved to be flexible and reliable for users. The finite element technique is an analysis tool rather than a design tool, and as such has some limitations when used for electric machine design. Detailed input data is required, however it does not account for many factors that affect the magnetic circuit of the machine. Parasitic effects which have important consequences on the field distribution and on torque production of the machine in dynamic conditions are disregarded. End winding inductance effects are ignored. However, such techniques are effective in helping to understand a theoretical problem that would otherwise be more difficult to solve. In practice, the supply waveforms for adjustable speed drives are not pure sinewaves. Simulation may be necessary to predict drive system performance for a given machine design over different ranges of operating conditions.

The finite element technique is popular for magnetic design [2.1]-[2.3]. Research work has been described which attempts to determine an optimum design for a synchronous reluctance machine, [2.1]. Finite element analysis was used to determine the number of magnetic segments and the lamination/barrier thickness ratio, and their effect on output performance. In reference [2.2] finite element analysis was used to optimise the design of the cageless reluctance synchronous machine. The conclusion was that it is possible to obtain a total (stator and rotor) unconstrained or constrained optimum design of the Synchrel machine using the proposed finite element analysis procedure. The flux-mmf diagram is used to compare and contrast the torque production mechanism in seven common machine types , [2.3], viz; the IM, Synchrel, SR, surface permanent magnet brushless ac motor, surface permanent magnet brushless dc motor, permanent magnet dc commutator motor and interior permanent magnet motor. The motor designs were reasonably optimised using a combination of commercially available motor CAD packages and a finite element analysis package.

This chapter addresses problems associated with the finite element design procedure of an axially laminated rotor for the Synchrel machine. Design parameters are important in optimising the rotor structure. The important parameters are magnetising inductances, output torque and inductance ripple.

2.2 The Stator

The test Synchrel machine investigated here uses the stator of a 25 hp squirrel cage IM. The full pitched stator windings are single-layered, integral slot and arranged to produce a four pole mmf. There are 36 slots equally spaced around the stator, each carrying 25 conductors. The stator stack length is 150 mm with outside diameter of 301 mm. The stator inside diameter and the rotor outside diameter are 200.1 mm and 199 mm

respectively, giving air gap length of 0.55 mm. No slot details were available.

2.3 Machine Analysis

Finite element analysis can cope with linear or nonlinear magnetic materials. Two dimensional finite element analysis has been used in this work to optimise the distribution of rotor magnetic material. Finite element analysis yields the magnetic vector potential.

The magnetic flux density B at any point P produced by a current distribution is given by [2.4]:

$$B = \frac{\mu}{4\pi} \iiint \frac{J_c \times \hat{r}}{r^2} \quad dv \tag{2.1}$$

where B : flux density, (T)

μ : permeability of the material, (H/m)

J_c : axial component of current density, (A/m^2)

$\hat{r}$: unit vector in direction of radius vector r, dimensionless

r : radius vector from volume element to point p, (m)

dv : volume element, (m^3)

Integration over the entire volume gives the total flux density. The divergence of the magnetic field density is zero; i.e.,

$$\nabla . B = 0 \tag{2.2}$$

Therefore B can be expressed as the curl of some other vector, which might be designated as A

$$B = \nabla \times A \qquad Wb \tag{2.3}$$

where ∇ is the curl operator and is given by $\nabla = \frac{\delta}{\delta x} i + \frac{\delta}{\delta y} j + \frac{\delta}{\delta z} k$ and A is called a

vector potential which also satisfies the following equation

$$\nabla . A = 0 \tag{2.4}$$

Taking the curl of Eq. (2.3) yields

$$\nabla \times \nabla \times A = \mu J_c \qquad Wb/m^3 \tag{2.5}$$

The magnetic field in the machine is governed by Eq. (2.5) which is known as Poisson's nonlinear equation. The permeability of the magnetic material is nonlinear and flux dependent. In electrical machines and electromagnetic devices a somewhat linear relationship between the flux density, B, and the current is desired, which can be approached by limiting the maximum current.

Finite element analysis involves discretising the geometry to be analysed into polygons. The software used to analyse the cross section of the reluctance machine uses triangular elements. A typical element is shown in Figure 2.1. The magnetic vector potentials A_n, A_{n+1} and A_{n+2} at the nodes n, $n+1$ and $n+2$ of the triangle are solved by the finite element software. First order finite elements are used, wherein A varies linearly across each element and the flux density is constant within elements.

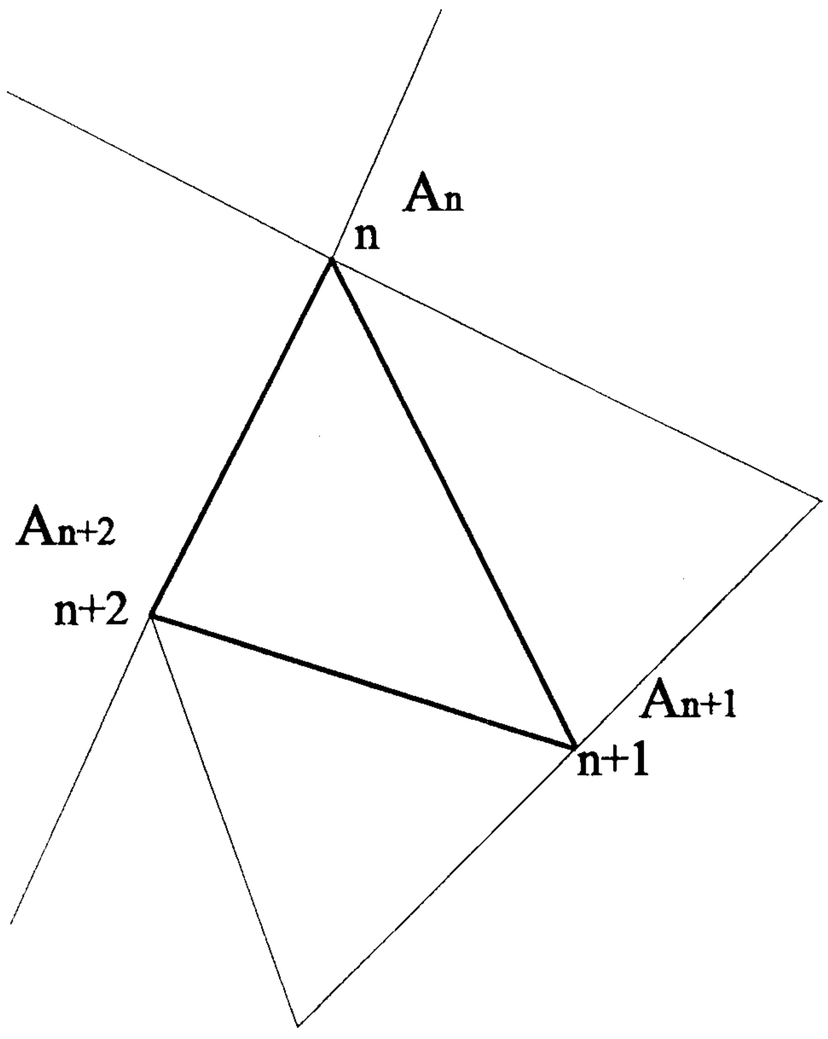

Figure 2.1 Typical triangular element used in finite element analysis

The magnetic flux linkage between nodes n, $n+1$ is given:

$$\lambda_{n,n+1} = (A_{n+1} - A_n).l \tag{2.6}$$

where l : device length (m)

A_n : magnetic vector potential at node n (Wb/m)

$\lambda_{n,\,n+1}$: flux linking nodes n and $n+1$ (Wb)

2.4 The Finite Element Analysis Systems

The analysis of an electromagnetic design with the finite element technique and the subsequent result retrieval can be divided into three parts [2.5]; preprocessing, solving and postprocessing. In principle, these amount to setting up the problem for solution, carrying out the mathematical analysis and evaluating the answer to produce some useful results.

2.4.1 Preprocessing

Preprocessing is the phase where the problem is described to the computer. This consists of two parts, the first is the geometric and topological description since the device has a certain shape and is made of certain materials which must be suitably described to the CAD system. This part may be viewed as simulating the construction of the prototype. In general, the prototype is modelled by a set of finite elements and most systems combine a description of the device itself with a statement of how it is to be represented in terms of finite elements. The second part of problem definition may be regarded as describing the experiments to be simulated on a prototype device, which includes boundary conditions and excitation. Both parts may be interfaced to the computer by the use of an interactive program. The final product is a completely defined, unique, mathematical problem ready for solution.

i Geometry Definition and Discretisation

Electric machines generally involve a complicated but highly repetitive geometric structure. The symmetry of rotary machines allows reduction of the modelled cross section from a full 360 mechanical degrees to 90 degrees. Periodicity at the radial boundaries is maintained by the use of binary constraints, Appendix A. The number of nodes and elements are limited by storage space available for both models and solutions or in order to maintain reasonable solution times. Symmetry reduces the number of elements required and hence decreases solution time and reduces storage requirements. A user written PASCAL shell was developed to generate model geometries thereby minimising the time spent to define rotor geometries. The program has the geometry dimensions as the input and generates a MAGNET compatible ASCII file for each rotor geometry. Element distribution is paramount in obtaining accurate results. Analysis using first order elements results in a constant flux density across individual elements. The spatial rate of change of flux density is high in the air gap, stator teeth tips and rotor segments tips therefore high element density should be high in these areas. On the other hand, the spatial rate of change of flux density is low in the back iron and lower element density is acceptable. For better results, element density should be varied over different sections of the machine.

ii Excitation and Material Definition

The physical properties and magnetization curves of the materials are used to analyse magnetic devices. Core losses are ignored in this analysis so stator slot currents are equal to magnetising currents. Defining slot currents provides the machine excitation, where $i_{dqs} = i_{dqm}$ (ignoring the core losses). The B-H magnetization curve for the stator iron is required for accurate results. However, insufficient data was available for the stator material. The magnetization curve, Figure 2.2, for the stripwound C-core used for the

axially laminated rotor was used as an approximation to define stator material. Although this material is grain oriented, these magnetisation characteristics should give an approximation of the stator iron.

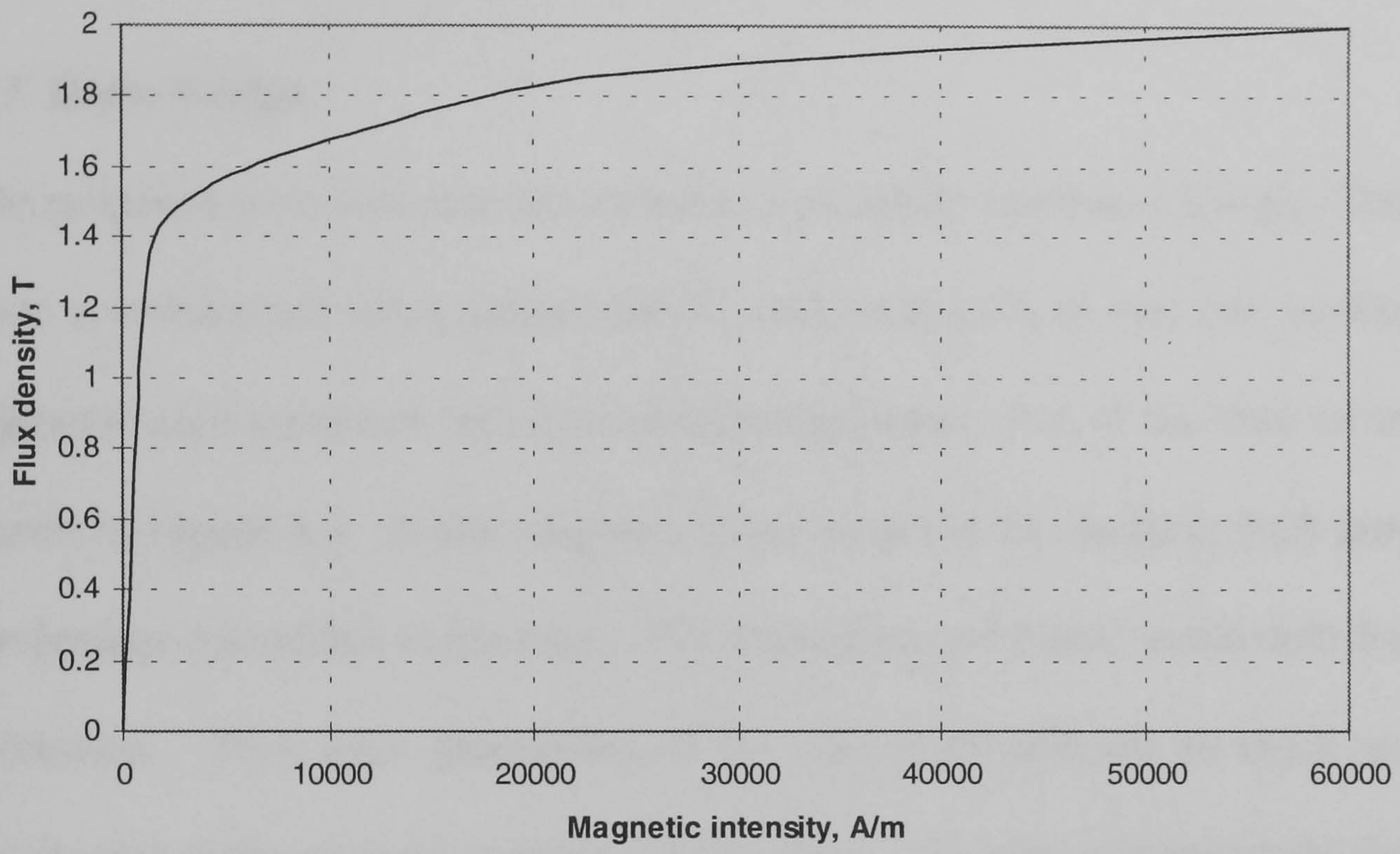

Figure 2.2 Magnetization curve for C-core material

2.4.2 Solution

Preprocessors are really problem defining programs, which account for all the data required to solve the problem. Solvers are programs for constructing the system of algebraic equations which mathematically model the physical situation and then produce solutions. The solver used was a non-linear, two-dimensional, magneto static solver in a Cartesian frame. It uses the Newton-Raphson method to solve the partial differential equations (2.5).

2.4.3 Postprocessing

The solution from the solver is the raw information about the electromagnetic field within the device, subject to the approximations made in the modelling and solution phases. The

required results may be extracted from the solver by further mathematical manipulation. Here, the post processor is used to examine the vector potential field, A, over the cross section of the machine for the defined excitation. The field solution is used to find the magnetizing inductances (L_{dm}, L_{qm}) and the torque output of the machine.

2.5 Rotor Design

The proposed rotor structure in this work is an axially laminated design. The four pole rotor is constructed using stripwound C-cores, each pole is split into twelve magnetic segments each separated by layers of insulating paper. Part of the rotor cross section is shown in Figure 2.3. A non magnetic frame keyed to the machine shaft provides rigid mechanical connection to the rotor. The laminations are bolted to the shaft for increased robustness. Five rotor geometries, G_1 to G_5, were analysed to reach an optimum distribution of the magnetic material over the rotor. The issue of stator tooth/ slot pitch was not considered due to accurate dimensions were difficult to get and one objective of this work is to investigate the torque ripple.

The ratio K_{fill} is different in each case, and is defined by:

$$K_{fill} = \frac{n_m t_m}{n_m t_m + (n_m - 1)t_p + t_f} \tag{2.7}$$

where

n_m : number of magnetic segments, which is 12

t_m : thickness of magnetic segments

t_p : thickness of insulation

t_f : thickness of non-magnetic frame

Details regarding the thickness and spacing of each segment are given in Table 2.1. For comparison a fixed width of magnetic segment plus insulation thickness was used, that is t_m+t_p is fixed. A value of n_m =12 was used through out the analysis.

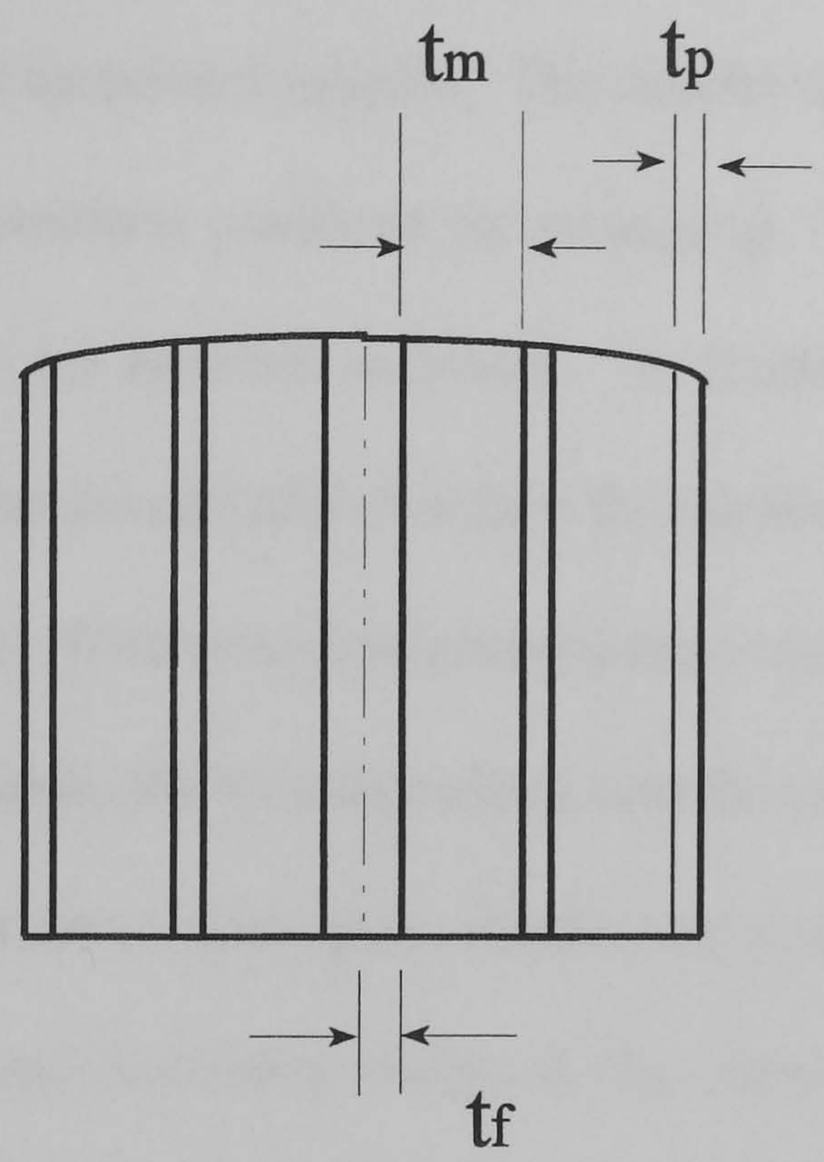

Figure 2.3 Axial view of a section of one pole of the stator

Most of the important performance parameters of the Synchrel machine depend on the saliency ratio (L_{dm}/L_{qm}), ζ, and the torque factor, K_{torque}, which is defined as (L_{dm}-L_{qm}). However, it does not follow that the highest saliency ratio rotor design gives the highest torque factor.

Saturation effects occur in the d axis due to the dominance of ferromagnetic paths. To investigate the saturation effect on the flux-current relationship, the machine has to be excited with different direct axis current, i_{ds}, from zero to rated current.

2.6 Stator Excitation

Suitable ampere turns have to be defined in each slot to produce the required mmf magnitude and orientation with respect to the *d* axis of the rotor. The rotor has to be incrementally stepped through a pole arc with the fundamental component of the mmf maintained at the required angle, α, with respect to the rotor direct axis. Each step requires a finite element model and associated solution. The smaller the incremental step, the larger the number of mmf distributions produced for averaging. Therefore a large number of models are required for an accurate solution. A fundamental current distribution approximation has been proposed [2.6] to reduce the number of finite element solutions required for each geometry. With sinusoidal phase current excitation and lumped windings, the mmf pattern developed by the windings alters significantly during rotation through a pole arc. Fourier analysis of the mmf space distribution produced by the stator windings shows that whilst the mmf waveform varies as the rotor rotates, for a fixed α, the fundamental magnitude remains constant. Each conductor slot is excited with ampere turns given by the integral of the fundamental mmf distribution over its slot pitch. Exciting the slots in this manner ensures that the mmf consists of the fundamental component with the low order space harmonics eliminated from the mmf pattern. The mmf still contains higher order harmonics at frequencies related to the number of slots per pole pair. The number of solutions to find average fundamental inductance values is reduced as the rotor needs only to be stepped across a slot pitch instead of over a full pole arc. A PASCAL program which interfaced to the MAGNET software was written to define stator slot excitation.

2.7 Results

The magnetising inductances L_{dm} and L_{qm} are required to evaluate machine performance. These values can be obtained from the magnetic field distribution, and evaluated if the *d*-

and q- axis flux linkages can be determined. A set of equivalent coils, n_d and n_q, that represent the d and q axis windings need to be defined [2.6]. Park's transformation can be used on the fundamental turns distribution of the three phase windings to yield an equivalent d and q axis turns distribution. Equivalent slot turns are defined by integrating the d and q axis turns over a slot pitch and lumping these into the slot. The total d and q axis flux linkages, ϕ_{dm} and ϕ_{qm}, are then calculated by summing the d and q axis linkage components from all the stator slots. The contribution from each slot is calculated using Eq. (2.6) and the equivalent axis turns in each slot. This also includes flux generated by slot leakage inductance. A further feature of this method is the ability to determine any cross-coupling effects between the direct and quadrature axes due to saturation or permeance variations. Table 2.1 defines each rotor geometry analysed and its performance. Figure 2.4 shows the variation of average direct axis flux, ϕ_{dm} with i_{dm}, for all five rotor geometries. Saturation effects are evident in all rotors. In the linear region ϕ_{dm} increases with i_{dm}, but the rate of the flux change decreases in the saturated region.

The variation of the saliency ratio with K_{fill} for all rotor geometries, for saturated and unsaturated conditions is shown in Figure 2.5. Increasing K_{fill} has the effect of decreasing the rotor path reluctance for the d-axis, hence increasing L_{dm}. This increase is slightly offset by an increase in L_{qm} (due to a q-axis decrease in reluctance path length). The q-axis path is air dominated, and iron saturation does not have a significant effect on L_{qm}. There is a slight increase in L_{qm} with K_{fill}, Table 2.1. When magnetic saturation is considered, the increase in L_{dm} with rotor K_{fill} is limited as the stator tooth iron is driven into saturation. Figure 2.6 shows K_{torque} plotted against K_{fill} for saturated and unsaturated conditions. This illustrates the need for non-linear analysis in order to obtain reasonable predictions for the torque output. In the unsaturated case, peak saliency occurs at $K_{\mathrm{fill}} = 0.67$ and the torque factor increases with K_{fill}. However the situation is different when saturation is accounted

for. Under this condition, the maximum saliency ratio occurs when $K_{fill} = 0.54$ and the peak value of k_{torque} occurs when $K_{fill} = 0.68$. Maximum ζ and K_{torque} do not coincide. A trade off between the rotor geometry with ζ and with K_{torque} is necessary.

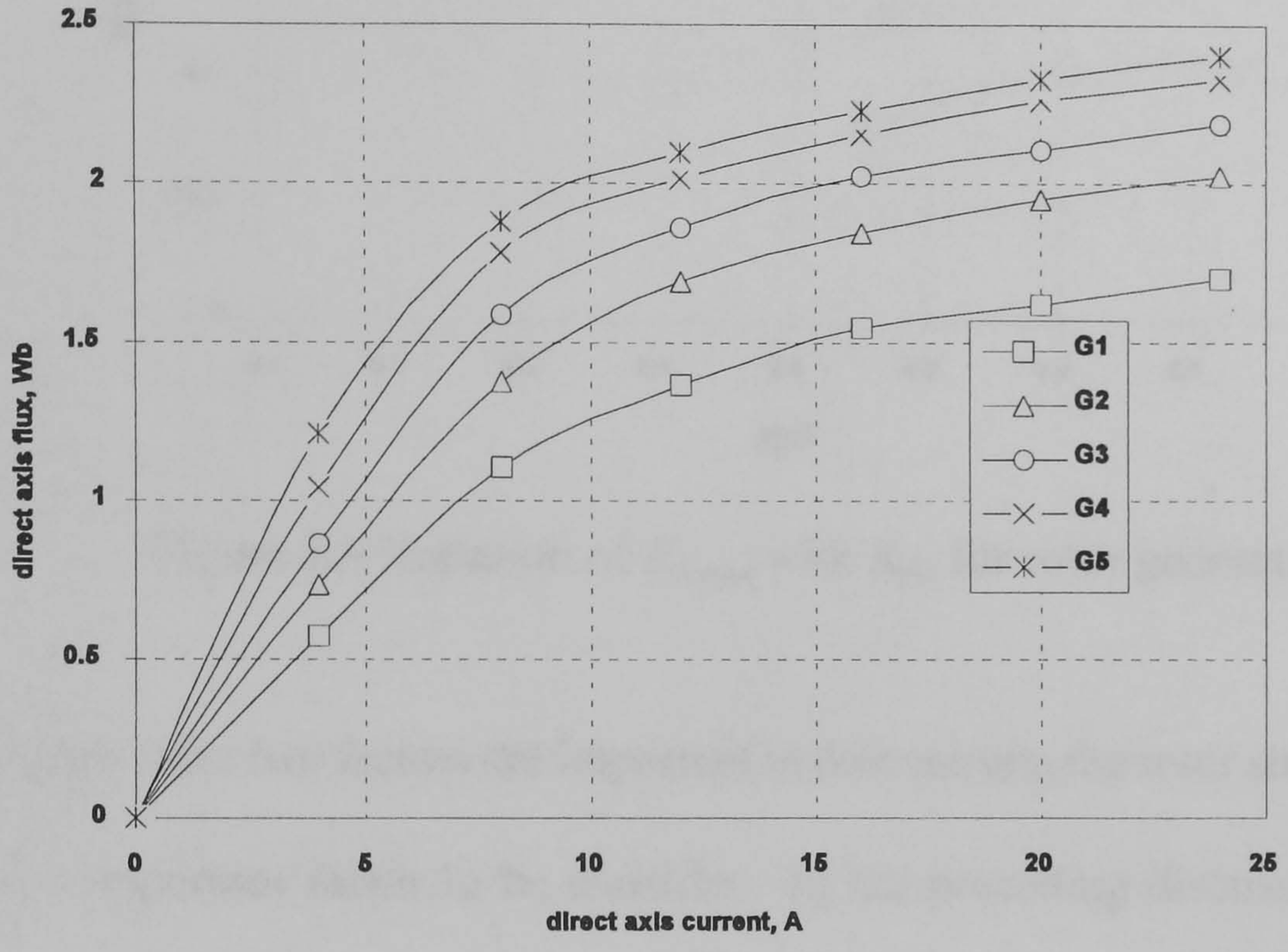

Figure 2.4 Variation of ϕ_{dm}-i_{ds} for rotor geometries G_1 to G_5

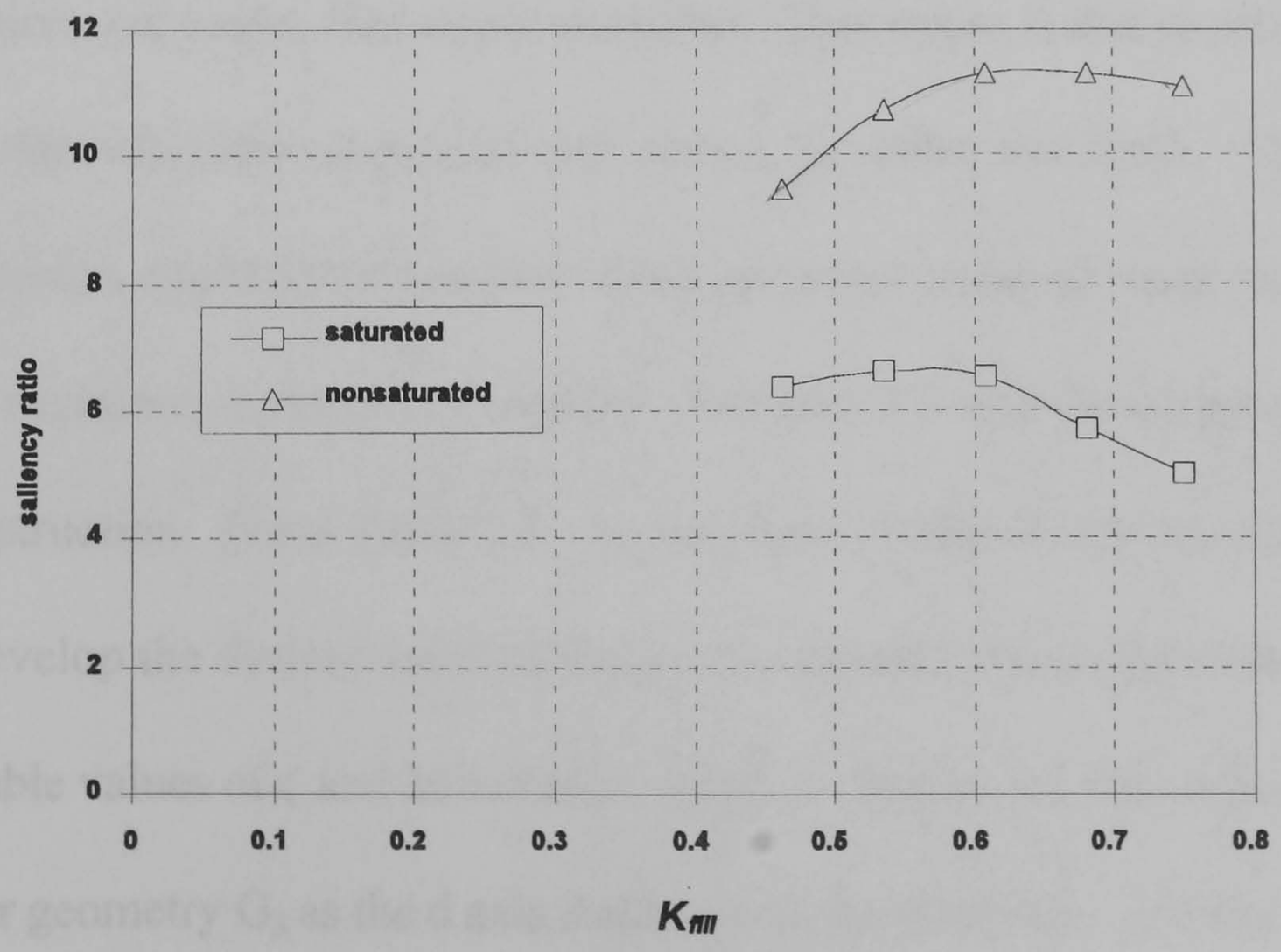

Figure 2.5 Saliency ratio, ζ, variation with K_{fill} for rotor geometries G_1 to G_5

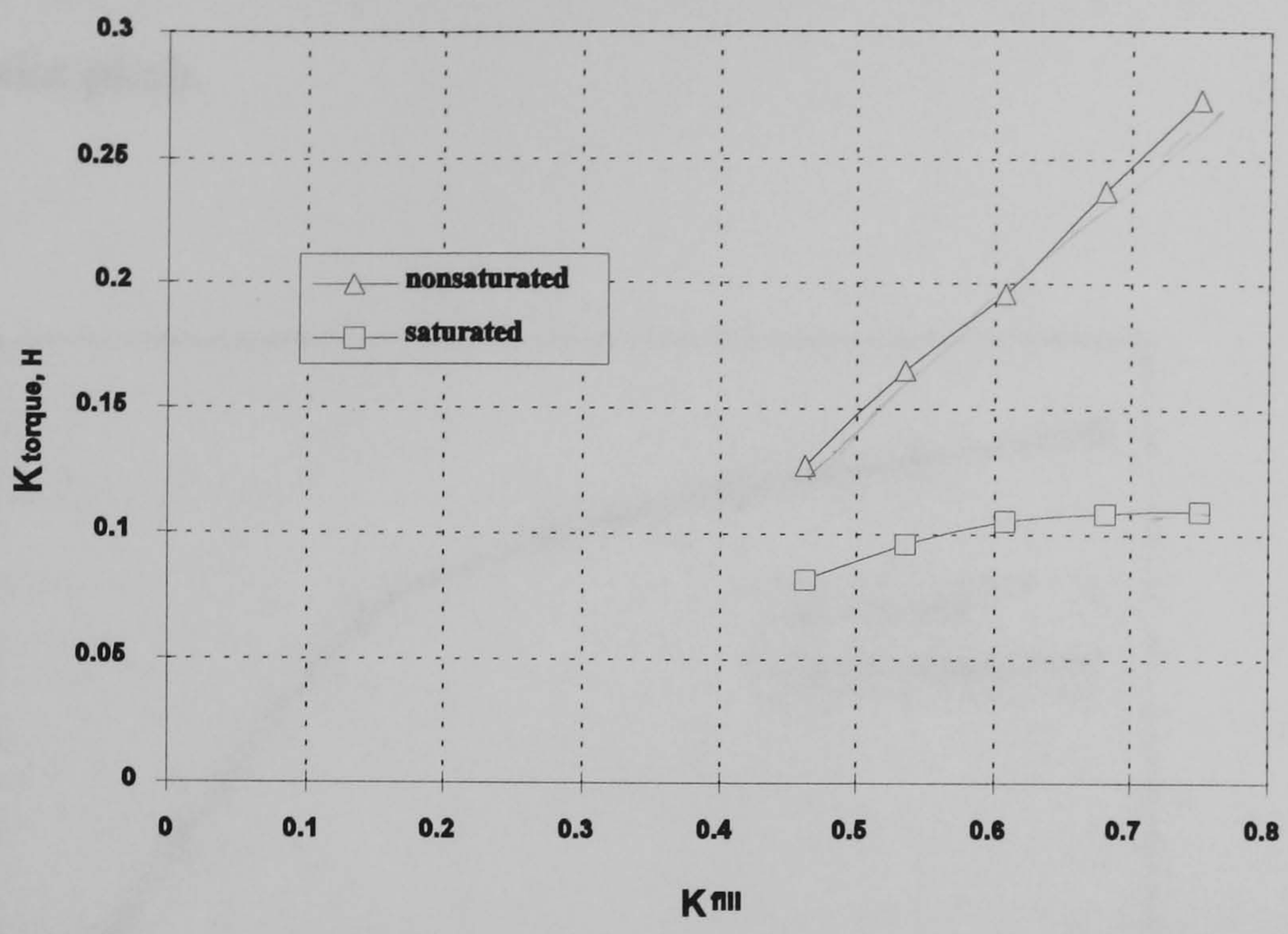

Figure 2.6 Variation of K_{torque} with K_{fill} for rotor geometries G_1 to G_5

Though these two factors are important in determining the rotor structure, inductance ripple is an important factor to be consider. In the preceding discussion, the flux ripple was averaged over a slot pitch. This was imposed so as to yield an initial estimate of ζ and K_{torque} or for each geometry. The post processing section of MAGNET has been used to estimate the percentage inductance variation for each geometry. With a constant mmf magnitude and angle, flux ripple occurred. This ripple is due to reluctance path changes as the rotor magnetic segments step across the stator slot pitch. This inductance ripple causes torque ripple in the machine when operating under constant axis current control, as will be explained in detail in Chapter 6. Structure G_3 was the compromised rotor selected for construction. From Table 2.1, G_3 does not give the minimum inductance ripple but it does develop the desired value of torque, compared with an IM of the same size, and has reasonable values of ζ and inductance variation. Figure 2.7 shows the ϕ_{dm}- i_{dm} relationship for rotor geometry G_3 as the d axis shifts across the slot pitch. The first curve has the d-axis

aligned with the center line of the slot. The second curve has the rotor shifted by five electrical degrees from this initial position with respect to the slot. This shift represents half a slot pitch.

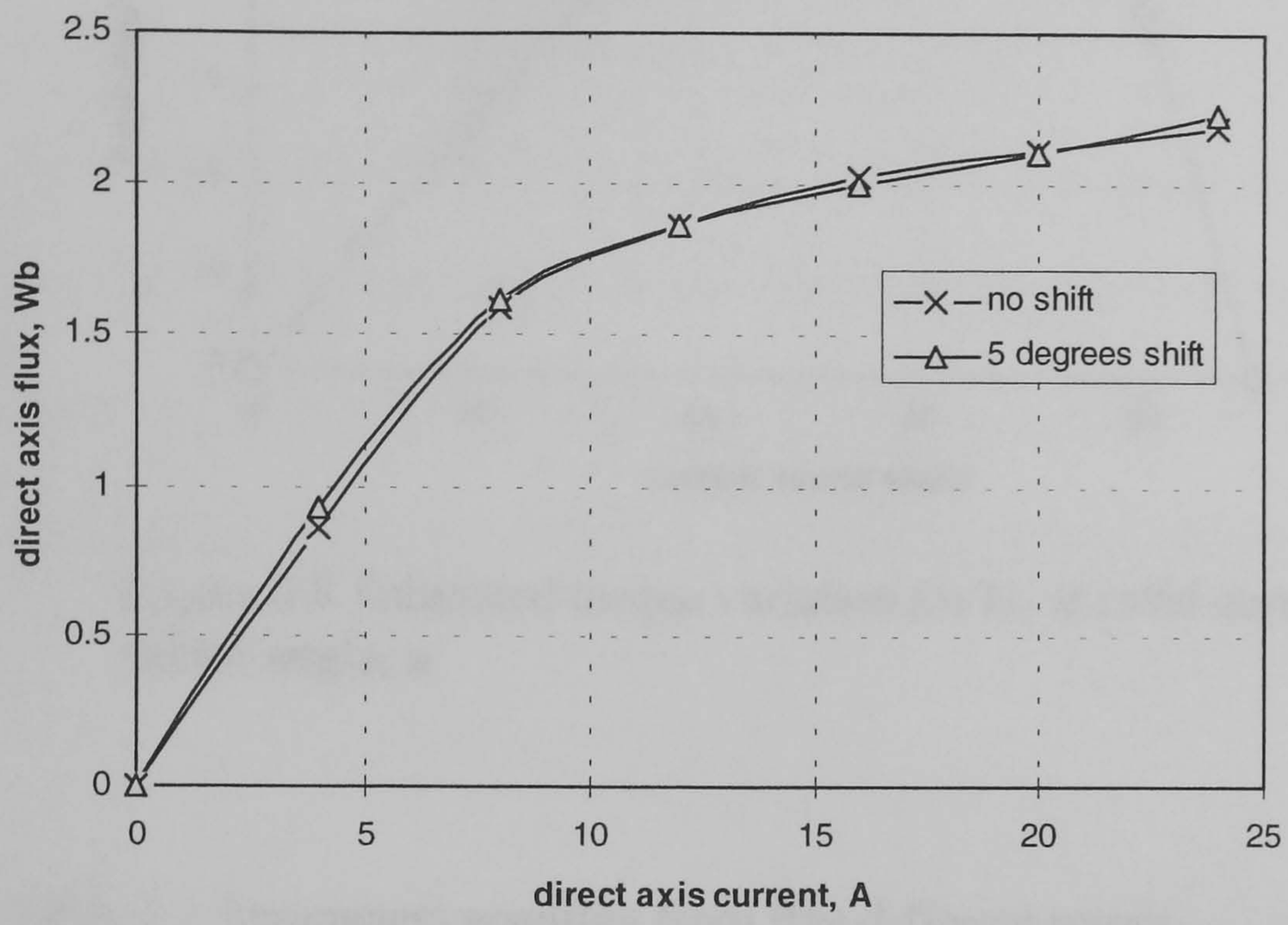

Figure 2.7 Variation in ϕ_{dm}-i_{dm} relationship over a slot pitch with G_3

Torque Estimation

The torque equation can be expressed by

$$T = \frac{3}{2} P(\phi_{dm} i_{qs} - \phi_{qm} i_{ds}) \tag{2.8}$$

The average torque output with an applied current vector can be estimated using this equation. The non-linear ϕ_{dm} - i_{dm} relationship for G_3 determines the torque- current vector angle, α, relationship shown in Figure 2.8. The q-axis flux is assumed linear and given by

$$\phi_{qm} = L_{qm} \; i_{qm} \tag{2.9}$$

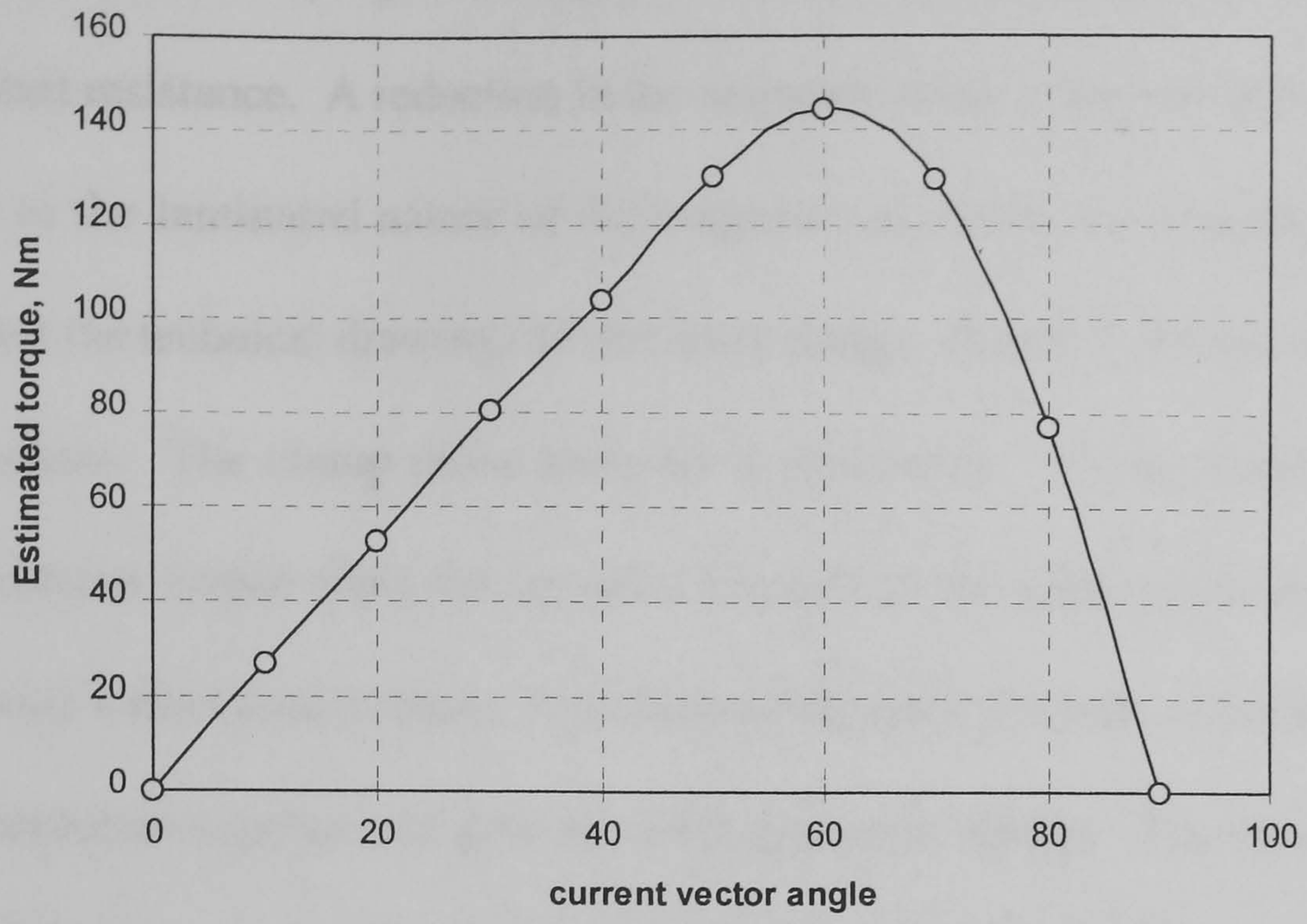

Figure 2.8 Estimated torque variation for G_3 at rated current with current vector angle, α

Table 2.1 Parameters resulting from five different rotors

	t_m *mm*	t_p *mm*	K_{fill}	ζ	T_{max} *Nm*	L_{dm} *H*	ΔL_d%	L_{qm} *H*
G_1	1.8	2.1	0.46	6.38	111	0.096	2.13	0.015
G_2	2.1	1.8	0.54	6.64	131.9	0.113	3.21	0.017
G_3	2.4	1.5	0.61	6.55	144.6	0.124	2.19	0.019
G_4	2.7	1.2	0.68	5.69	148	0.13	1.33	0.023
G_5	3.0	0.9	0.75	5	148.6	0.135	0.75	0.027

2.8 Constructional Details of The Rotor Design

A prototype rotor was designed and built with a K_{fill} value of 0.61, which was constrained by lamination and non-magnetic spacer thickness. Stripwound C-cores were used as the basis for constructing the rotor. The magnetic segments in each pole consist of groups of laminations from the C-cores. Electrically insulation between the magnetic laminations is

provided by both epoxy resin used in the core manufacture and by the high inter-lamination contact resistance. A reduction in the magnetic cross sectional area of the segment occurs due to the laminated nature of the magnetic segments, viz, 'stacking effects'. Figure 2.9 shows the technical drawings of the rotor design. Figure 2.10 shows a pole arc of the rotor structure. The clamp piece material is aluminum. These clamps are used to transfer developed torque from the inverted C-cores to the steel shaft through the bolts and to provide a rigid construction. Non-ferrous, phosphor-bronze, cross bolts are used to clamp the structure together and give the whole structure rigidity. The cross bolts are electrically insulated to avoid a closed-loop current path and the formation of a squirrel cage.

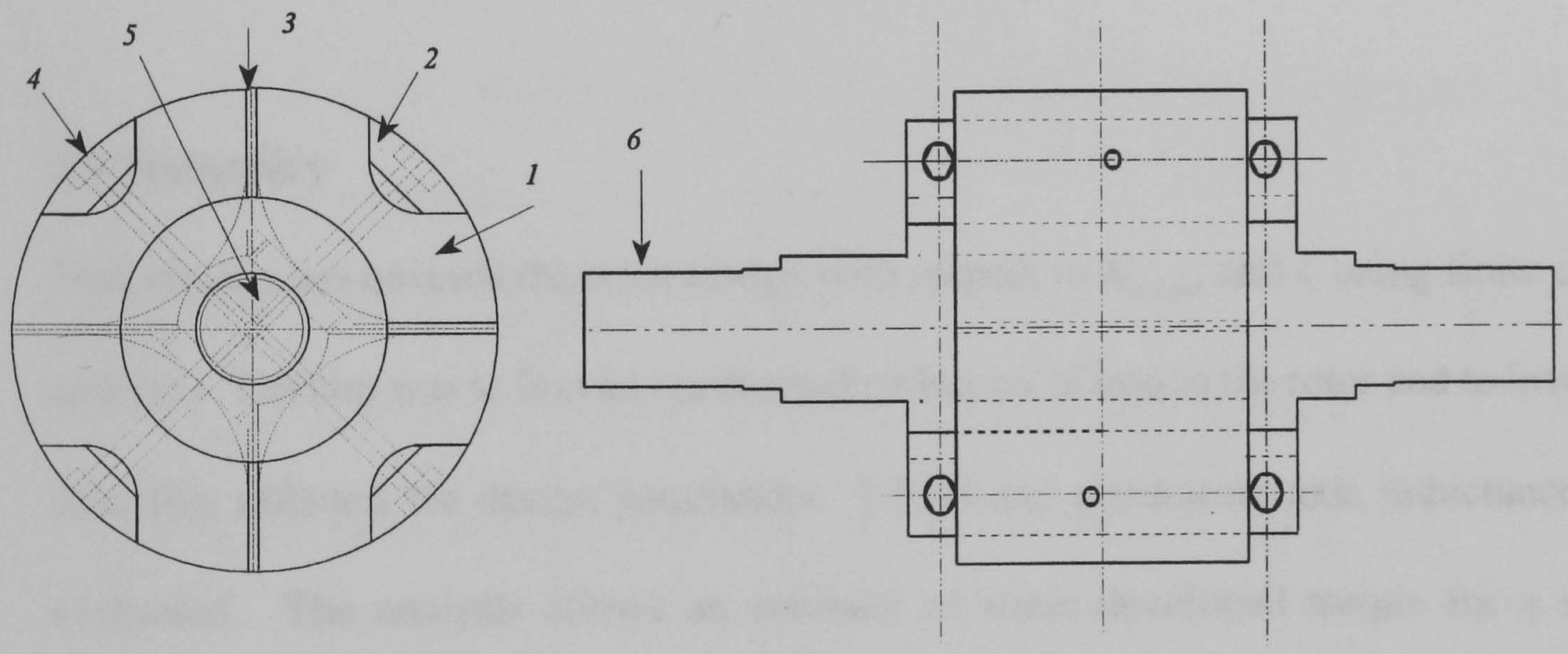

Figure 2.9 Mechanical drawings of the rotor design
a side-view b elevation

1 Lamination section
2 Aluminum clamp
3 Non-magnetic frame
4 Clamp bolts
5 Stainless bolts
6 Rotor shaft

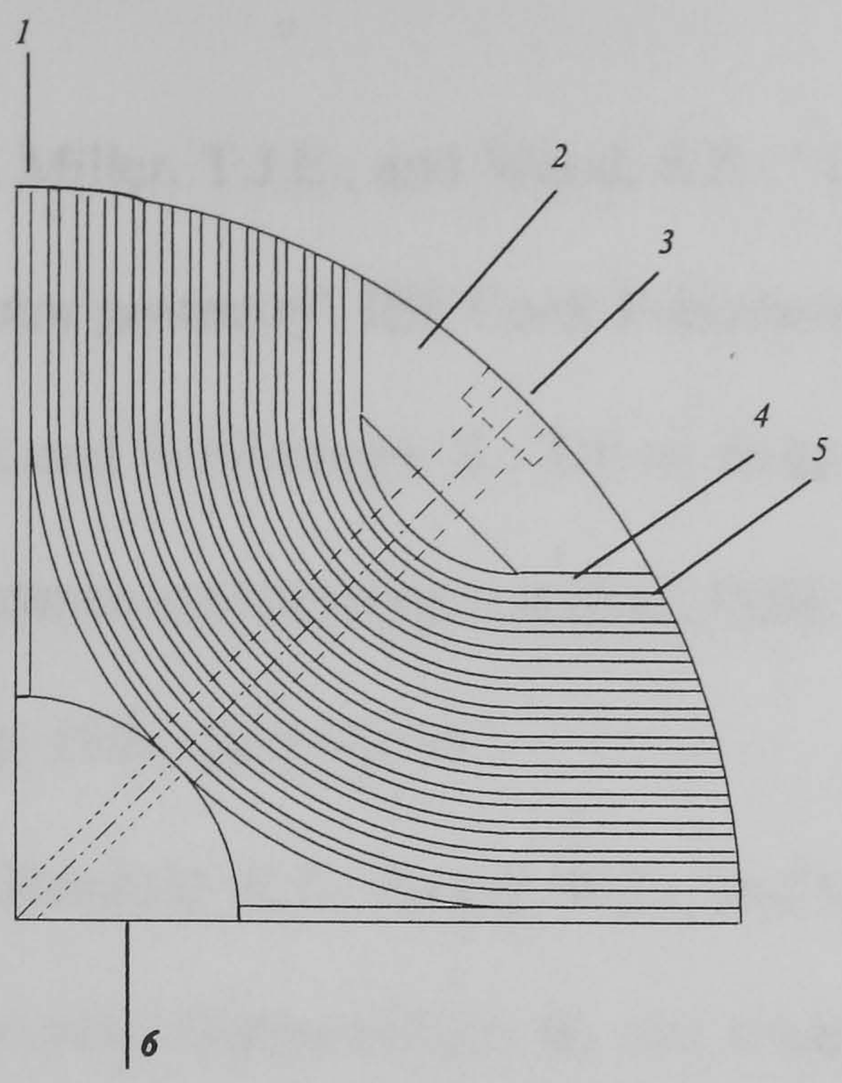

Figure 2.10 Pole arc of the rotor structure

1 Non-magnetic frame
2 Aluminum clamp
3 Cross bolts (isolated)
4 Magnetic lamination
5 Insulating paper
6 Shaft

2.9 Summary

This chapter has covered the rotor design with respect to K_{torque} and ζ using finite element analysis. The aim was to find an optimum distribution of iron in the rotor and to investigate how this affected the design parameters. Direct and quadrature axis inductances were evaluated. The analysis allows an estimate of static developed torque for a specific excitation. The analysis does not account for the effects of loss phenomenon in the ferromagnetic material and their effects on the field distribution and torque production of the machine. End winding inductance effects have been neglected. A detailed design of the prototype rotor was presented.

References

2.1 Staton, D.A., Miller, T.J.E., and Wood, S.E.: ' Optimisation of the synchronous reluctance motor geometry', IEE Conf. Publication, 1991, No. 341, pp. 156-160

2.2 Kamper, M.J, and Williamson, S.: 'Direct finite element design optimisation of cageless reluctance synchronous machine', IEEE Trans. Energy Conversion, Vol. 11, No. 3, Sep. 1996, pp 547-555

2.3 Staton, D.A, Deodhar, R.P., Soong, W.L., and Miller, T.J.E.: 'Torque prediction using the flux-mmf diagram in ac, dc, and reluctance motors', IEEE Trans. Ind. Applicat., Vol. 32, No. 1, Jan. /Feb .1996, pp. 180-188

2.4 Kraus, J.:' Electromagnetics', Third Edition, McGraw-Hill Book Co., Singapore, 1988

2.5 Lowther, D.A., and Silvester, P.P.: 'Computer aided design in magnetics', Springer-Verlag New York Inc., New York, 1986

2.6 Chari, M.V.K, Csendes, Z.J., Minnich, S.H, Tandon, S.C. and Berkery, J.: 'Load characteristics of synchronous generators by the finite element method', IEEE Trans. Power App. and Sys., Vol. 100, No. 1, Jan. 1981, pp.1- 9

Chapter 3

Drive System Description

3.1 Introduction

The hardware implementation for vector control of the Synchronous reluctance machine (Synchrel) and position control using the sliding mode technique is described in this chapter. The computing performance required to implement vector control and the sliding mode algorithm can be achieved with a 16-bit fixed point SAB 80C 166 embedded controller. This controller has integrated peripheral subsystems to reduce CPU intervention to a minimum. It performs analogue to digital conversion, pulse width modulation (PWM) generation and interfaces the shaft encoder.

3.2 System Requirements

Vector control of the Synchrel machine can be achieved by regulating the magnetising current vector, i_{dqm}, or the stator current vector, i_{dqs}, if core losses are disregarded. This can be done by monitoring the stator phase currents i_a, i_b and i_c and rotor position.

The hardware required to implement vector control and the sliding mode algorithm comprises the following major components:

i) A processor board to carry out the calculations necessary for vector control and sliding mode control. The micro-controller SAB 80C 166 was chosen to perform the drive system control since it integrates peripherals and is available as a fully supported development system.

ii) A PWM generator circuit with three phase complementary channels and dead time

included. This dead time is to prevent two series connected devices being simultaneously energised.

iii) A multi-channel analogue to digital converter.

iv) An interface for a shaft position encoder. The interface circuit keeps track of absolute position and provides an interrupt to the processor when the position changes.

v) A board for measurement of the currents applied to the motor, with isolation between the motor supply and the signals supplied to the SAB 80C 166 A/D.

vi) Gate drive circuits that convert the TTL PWM generator signals into isolated high and low side gate signals of the correct drive voltage to turn the power switches on or off.

vii) A power inverter is required to provide the machine input power (the machine rating is 15 kW, 415 V).

An overview of the complete system is given in the next section.

3.3 Drive System Overview

The structure of the drive system is shown in Figure 3.1. The Synchrel machine is connected to the dc machine via a strain gauge torque transducer, and the shaft position encoder is mounted on the other shaft end. The PC is used to down load the control algorithm to the micro-controller. The SAB 80C 166 reads the inputs, current

measurements via Hall-effect current transducers and rotor position using a 2048 pulse per revolution incremental shaft encoder. The processor carries out the control algorithm for vector control and sliding mode for position control. The phase voltage commands are calculated and transferred to the gate drive circuits of the inverter, thereby providing the voltage vector applied to the machine. The torque measurement transducer is a strain gauge type. The resistive load for the dc generator load is rated at 15 kW and has a fan for ventilation.

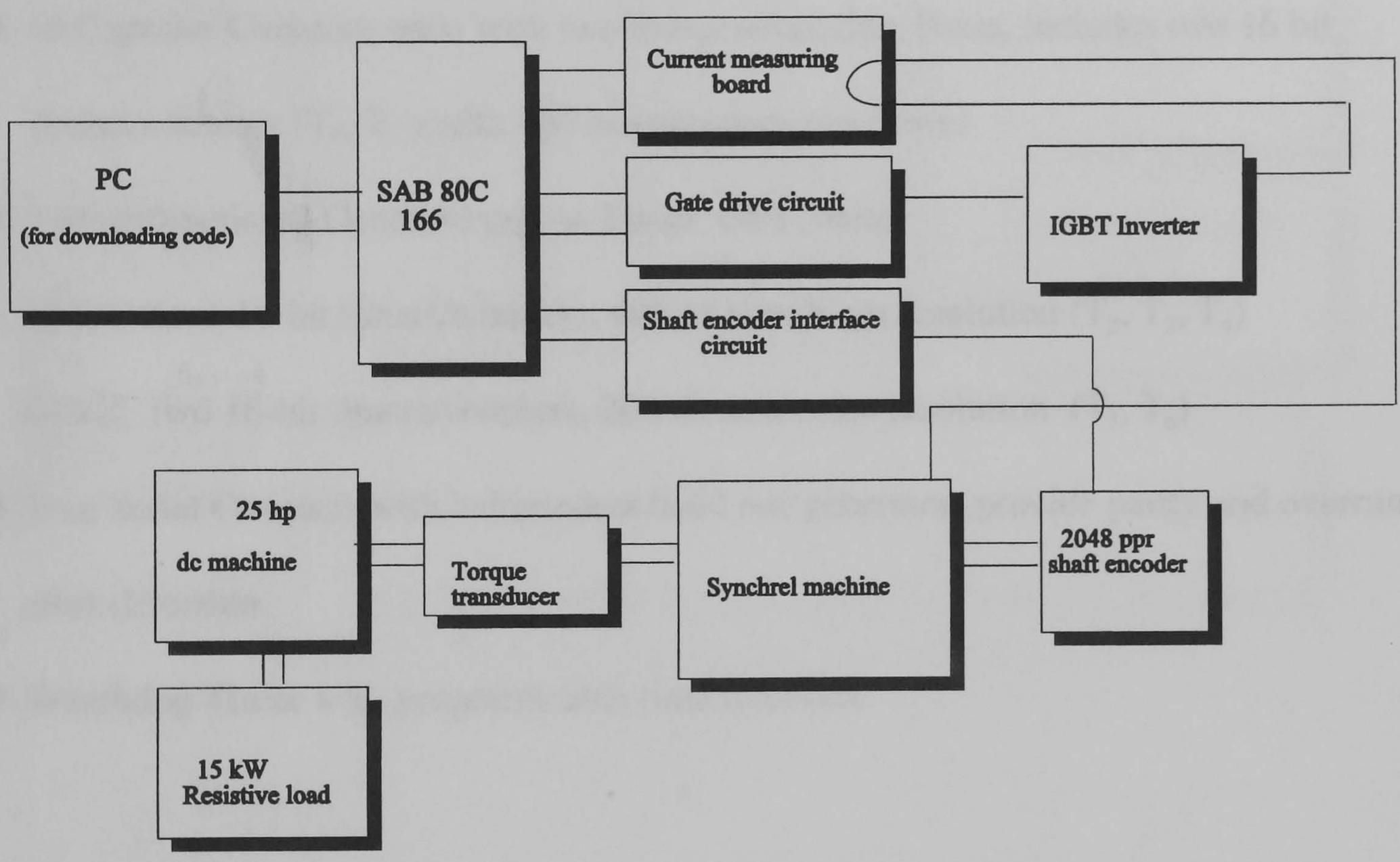

Figure 3.1 Overall view of drive system structure

3.3.1 SAB 80C 166 Board

The fixed-point 16-bit SAB 80C 166 micro-controller for embedded control applications is from Siemens. Embedded control applications often have restrictions concerning board space, power consumption and overall system cost. Therefore, micro-controllers which provide a high level of system integration eliminate the need for additional peripheral

devices. The SAB 80C 166 has been designed to meet the high performance requirements of real-time embedded control applications. It operates at a clock frequency of 20 MHz, and has a 100 ns minimum instruction cycle time, with most instructions executed in one cycle. The Intelligent peripheral subsystems are integrated to minimise CPU intervention. The SAB 80C166 functional block diagram in Figure 3.2 shows the intelligent peripheral modules that have been integrated on the embedded controller.

Intelligent peripheral subsystems:

- 10-Channel 10 bit A/D Converter, 15 µs conversion time with four conversion modes
- 16 Capture/ Compare units with two independent time bases, includes two 16 bit timers/counters (T_0, T_1) with 400 ns maximum resolution
- 2 Multifunctional General Purpose Timer, GPT, units:

  GPT1: three 16-bit timers/counters, 400 ns maximum resolution (T_2, T_3, T_4)

  GPT2: two 16-bit timers/counters, 200 ns maximum resolution (T_5, T_6)
- Two Serial Channels with independent baud rate generators provide parity and overrun error detection
- Watchdog Timer with programmable time intervals

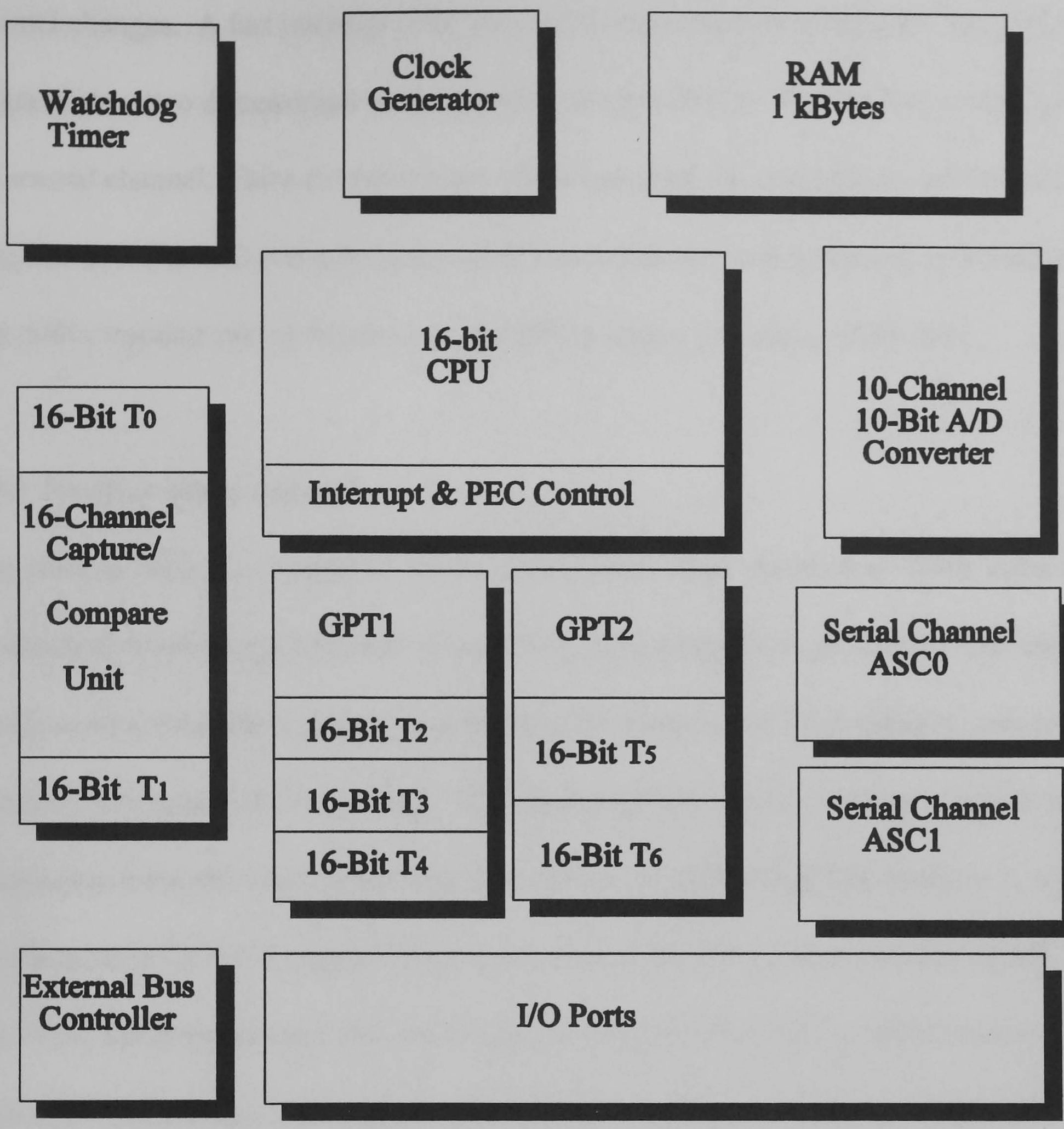

Figure 3.2 SAB 80C 166 Functional Block Diagram

3.3.2 Current Measurement

The machine line currents must be monitored. Hall-effect current transducers are used for these measurments and give isolation between power and measurement circuits. The SAB 80C 166 supports four different A/D conversion modes, viz., single channel, single channel continuous, auto scan, and auto scan continuous conversion. In this application, two channels are used for i_a and i_b and the third phase, i_c, will be the negative sum of the first two currents. The auto scan conversion mode was chosen to perform this conversion. In

this mode any set of analogue input channels can be converted without requiring software channel changes. A fast interrupt (PEC) is used to move the converted data from the result register into a two dimensional array stored in on-chip RAM. The process is repeated for the second channel. Once the conversion of the two channels is complete, a CPU interrupt is generated. The A/D converter waits until a start conversion is generated by the software. The A/D sampling rate is the same as the PWM carrier frequency (4.88 kHz).

3.3.3 Position Measurement

The rotor position is measured by an incremental shaft encoder of 2048 pulses per mechanical revolution. The shaft encoder has three channels A, B and Z. The encoder interface uses these three signals to determine the direction of shaft rotation and to keep a count of the current shaft position. The shaft position count is reset by a marker pulse, Z, received once per revolution from the encoder. A differential line receiver is used to interface the +5 V-24 V signals from the encoder to the TTL levels of the SAB 80C 166. An 11-bit up/down counter that recirculates a count of 0 to 2047 is implemented in the SAB 80C 166 using a GPT1 timer. This timer is clocked at an external input pin by an encoder transition. Another pin is used to determine the count direction, up or down. The Z-pulse ensures absolute shaft position once per revolution by reseting the counter every mechanical revolution. The counter interrupts the processor when a position change is detected. A fast interrupt is used to read the new position data. For high precision control of the Synchrel machine, absolute position information is essential. However absolute encoders are more expensive than incremental types. Thus the former are not viable for commercial low cost drive systems. Incremental encoders can be used to give absolute position but require uncontrolled motor rotation at start-up to facilitate system synchronisation. This ensures that the up/down counter is synchronised with the Z pulse.

Speed information is needed for the sliding mode algorithm. This was obtained by measuring the period between two consecutive pulses from the position sensor thereby acheiving good precision at low speeds.

3.3.4 Pulse Width Modulation Generator

Pulse width modulation, PWM, is an alternative to feeding the drive with pure three phase sinewaves from the mains supply. Since the sine waves are synthesised, variable sine wave frequency and magnitude allows variable motor speeds. With this technique, motor starting becomes controlled and simple.

A fixed carrier frequency (4.88 kHz) pulse width modulation scheme is implemented. A saw-tooth wave with the aformentioned frequency was generated using the 16-bit Capture and Compare units and a 16 bit timer, T_1, with 0.4 μs resolution. By cascading two compare registers to drive a single I/O pin, center aligned (triangular) PWM is produced. A 120 degrees phase shift between the three PWM channel is introduced. In addition to three PWM channels, a further three PWM complementary outputs were produced by identical software except the initial value of the I/O pin is set to 1 rather than 0. Dead time, or under-lap period, is introduced to prevent two series connected power devices conducting simultaneously. A 1.2 μs under-lap time was chosen (according to the charateristics of the inverter devices) to delay turn on. However using dead time will reduce the maximum possible duty cycle ratio of the PWM, hence reducing output voltage.

3.3.5 Digital to Analogue Converter

A digital to analogue, D/A, converter was used to display system variables on an oscilliscope. These variables are *d*- and *q* axis currents and voltages, position and speed. The D/A was positioned on the wirewrap-field of the evalution controller. A quad 8-bit

voltage output D/A converter was used to allow monitoring of four variables simultaneously. Additional software and hardware is needed to interface the D/A conveter. Each D/A channel is updated after every control cycle period.

3.3.6 The power stage

Figure 3.3 shows the inverter bridge connected to the Synchrel machine. The power

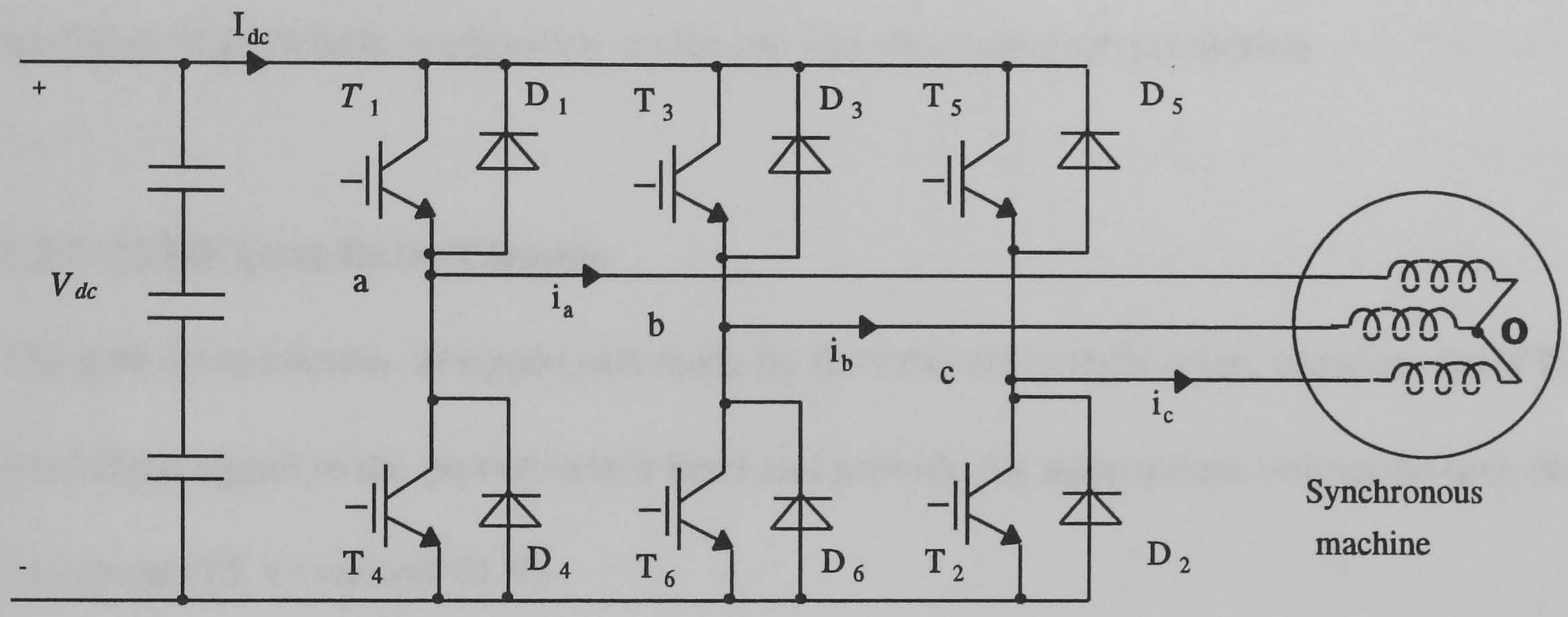

Figure 3.3 Inverter bridge connected to the Synchrel machine

inverter consists of a dc link, six gate drive circuits and a six switch bridge. The dc link is obtained from three-phase bridge rectification of the mains (415 V). The rectified dc output from the rectfier bridge (600 V) is smoothed by an electrolytic capacitor bank. The capacitor bank comprises three series connected 8500 μf, 250 V capacitors with a 10kΩ, 5W sharing resistor on each capacitor. These resistors balance the voltage distribution across each capacitor due to different leakage currents and also provide a capacitor energy discharge path at power down [3.1].

The inverter switching devices, T_n, figure 3.3, are insulated gate bipolar transistors (IGBT), Siemens of type BSM150GB160D (150 A and 1600 V). The inverter consists of three modules, each has two IGBTs and two freewheeling diodes. Each leg module is decoupled

at its terminals by a polypropylene capacitor.

The three isolated IGBT modules are mounted directly on a fan-cooled heat sink. Two fans are used to provide forced air cooling so as to enhance heatsink utilisation and hence lower device junction temperatures, thus improving device reliability. Stray inductances were minimised by making interconnection lengths as short as possible. A high speed semiconductor fuse is placed between the dc link capacitors and the inverter to help protect the switching devices. Further signal level hardware protection is afforded by discrete hardware logic which implements under-lap and shoot through protection.

3.3.7 IGBT Gate Drive Circuits

The gate drive circuits, designed and made by the laboratory technician, translate the TTL level input signal to the power switch level and provide the appropriate voltage to turn the switch on (15 V) and off (0 V).

Each IGBT has an associated drive board to control its gate charge. Electrical isolation between the input circuity of the drive board and the gate drive electronics was provided by two ferrite cored transformers. The 15 V unipolar supply for the gate drive circuity on the device side is derived from a 2 MHz switched mode supply, transformed through one of the small toriodal cores. The second transformer was used to transmit the PWM signal to the gate drive electronics. The ferrite transformers provided isolation between the IGBT highside voltage levels and the low voltage control electronics supplying the PWM signals.

3.4 SAB 80C 166 Programming

The machine drive system shown in Figure 3.1, consists of a Synchrel machine, a mechanical load (dc machine loaded with resistive load) and a power electronic converter (current controlled voltage source IGBT three phase inverter). The controller handles the

power flow to the machine so as to achieve the desired rotational performance. The performance of any drive system is largely dependent on the control algorithm and its implementation. A SAB 80C 166 embedded controller was used to implement vector control and sliding mode algorithms with sampling rates of 2.45 kHz and 1.63 kHz respectively. The block diagram in figure 3.4 shows the algorithm required for the practical implementation of vector control. The code was written in 'C'-language. As programs for embedded control applications become larger, high level languages are preferred since the code is easier to write and debug. Siemens offers a complete set of software and hardware development tools, including a 'C' compiler, assembler, linker, locater, librarian, object-to-hex converter, simulator and in circuit emulator. These factors are important in a control system with a short, specified execution cycle as in this drive system. The code written for torque vector control is given in Appendix B and the additional code for the sliding mode algorithm is in Appendix C.

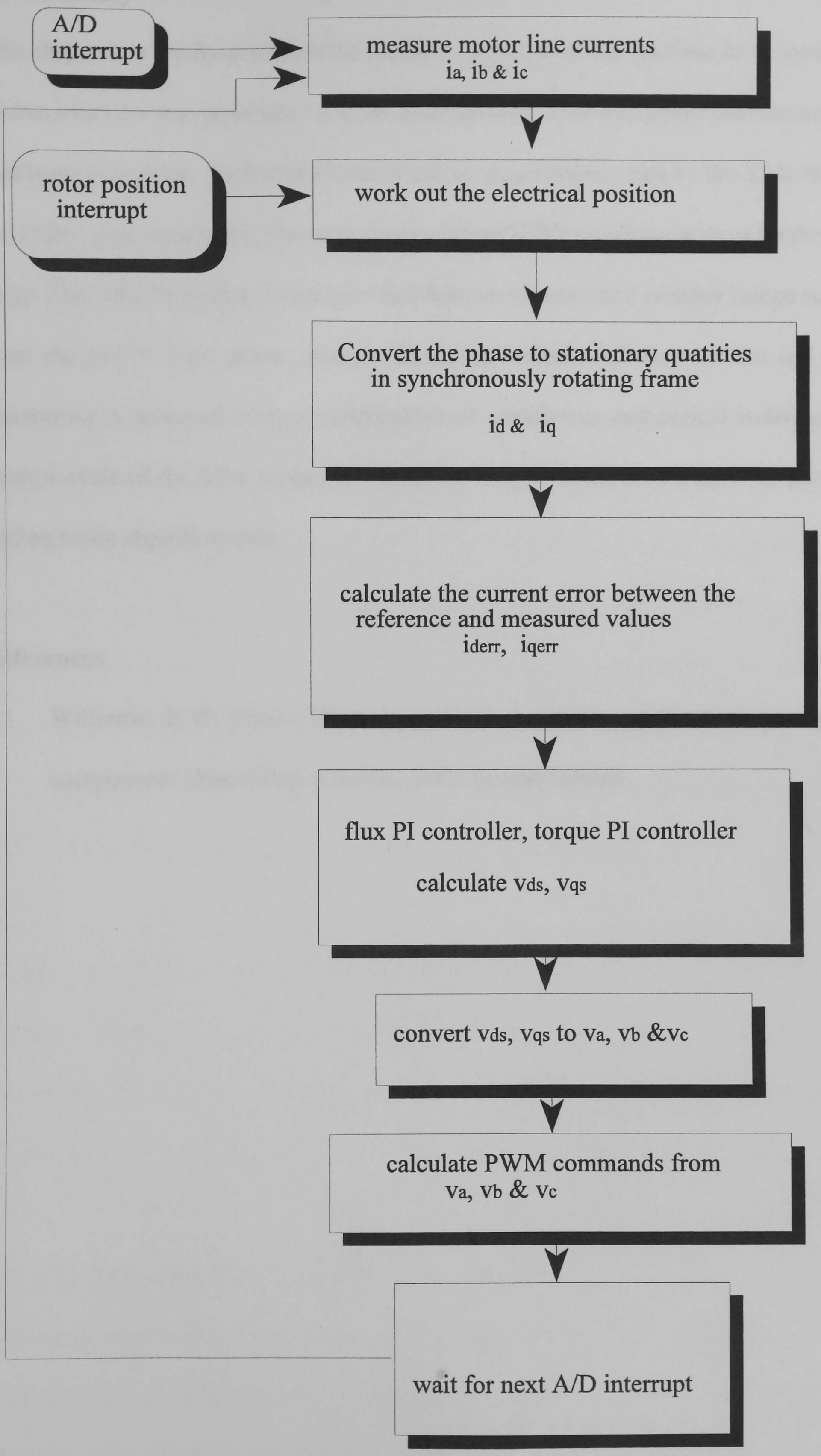

Figure 3.4 Vector control algorithm as implemented on the SAB 80C 166 board

3.5 Summary

This chapter has briefly described the hardware structure of the machine drive system. A system overview was presented. A brief description of current and position measurement hardware was given. Embedded control and its requirements, met by the SAB 80C 166 controller, were mentioned. The drive system utilises IGBT switching devices for the power stage. They operate from a dc link provided from an uncontrolled rectifier bridge supplied from the 415 V three phase mains. Electrical isolation between control and power electronics is achieved using a combination of transformer and optical isolation. The control cycle of the drive system is 408 μs for torque vector control and 612 μs for the sliding mode algorithm code.

References

3.1 Williams, B.W.:'Power Electronics: Devices, drives, applications and passive components', Macmillan, London, 1992, Second Edition.

Chapter 4

Vector Control

4.1 Introduction

Electric drives are mostly chosen to perform motion control, which can be defined as torque, speed and position control. Continual advances in power electronics and digital control through the use of micro-controllers or digital signal processors have led to significant developments in variable speed drive systems for applications such as computer peripherals and servo applications which includes machine tools and robotics. Brushless machines in drives are a mature technology, with a sizeable world market that is expanding faster than that of the dc machines. Vector control techniques have made it possible to use brushless machines in high performance applications where dc machines were traditionally used. With a vector control strategy, controllers control both the amplitude and phase of ac excitation. In other words *d*- and *q*-axis components of the stator current vector are decoupled, so as to give independent control of each component.

In this chapter, the *d-q* transformation for the Synchrel machine in a synchronously rotating reference frame is outlined from which the torque equation is deduced. Two vector control strategies are considered. Maximum torque per ampere control (MTC) and constant current in the inductive axis control (CCIAC) techniques are experimentally assessed.

4.2 D-Q Transformation of the Synchrel Machine

A dynamic model of the machine is necessary for the understanding and design of a vector controlled drive. In the late 1920s, Park introduced a new approach to electric machine analysis. The variables, voltages, currents and flux linkages, of the stator windings of a

synchronous machine are replaced with variables associated with fictitious windings rotating on the rotor. Park's transformation revolutionized electric machine analysis. This is because this transformation has the unique property of eliminating all time varying inductances from the voltage equations of the synchronous machine. These time varying coefficients arise due to the relative motion of electric circuits and varying magnetic reluctance of the magnetic circuit. Kron introduced a change of variables which eliminated the time varying inductances of a symmetrical induction machine by transforming both the stator and rotor variables to a synchronously rotating reference frame. Other researchers developed similar variable changes to suite the particular application. Later it was found that the transformations used for induction machine analysis are contained in one general transformation, which refers the stator and rotor variables to what is called arbitrary reference frame where the appropriate speed of rotation is assigned to this frame. The stator variables of a synchronous machine can be referred to the arbitrary reference frame. Subsequently it was found [4.1] that the time varying inductances of a synchronous machine are eliminated only if the variables are referred to a reference frame fixed to the rotor.

Variables which formulate a transformation of the three phase variables of the stationary circuit elements to the synchronously rotating reference frame may be expressed as follows:

$$f_{dq0} = K_p f_{abc} \tag{4.1}$$

where f can be voltage, current or flux

$$(f_{dq0})^T = [f_{ds} \quad f_{qs} \quad f_{0s}]$$

$$(f_{abc})^T = [f_a \quad f_b \quad f_c]$$

$$K_p = \sqrt{2/3}\begin{pmatrix} \cos\theta & \cos(\theta-2\pi/3) & \cos(\theta-4\pi/3) \\ \sin\theta & \sin(\theta-2\pi/3) & \sin(\theta-4\pi/3) \\ 1/2 & 1/2 & 1/2 \end{pmatrix} \tag{4.2}$$

The transformation to the arbitrary reference frame involoves a change of variables that need no physical connotation. However it is convenient to visualize the transformation equations in a phasor diagram, Figure 4.1.

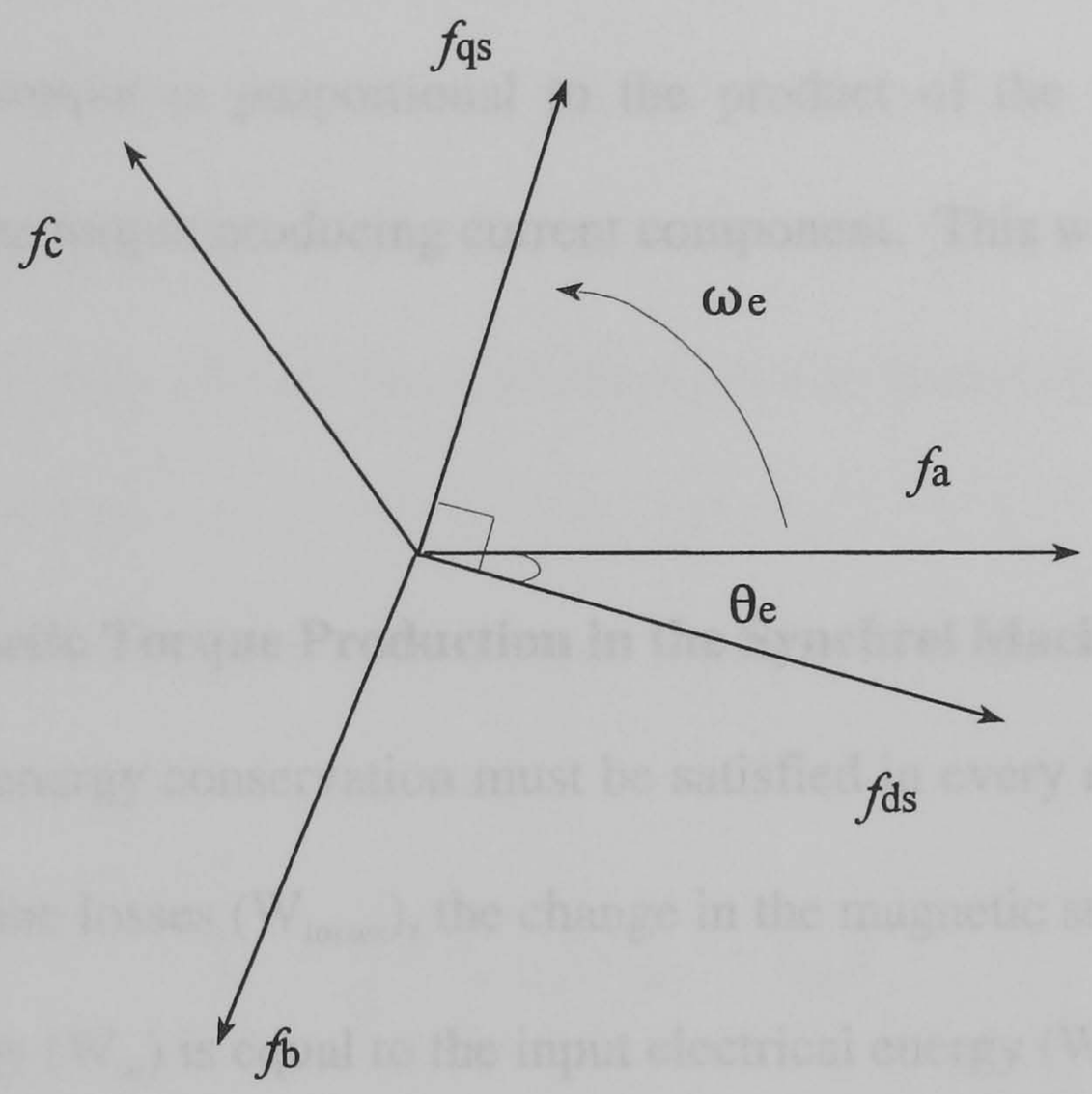

Figure 4.1 phasor diagram of three phase system, *abc* transformation to *d-q* reference frame

The *d-q* equations representing the machine in the synchronously rotating reference frame given in (1.6) are presented as:

$$\begin{aligned} v_{ds} &= r_s i_{ds} + \frac{d\phi_{dm}}{dt} - \omega_e \phi_{qm} \\ v_{qs} &= r_s i_{qs} + \frac{d\phi_{qm}}{dt} + \omega_e \phi_{dm} \end{aligned} \tag{4.3}$$

The total instantaneous power is expressed in the *abc* frame as

$$P_{abc} = v_a i_a + v_b i_b + v_c i_c \tag{4.4}$$

The total power expressed in the *d-q* frame must equal the total power expressed in the *abc*

frame to maintain 'invariant power' which yields

$$P_{dq0} = \frac{3}{2}(v_{ds}i_{ds} + v_{qs}i_{ds} + 2v_0 i_0) \tag{4.5}$$

In a balanced three phase system, the zero sequence component equals zero, so the third term in Eq. (4.5) is omitted.

The purpose of vector control of ac machines is to obtain high dynamic performance, similar to that obtained from dc machines. To this end, it is necessary to prove that electromagnetic torque is proportional to the product of the flux producing current component and the torque producing current component. This will be shown in the next section.

4.3 Electromagnetic Torque Production in the Synchrel Machine

The principle of energy conservation must be satisfied in every machine during motion. The sum of machine losses (W_{losses}), the change in the magnetic stored energy (W_{field}) and mechanical energy (W_m) is equal to the input electrical energy (W_e)

$$W_e = W_{losses} + W_{field} + W_{mech} \tag{4.6}$$

from which the differential input electrical energy can be obtained

$$dW_e = dW_{losses} + dW_{field} + dW_{mech} \tag{4.7}$$

Electric input energy can be obtained by re-writing Eq.(4.5) as

$$dW_e = \frac{3}{2}(v_{ds}i_{ds} + v_{qs}i_{qs})\,dt \tag{4.8}$$

The following expression can be written for the input electrical power by substituting Eq. (4.3) in (4.8)

$$P_e = \frac{3}{2}\left[r_s(i_{ds}^2 + i_{qs}^2) + i_{ds}\frac{d\phi_{dm}}{dt} + i_{qs}\frac{d\phi_{qm}}{dt} + \omega_e(\phi_{dm}i_{qs} - \phi_{qm}i_{ds})\right] \tag{4.9}$$

In the above expression, the first term is the ohmic losses, while the second and the third are the rate of change of stored magnetic energy in the machine. The fourth term is the output power and its corresponding electrical torque. Therefore, it follows that only the rotational voltages are responsible for torque, hence the torque per pole is

$$T_e = \frac{3}{2}\left[(\phi_{dm} i_{qs} - \phi_{qm} i_{ds})\right] \tag{4.10}$$

In the torque expression, the first component is due to the interaction between the direct axis flux and the quadrature axis current and has a positive sign. The second component is due to the interaction between the quadrature axis flux and the direct axis current and has a negative sign. No torque is produced by the interaction between the flux and current on the same axis.

Disregarding saturation and assuming a linear relationship between the fluxes and currents the torque equation can be re-written as

$$T_e = \frac{3}{2} P\ i_{ds} i_{qs} [L_{dm} - L_{qm}] \tag{4.11}$$

where P is the number of pole pairs. This equation can be written in terms of the phase current, I_{ph}, and current vector angle, α. From Figure 1.2, i_{ds} and i_{qs} can be written as

$$\begin{aligned} i_{ds} &= I_{ph} \cos\alpha \\ i_{qs} &= I_{ph} \sin\alpha \end{aligned} \tag{4.12}$$

Then Eq.(4.11) has the following form

$$T_e = \frac{3}{2} P\ \frac{I_{ph}^2}{2} [L_{dm} - L_{qm}]\ \sin(2\alpha) \tag{4.13}$$

Specific torque can be obtained by regulating current vector components, $i_{ds}$and i_{qs}. There are many d- and q-axis combinations, each defining a particular machine output torque. Different control schemes of vector control are highlighted in Chapter 1. Two methods are

experimentally implemented and the results are presented in this chapter. The first one involoves a commonly used technique of using a constant current in the inductive axis (CCIAC). The direct axis current is maintained constant at a value that keeps the machine fully fluxed. The torque is regulated by controlling the q-axis current. Fast transient response is achieved with this method. This is because the torque response is determined by the quadrature axis time constant which depends on the value of quadrature axis inductance, which is smaller than direct axis inductance. The second control method is termed maximum torque per ampere (MTC). The highest steady state efficiency can be achieved with this method as the flux and current level in the machine are minimum for a given output torque. Lower copper and iron losses are obtained.

The next section outlines the setup and tests on the Synchrel machine.

4.4 Software Description

Torque control requires regulation of i_{dqs}, ignoring the core losses, thereby simplifying the control algorithm. The hardware described in Chapter 3, has current and position sensors

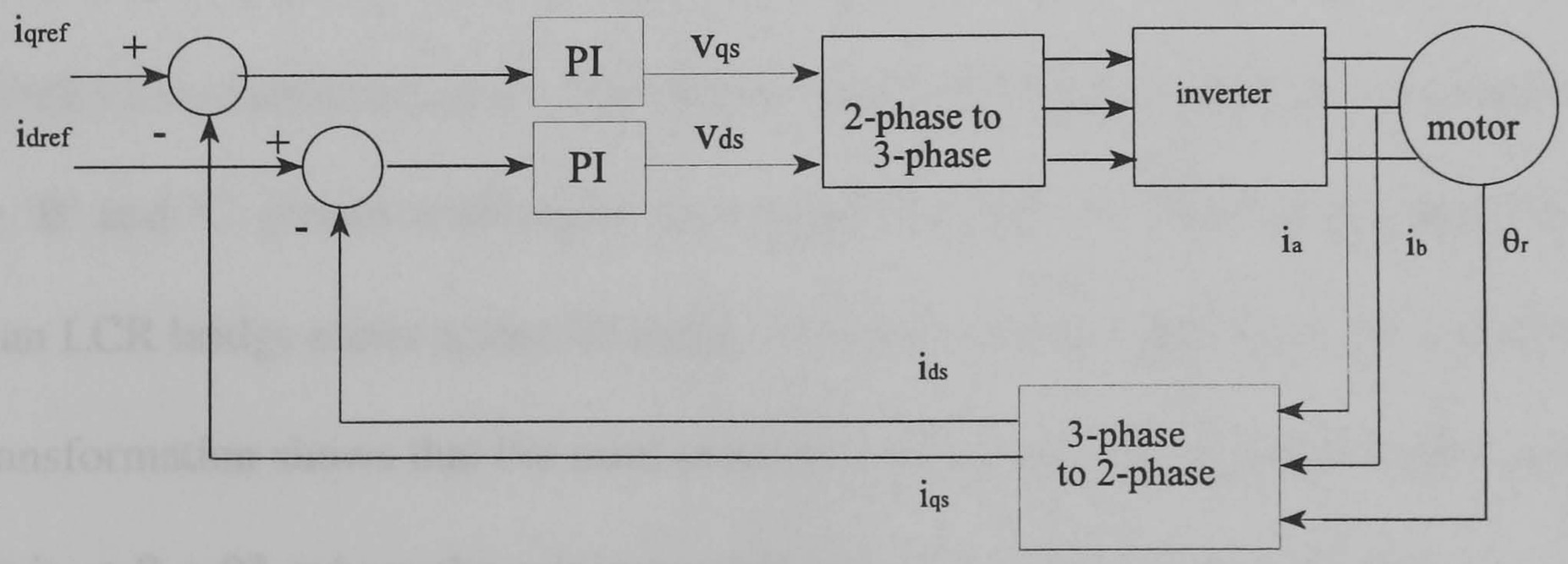

Figure 4.2 Block diagram for the implemented control algorithm

to estimate i_{dqs} and to control v_{dqs} as desired. A block diagram of the control algorithm implemented is shown in Figure 4.2. The estimated i_{dqs} is obtained from Eq. (4.1) using the measured phase currents i_a, i_b and i_c and rotor position, θ yielding i_{ds} and i_{qs}. These values are compared with the reference values, i_{dref} and i_{qref}. The resultant error signals are input to the proportional and integral (PI) compensators which outputs v_{ds} and v_{qs}. The Euler integral method was used with limiting functions. The inverse Park's transformation is applied to v_{ds} and v_{qs} to generate the required phase voltages, v_a, v_b and v_c. The phase voltages are interpreted as duty cycle ratios for the pulse width modulation, PWM, scheme. The reference values, i_{dref} and i_{qref} are user inputs, such that different torque values can be measured under different excitation conditions. The control algorithm language is 'C' , and is listed in Appendix B.

4.5 Initial Set up

This section outlines the preparation prior to experimental vector control.

4.5.1 The Marker Pulse, 'Z', Orientation

The most important set up procedure was to orientate the Z-pulse from the shaft encoder such that the rotor direct axis coincided with the phase 'A' flux axis as prescribed by the form of Park's transformation used. The method used was to leave phase 'A' unexcited and energise 'B' and 'C' phases with equal and opposite currents. The second step was to connect an LCR bridge meter across 'B' and 'C' terminals with the machine star connected. Park's transformation shows that the mmf produced will excite the quadrature axis only if the rotor is at $\theta = 0°$, where the minimum inductance will be measured. The rotor was manually turned to this position. The mechanical coupling between the encoder and the rotor shaft was adjusted to align the Z-pulse with this rotor position.

4.5.2 Determination of Direct and Quadrature Axes Inductances

From the previous subsection, the quadrature inductance, L_q, is given by :

$$L_q = \frac{1}{2} L_{measured}$$

where $L_{measured}$ is the minimum measured inductance. The core loss effects are minimised by setting the inductance meter on the lowest exciting frequency. However the measured inductance values (two stator phases in series) includes the slot leakage and end winding inductance. This inductance can be roughly estimated by measuring the winding inductance when the rotor is removed from the stator. This was measured at 7.75 *mH*. The *d-q* reference frame transformation gives an equivalent leakage term, L_s, in both axes of 7.75 *mH*. The *q*-axis inductance L_{qm} is found by subtracting L_s from L_q, L_{qm} = 14.95 *mH*.

A second method was also used to determine both the direct and quadrature axis inductances. Only phase 'A' is excited and the rotor is incrementaly stepped a small angle with the phase 'A' inductance being measured after each step. This was repeated until the rotor stepped 90° from the initial position. The variation of phase 'A' inductance over one pole arc is shown in Figure 4.3.

The self inductance of phase 'A' can be expressed as:

$$L_A = L_{av} + L_{pk}\cos(2\theta) \qquad (4.14)$$

where

$$L_{av} = \frac{L_{\max} + L_{\min}}{2}$$
$$L_{pk} = \frac{L_{\max} - L_{\min}}{2} \qquad (4.15)$$

L_{av} : phase 'A' inductance average value

L_{pk} : phase 'A' inductance peak value

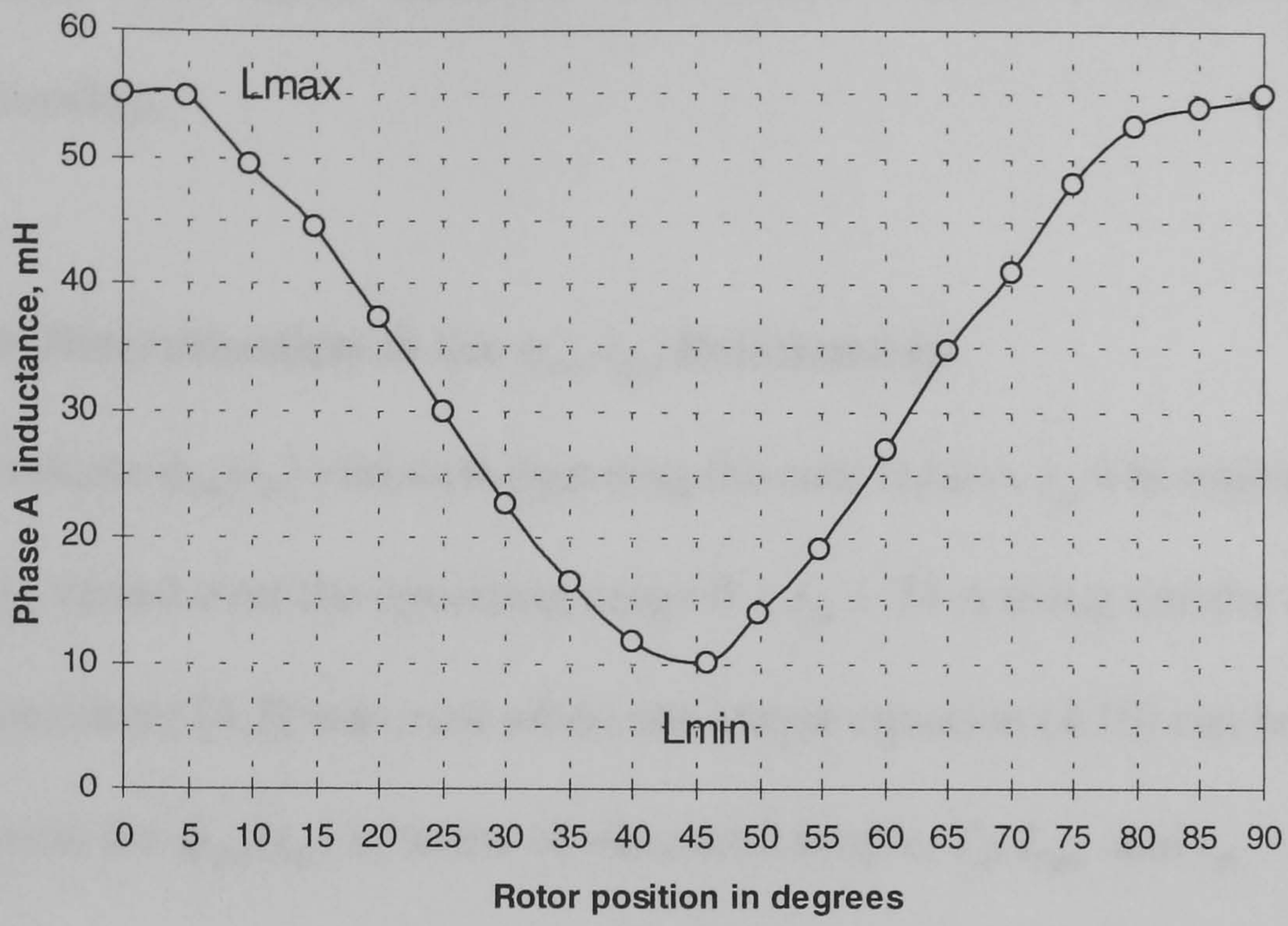

Figure 4.3 Phase 'A' inductance variation with rotor position

Inductances L_d and L_q can be found from the following equations [4.2]:

$$L_d = -0.5L_s + \frac{3}{2}(L_{av} + L_{pk})$$
$$L_q = -0.5L_s + \frac{3}{2}(L_{av} - L_{pk}) \qquad (4.16)$$

From Figure 4.3, the values of L_{max} and L_{min} are found to be 55.31 *mH* and 10.11 *mH* respectively . The values of L_{av} and L_{pk} determined from Eq.(4.15) are 32.52 *mH* and 22.45 *mH* respectively. Therefore estimated values of direct and quadrature axes inductances, L_d and L_q from Eq.(4.16) are 78.6 *mH* and 11.25 *mH* respectively, resulting in a saliency ratio, ζ, of 6.98, which is slightly higher than the predicted value in Table 2.1. The inductance values can be compared with the finite element results given in Table 2.1 for G_3. The figures in the Table are slightly larger than the measured values as the finite element analysis does not account for end winding inductance effects or parasitic effects. The excitation current used in this method is low, so smaller inductance values are

obtained. The magnetization curve of the machine is nonlinear at low magnetising current due to low permeability. A more accurate value of L_d can be determined if we excite the machine with higher currents. This can be achieved by knowledge of the ϕ_{dm}-i_{dm} relationship.

4.5.3 Determination of the ϕ_{dm}-i_{dm} Relationship

To evaluate $\phi_{dm}(i_{ds})$ variation (ignoring the core losses), i_{qs} was maintained constant at 21 A and i_{ds} varied over the operating range $0 \le i_{ds} \le 24$ A using current control. Direct torque measurement [4.3] was used where the torque equation (4.10) can be rearranged to give an equation for $\phi_{dm}(i_{ds})$ in terms of measured torque, T_e, L_{qm} and i_{qs}.

$$\phi_{dm}(i_{ds}) = \frac{2}{3Pi_{qs}} T_e + L_{qm} i_{ds} \tag{4.17}$$

The machine was allowed to rotate at low speed to minimise the effect of core and mechanical losses. The load was provided by a dc machine. The value of L_{qm} was assumed to be constant, 14.95 *mH*. Torque production is not affected by slot leakage and end winding inductance, hence they do not affect the results shown in Figure 4.4. From the figure, the estimated value of L_{dm} is 100 *mH* at i_{ds} =16.44 A. The saliency ratio, ζ, obtained from the practical result is 6.69 which is very close to that predicted by the finite element analysis. However the values in Table 2.1 are still slightly larger than the measured values and this is due to the aforementioned reasons.

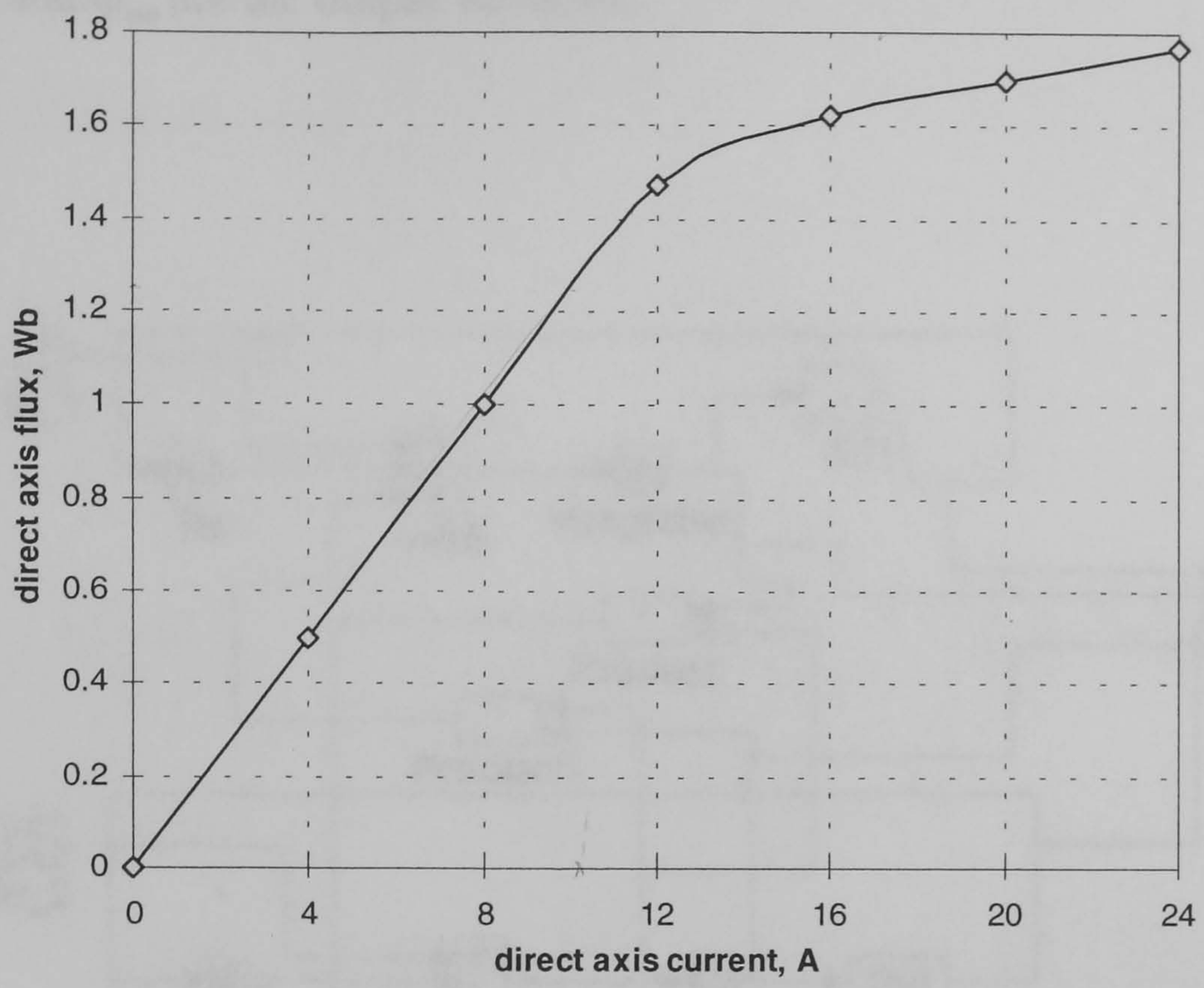

Figure 4.4 ϕ_{dm}-i_{dm} relatioship evaluated using direct torque measurment

4.5.4 System Simulation

With the magnetising inductances for the direct and quadrature axis determined, the machine can be now modelled for simulation purposes. A simulation was first carried out in order to determine the proportional-integral controllers gains, which were then implemented practically. The simulation used MATLAB with its graphical user interface, SIMULINK, running on a PC platform. Eq.(4.3) can be rearranged for simulation purpose as

$$\begin{aligned} \frac{d\phi_{dm}}{dt} &= v_{ds} - r_s i_{ds} + \omega_e \phi_{qm} \\ \frac{d\phi_{qm}}{dt} &= v_{qs} - r_s i_{qs} - \omega_e \phi_{dm} \end{aligned} \tag{4.18}$$

The ϕ_{dm}-i_{dm} characterstics given in Figure 4.4 can be incorporated in the machine model by the use of a look-up tabel, fid1, which has ϕ_{dm} as the input and i_{dm} as the output. The ϕ_{qm}-i_{qm}

relationship is assumed linear. The SIMULINK file of the machine model 'synchrel' is shown in Figure 4.5, where v_{ds}, v_{qs} and ω_e (electrical speed) are the input variables and i_{ds}, i_{qs}, ϕ_{dm} and ϕ_{qm} are the output variables.

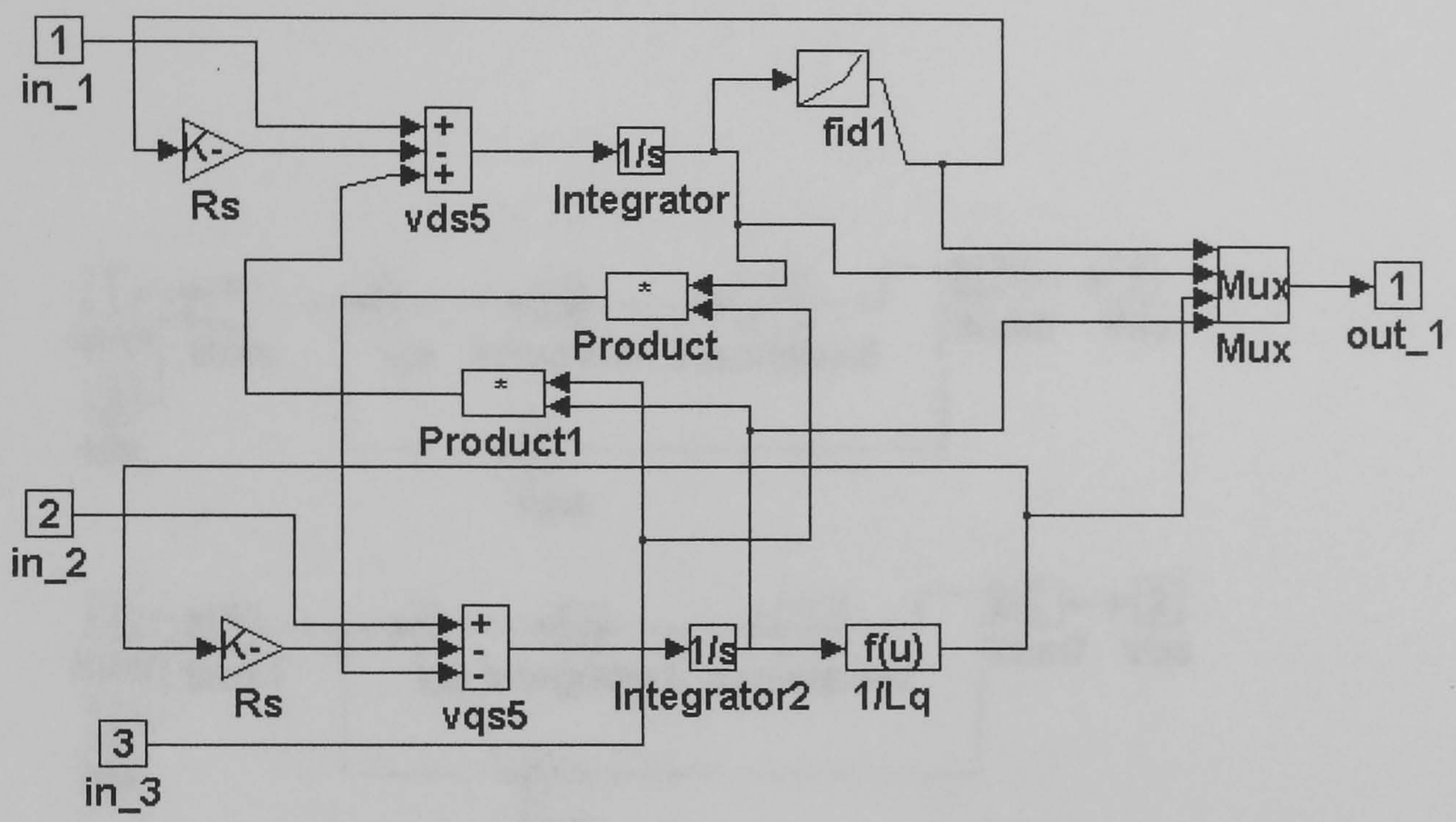

Figure 4.5 SIMULINK file 'synchrel', machine model

The SIMULINK file 'controller' for the flux PI controller (*d*-axis current) and torque PI controller (*q*-axis current) are shown in Figure 4.6. The parameters kpd, kid are the proportional and integral gains in the direct axis respectively, and kpq, kiq are those for the quadrature axis. The machine electrical model 'synchrel' and mechanical model 'mechanical1' are incorporated with the controller file 'controller' in the block diagram of the drive system as shown in Figure 4.7. The input torque to the SIMULINK file 'mechanical1' is given by Eq.(4.10), which is written in 'tor_fn'. The block diagram of this file is shown in Figure 4.8 in which the following equation is implemented:

$$T_e - T_L = J\frac{d\omega}{dt} + B\omega \qquad (4.19)$$

where

B viscous coefficient ($Nm/ rad\ s^{-1}$)

J moment of inertia ($kg\ m^2$)

T_L load torque (Nm)

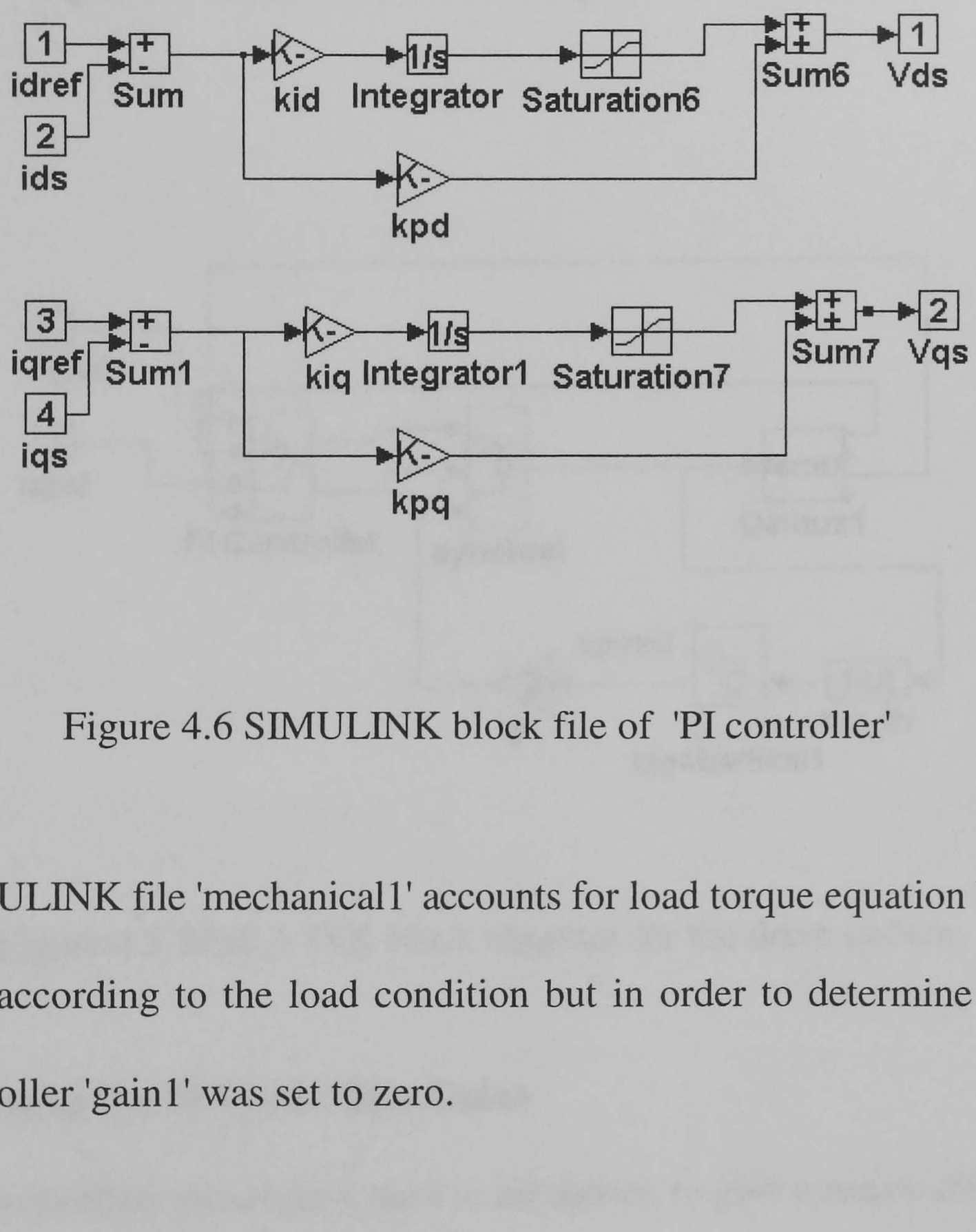

Figure 4.6 SIMULINK block file of 'PI controller'

The SIMULINK file 'mechanical1' accounts for load torque equation by 'gain1'. However it is set according to the load condition but in order to determine the set of gains for the controller 'gain1' was set to zero.

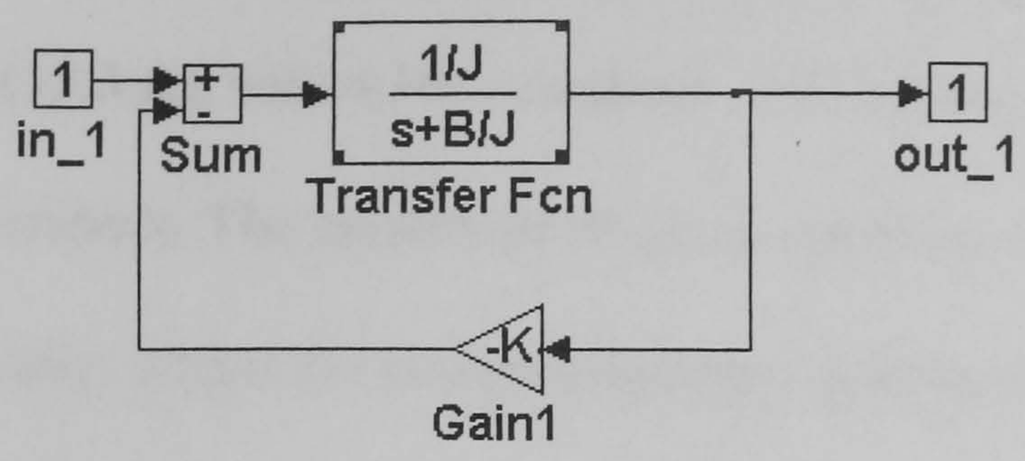

Figure 4.7 SIMULINK block diagram for 'mechanical1'

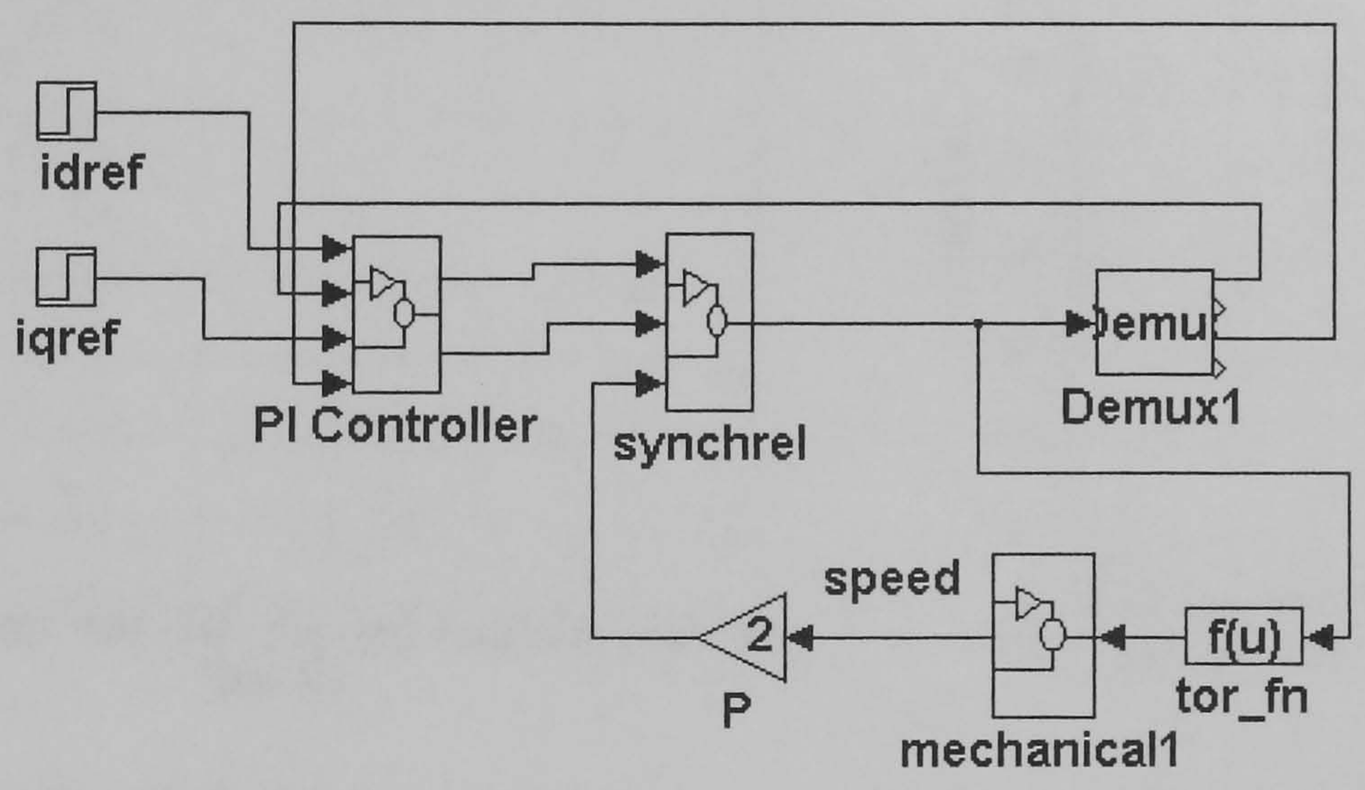

Figure 4.8 SIMULINK block diagram for the drive system

4.5.5 Setting the PI Controllers Gains

The PI controllers parameters need to be chosen to give a reasonable current response in both axes under the constraint of having limited volts available from the inverter. A trial and error solution was used to find a set of gains which gives a reasonable response in each axis. The solution consisted of demanding various step changes in either i_{ds} or i_{qs} reference values and examining the current response obtained in terms of overshoot and rise time. This was obtained by simulating the drive system with these conditions. A typical current

response in the direct and quadrature axes for the chosen set of gains are given in Figures 4.9 and 4.10 respectively. The response time of the *d*-axis current is about 105 ms to 90% of the final value (15.3 A), with 4.3% overshoot. The corresponding figures for *q*-axis are 26 ms with no overshoot. The chosen set of gains are given in appendix D. These values were used practically, where the current responses in both the *d* and *q* axes are shown in Figures 4.11 and 4.12. The rise time of the *d*-axis current is 120 ms with 5.6 % overshoot. The current response in *q*-axis is quicker than the *d*-axis current with a rise time of 30 ms and no overshoot.

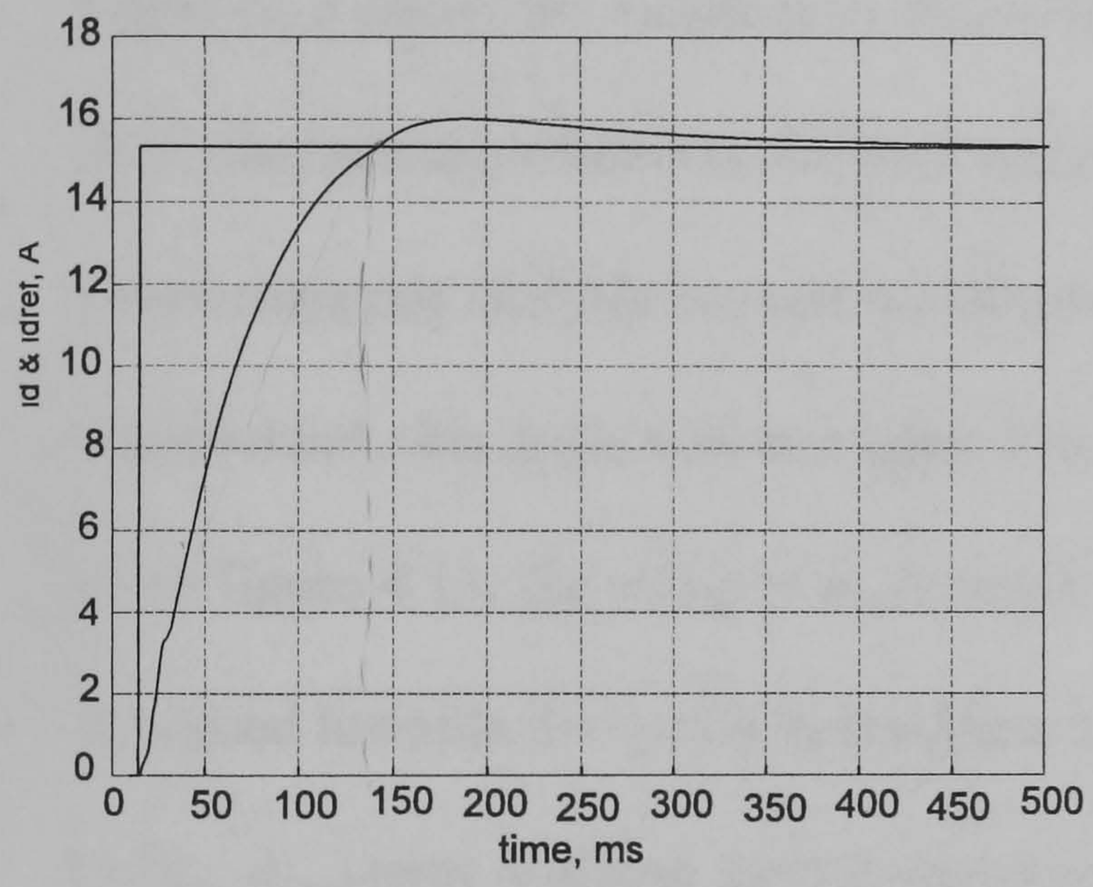

Figure 4.9 Simulated step response to increase in i_{ds} reference from 0 to 15.3 A

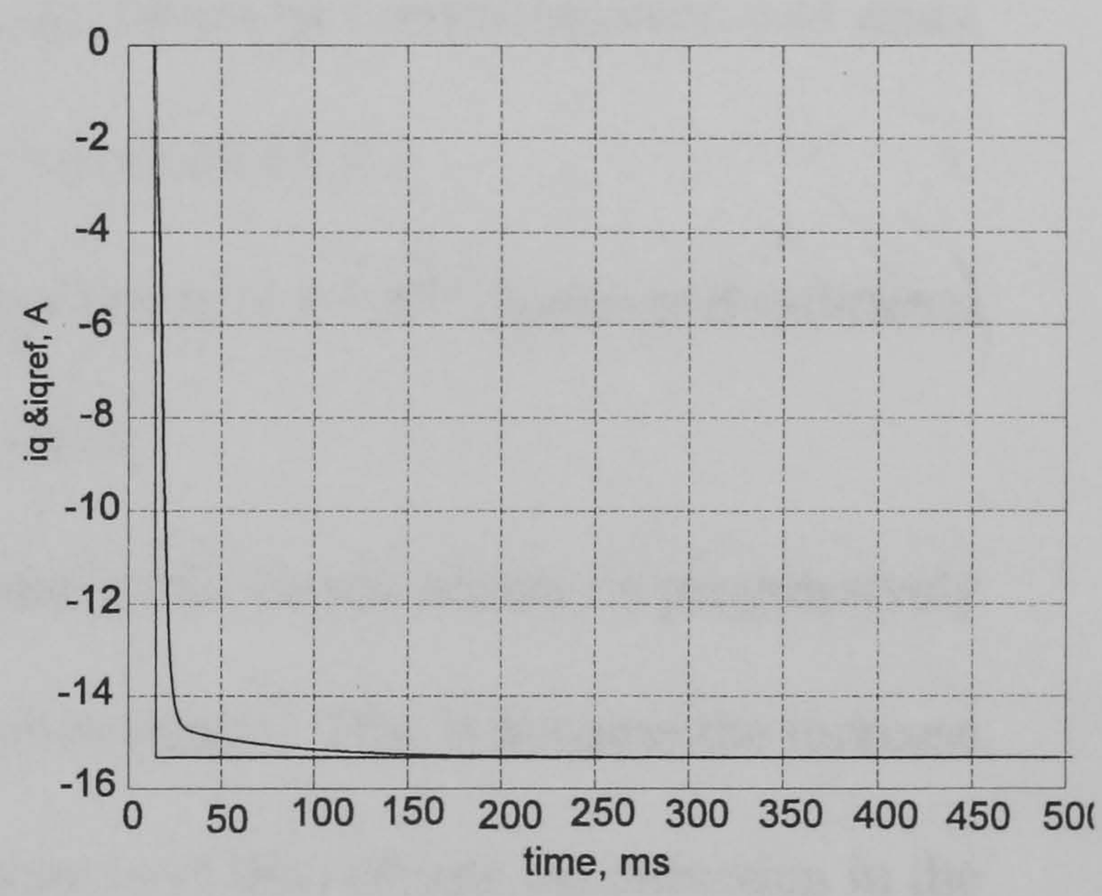

Figure 4.10 Simulated step response to decrease in i_{qs} reference from 0 to -15.3 A

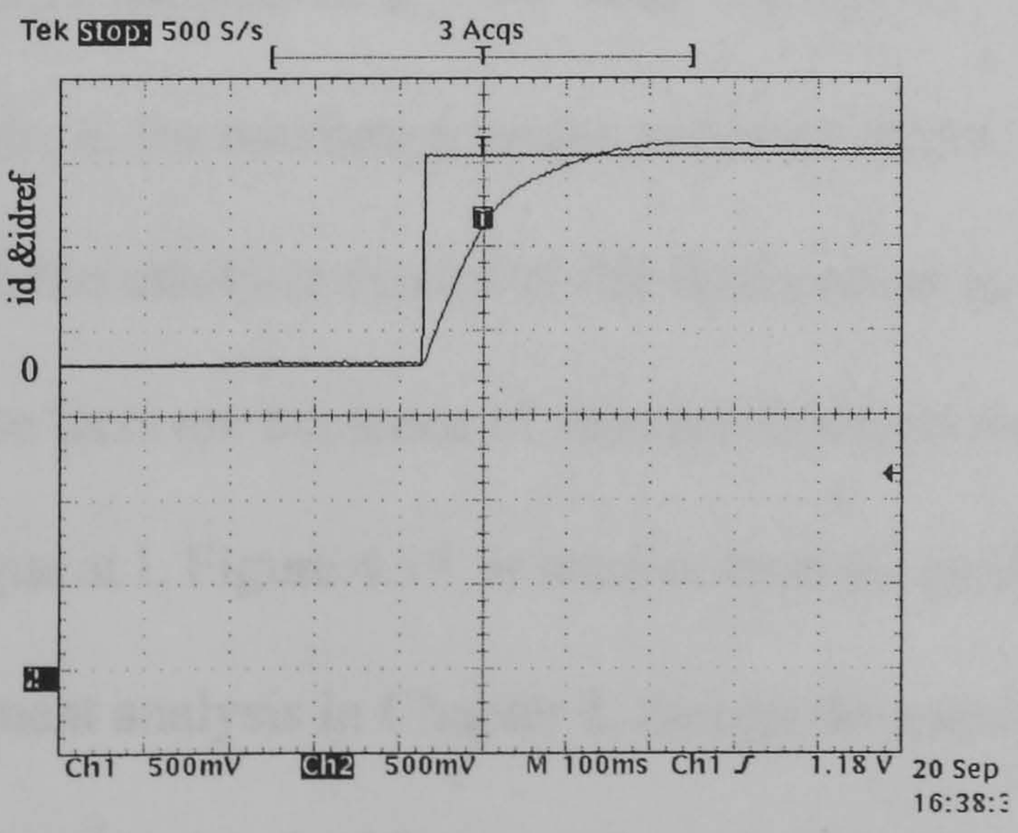

Figure 4.11 Practical current response in the *d*-axis
Vertical scale: 6.12 A/div
Horizontal scale 100 ms/div

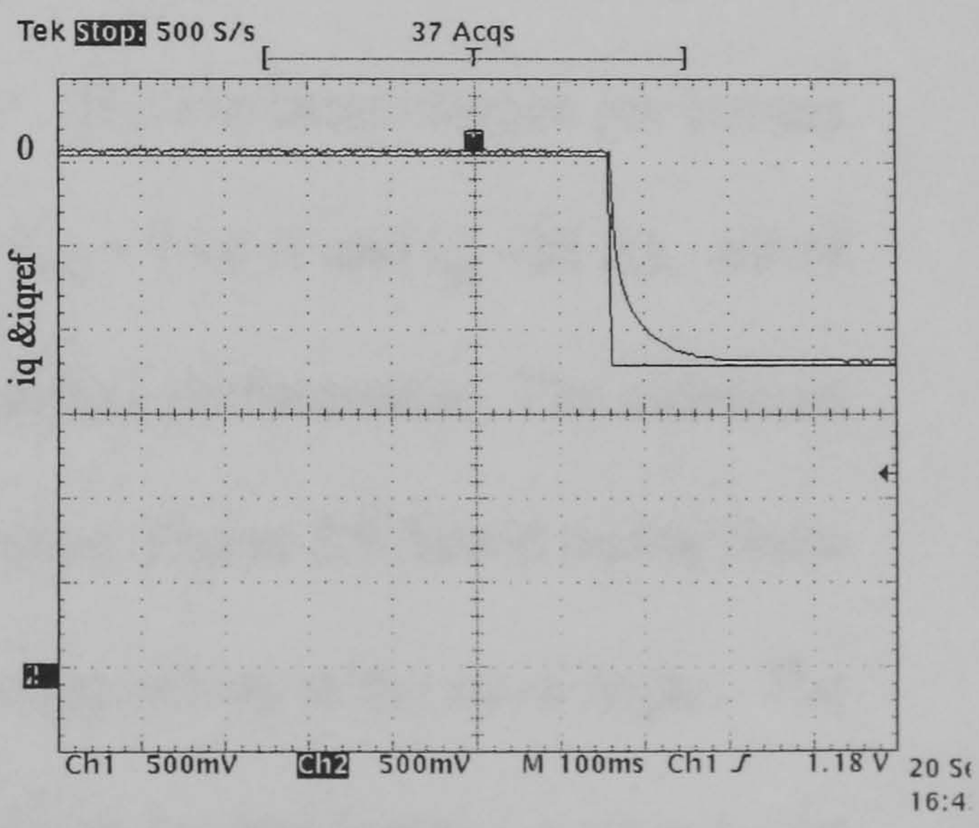

Figure 4.12 Practical current response in the *q*-axis
Vertical scale: 6.12 A/div
Horizontal scale 100 ms/div

4.6 Drive System Results

With the control algorithm programmed and initial setup procedures carried out, the drive system is ready to be tested.

Test 1

In this test the machine was connected to dc machine with its armature terminals short-circuited, therby obtaining high load torque at low speed. This is to minimise the displacement of the magnetising current vector, i_{dqm}, from stator current vector, i_{dqs}, due to core losses. The current vector magnitude is held constant and its angle, α, changes. Figure 4.13 shows the variation in torque with α for the phase current between 0.6I and I (0.2 I increment), where the full load current, I, equals 18.85 A.

Linear magnetic analysis assumes maximum torque occurs at $\alpha = 45°$, however if saturation is accounted, this angle will be higher than this value.

From figure 4.13, the value of α, at which the maximum torque occurs, is progressively displaced towards the q-axis as the phase current increases. This is because the increase in $(L_{dm} - L_{qm})$ term resulting from reduced saturation more than offsets the reduction in the sin (2α) term in equation (4.13) as α increases above 45°. The maximum torque per ampere happens at $\alpha = 50°$ with $0.6\ i_{f.l}$ (11.3 A). With $0.8 i_{f.l}$ (15.1 A), the current vector angle, α, for maximum torque becomes larger, $\alpha = 55°$. The maximum torque per ocuurs with the machine excited at full load current at $\alpha = 60°$ (i_{ds} = 16.4 A and i_{qs} =28 A). All of these facts are evidence of saturation effects on the machine performance. The measured torque at I, Figure 4.13, is smaller than the predicted torque, Figure 2.8, based on the finite element analysis in Chapter 2, though the maximum torque occurs at the same angle. The difference is significant and probably primarly caused by incorrectly assumed slot dimension (stator input information is not exact and includes approximation), friction in

the test machine bearings and slight eddy current damping of the flux.

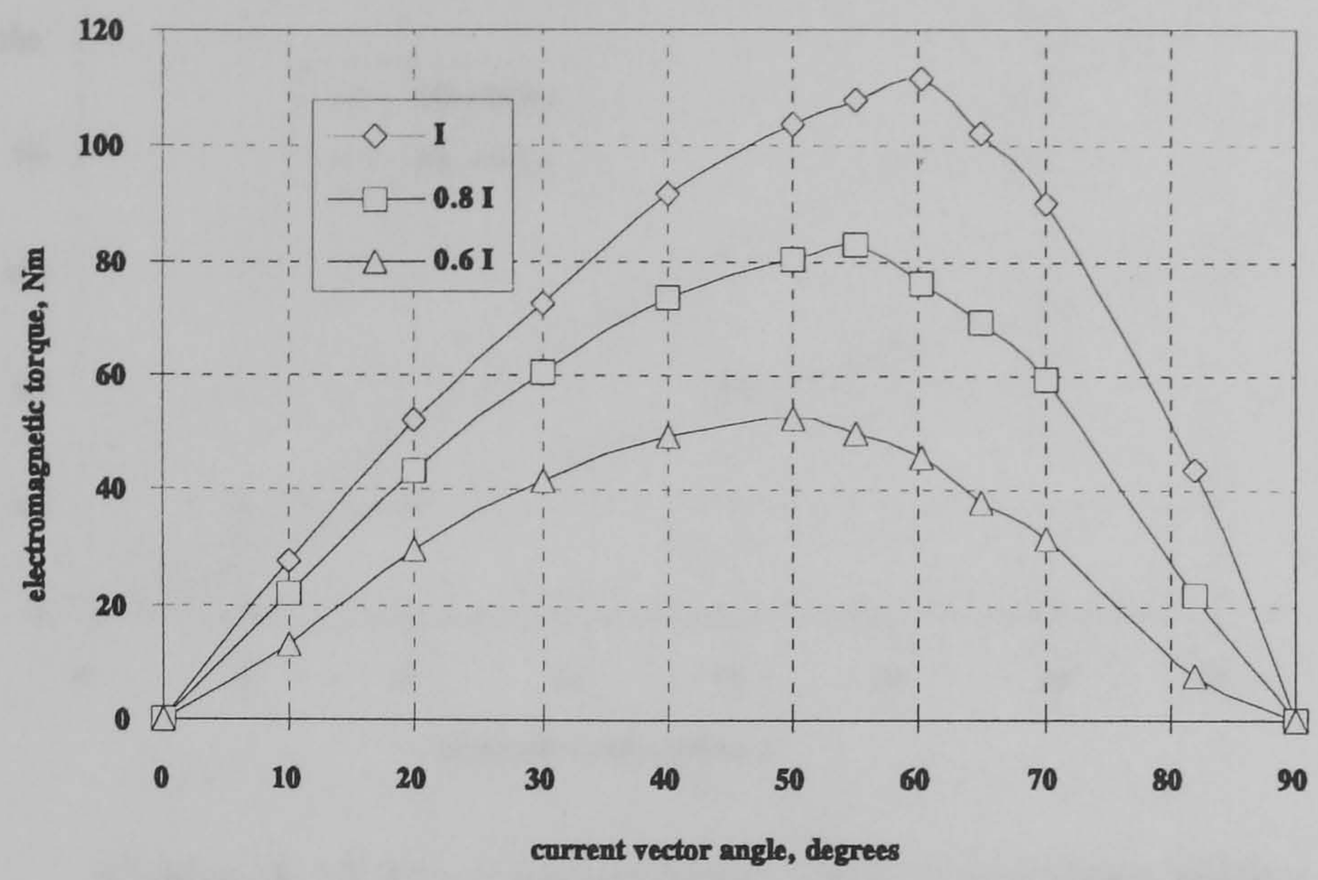

Figure 4.13 Variation in torque/ampere with phase current and current vector angle, α

Test 2

The second test is with constant current in the direct axis current, termed (CCIC). In this test the *d*-axis current is maintained at a constant value and the torque is controlled by regulating the *q*-axis current. Figure 4.14 shows the output torque variation with quadrature axis current when the direct axis current is kept constant at i_{ds} = 16.44 A (*d*-axis current corresponds to maximum torque per ampere at $\alpha = 60°$) and i_{ds} = 8.22 A. The maximum torque output (111.6 Nm) developed by this machine compares well with that of the original induction motor (120 Nm). However the calculated value of the torque using equation (4.10) gives 120.45 Nm. The difference is due to the mechanical loss component which has been subtracted from the electromagnetic torque. The ratings of the Synchrel machine are given in Appendix D.

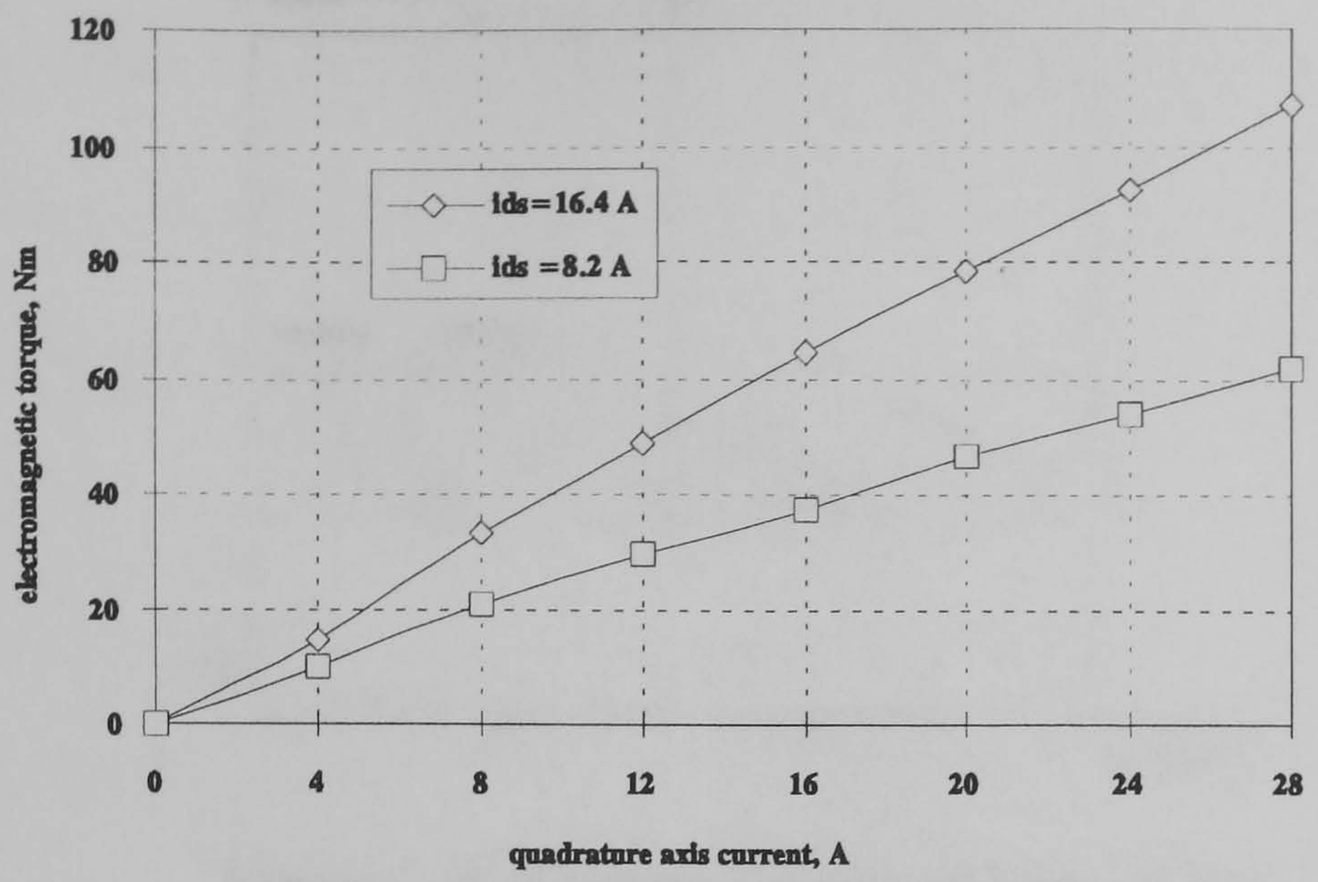

Figure 4.14 Electromagnetic torque response with i_{qs}

Test 3

The Synchrel machine was operated on load. The current vector was set such that the machine was maintained fully fluxed and the torque component current was varied to control the speed. Figure 4.15 shows the phase current and voltage waveforms at low speed. The current varies in a sinusoidal fashion and the voltage is reasonably sinusoidal. However when the speed is increased, higher ripple level is observed in both waveforms, Figure 4.16. It is expected that at the rated speed of the machine, the effect of the inductance ripple will be remarkable on the waveforms as the controller is not fast enough to respond well to these changes. The effects of the inductance ripple is investigated in Chapter 6.

Figure 4.15 Voltage and current plots at low speed (168 rpm)
Current scale: 16.26 Amp/div
Voltage scale: 194.32 volt/div
Time scale : 100 ms/div

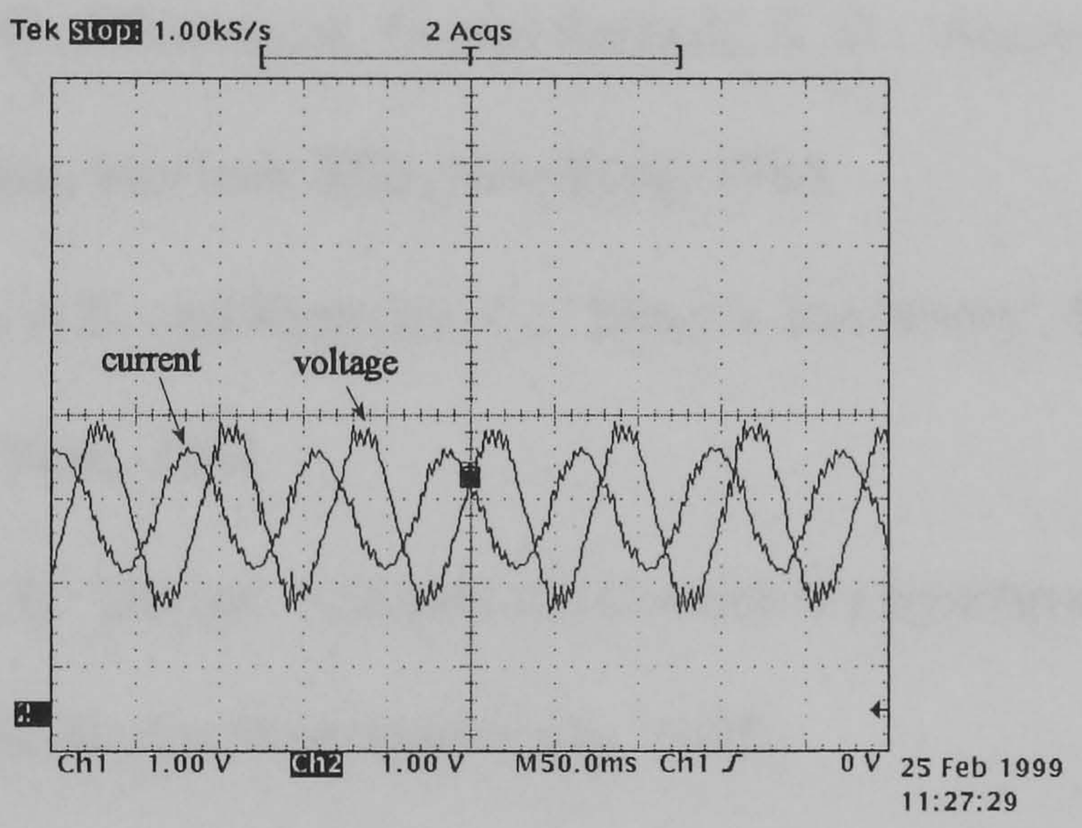

Figure 4.16 Voltage and current plots at low speed (356 rpm)
Current scale: 16.26 Amp/div
Voltage scale: 194.32 volt/div
Time scale : 50 ms/div

4.7 Summary

This chapter has outlined the methods by which the Synchrel machine parameters were measured. The magnetisation curve of the machine has been determined and included in a SIMULINK file. The drive system has been simulated for a step increase demand in *d*-axis current and a step decrease in *q*-axis current to determine flux and torque PI

controllers gains. The chosen set of gains were implemented practically and good correlation between the simulated and practicals results was obtained for the current responses in the *d* and *q* axes . Two control strategies for vector control were considered. Maximum torque per ampere control (MTC) and constant current in the inductive axis control (CCIAC) were experimentally assessed. The maximum torque obtained from the machine with both methods is similar to that of the induction motor with the same stator. The machine was tested on load at low speeds, the effect of inductance ripple is obvious in the voltage and current waveforms.

References

4.1 Krause, P.C., Wasynczuk, O. and Sudhoff, S. D.: 'Analysis of Electric machinery', First Edition, McGraw-Hill, NewYork, 1986.

4.2 Fitzgerald, A.E. and Kingsley, C.: ' Electric machinery', Second Edition, McGraw-Hill, NewYork, 1961.

4.3 Fletcher, J.E.: 'Design, Analysis and Control of a Synchronous Reluctance Machine', Ph.D thesis, Heriot-Watt University, 1995.

Chapter 5

Sliding mode control

5.1 Introduction

Variable structure control (VSC) with the existence of sliding modes was pioneered in the early 1950's in the Soviet Union. The plant considered for initial presentation of this technique was a linear second order system [5.1]. In fact VSC did not receive wide attention before 1970, this was mainly due to the lack of a general design procedure and the existence of chattering. However, the important features of VSC such as invariance and robustness to parameter variation have long been recognised. Since then, important developments in VSC have been made. Sliding mode control, which is a special case of VSC, has been discussed in some reports [5.1]-[5.6]. The basic property of sliding mode is that the controller changes structure, switching continuously between different regimes, across a switching surface, embedded in the state space structure of the system. Classical sliding mode control theoretically features excellent robustness to parametric uncertainty. However it possesses several important drawbacks that limit its practical applicability. The theory of sliding mode control assumes a continuous-time framework where the actuator can switch at an infinite rate. Since the practical implementation of the control switching cannot be instantaneous, this leads to chattering. This is generally undesirable as it excites the high frequency unmodelled dynamics. Slotine and Sastry [5.7] proposed a methodology to remove some of these drawbacks by replacing the discontinuous control by a smooth control interpolation in the boundary layer in a time-varying surface. In particular this methodology involved a trade off between tracking precision and robustness to unmodelled high frequency dynamics. Slotine [5.8] completed this methodology by showing how to achieve optimal tracking performance given bandwidth requirements and monitoring the

boundary layer width so as not to excite the high frequency unmodelled dynamics. Sliding mode control has been applied previously to the Synchrel machine for position and speed control but not using Slotine's approach as is reported in this chapter.

In this work we consider the control of a single input nonlinear system using Slotine's approach to sliding mode control. Position control of a vector controlled Synchrel machine using sliding mode control and a fixed gain controller are implemented. A comparison is made between the performance of a fixed gain controller and two sliding mode controllers for both the regulator and servo cases. Slotine's approach to sliding mode control shows superiority over the fixed gain controller.

5.2 Slotine's Approach to Sliding Mode Control

Sliding mode control is a form of nonlinear control, where model imprecision can be tolerated. Model imprecision may result from parametric uncertainty or the simplified representation of the system dynamics. Slotine's work [5.9] is based on the remark that is easier to control first order systems, be they nonlinear or uncertain, than it is to control higher order systems. Perfect performance can be obtained from the transformed system at the price of high control activity.

Slotine's methodology considers the control law to consist of two components, a continuous one reflecting knowledge of the system dynamics, and a discontinuous one to account for the presence of modelling imprecision and of disturbances. The theory of sliding mode control is applicable to systems of order *n*. However a vector controlled Synchrel machine can be represented as a second order system with a general type of mechanical load, therefore sliding mode control theory is presented for *n=2*.

The control problem is to get the system state $x=[\theta_r \quad \dot{\theta}_r]^T$ to track a specific time-varying state $x_d=[\theta_d \ \dot{\theta}_d]^T$ in the presence of model imprecision, where θ_r = rotor position and $\dot{\theta}_r$ =

rotor speed. If $s(x;t)=0$ is a scalar equation in the time-varying surface $S(t)$ then

$$s(x;t)=(\frac{d}{dt} + \lambda)\ \theta_e \tag{5.1}$$

where θ_e is the tracking error = θ_r - θ_d, and λ is a strictly positive constant that gives an indication of the system bandwidth.

The problem of tracking x_d is equivalent to that of remaining on the surface $S(t)$ for all $t>0$ and implies that the scalar quantity s is kept at zero. The bounds on s can be directly translated into bounds on the tracking error θ_e, and therefore the scalar s represents a true measure of tracking performance. For a second order system the switching surface is a line, thus the second order tracking problem is replaced by a first order stabilisation problem. Then the simplified problem of keeping the scalar s at zero can be achieved by choosing a control law to satisfy the sliding condition as defined by Slotine:

$$\frac{1}{2}\frac{d}{dt}s^2 \leq -\eta |s| \tag{5.2}$$

where η is a strictly positive constant. The sliding surface is a line in the phase plane of slope $-\lambda$. Starting from any initial condition, the state trajectory reaches the time varying surface in a finite time smaller than $|s(t=0)/\eta|$, and then slides along the surface towards x_d exponentially, with a time constant of $1/\lambda$.

The vector controlled Synchrel machine can be represented as

$$\ddot{\theta}_r = f(\theta_r,\dot{\theta}_r) + bi_{qs}^* \tag{5.3}$$

or for brevity

$$\ddot{\theta}_r = f + bi_{qs}^* \tag{5.4}$$

where i_{qs}^{*} is the torque current command, f is the dynamics of the system, possibly nonlinear or time-varying and is estimated as $\hat{f}$.

Differentiating Eq. (5.1) with respect to time gives:

$$\dot{s} = \ddot{\theta}_r - \ddot{\theta}_d + \lambda\dot{\theta}_e \tag{5.5}$$

Substituting for $\ddot{\theta}_r$,

$$\dot{s} = f + bi_{qs}^{*} - \ddot{\theta}_d + \lambda\dot{\theta}_e \tag{5.6}$$

The best approximation i_{qs}^{*}, of a continuous control law that would achieve the condition $\dot{s}=0$ is

$$i_{qs}^{*} = \frac{\hat{u}^{*}}{\hat{b}} \qquad \hat{u}^{*} = -\hat{f} + \ddot{\theta}_d - \lambda\dot{\theta}_e \tag{5.7}$$

This condition $\dot{s}=0$ allows the discontinuous component to be solely responsible for ensuring that the Lyapunov function $s\dot{s}$ is strictly negative definite (and ensuring sliding occurs). However to account for the presence of modelling imprecision and system disturbances, the control law has to be discontinuous across *S(t)*:

$$i_{qs}^{*} = \frac{(\hat{u}^{*} - k\,sat(s/\phi))}{\hat{b}} \tag{5.8}$$

The estimation error for f is assumed to be bounded by some known function $F=F(\theta_r, \dot{\theta}_r)$, where

$$|f-\hat{f}| \le F \tag{5.9}$$

The control gain is unknown but has known bounds

$$0 < b_{\min} \le b \le b_{\max} \tag{5.10}$$

The estimate $\hat{b}$ of gain b is the geometric mean of the above bounds

$$\hat{b} = (b_{\min} b_{\max})^{1/2} \tag{5.11}$$

Eq.(5.10) can be written in the form

$$\beta^{-1} \leq \frac{\hat{b}}{b} \leq \beta \tag{5.12}$$

where

$$\beta = (b_{max}/b_{min})^{1/2} \tag{5.13}$$

The value of k must be chosen largely enough such that sliding occurs, and must satisfy the inequality

$$k \geq \beta(F+\eta)+(\beta-1)|\hat{u}^*| \tag{5.14}$$

The value of η determines the degree to which the state of the system is attracted to the switching line. Increasing this value in the regulator condition reduces the reaching time and in the servo condition reduces the trajectory following error. In Slotine's approach the value of k increases when the parameter uncertainty is large. Better parameter value knowledge reduces k and leads to a smoother control response.

5.3 Drive System Description

The block diagram description of the machine drive system is shown in Figure 5.1. The system consists of a Synchrel machine, a mechanical load, and a power electronic converter (current controlled voltage source IGBT three phase inverter). The controller handles the power flow to the machine to achieve the desired rotational performance. The performance of any drive system is largely dependent on the control algorithm and its implementation. The control scheme is indirect vector control of a Synchrel machine, using Slotine's sliding mode approach for position control. For comparison another scheme for position control using fixed gain control is also presented. The position control loop comprised of nested position and speed loops with proportional and proportional integral controllers respectively.

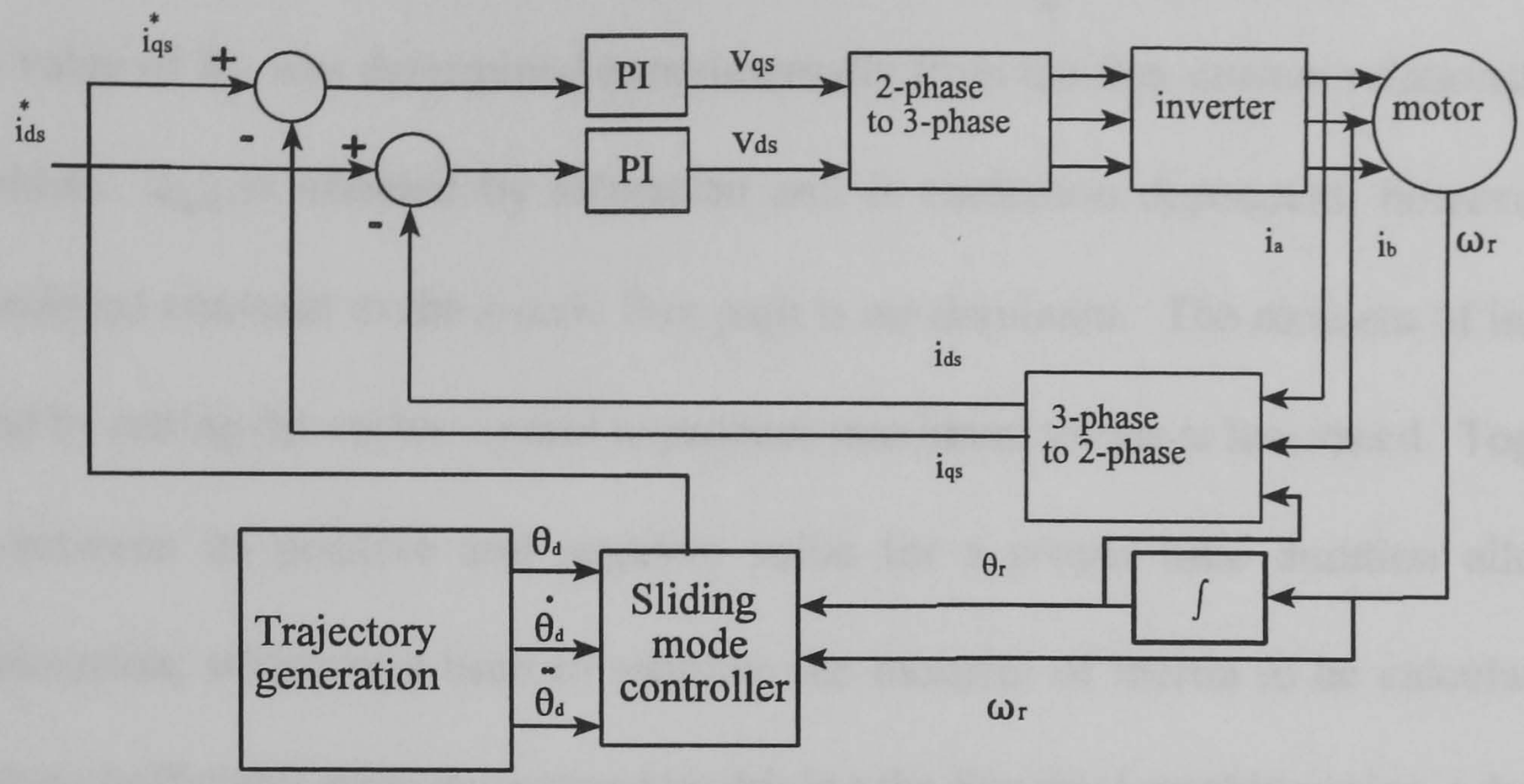

Figure 5.1 Drive system for position control of a vector controlled Synchrel machine using sliding mode control

The position information is provided via a 2048 pulses per revolution encoder and the speed is obtained by measuring the period between consecutive position sensor pulses to achieve high resolution at low speeds. The sampling rate of 1.63 kHz is used to implement vector control and the sliding mode algorithm. In fact a lower sampling rate could be used, but the aforementioned value did not present any problem and it was easy to implement in the micro-controller.

The electro-mechanical model for the proposed system can be expressed in the following form:

$$T_e = J\ddot{\theta} + B_1\dot{\theta}_r + B_2 sgn(\dot{\theta}_r) + B_3\dot{\theta}_r^2 \qquad (5.15)$$

where

J moment of inertia, ($kg\ m^2$)

B_1 viscous friction constant, ($Nm/rad\ s^{-1}$)

B_2 coulomb friction constant, (Nm)

B_3 winding friction constant, ($Nm/rad^2\ s^{-2}$)

T_e electro-magnetic torque , (Nm), $T_e = K_T i_{qs}, K_T = \frac{3}{2} p (L_{dm} - L_{qm}) i_{ds}$

The value of K_T was determined experimentally from the flux-current relationship of the machine. L_{dm} is affected by saturation and is excitation dependent, however L_{qm} is considered constant as the q-axis flux path is air dominant. The moment of inertia was found by setting the vector control to produce maximum torque at low speed. Toggling the i_{qref} between its positive and negative value for a proper time duration allowed the acceleration, which was used to estimate the moment of inertia to be calculated. The friction coefficients were determined by driving the Synchrel machine using a dc machine at high speed, then switching the power off and recording the speed decay curve. A MATLAB curve fitting m-file enabled the values to be obtained.

To test the robustness of Slotine's approach, the moment of inertia was increased to over twice the original by mounting a flywheel on the machine shaft. The mechanical parameters are shown in Table 5.1.

J_{min}	J_{max}	B_1	B_2	B_3
0.289	0.638	0.0012	0.0807	0
$kg\ m^2$	$kg\ m^2$	*Nm/rad/s*	*Nm/rad/s*	*Nm/rad/s*

Table 5.1 Machine and system constants

In the next two sections regulator and servo performances are investigated using three different controller types. These are a fixed gain controller, Slotine's approach to sliding mode, which accounts for the load dynamics (hereafter referred to as the dual-component sliding mode controller), and a third controller (hereafter referred to as the single-

component sliding mode controller) which is defined by :

$$i_{qs}^{*} = -k \ sat(s/\phi) \tag{5.16}$$

where k is a positive constant, and the saturation function is

$$sat(s/\phi) = \begin{cases} sgn(s) & |s| > \phi \\ \dfrac{s}{\phi} & |s| \le \phi \end{cases} \tag{5.17}$$

5.4 Regulator Performance

The regulator performance for the three controllers is now presented. Performance comparisons between standard and high inertial loads are undertaken. In both cases the machine starts with a zero initial rotor angle, and is demanded to move to $\theta_r = 2.5$ radians. For comparison, the parameters of the fixed-gain controller are tuned to give a similar transient response to the sliding mode controllers. These parameters are given in Appendix D, for the regulator case and servo applications. Figures 5.2 and 5.3 show the position (lower channel) and speed (upper channel) response for each case with the standard and high inertial load respectively.

The phase plane plot is a graphical method for studying the dynamic behaviour of second order systems. The basic idea of this method is to generate, in the state space, motion trajectories to investigate the qualitative features of the trajectories. It allows one to visualise nonlinear system behaviour starting from various initial conditions. The phase plane plots are shown in Figure 5.4. As expected, the fixed gain controller does not follow the switching line and it is seen to cross the line. There is evidence that the closed loop system dynamics alter as the inertia is increased. One of the problems of sliding mode control is the reaching phase where the system is sensitive to parameter variation. This is evident from these figures, the control effort of the single component sliding mode controller saturates during the reaching phase, Figs. 5.5 and 5.6. However, for both sliding

mode controllers the reaching time is between 300 ms and 320 ms. This is an undesirable feature that could be reduced by reducing the reaching time. After that time, sliding occurs along the switching line s=0. The switching variable during the reaching phase s is not zero, Figures 5.5 and 5.6, and sliding takes place when s=0. The reaching time can be reduced by reducing the system bandwidth λ or increasing the boundary layer width,ϕ. A trade off between the two values is therefore necessary. The values chosen were ϕ =0.8 radians, and λ =4.32 rad/s. Sliding mode control provides robustness to parameter variations and thus maintains an invariant first-order response only when on the switching line. In the next section, a servo application is demonstrated which is another application benefiting from sliding mode control.

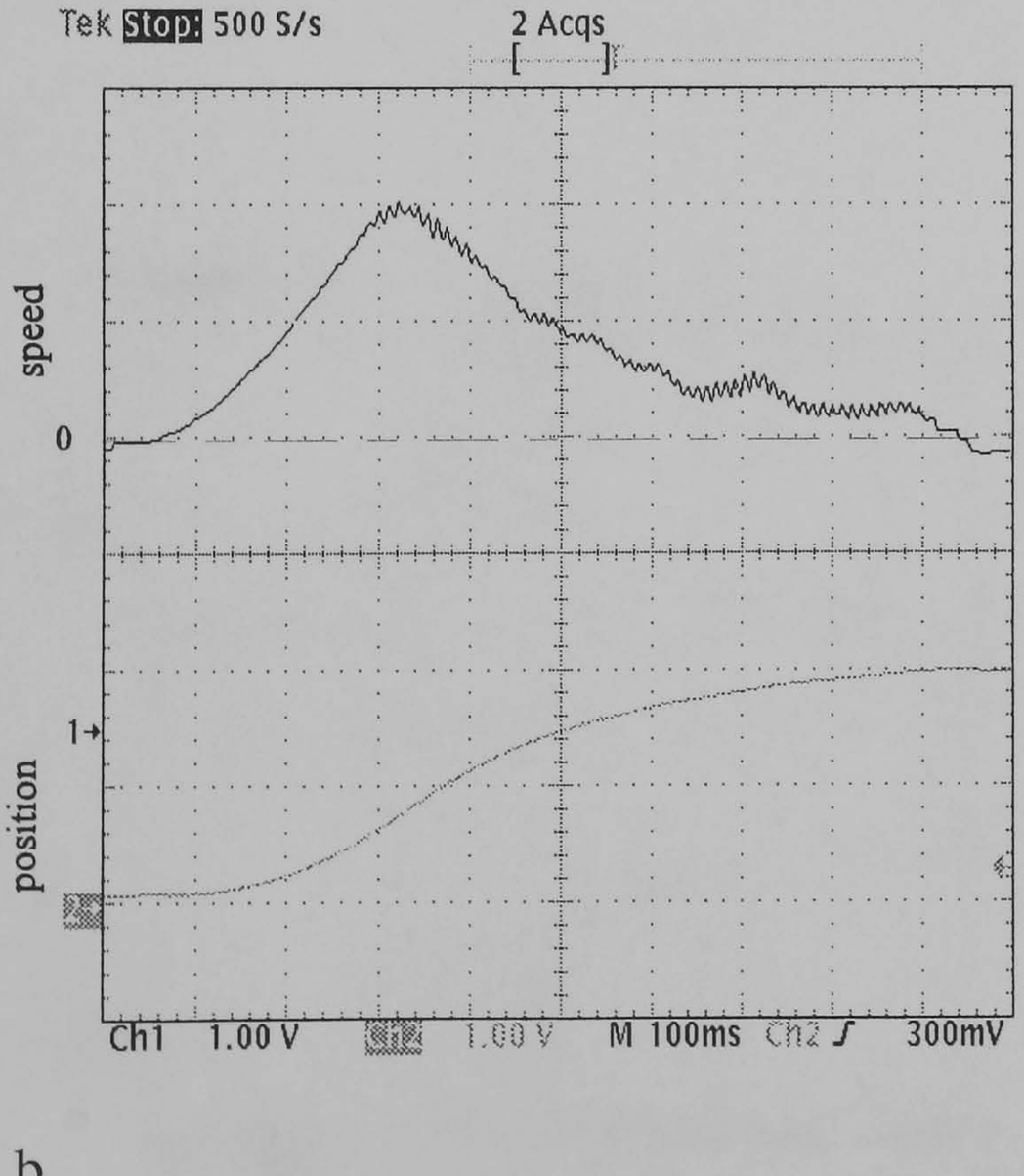

b

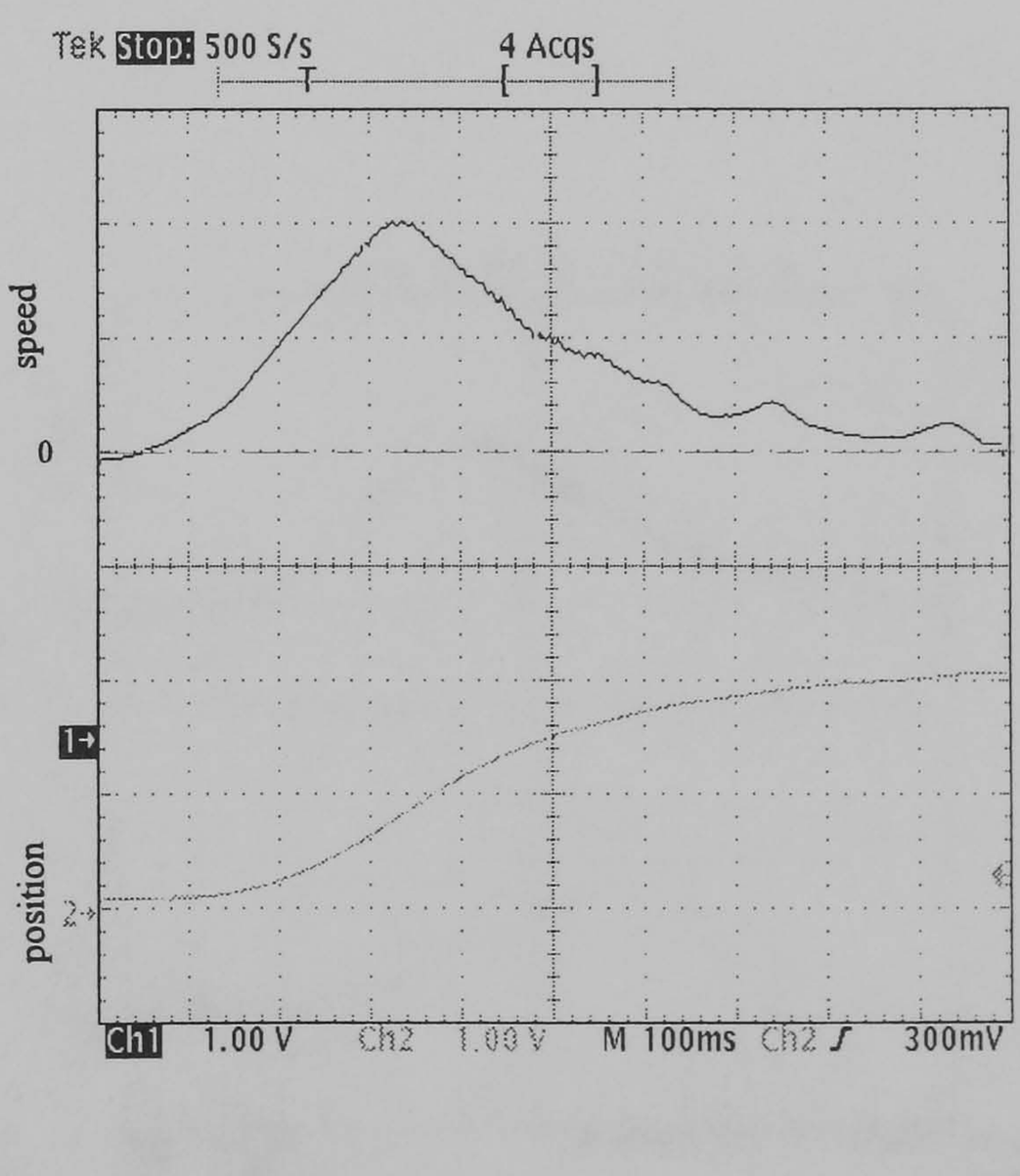

a

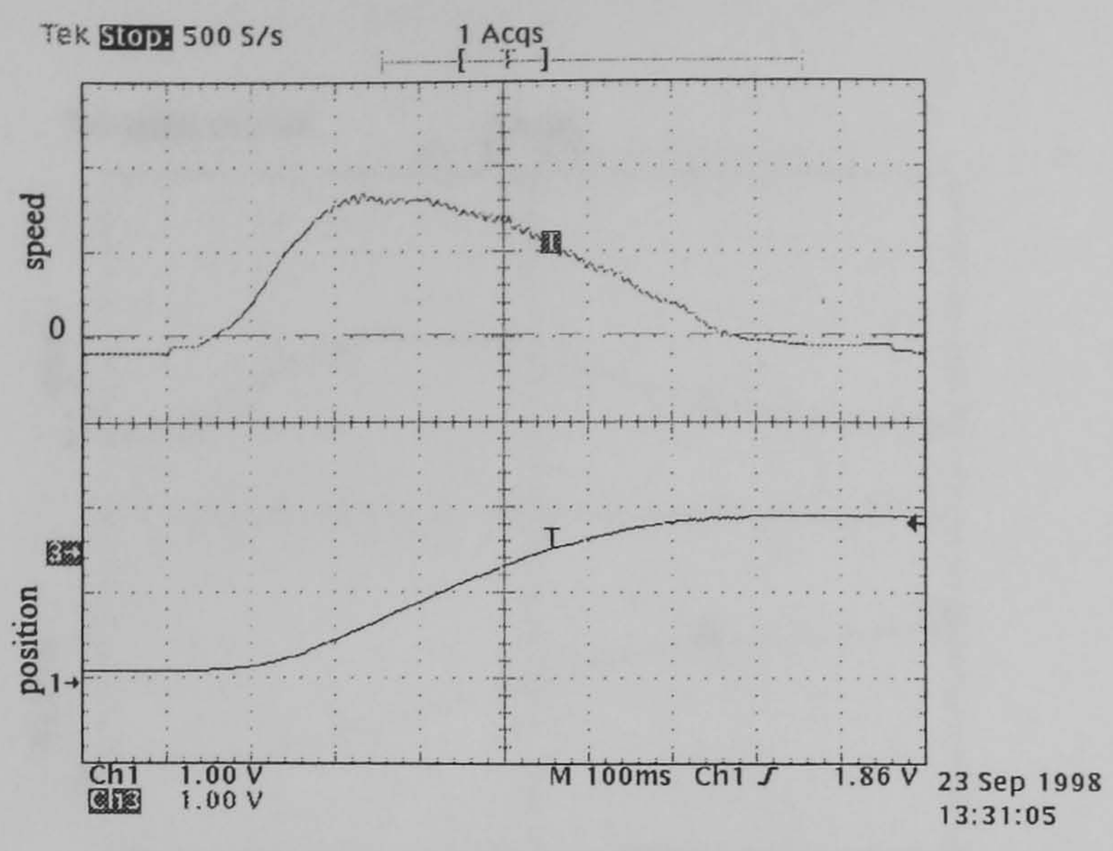

c

Figure 5.2 Regulator performance with
standard inertial load
a single component b dual component
c fixed gain
Vertical scale: 1.25 rad/div (position)
3.26 rad/s/div (speed)
Horizontal scale: 100 ms/div

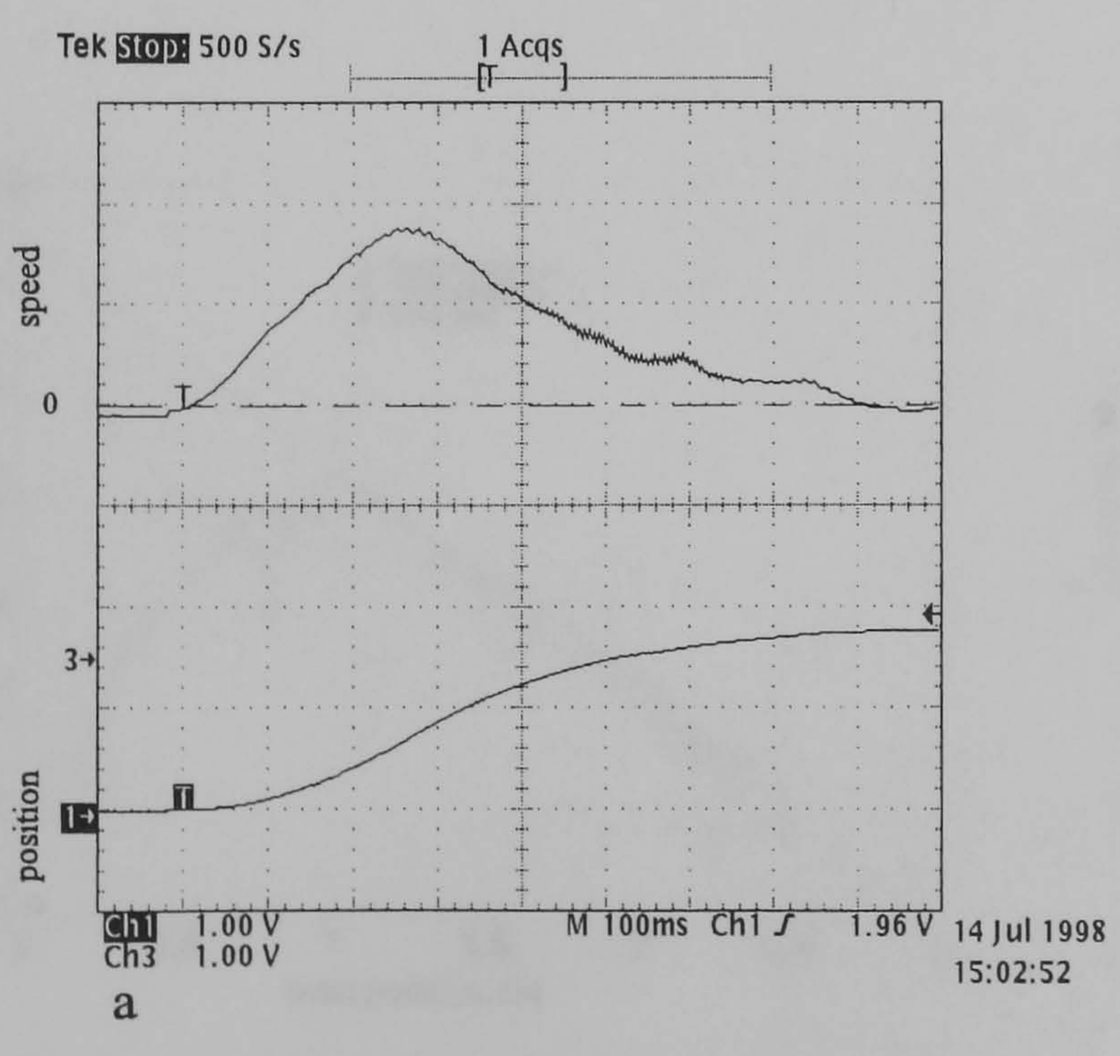

a

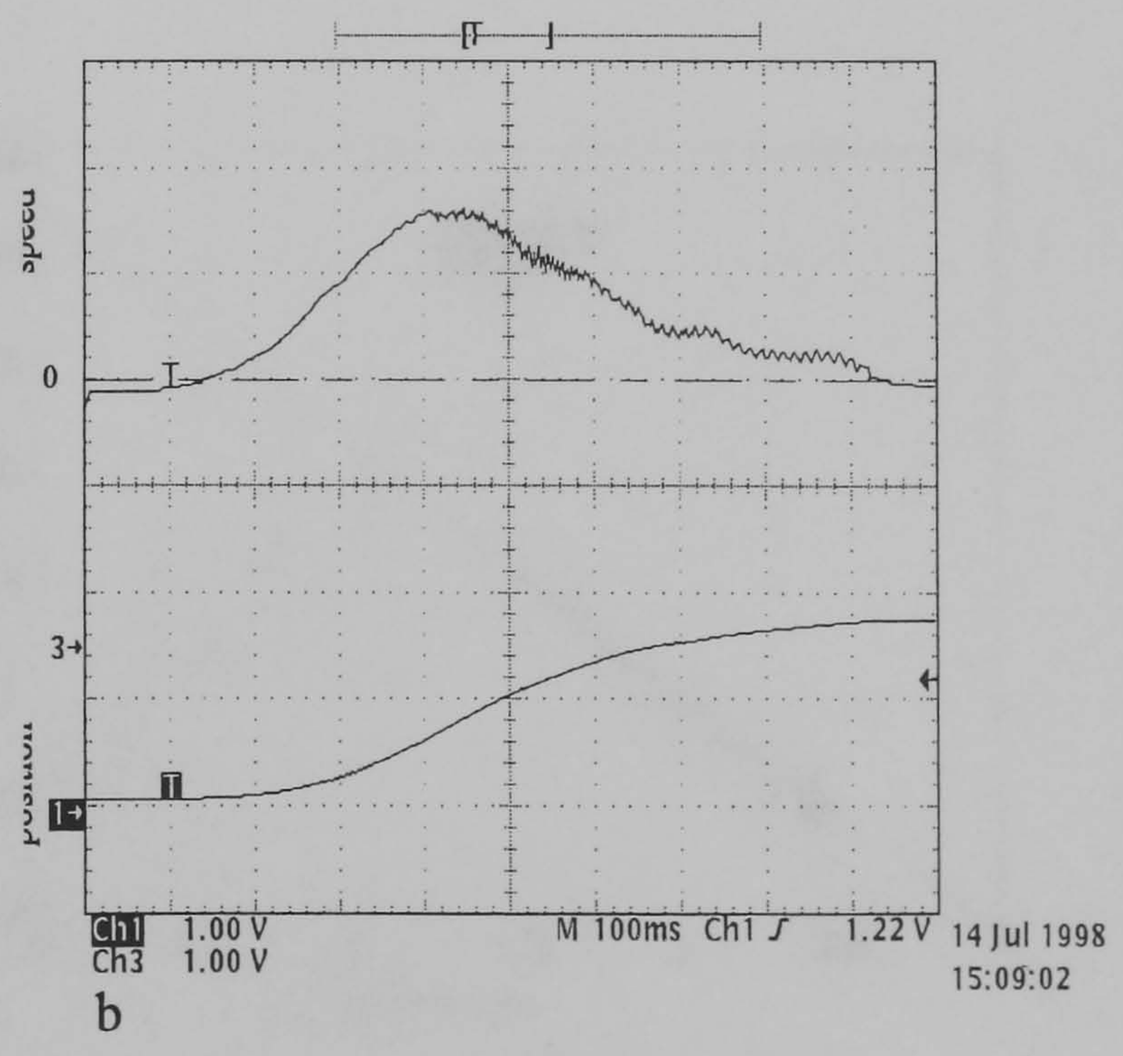

b

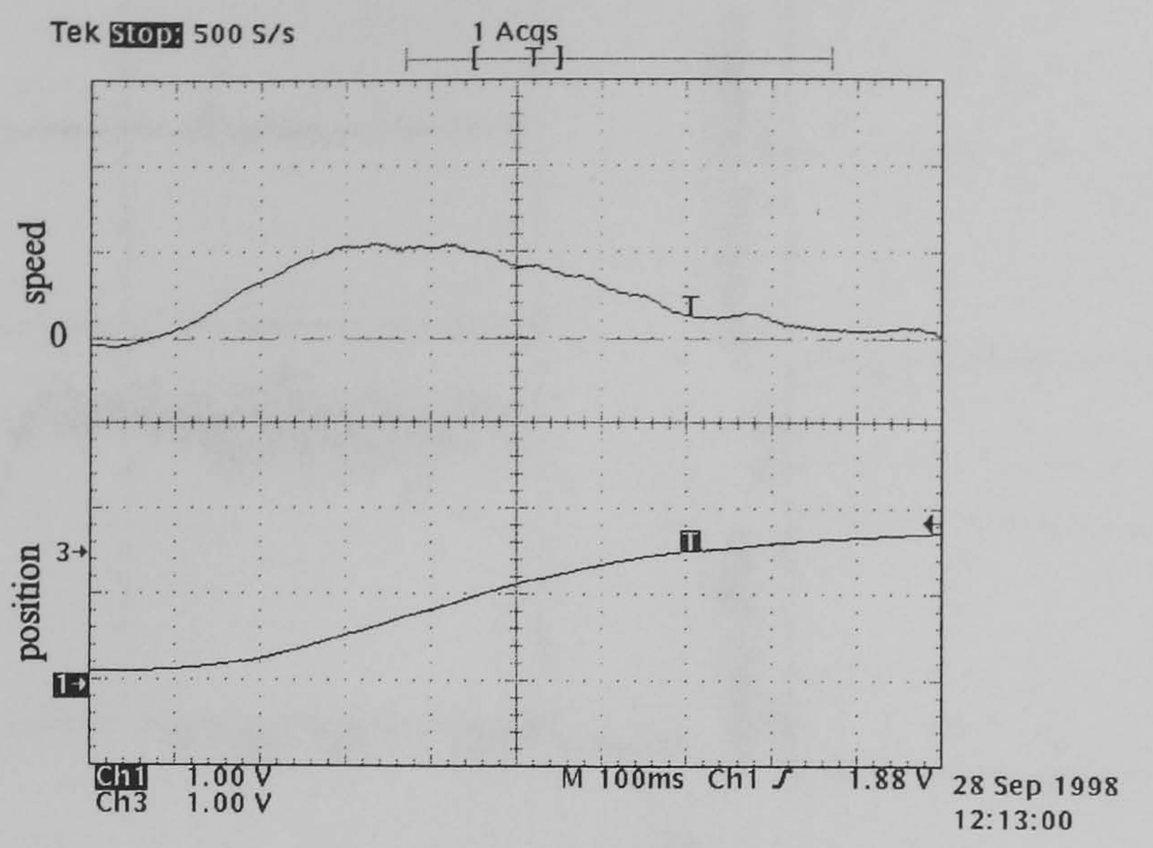

Figure 5.3 Regulator performance with
high inertial load
a single component b dual component
c fixed gain
Vertical scale: 1.25 rad/div (position)
3.26 rad/s/div (speed)
Horizontal scale: 100 ms/div

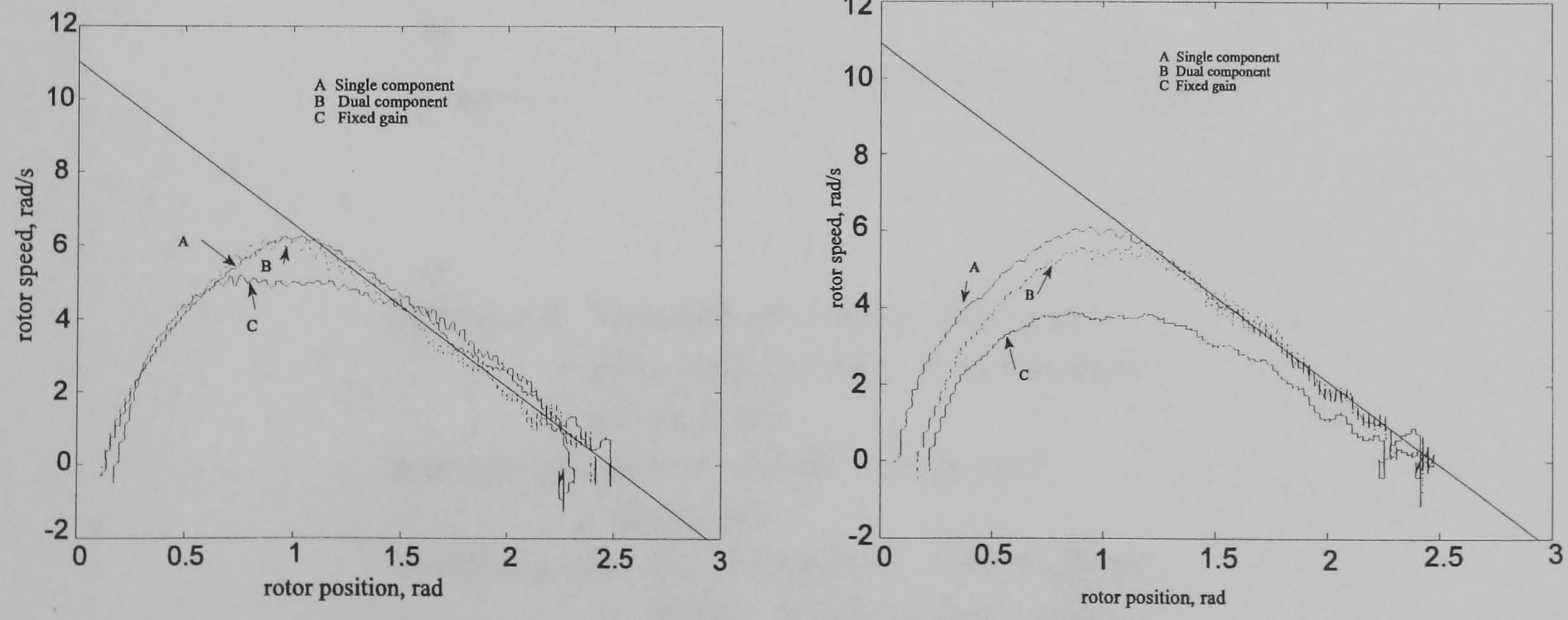

a standard inertial load

b high inertial load

Figure 5.4 Phase plane plot

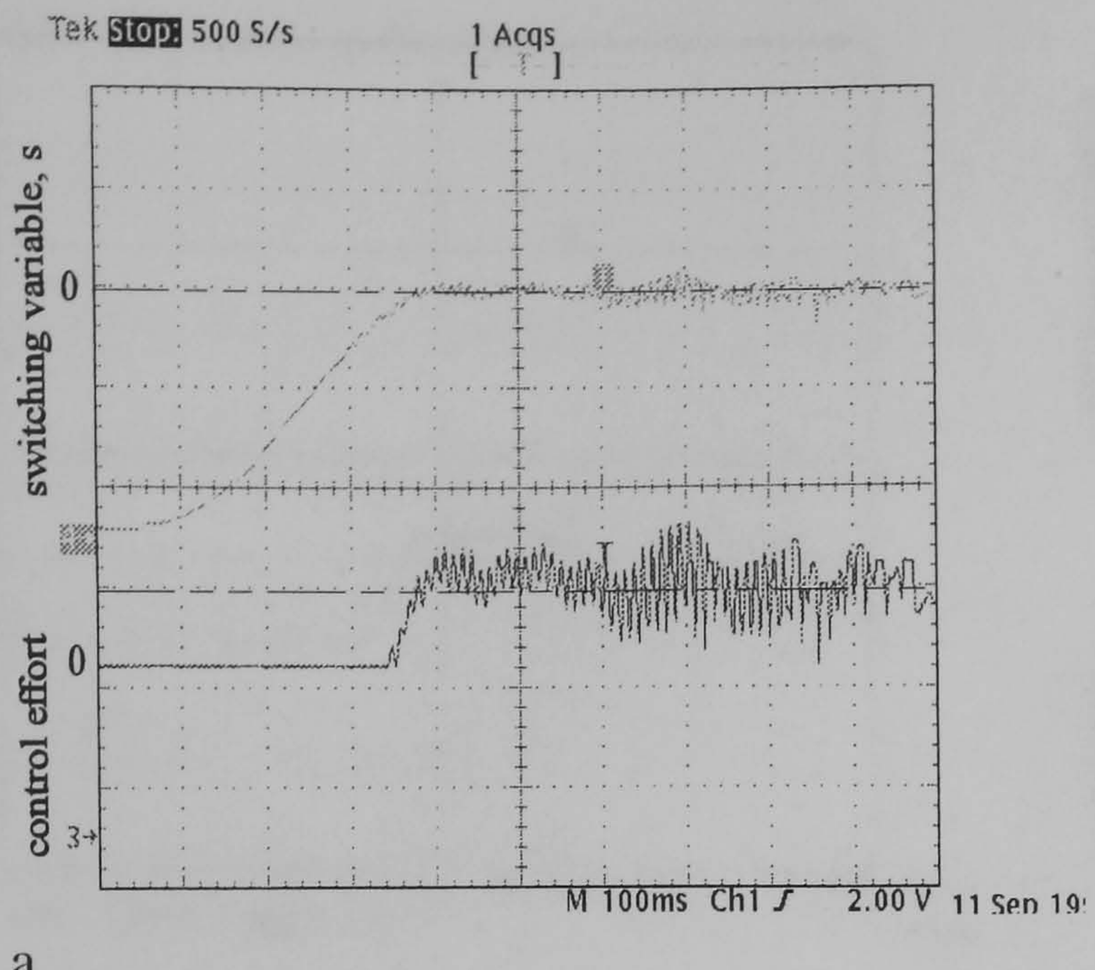

a

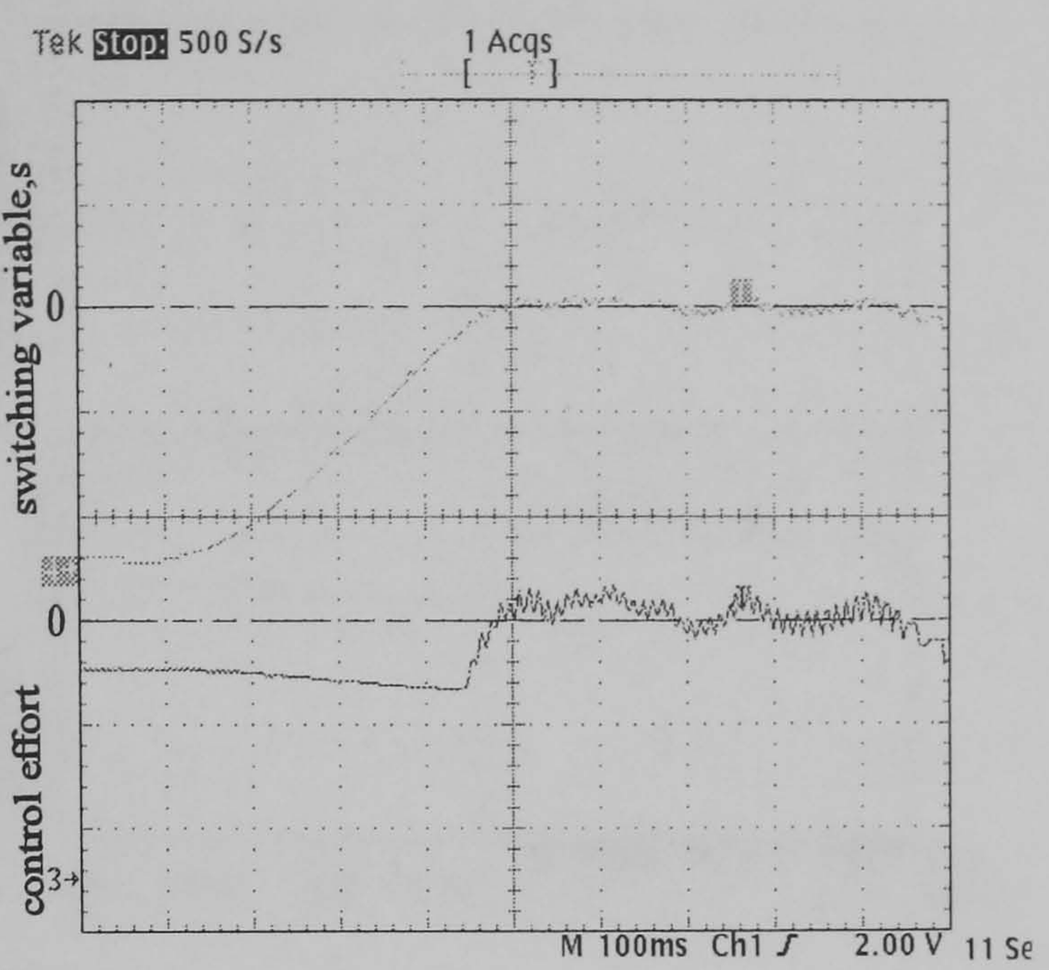

b

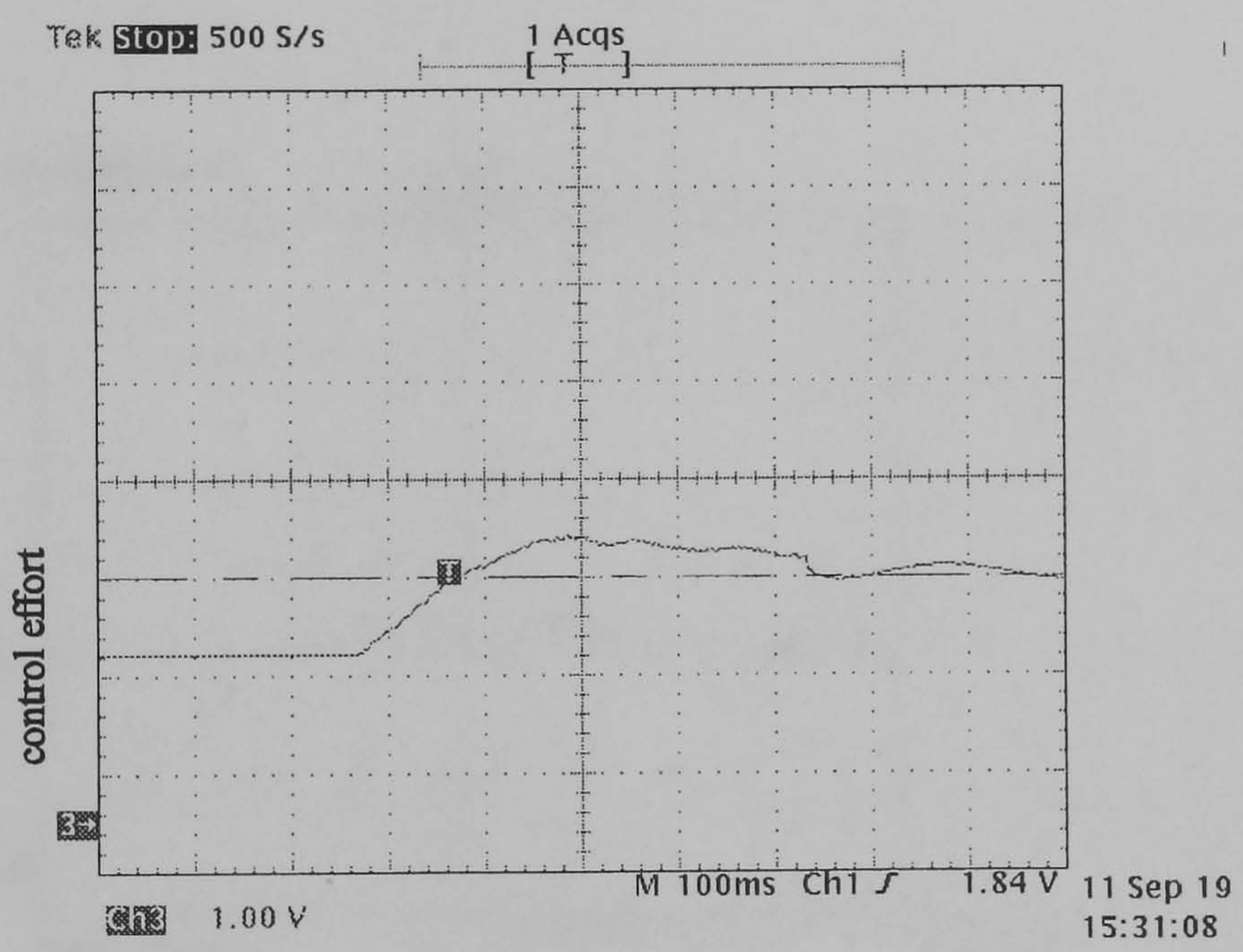

c

Figure 5.5 Variation of control effort and switching variable with standard inertia load

a single component b dual component

c fixed gain

Vertical scale: 16.67 Amp/div (control effort)

4/ div (switching variable)

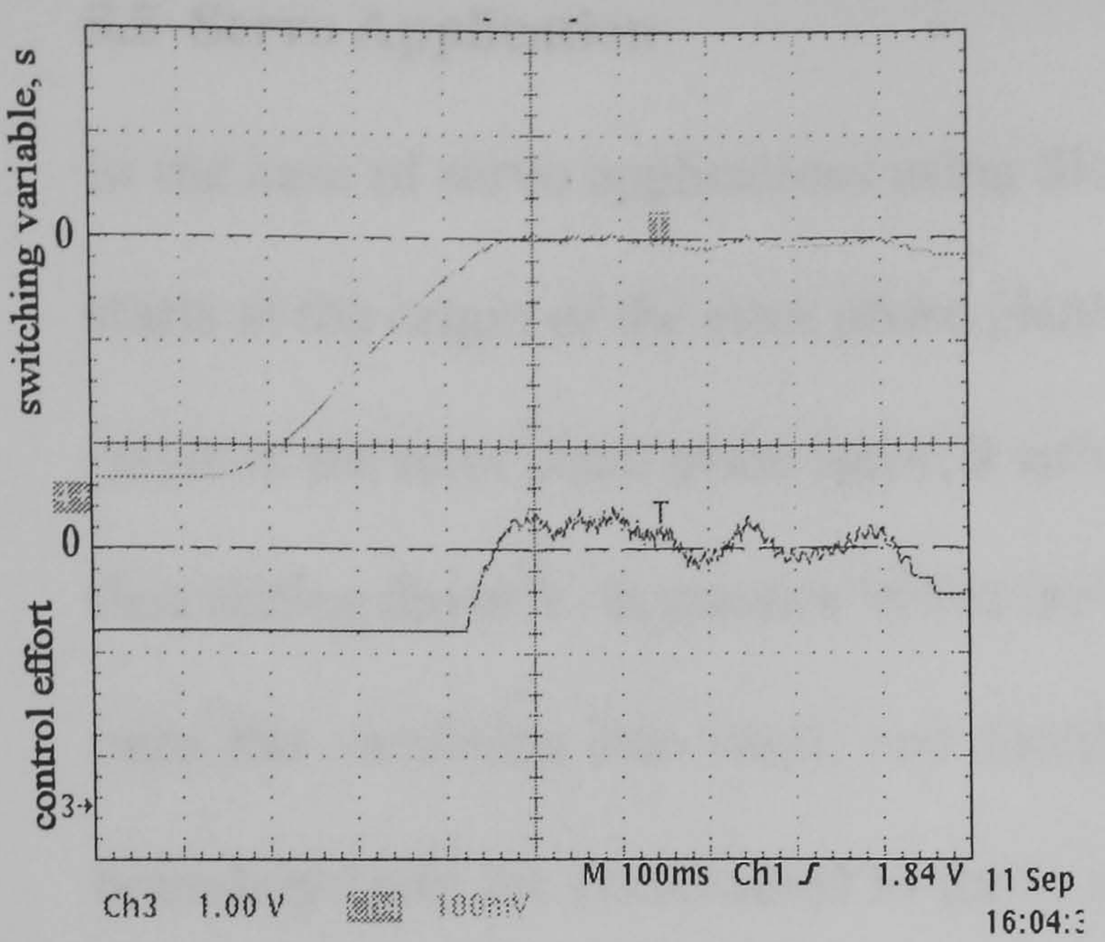

a

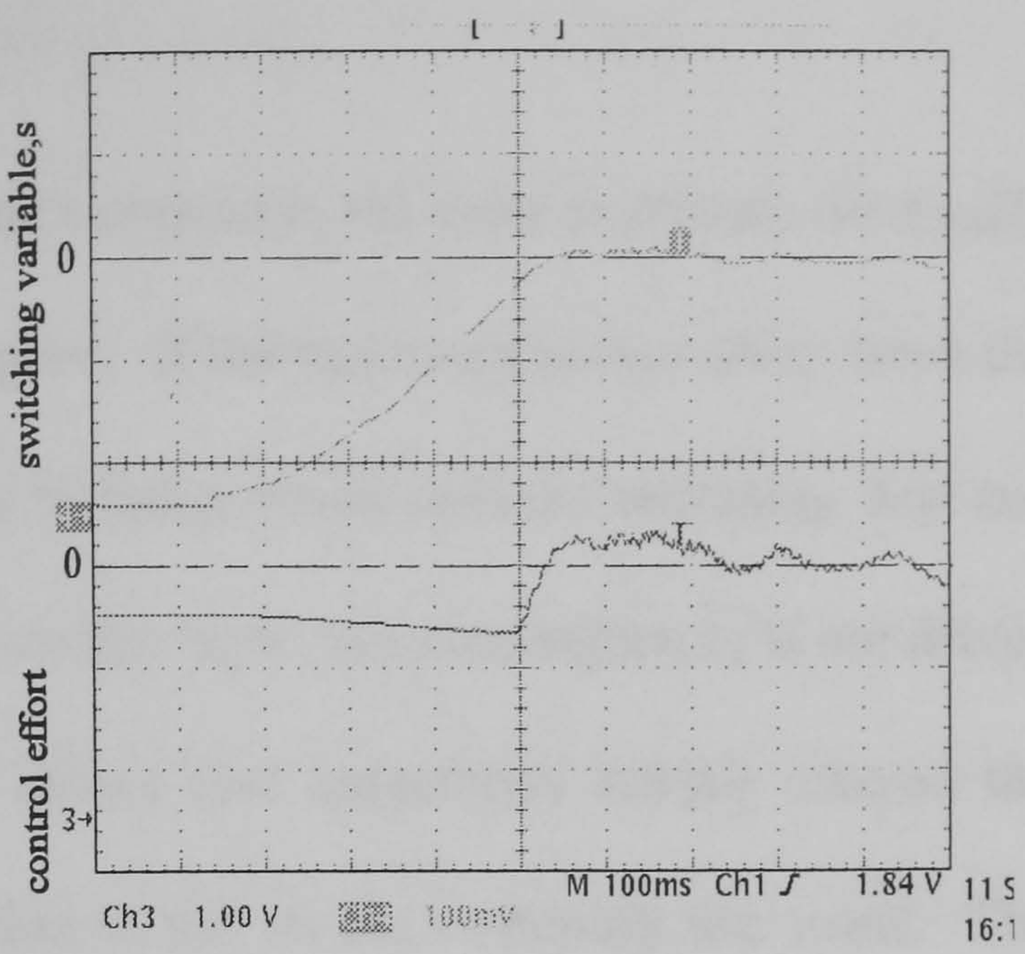

b

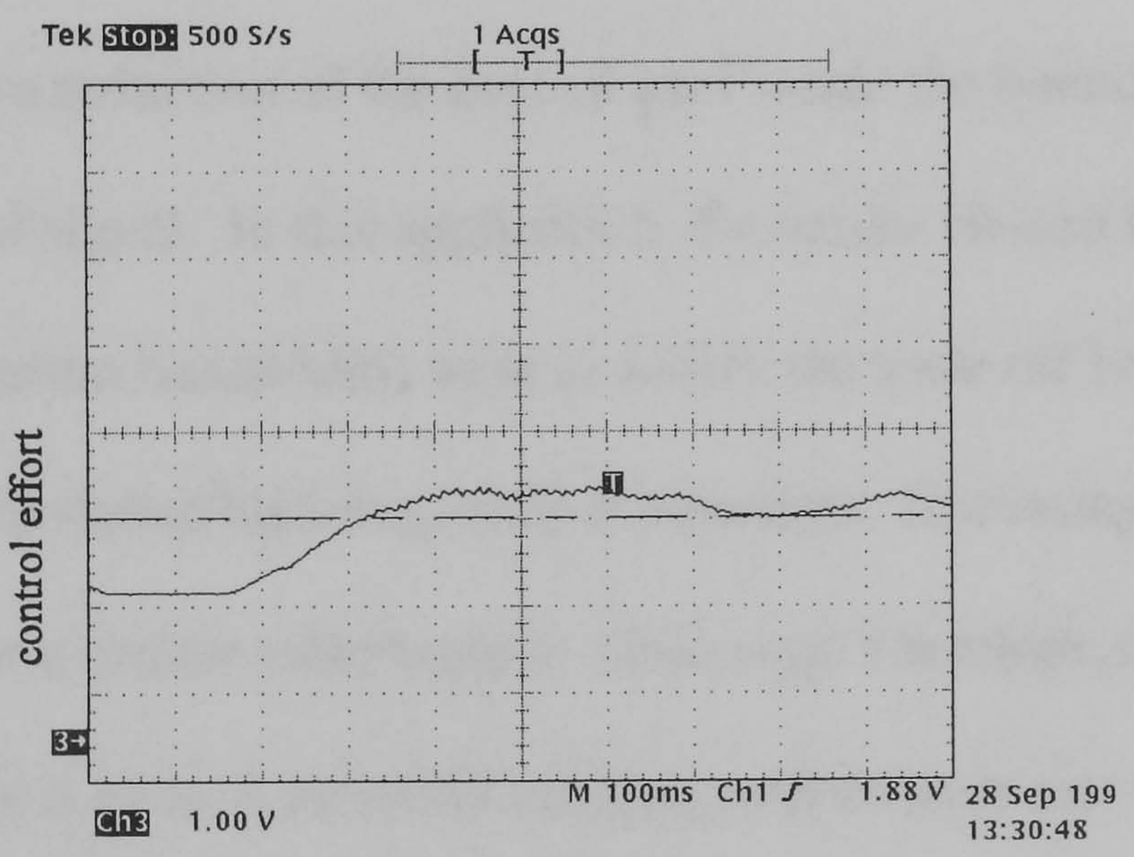

c

Figure 5.6 variation of control effort and switching variable with high inertia load

a single component b dual component c fixed gain

Vertical scale: 16.67 Amp/div (control effort)
4/ div (switching variable)

5.5 Servo Application

In the case of servo applications using Slotine's approach, the error trajectory nominally starts at the origin of the error phase plane space. If the trajectory moves away from the origin of the error phase plane space, it returns by being driven onto the switching line and then sliding down it. In practice within the boundary layer, the state trajectory is not driven onto the switching line itself, and Slotine shows that trajectories having entered the boundary layer are constrained to move within it, not on the switching line itself. The theoretical maximum deviation of the rotor angle from the switching line (tracking error) is given by:

$$\varepsilon = \frac{\phi}{\lambda}$$

This amounts to a reduction of the control gain inside the boundary layer and results in a smoother control signal. In this application, the values chosen for ϕ (the boundary layer width) and λ (system bandwidth) were to satisfy the trade off between tracking error and robustness to unmodelled high frequency components. Increasing ϕ will increase the error, lowering it below a certain value leads to chattering. Therefore, even if the estimate of the system dynamics is poor, reasonable tracking performance can be obtained if the system bandwidth is sufficiently large. The design procedure implementation for the dual component sliding mode controller with incorporated load dynamics is given in Appendix E. The chosen values for ϕ= 0.7 and λ=6 in this case gives a theoretical tracking error of 0.116 radians. The desired speed and position trajectories are shown in Figure 5.7. The results from the two sliding mode controllers show the tracking errors are within that range, with the standard inertial load, Figures 5.8 and 5.9. The fixed gain controller shows good results (control efforts of the three controllers are approximately the same magnitude). However, with increased inertia, the tracking errors of the fixed gain controller increases

which is not the case with the two sliding mode controllers. Table 5.2 shows the range of tracking error values for the three controllers. From the values in the table, both sliding mode controllers exhibit increased tracking errors for a high inertial load. The dual component controller with load dynamics incorporated is superior to the single component controller, in terms of peak errors. Figures 5.10 and 5.11 show the variation of the switching variable s with the high and standard inertial load. In the standard inertia case, the boundary layer width is not exceeded proving that sliding occurs and these values are shown in Table 5.2. Figures 5.12 and 5.13 show plots of control effort, i_{qs}^{*} versus time, for the three controllers. The control effort of the fixed gain controller is smoother than both the sliding mode controllers in the standard inertia case. The control efforts of the two sliding mode controllers are similar, chattering is obvious in the waveforms. Both chattering and inductance ripple affect performance. The apparent "chattering" seen in the control effort of the fixed gain controller is in fact due to inductance ripple effects, since this type of controller does not chatter. The saturated segments in the control effort in Figure 5.13 c occurs when the inverter current limit is reached. A machine model accounting for inductance ripple is presented in the next chapter. Increasing the inertia leads to higher chattering levels in the single-component sliding mode controller. However the dual-component sliding mode controller with load dynamics incorporated shows greater robustness to inertia variation and inductance ripple.

With constant d and q axis currents, the inductance ripple causes cyclic changes in the output torque of the Synchrel machine as it rotates over a stator slot pitch. To maintain a constant output torque with constant d-axis excitation (as in this case) the q axis current must vary to compensate for the torque variation caused by inductance ripple. This is explained in Chapter 6.

In the case of the fixed gain controller, the torque equation is assumed as given in section

(5.3) with the appropriate energised *d*-axis current setting the machine gain K_T which is then assumed constant. However, the influence of inductance ripple is to vary the effective gain K_T of the machine which will in turn affect the tracking performance of the controller. This is clearly seen in the practical results for both standard and high inertial loads, Figures 5.8 and 5.9. At high load inertias the effect is more pronounced as the torque requirement and thus i_{qs}^* is higher and hence the variations required in i_{qs}^* to maintain a constant torque output are higher. To minimise the effects of torque ripple a high controller gain is required in the fixed gain case which is difficult to achieve in practice.

In this chapter, the effect of varying the load inertia J has been investigated and the single and dual component controllers are shown to have superior performance with respect to changes in load conditions compared to the fixed gain controller. A further feature of these sliding mode controllers are their potentially high controller gains. The high gains can effectively compensate for the changes in K_T as the machine rotates and hence alleviate the tracking errors associated with inductance ripple effects, Figures 5.8 and 5.9. Further, in the case of the dual component controller allowance can be made in the choice of controller gain b to account for the known variations in K_T due to inductance ripple. Alternatively, from Eq. (3) in Appendix E a variation in K_T can be regarded as equivalent to a change in load inertia with regards to the choice of gain b. If the controller is invariant to changes in J then it will also be invariant to changes in K_T. Hence the effects of inductance ripple on the tracking capabilities of the controller will be minimised and can be accounted for in the choice of gain. In short, inductance ripple impacts significantly on the performance of the fixed gain controller but has a minimal effect on the performance of the sliding mode controllers.

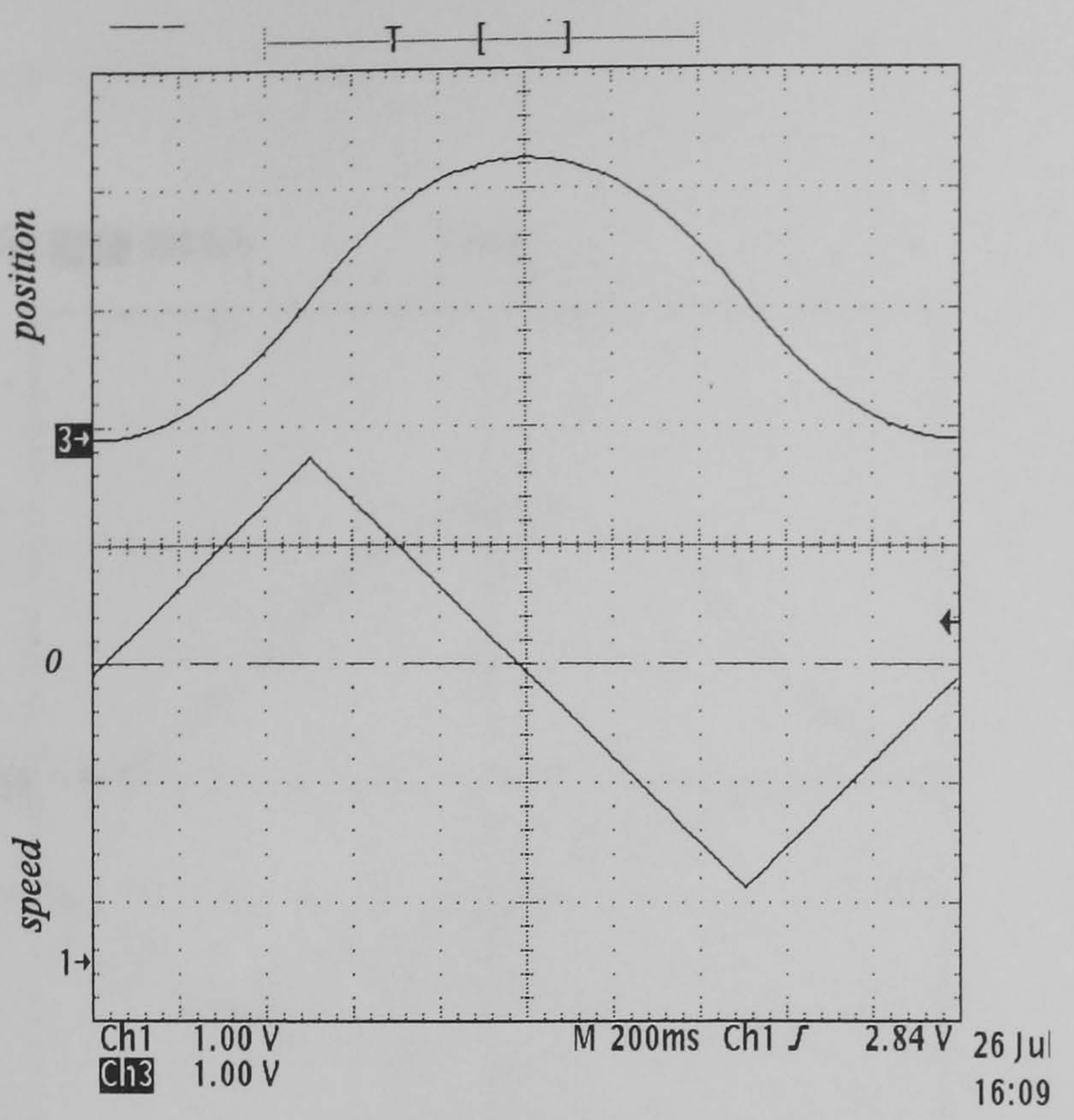

Figure 5.7 Reference position and speed trajectories
Vertical scale: 1.25 rad/div(position)
3.26 rad/s/div(speed)
Horizontal scale: 200 ms/div

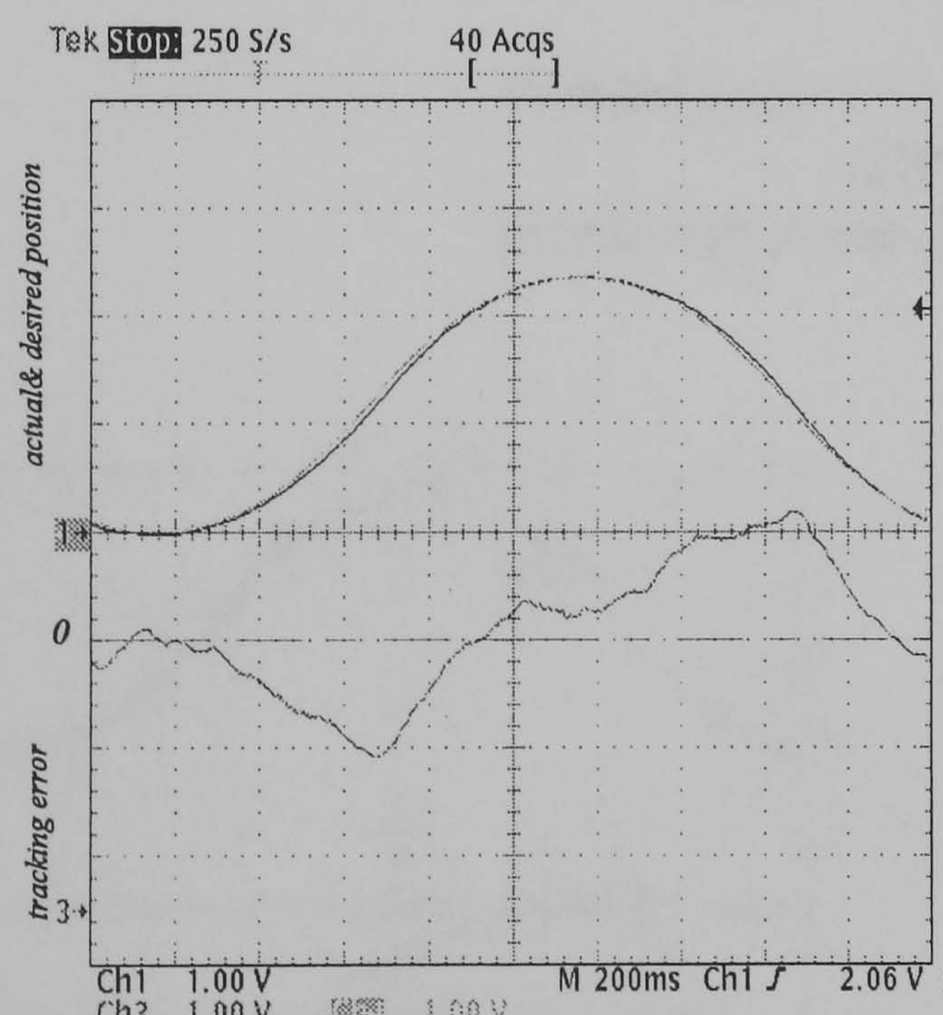

a

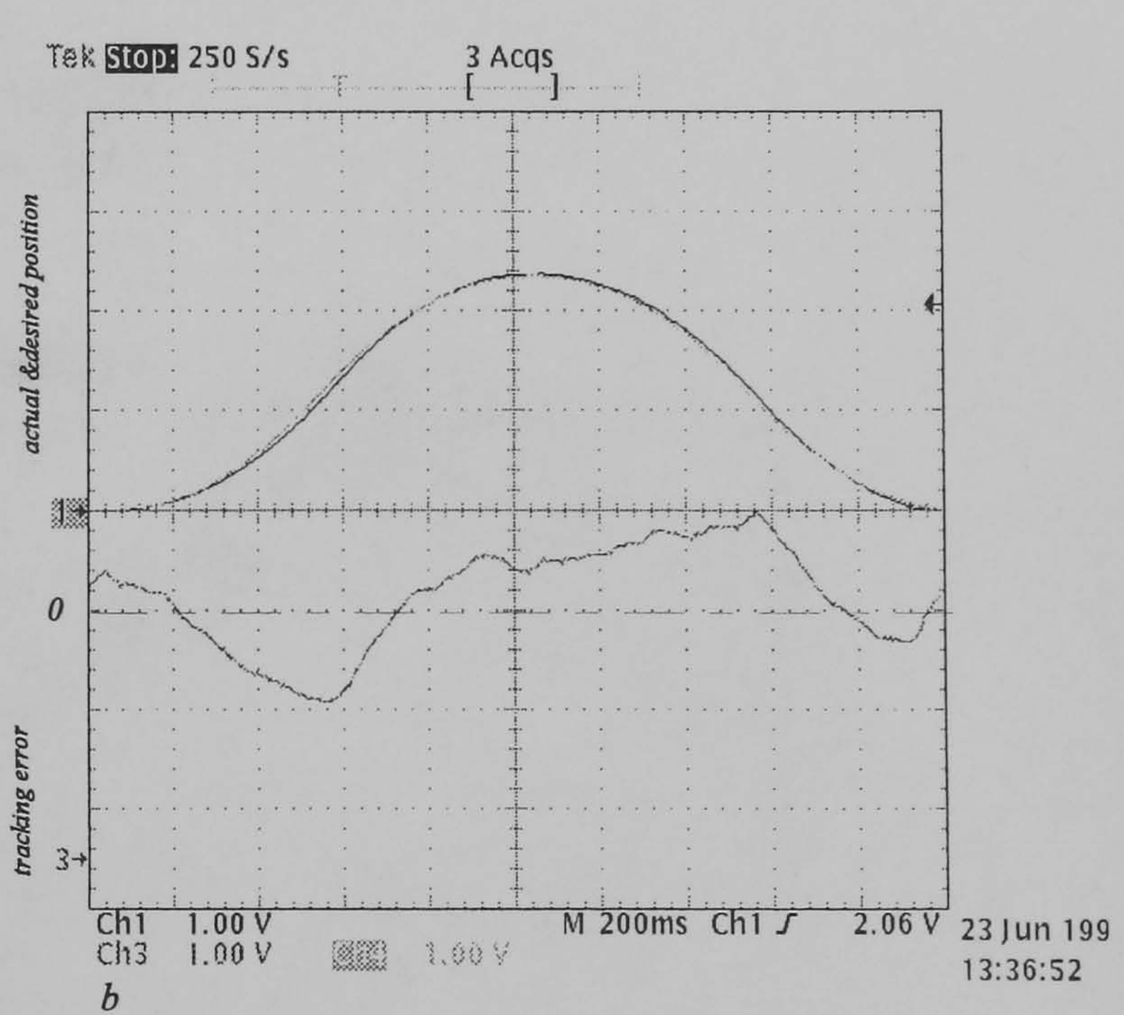

b

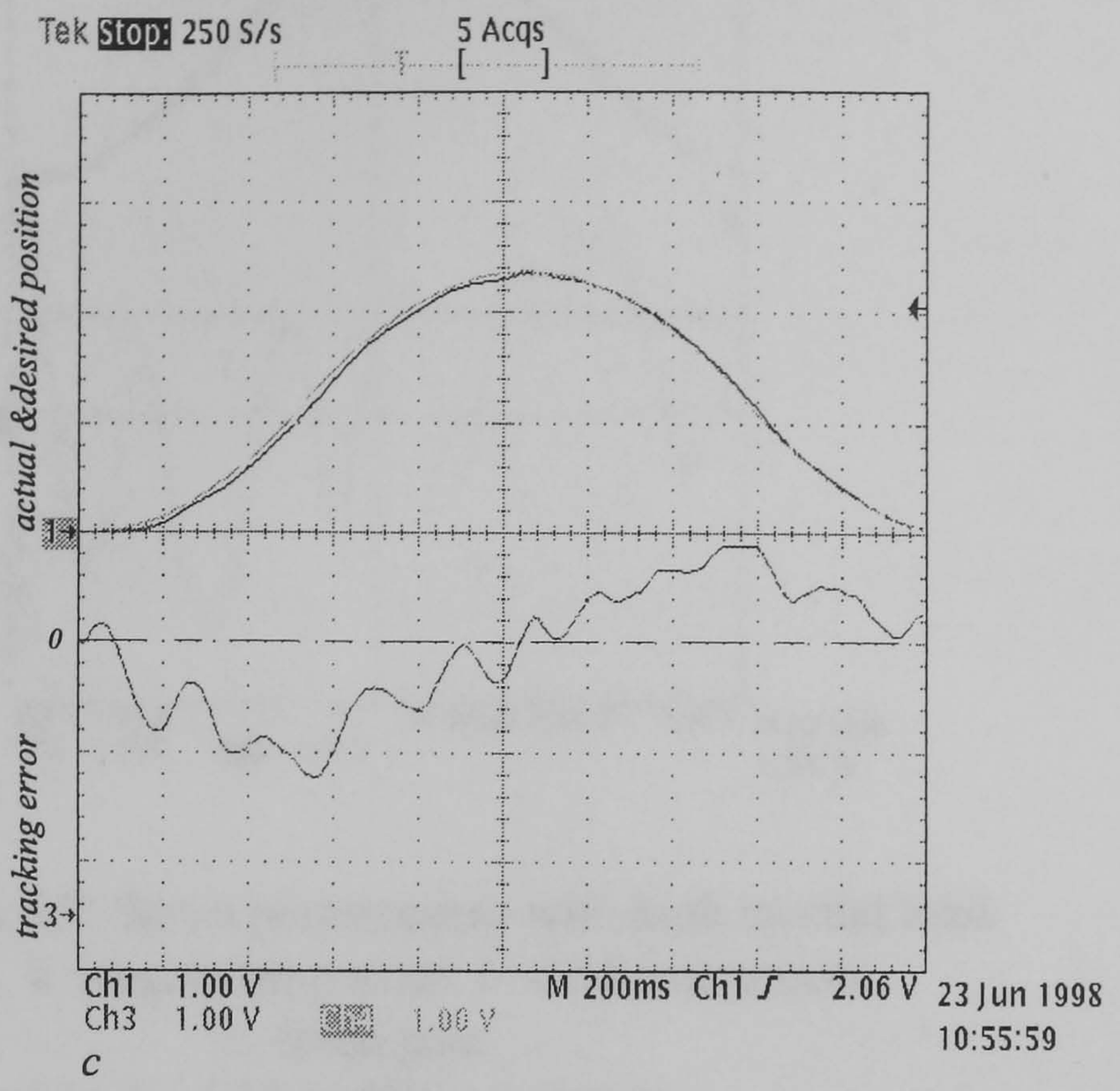

Figure 5.8 Servo performance with standard inertial load

a single component b dual component

c fixed gain

Vertical scale: 1.25 rad/div (position)

0.085 rad/div (error)

Horizontal scale: 200 ms/div

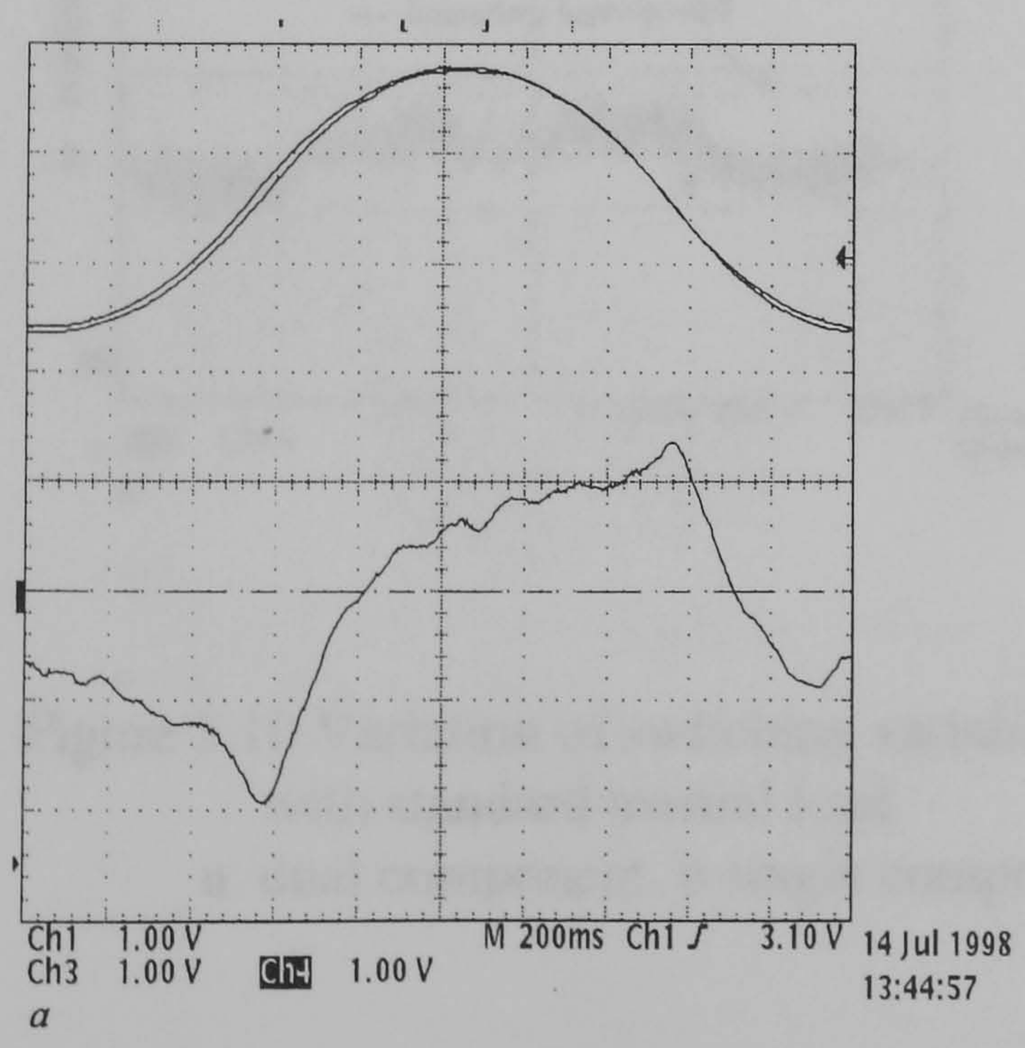

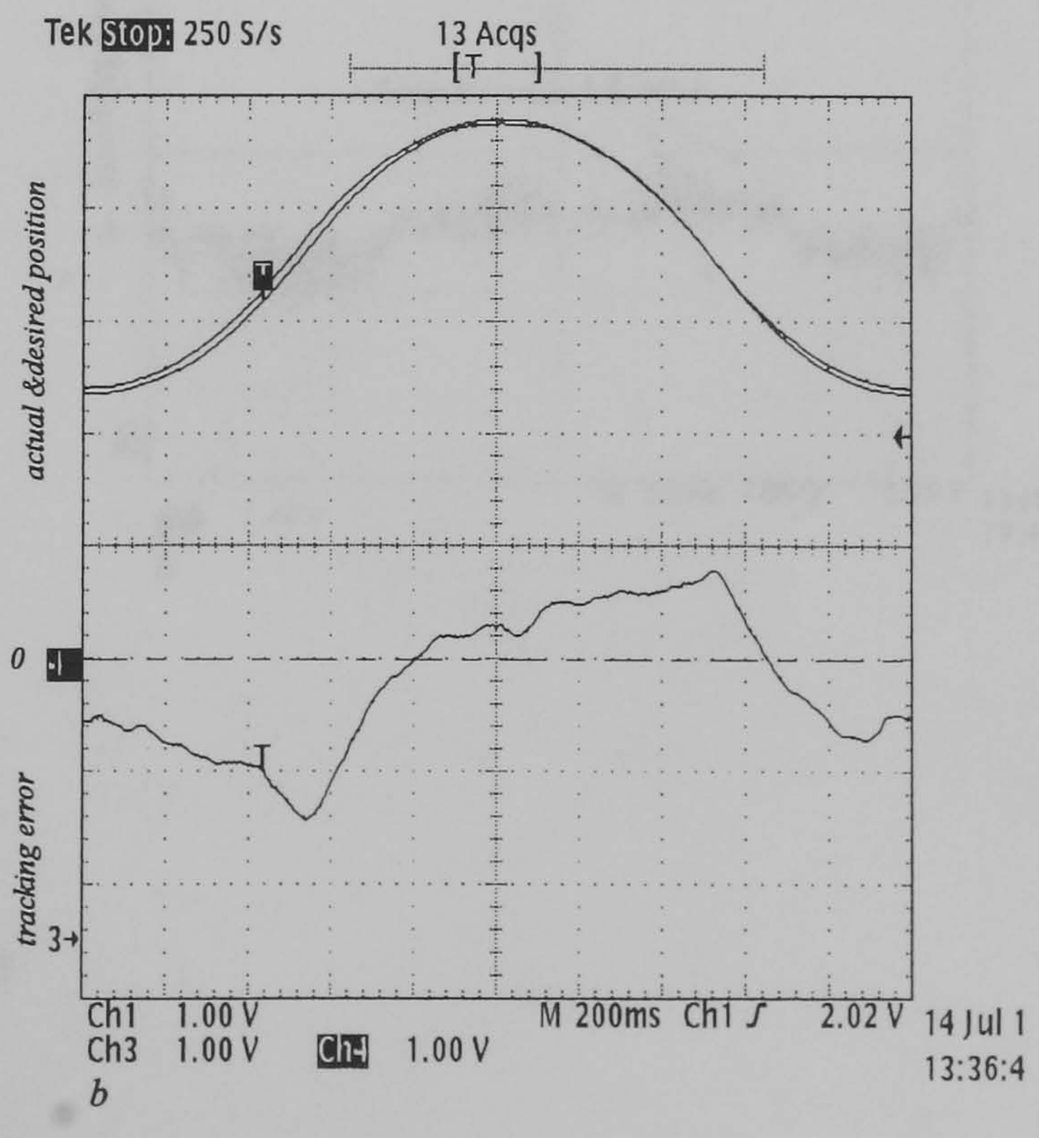

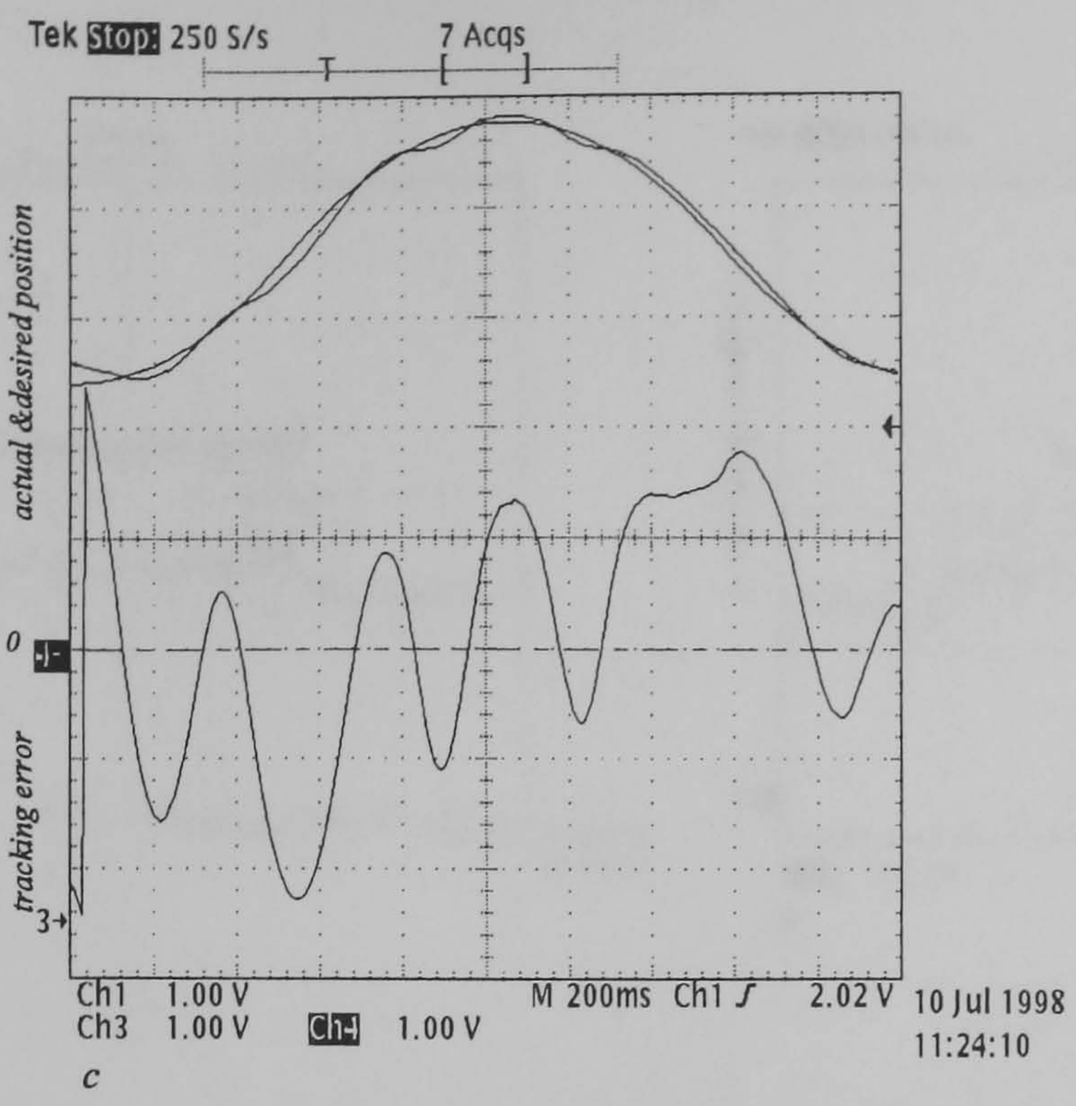

Figure 5.9 Servo performance with high inertial load
a single component b dual component
c fixed gain
Vertical scale: 1.25 rad/div (position)
0.085 rad/div (error)
Horizontal scale: 200 ms/div

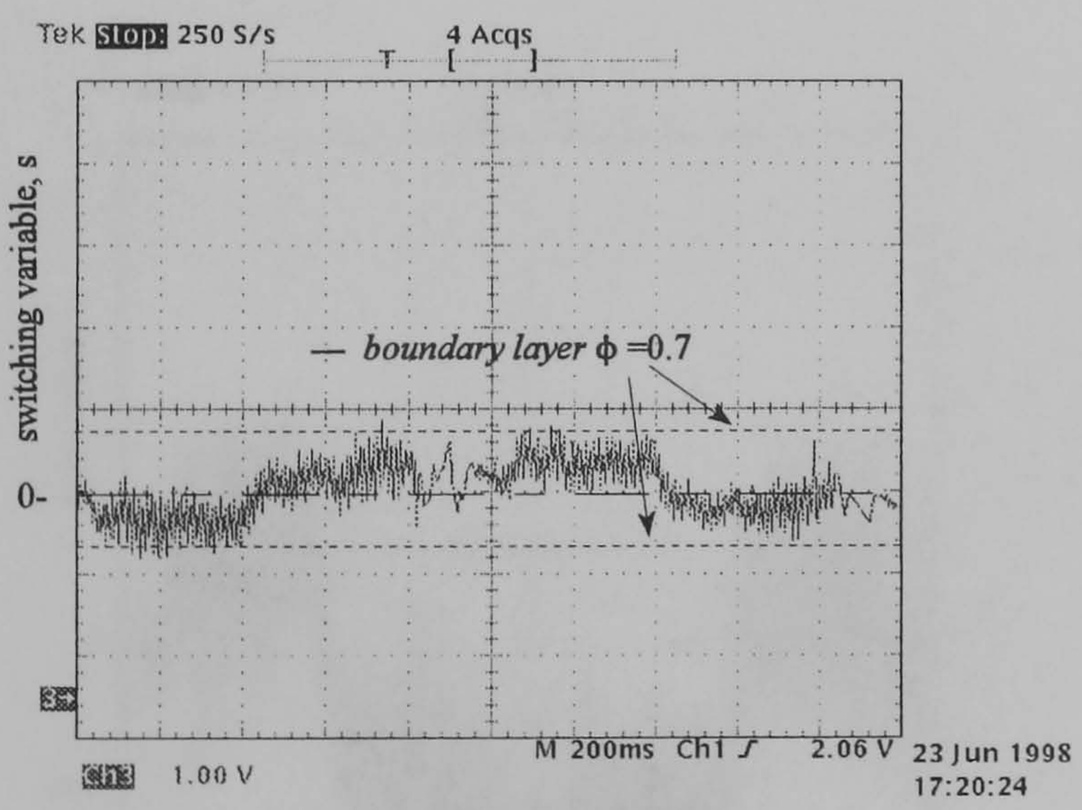

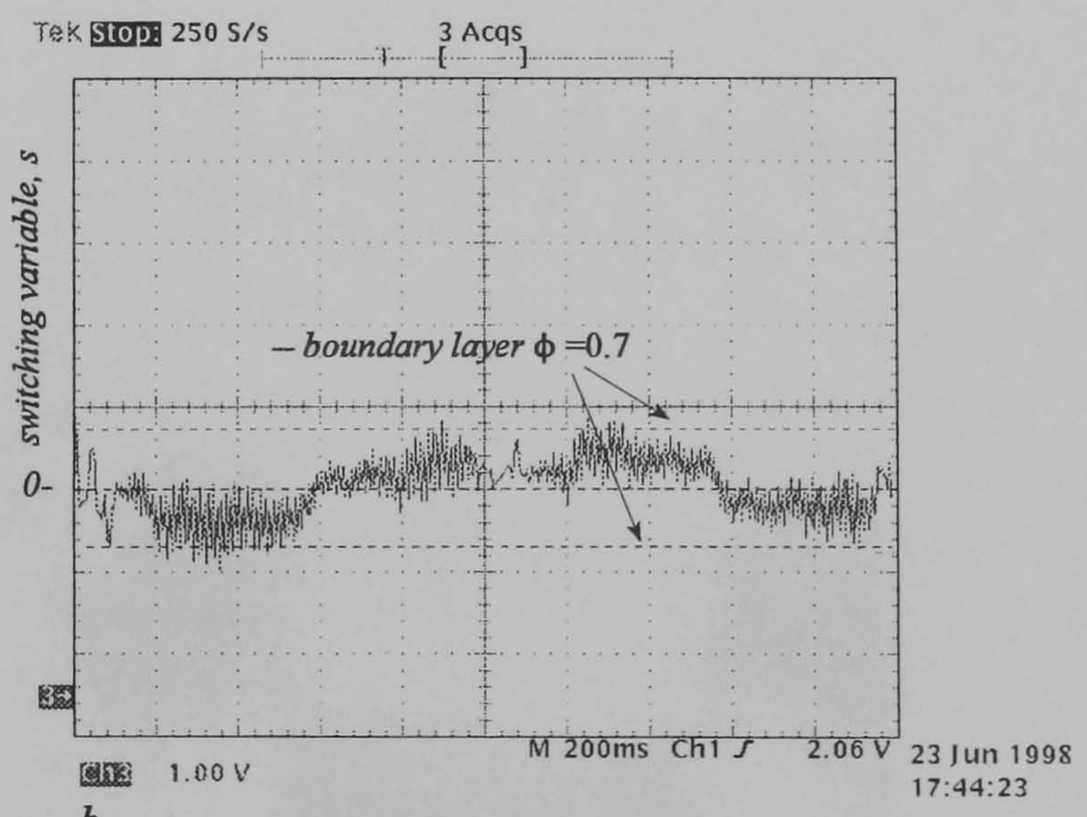

Figure 5.10 Variation of switching variable, s
with standard inertial load
a dual component b single component

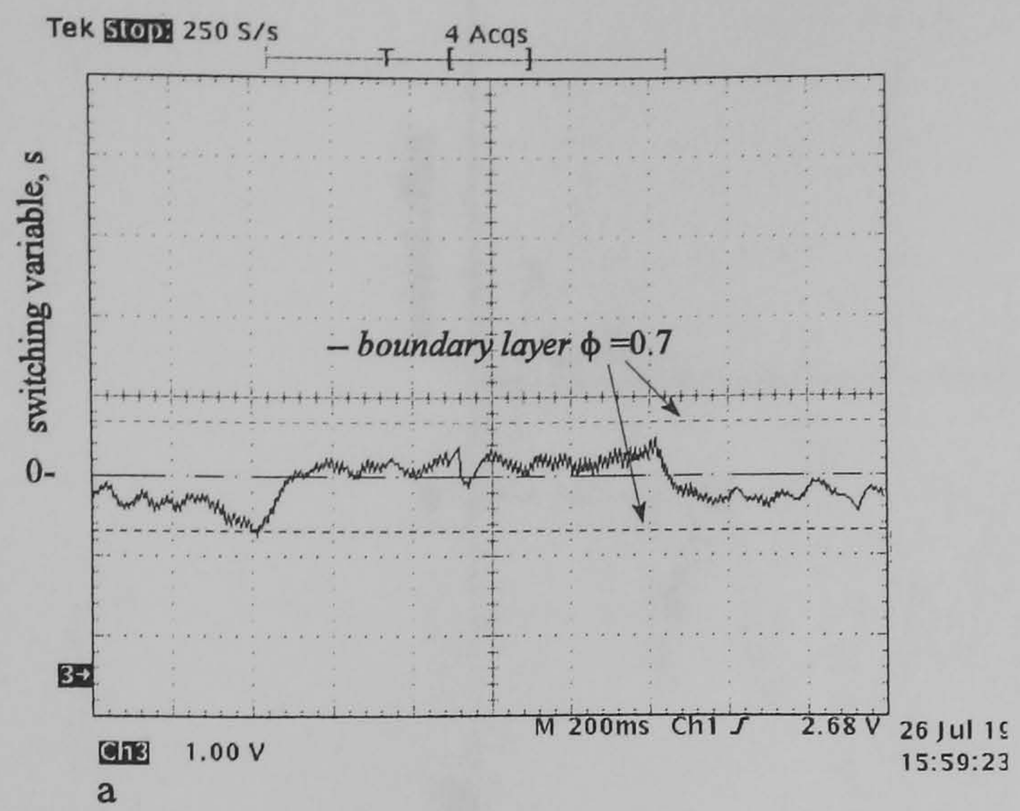

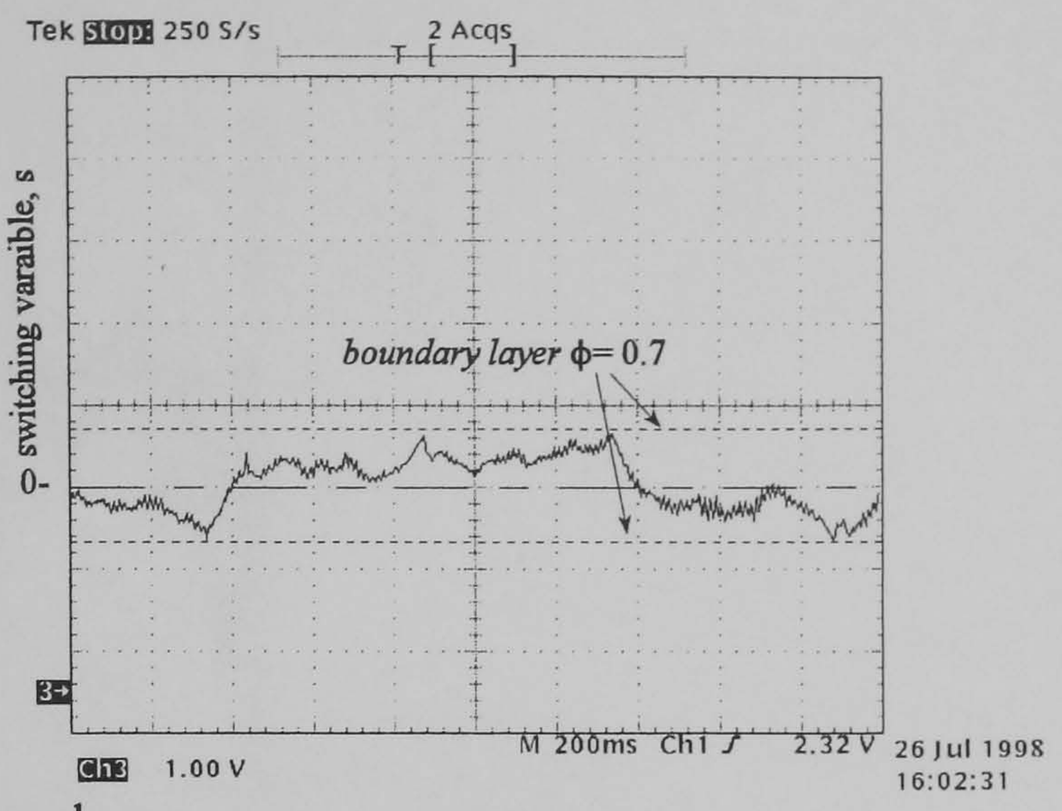

Figure 5.11 Variation of switching variable, s
with high inertial load
a dual component b single component

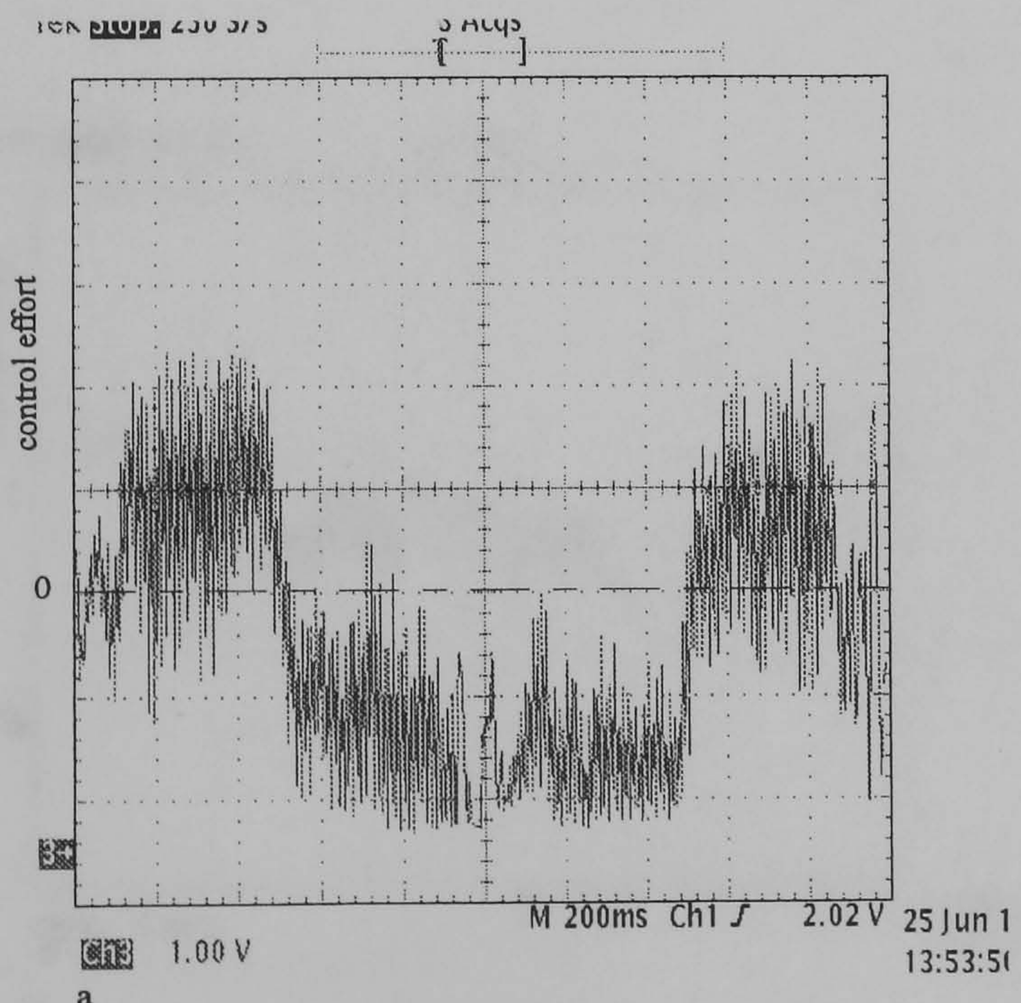

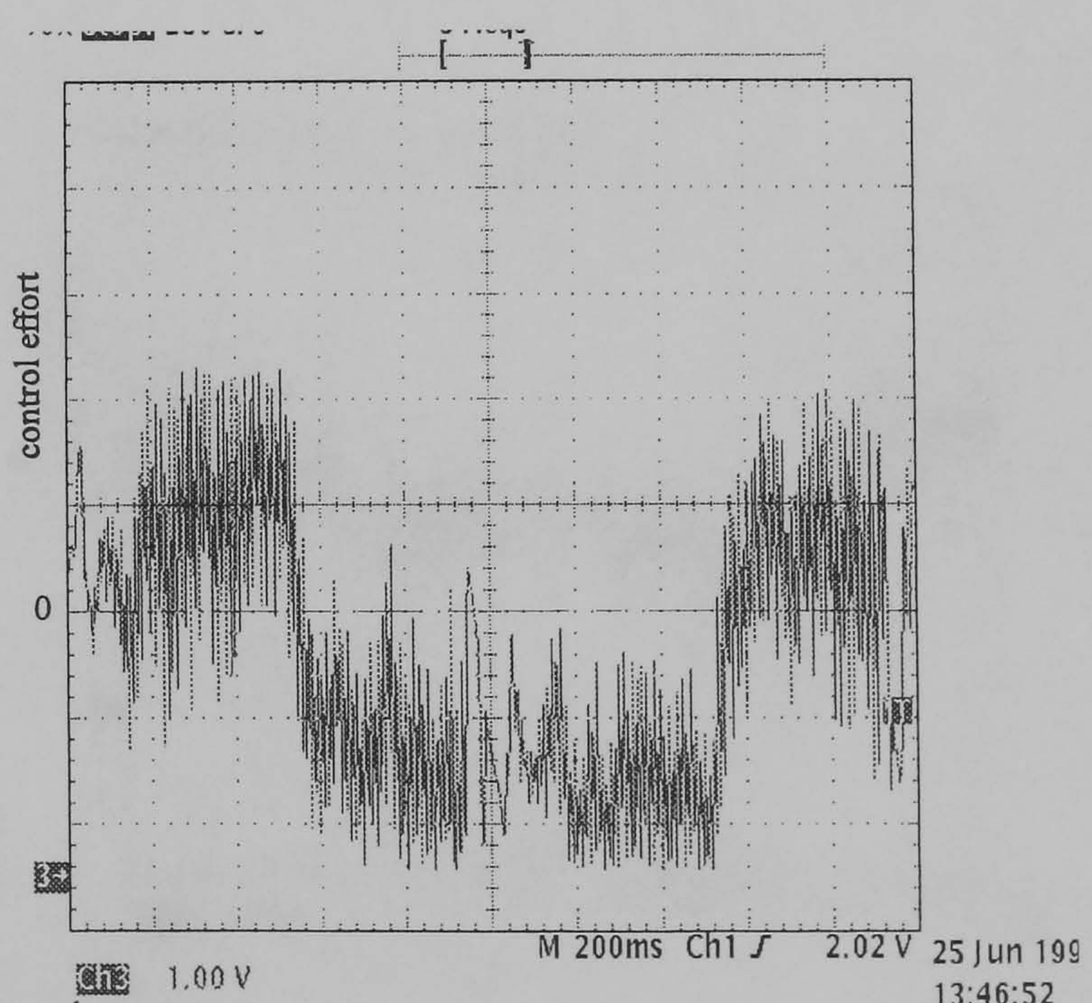

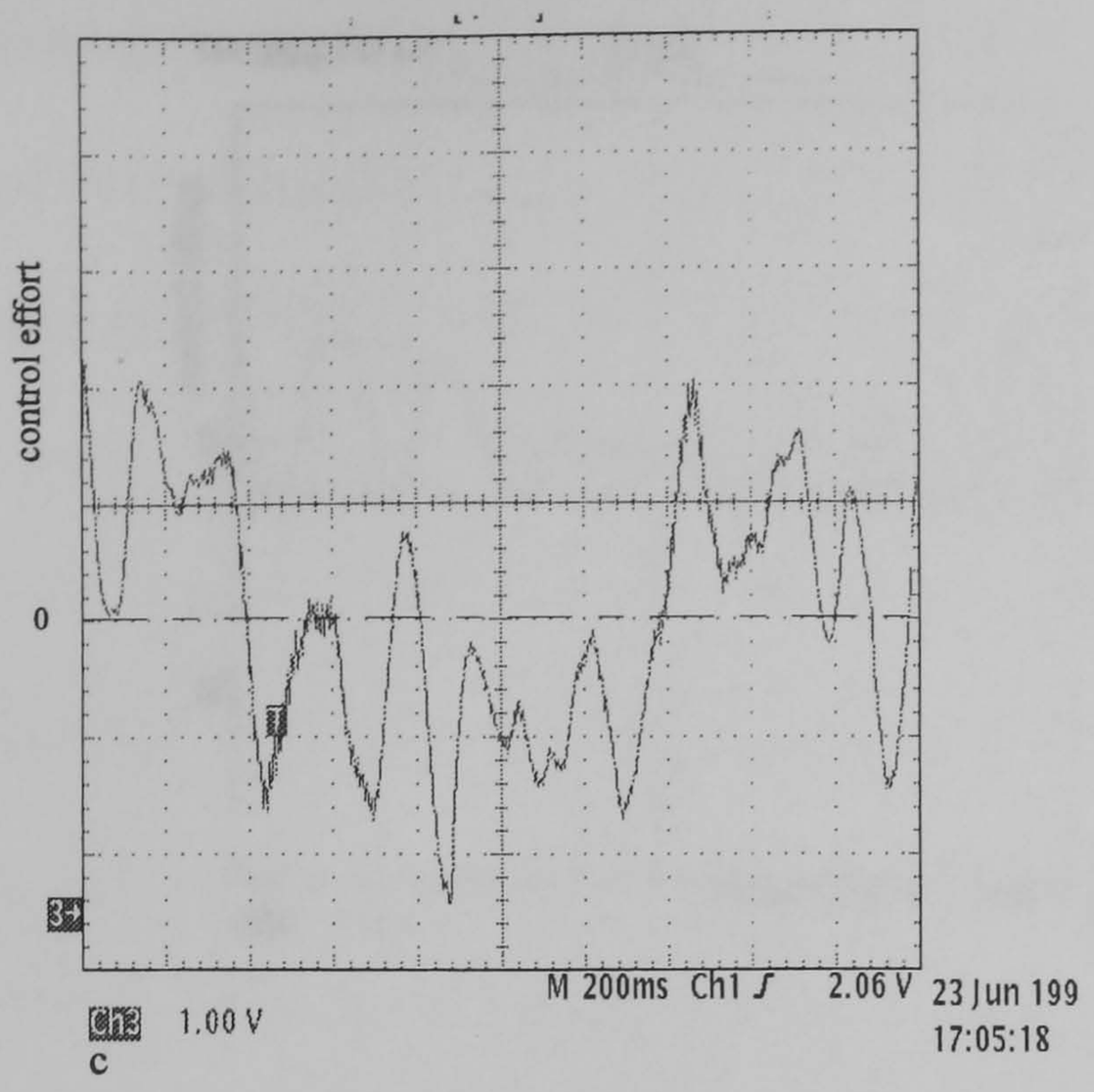

c

Figure 5.12 Control effort with standard inertial load

a single component b dual component

c fixed gain

Vertical scale: 5 Amp/div

Horizontal scale: 200 ms/div

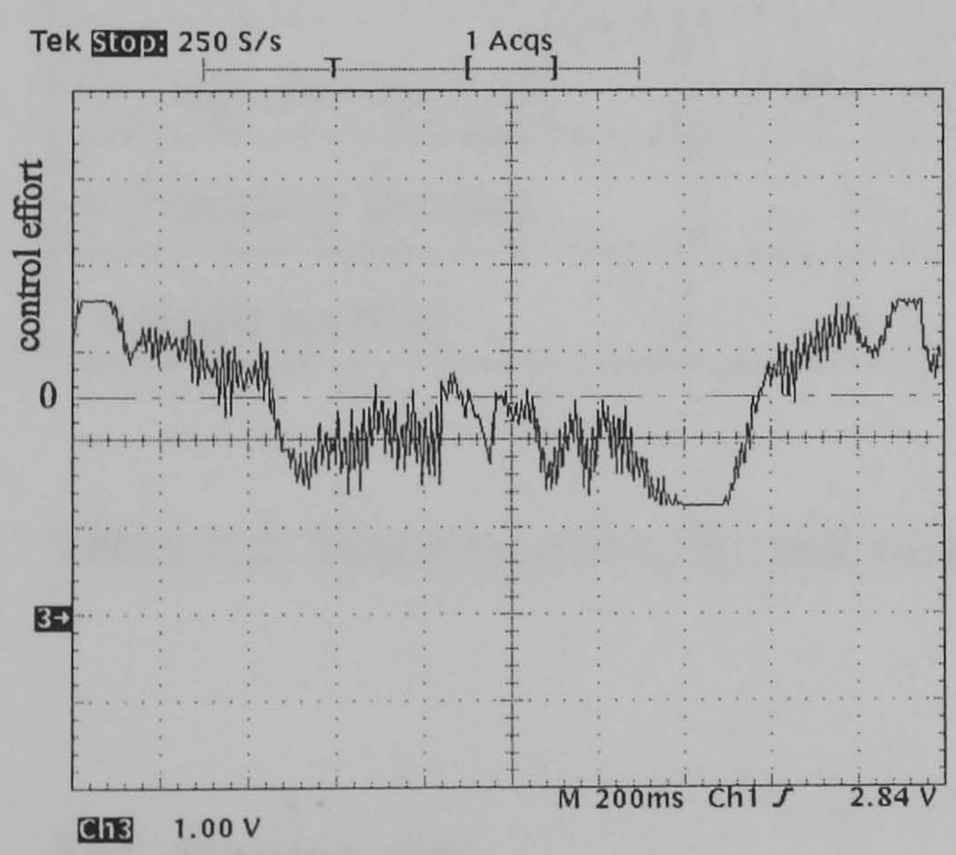

a

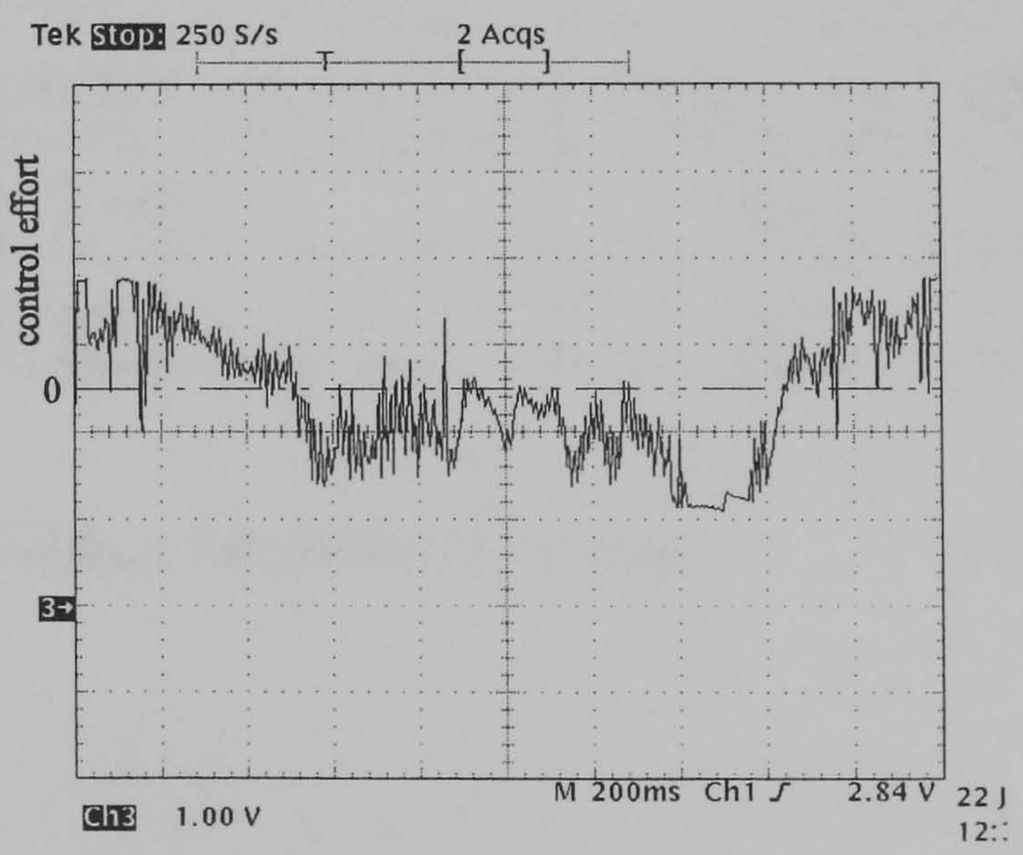

b

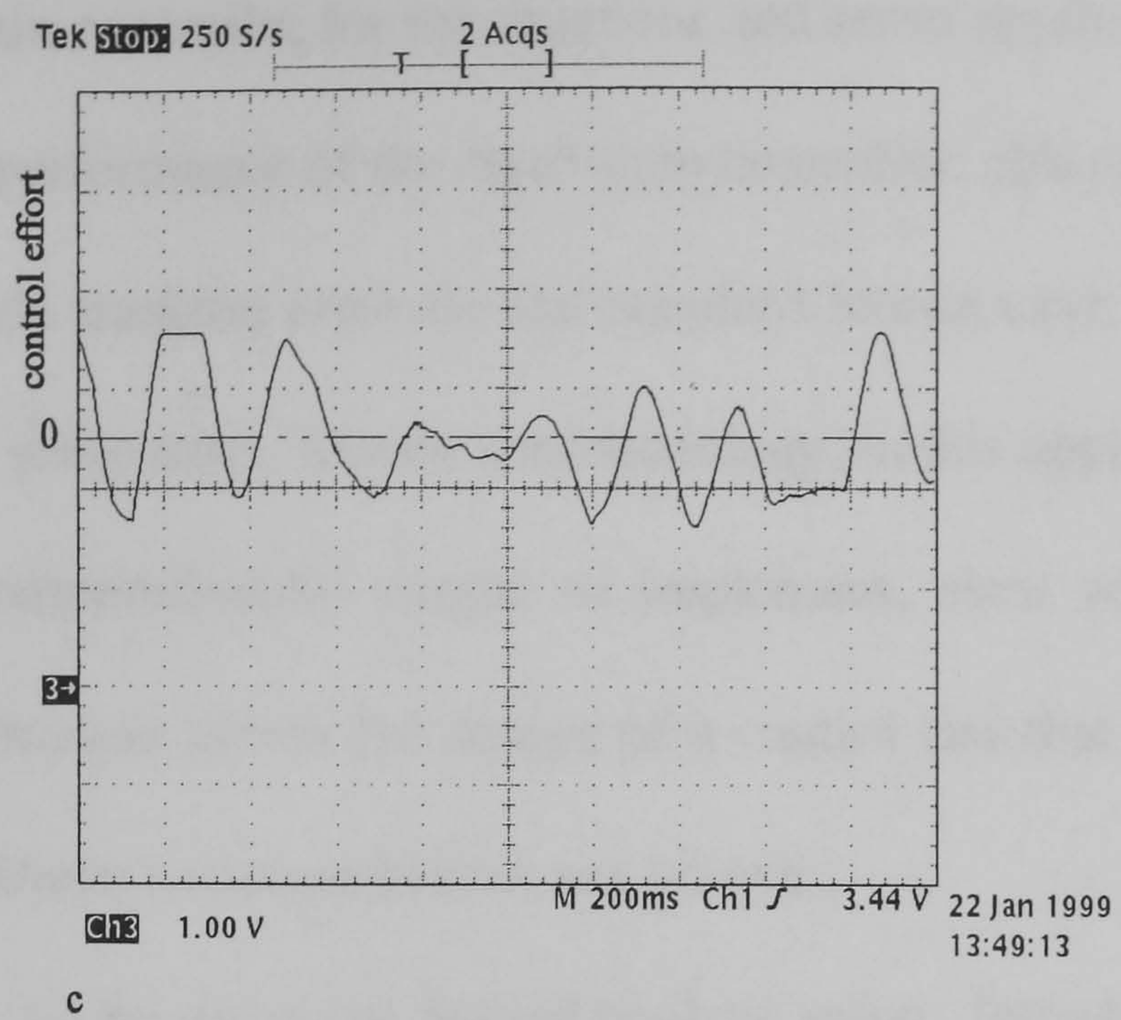

c

Figure 5.13 Control effort variation with high inertial load
a single component b dual component
c fixed gain
Vertical scale: 10 Amp/div (a,b)
16.67 Amp/div (c)
Horizontal scale: 200 ms/div

	fixed gain	single component	dual component
θ_e(standard inertia), rad	$-0.104 \le \theta_e \le 0.076$	$-0.104 \le \theta_e \le 0.089$	$-0.08 \le \theta_e \le 0.08$
θ_e (high inertia), rad	$-0.205 \le \theta_e \le 0.205$	$-0.162 \le \theta_e \le 0.119$	$-0.09 \le \theta_e \le 0.109$
s (standard inertia)	×	± 0.65	±0.65
s (high inertia)	×	±0.7	±0.7

Table 5.2 Tracking error, θ_e and switching variable, s values for servo case

5.7 Summary

Slotine's approach to sliding mode control has been assessed in this chapter for position control of a vector controlled synchronous reluctance machine for both the regulator and servo cases. Practical results show greater robustness to variation of moment of inertia

compared to a fixed gain controller for the regulator and servo applications. It has been demonstrated that the performance of the fixed-gain controller, although it has a smooth response and reasonable tracking error for the standard inertia case, degrades with the increased inertia in the servo case. Slotine's methodology, in this application, produces a control law that is computationally simple to implement, even with load dynamics incorporated. The technique allows the design of a control law that is both robust and stable, as long as parameter variation bounds are known.

The system bandwidth can be set to any desired realistic value. Introducing the boundary layer allows accurate prediction of the magnitude of the errors in the servo application and alleviates the problem of chattering in this form of control. However the apparent "chattering" in the control effort of fixed-gain controller is due to inductance ripple. The effect of inductance ripple with increased inertia is more significant on the performance of the fixed gain controller. However the dual component sliding mode controller provides robustness even to this effect.

5.8 References

5.1 Hung, J.Y., Gao, W., and Hung, J.C.:'Variable structure control: a survey', IEEE Trans. Ind. Elect., Vol. 40, No. 1, Feb. 1993, pp.2-23.

5.2 Gao, W., and Hung, J.C.:'Variable structure control of nonlinear systems: a new approach' IEEE Trans. Ind. Elect., Vol. 40, No. 1, Feb. 1993, pp.45-55.

5.3 Nandam, P.K., and Sen, P.C.:'Accessible-states-based sliding mode control of a variable speed drive system ', IEEE Trans. Ind. Applicat., Vol. 31, No. 4,July/Aug. 1995, pp.737-743.

5.4 Nandam, P.K., and Sen, P.C.:'Sliding mode speed control of a self-controlled synchronous motor based on state estimation (observer) and digital differentiation,' IPEC, Tokyo, Apr. 1990, pp.291-295.

5.5 Utkin, V.I.:'Sliding mode control design principles and applications to elecrtic drives', IEEE Trans. Ind. Elect., Vol. 40, No. 1. Feb. 1993, pp.23-36.

5.6 Utkin, V.I.:'Variable structure systems with sliding modes', IEEE Trans. Automatic. Control, Vol AC-22, No. 2, April 1977, pp.212-222.

5.7 Slotine, J.J.E., and Sastry, S.S.:' Tracking control of nonlinear systems using sliding surfaces, with application to robot manipulator', Int. J. Control, 1983, Vol. 38, No. 2, pp. 465-492.

5.8 Slotine, J.J.E.: ' Sliding controller design for nonlinear systems', Int. J. Control, 1984, Vol. 40, No. 2, pp. 421-434.

5.9 Slotine, J.J.E. and Weiping, L.,' Applied nonlinear control', Prentice-Hall, 1991.

Chapter 6

Inductance ripple

6.1 Introduction

Production of smooth torque is the main goal in torque control of the Synchrel machine.

However due to various factors, torque ripple is observed. The saliency in all rotor structures for the Synchrel machine produces air gap harmonics which are responsible for torque ripple. The primary reason for the torque ripple is the interaction between rotor segments and stator teeth. Other reasons are related to the control system and factors such as offset current, unbalance of peak current and phase angle, and current lag time. Therefore both the so called cogging torques (which are due to slotting) and the pulsating torques (due to space and time harmonics) must be reduced. Various proposals to solve this problem have been suggested [6.1]-[6.3].

Inductance ripple effects due to the interaction of stator and rotor salient features have been indicated by finite element analysis in Chapter 2. This chapter considers these effects in greater depth and a mathematical model accounting for inductance variation is presented. The first harmonic of the inductance ripple in the machine is determined using direct torque measurement.

Drive system simulation accounting for inductance ripple is carried out for the fixed gain controller and two sliding mode controllers using Slotine's approach for the servo case. The nonlinearity in the machine mechanical model is also taken into account. Good agreement occurs between the simulated and practical results given in section 5.5.

6.2 Inductance Ripple Effects

Inductance ripple in the Synchrel machine affects torque production and core losses. Skewing is commonly used to reduce high frequency torque ripple and acoustic noise can arise from slotting effects. However the absence of skewing in the axially laminated rotor leads to a torque ripple problem. With this rotor structure, periodical changes in stator inductances are generated when the rotor rotates. For example if both lamination ends are situated opposite stator teeth, the overall reluctance is smaller than if both ends are opposite stator slots. This change in reluctance causes flux variations in the segments. This effect can be reduced if the magnetic segment width is equal to the stator slot pitch. However this decreases the reluctance of zig-zag leakage paths between the stator and rotor, increasing $L_{q.}$

6.3 Machine Equations

Since the field in the Synchrel machine is rotating, the ripple produced is much lower than in a switched reluctance machine. The absence of a starting cage means that there is no damping on belt and slot harmonics. However, the mmfs generated by the stator windings can be considered sinusoidal if the effect of the belt harmonics is disregarded. The machine equations presented in Chapter 1 ignored the mutual coupling between the *d*- and *q*- axes. However the effective inductances are functions of rotor position. From finite element analysis there is appreciable ripple in L_d. However not only self inductances vary with the position of rotor segment with respect to slots, but so do the mutual inductances. The mutual inductances result from what is called the 'polarising' effect. The results of this effect are that direct axis flux can be produced by quadrature axis current, and vice-versa. In the analysis to follow, the first harmonic components of the variation of self and mutual axes inductances over a slot pitch are considered. If the magnetic nonlinearity is

disregarded and stator mmf is assumed to be sinusoidal, then the flux-current relationship can be rewritten as:

$$\begin{pmatrix} \phi_{dm} \\ \phi_{qm} \end{pmatrix} = \begin{pmatrix} L_{dm}(\theta) & L_{dq}(\theta) \\ L_{dq}(\theta) & L_{qm}(\theta) \end{pmatrix} \begin{pmatrix} i_{dm} \\ i_{qm} \end{pmatrix} \tag{6.1}$$

$$\frac{\delta \phi_{dm}}{\delta i_{qm}} = \frac{\delta \phi_{qm}}{\delta i_{dm}} \tag{6.2}$$

The inductance matrix in Eq. (6.1) is symmetrical because of the condition in Eq.(6.2). This condition is required so that the co-energy becomes a state function. When stator teeth and rotor segments are aligned, L_d is maximum, and a minimum when they are not aligned. The L_d variation can be considered sinusoidal and can be written as:

$$L_d(\theta) = \frac{L_{dmax} + L_{dmin}}{2} - \frac{L_{dmax} - L_{dmin}}{2} \cos(n_{slots}\theta) \qquad H \tag{6.3}$$

Eq.(6.3) can be written as

$$L_d(\theta) = L_{do} - \Delta L_d \cos(n_{slots}\theta) \qquad H \tag{6.4}$$

where L_{do} average d axis inductance over a slot pitch

ΔL_d peak fundamental ripple in L_{dm} over a slot pitch

$L_d(\theta)$ d axis self inductance ripple with respect to the rotor position

n_{slots} number of slots per pole pair

θ electrical rotor position

The L_q variation with rotor position is caused by variations in the air gap flux which is modulated by the mutual position of teeth and segments. A similar expression for L_q can be derived from considering the zig-zag leakage paths in aligned and non-aligned positions.

When the stator teeth and magnetic segments are unaligned, circulation flux paths are present. These are produced by the difference in stator and rotor magnetic potentials. An additional contribution to L_q is produced by these paths. This contribution depends on the rotor position. The L_q inductance is a maximum at this unaligned position. When rotor segments are aligned with stator teeth, L_q is minimum. With sinusoidal variation, L_q can be written as:

$$L_q(\theta) = \frac{L_{qmax} + L_{qmin}}{2} - \frac{L_{qmax} - L_{qmin}}{2} \cos(n_{slots}\theta) \qquad H \tag{6.5}$$

which can be simplified as:

$$L_q(\theta) = L_{qo} - \Delta L_q \cos(n_{slots}\theta) \qquad H \tag{6.6}$$

where L_{qo} average q axis inductance over a slot pitch

ΔL_q peak fundamental ripple in L_{qm} over a slot pitch

$L_q(\theta)$ q axis self inductance ripple with respect to the rotor position

In addition to the self inductance ripple there is also the polarising effect to consider. Considering that only the d-axis is excited, the field distribution will be symmetrical around the d-axis and no cross coupling occurs. If the rotor and mmf are is shifted slightly from the symmetrical position, the rotor will be magnetically polarised and some q- axis flux appears. The flux vector is composed of both d and q components. This effect will lead to the inductance $L_{dq}(\theta)$, which has a zero average value. The first harmonic component of the mutual inductance ripple is modelled as:

$$L_{dq}(\theta) = -\Delta L_{dq} \sin(n_{slots}\theta) \qquad H \tag{6.7}$$

and the mutual fluxes induced are:

$$\begin{aligned} \phi_{dqm} &= -i_{qm} \Delta L_{dq} \sin(n_{slots}\theta) \qquad Wb \\ \phi_{qdm} &= -i_{dm} \Delta L_{dq} \sin(n_{slots}\theta) \qquad Wb \end{aligned} \tag{6.8}$$

The equivalent magnetising inductances L_{dm}, L_{qm}

$$L_{dm} = L_d(\theta) + L_{dq}(\theta) \qquad H$$
$$L_{qm} = L_q(\theta) + L_{dq}(\theta) \qquad H \qquad (6.9)$$

6.4 Torque Equation

Since saturation is disregarded, the d and q axes fluxes given by Eq. (6.1) are valid. Substituting equations (6.4), (6.6) and (6.7) into Eq. (6.1) gives:

$$\begin{aligned}\phi_{dm} &= [L_{do} - \Delta L_d \cos(n_{slots}\,\theta)]\,|I_{dq}|\cos(\theta-\alpha) \\ &\quad - \Delta L_{dq}\sin(n_{slots}\,\theta)\,|I_{dq}|\,\sin(\theta-\alpha) \qquad Wb \\ \phi_{qm} &= [L_{qo} + \Delta L_q \cos(n_{slots}\,\theta)]\,|I_{dq}|\sin(\theta-\alpha) \\ &\quad - \Delta L_{dq}\sin(n_{slots}\,\theta)\,|I_{dq}|\,\cos(\theta-\alpha) \qquad Wb\end{aligned} \qquad (6.10)$$

where $|I_{dq}|\cos(\theta - \alpha) = i_{dm}$

$$|I_{dq}|\sin(\theta - \alpha) = i_{qm}$$

The stored energy is

$$E_{stored} = \frac{3}{2}(\phi_{dm}\, i_{dm} + \phi_{qm}\, i_{qm}) \qquad J \qquad (6.11)$$

and substituting (6.10) into (6.11) gives the stored energy function of α. The torque will be obtained by differentiating with respect to α:

$$\begin{aligned}T = \frac{3}{2}p\,[&i_{dm}\,i_{qm}[L_{do} - L_{qo}] - i_{dm}\,i_{qm}[\Delta L_d + \Delta L_q + n_{slots}\,\Delta L_{dq}]\cos(n_{slots}\,\theta) \\ &+ i_{dm}^2[\frac{n_{slots}}{2}\Delta L_d + \Delta L_{dq}]\sin(n_{slots}\,\theta) \\ &- i_{qm}^2[\frac{n_{slots}}{2}\Delta L_q + \Delta L_{dq}]\sin(n_{slots}\,\theta)] \qquad Nm\end{aligned} \qquad (6.12)$$

In Eq. (6.12) the main torque and the torque ripple components are shown. The first term gives the constant torque which is the same as that in Eq. (1.7). The coefficient of $\cos(n_{slots}\,\theta)$ gives a ripple component which is proportional to the main torque component. The third term is the only term present at no load ($i_q = 0$). ΔL_d, ΔL_q and ΔL_{dq} define

machine behaviour in terms of flux and torque ripple. These parameters are determined in the next section.

6.5 Parameter Determination

The direct torque measurement method is used to determine the first harmonic coefficients of machine inductances. A strain gauge transducer was used to measure torque. This type of transducer has sufficient bandwidth to measure the torque ripple at low speeds. Operating at low rotational frequencies ensures the magnetising vector and applied stator current vector are the same, since this minimises the displacement caused by core loss phenomena.

The direct torque measurement was carried out in three steps:

Step 1

The machine current vector was set to excite the direct axis with $i_d = 16.44$ A (to keep the machine fully fluxed) and $i_q = 0$. The dc machine was used to drive the Synchrel machine.

The torque equation (6.12) under these condition will be:

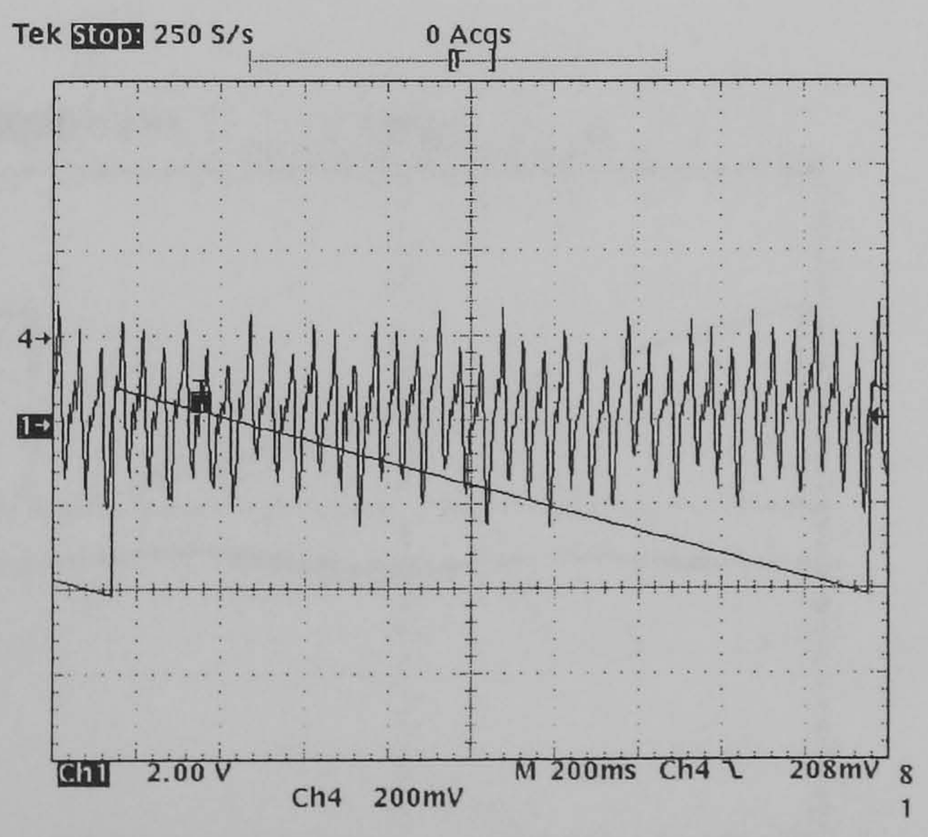

Figure 6.1 Output torque (Ch4) with rotor position (Ch 1) for Step 1
Torque scale: 8.4 Nm/div

$$T_e = \frac{3}{2} P \left[i_{ds}^2 \left(\frac{n_{slots}}{2} \Delta L_d + \Delta L_{dq} \right) \sin(n_{slots} \theta) \right] \tag{6.13}$$

Figure 6.1 shows the torque variation with rotor position. The torque conversion factor is 0.042 Nm/mv. The ramp waveforms shows the position of the rotor over one cycle. It is noted from the torque waveform that there is ripple with a fundamental frequency given by:

$$f_{ripple} = n_{slots} f_{elec} \tag{6.14}$$

The peak torque ripple was estimated from the figure as 8.89 Nm. It is assumed that this magnitude represents that of the first harmonic of ripple given in Eq. (6.12). Therefore

$$0.011 = 9 \Delta L_d + \Delta L_{dq} \tag{6.15}$$

Step 2

The current vector was set to excite the q-axis with 8.95 A and $i_d = 0$, and the dc machine

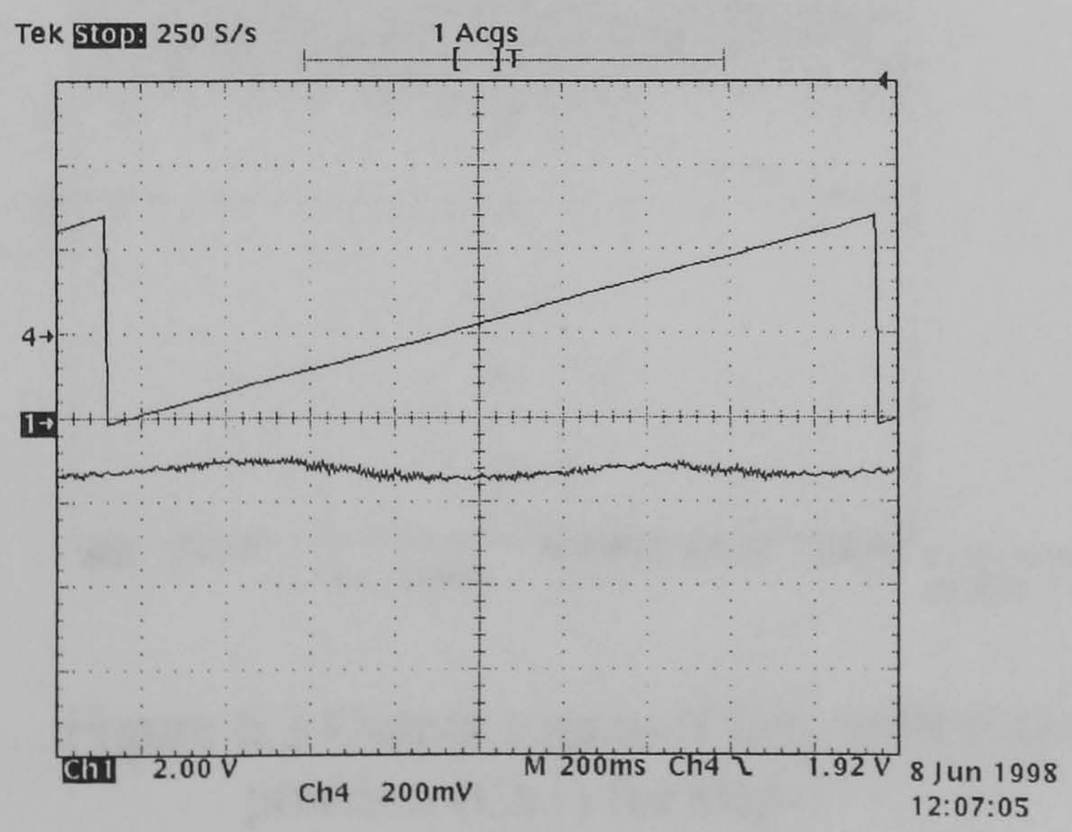

Figure 6.2 Output torque (Ch4), with rotor position (Ch1) for step 2

Torque scale: 8.4 Nm/mv

conditions as in step1. The torque equation (6.12) becomes:

$$T_e = \frac{3}{2} P[-i_{qs}^2(\frac{n_{slots}}{2}\Delta L_q + \Delta L_{dq})\sin(n_{slots}\,\theta)] \tag{6.16}$$

Figure 6.2 shows the measured torque waveform of the Synchrel machine. The torque ripple in this case is small compared to that obtained in step 1. The estimated peak torque ripple is 0.85 Nm, thus:

$$0.0035 = 9\Delta L_q + \Delta L_{dq} \tag{6.17}$$

Step 3

The current vector was set to excite the axes current with $i_d = 16.44$ A, and $i_q = 8.89$ A. The Synchrel machine can drive the dc machine under these conditions. The peak torque ripple found from Figure 6.3 is 10.19 Nm. The torque ripple magnitude for this condition is given by Eq.(6.18).

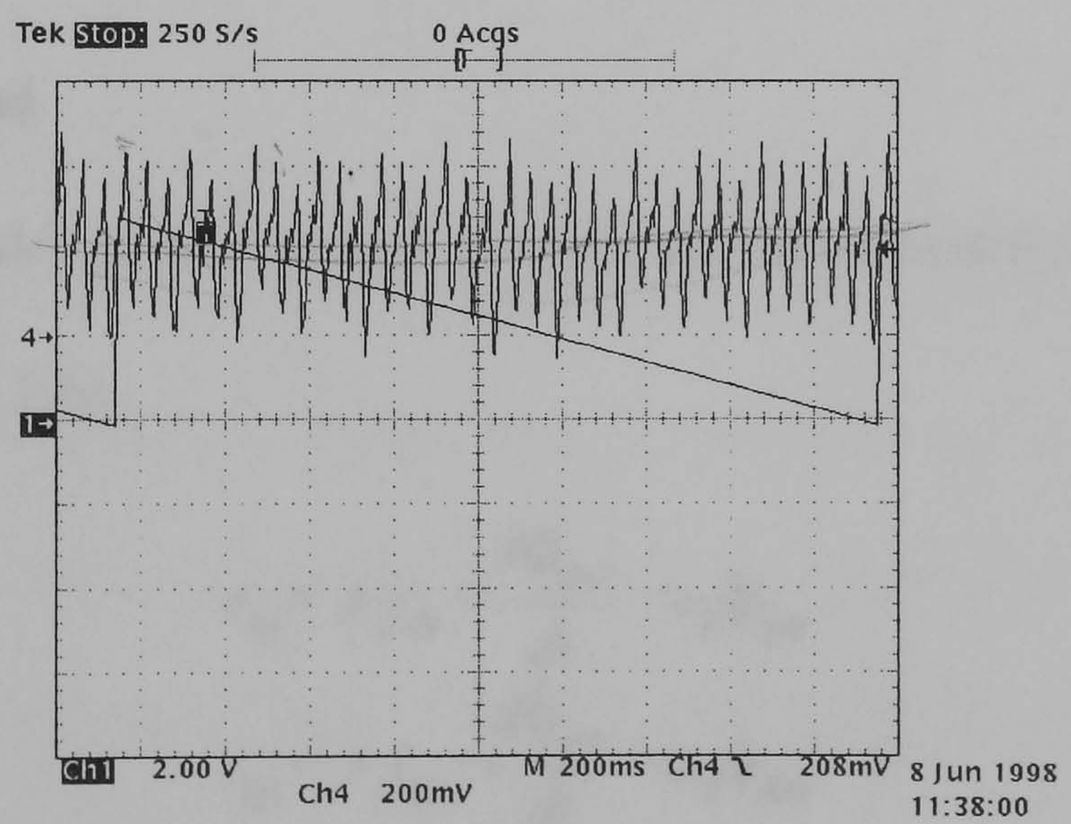

Figure 6.3 Output torque (Ch4), with rotor position (Ch1) for step 3
Torque scale: 8.4 Nm/div

$$\frac{T}{3/2p} = \sqrt{(i_{dm} i_{qm}[\Delta L_d + \Delta L_q + n_{slots}\Delta L_{dq}])^2 + (i_{dm}^2[\frac{n_{slots}}{2}\Delta L_d + \Delta L_{dq}] - i_{qm}^2[\frac{n_{slots}}{2}\Delta L_q + \Delta L_{dq}])^2} \quad (6.18)$$

substituting (6.15), (6.17), in (6.18) gives

$$0.0143 = [\Delta L_d + \Delta L_q + 18\Delta L_{dq}] \quad (6.19)$$

Solving simultaneous equations (6.15), (6.17), and (6.19) gives the inductance ripple coefficients ΔL_d, ΔL_q, and ΔL_{dq} , Table 6.1.

L_{dm}	L_{qm}	ΔL_d	ΔL_q	ΔL_{dq}
0.1	0.0149	0.0011	0.0003	0.0007
H	H	H	H	H

Table 6.1 Machine and system constants

It is noted from the three tests conducted that torque ripple is related mainly to inductance variation parameters ΔL_d and ΔL_{dq}, the effect of ΔL_q is negligible.

6.6 Machine model

The state space model of the Synchrel machine can be defined by incorporating the voltage equations (Section 1.6) :

$$\begin{aligned} v_{ds} &= r_s i_{ds} + \frac{d\phi_{dm}}{dt} - \omega_e \phi_{qm} \\ v_{qs} &= r_s i_{qs} + \frac{d\phi_{qm}}{dt} + \omega_e \phi_{dm} \end{aligned} \quad (6.20)$$

that need to be modified to account for inductance ripple by flux equations given by Eq. (6.1), where the transformer voltages are given by

$$\frac{d\phi_{dm}}{dt} = \frac{di_{dm}}{dt}(L_{do} - \Delta L_{dm}\cos(n_{slots}\theta)) + \omega_e \Delta L_{dm} i_{dm} n_{slots}\sin(n_{slots}\theta)$$
$$- \frac{di_{qm}}{dt} L_{dq}\sin(n_{slots}\theta) - \omega_e L_{dq} i_{qm} n_{slots}\cos(n_{slots}\theta)$$
$$\frac{d\phi_{qm}}{dt} = \frac{di_{qm}}{dt}(L_{qo} + \Delta L_{qm}\cos(n_{slots}\theta)) - \omega_e \Delta L_{qm} i_{qm} n_{slots}\sin(n_{slots}\theta) \quad (6.21)$$
$$- \frac{di_{dm}}{dt} L_{dq}\sin(n_{slots}\theta) - \omega_e L_{dq} i_{dm} n_{slots}\cos(n_{slots}\theta)$$

Equations (6.10), (6.20) and (6.21) can be used as the basis for a state space model of the machine incorporating the inductance ripple such that

$$\dot{x} = A\,x + B\,u$$
$$y = C\,x \quad (6.22)$$
$$x = \begin{pmatrix} i_{dm} \\ i_{qm} \end{pmatrix}, \quad u = \begin{pmatrix} v_{ds} \\ v_{qs} \end{pmatrix}, \quad C = \begin{pmatrix} 1 & 0 \\ 0 & 1 \end{pmatrix}$$

where A (system matrix) and B (input matrix) are time variant. The machine model in state space form is written in a S-function, 'ripp_tor', given in Appendix F. This S-function is incorporated into drive system simulation to show the effects of the torque ripple on tracking performance. This is illustrated in the next section.

6.7 Drive System Simulation

The machine can be now modelled for simulation purpose. The simulation uses MATLAB and its graphical user interface, SIMULINK, on a PC platform. The drive system has been simulated for the fixed gain controller and the two sliding mode controllers in the servo application (practical results presented in section 5.5) with and without the effects of inductance ripple. The fixed gain controller for position control, servo application, was modelled as shown in Figure 6.4. In this simulation, a non-linear mechanical model of the machine is incorporated, in which static friction is accounted for. The torque equation given in section (5.3) is

$$T_e = J\ddot{\theta} + B_1\dot{\theta}_r + B_2 sgn(\dot{\theta}_r) + B_3\dot{\theta}_r^2 \tag{6.23}$$

which can be re-arranged as

$$\ddot{\theta} = \frac{1}{J}\left[T_e - B_1\dot{\theta}_r - B_2 sgn(\dot{\theta}_r)\right] \tag{6.24}$$

This equation is implemented in a SIMULINK file as shown in Figure 6.5.

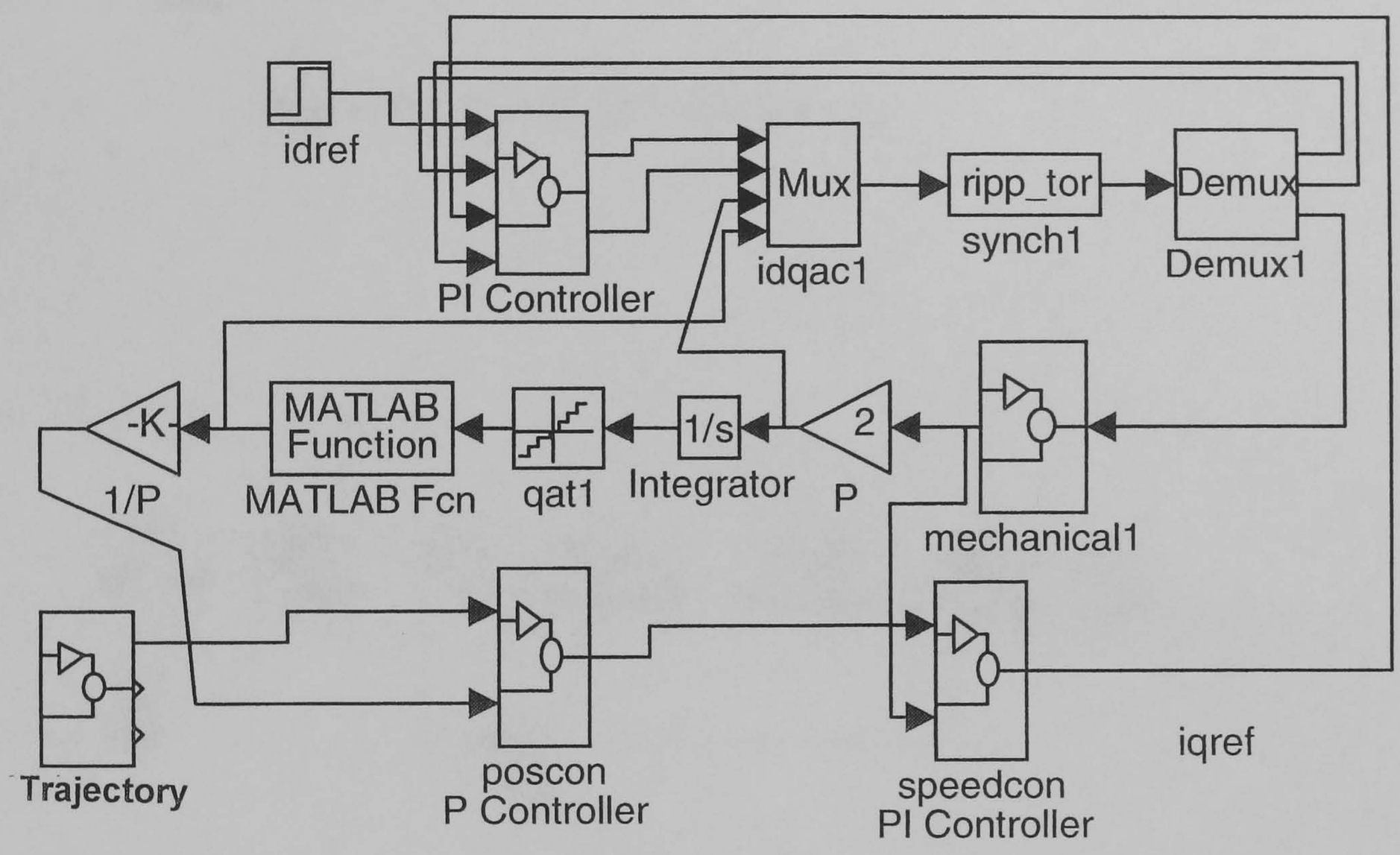

Figure 6.4 SIMULINK block diagram of the drive system with fixed gain controller

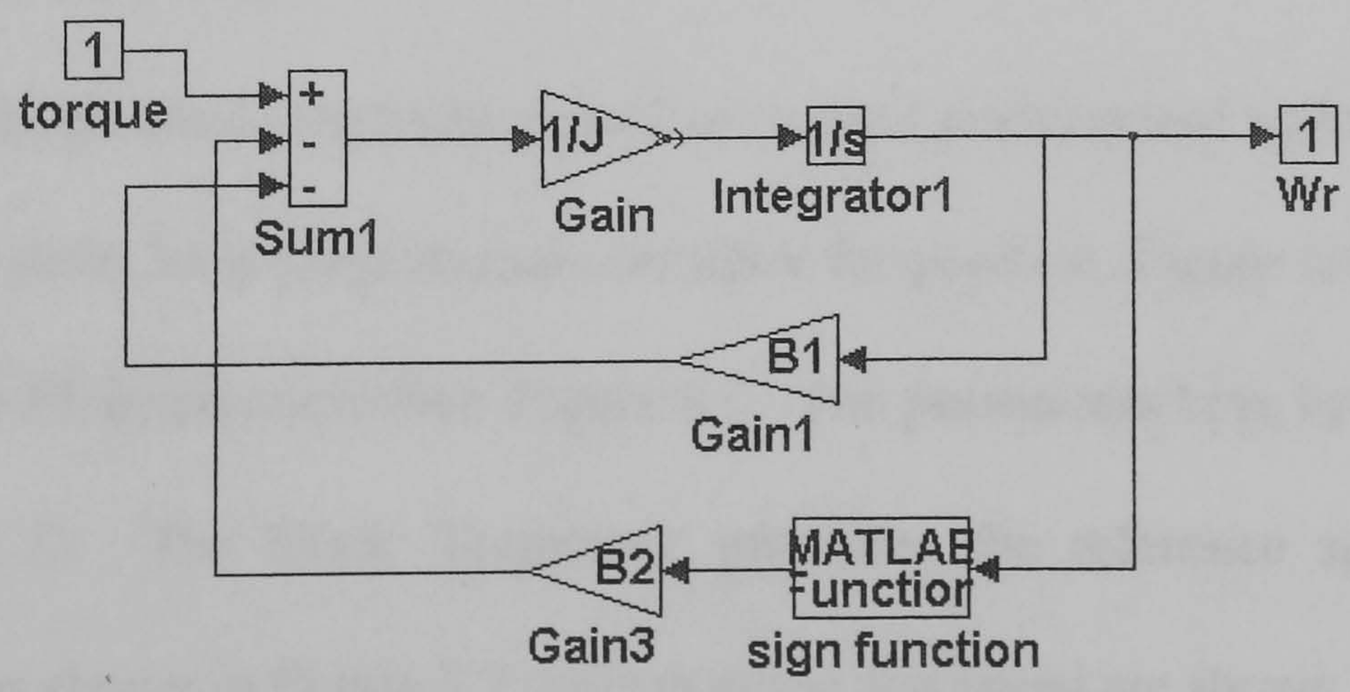

Figure 6.5 SIMULINK block diagram of subsystem 'mechanica11'

The block 'PI Controller' comprises a PI controller for flux by controlling the d-axis current (flux) and a PI torque controller which controls the q-axis current, as shown in Figure 4.6.

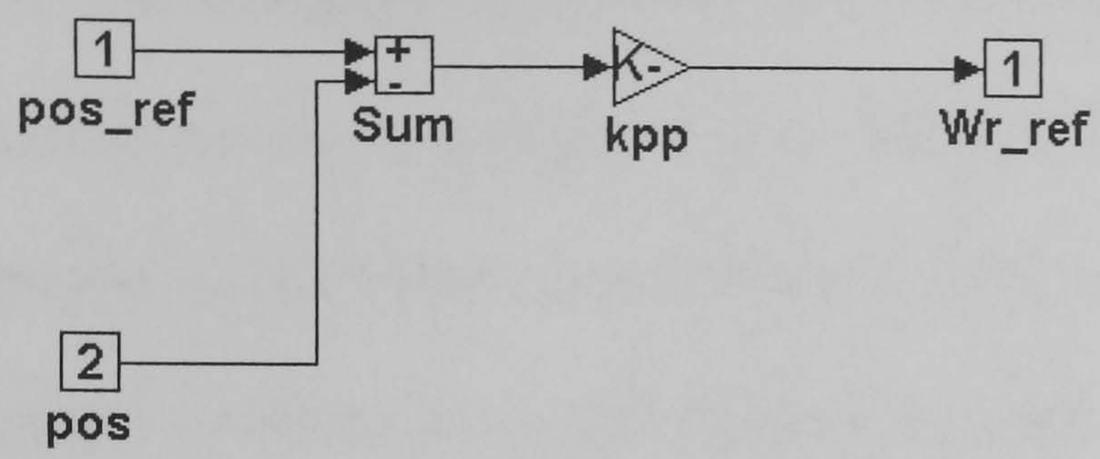

Figure 6.6 SIMULINK file 'poscon'

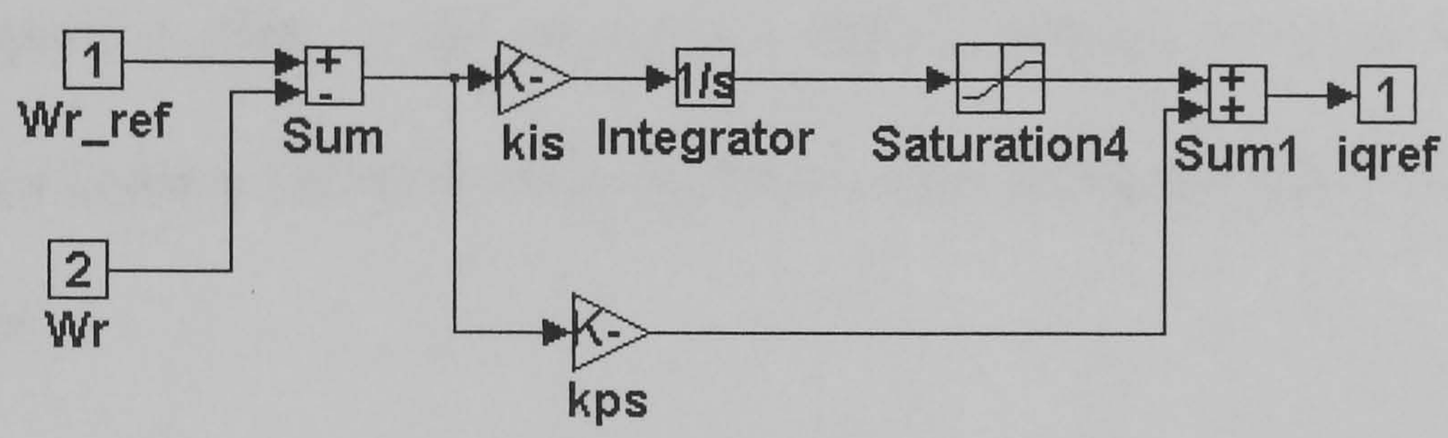

Figure 6.7 SIMULINK file 'speedcon'

i) Fixed gain controller

The fixed gain position controller comprises nested position and speed loops. The block 'poscon' is an outer loop proportional controller for position, Figure 6.6, and 'speedcon' is an inner loop PI speed controller, Figure 6.7. The parameters kpp, kps and kis are given in Appendix D. The block 'Trajectory' generates the reference speed, position and acceleration as shown in Figure 5.7 (only position and speed are shown in this figure). The S-function 'trajectory' which generates the speed reference is given in Appendix G. The reference position can be obtained by integrating speed, and the acceleration is obtained by

differentiating speed.

Figure 6.8 shows the simulated control effort of the fixed gain controller when the standard inertial load is used. The effect of inductance ripple is obvious in the waveform, Figure 6.8 b. The corresponding experimental results for the fixed gain controller of this simulated system are shown in Figure 5.12 c. The inductance ripple manifests itself as a ripple component in the control effort during servo trajectory following application. The number of ripple 'cycles' in the control effort corresponds to the number of slots the rotor passes during the trajectory (34 in this case), Figure 6.8 b. At higher speeds, the ripple magnitude in the control effort is small. In the equivalent practical case, Figure 5.12 c, such ripple is evident, although it is difficult to precisely determine the number of control effort ripple 'cycles' during the trajectory from the experimental result - especially during the higher speed regions of the trajectory. This difference between experimentation and simulation is due to factors such as saturation, core losses, etc (the model does not account for them).

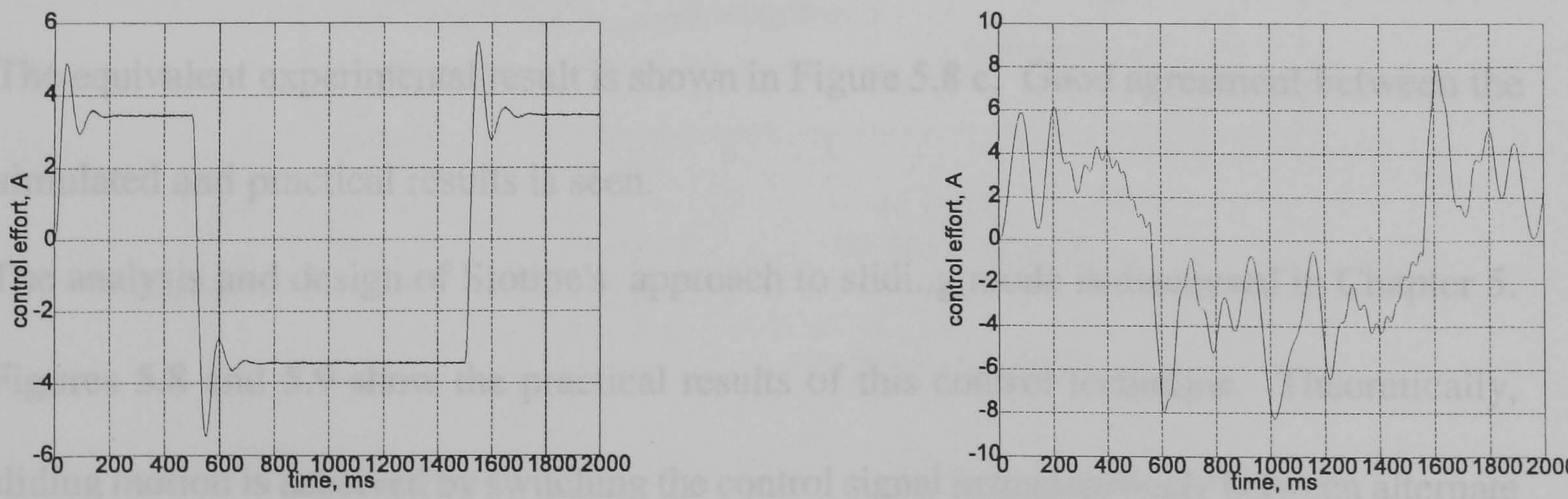

a without accounting for inductance ripple b when accounting for inductance ripple

Figure 6.8 Simulated control effort for fixed gain controller

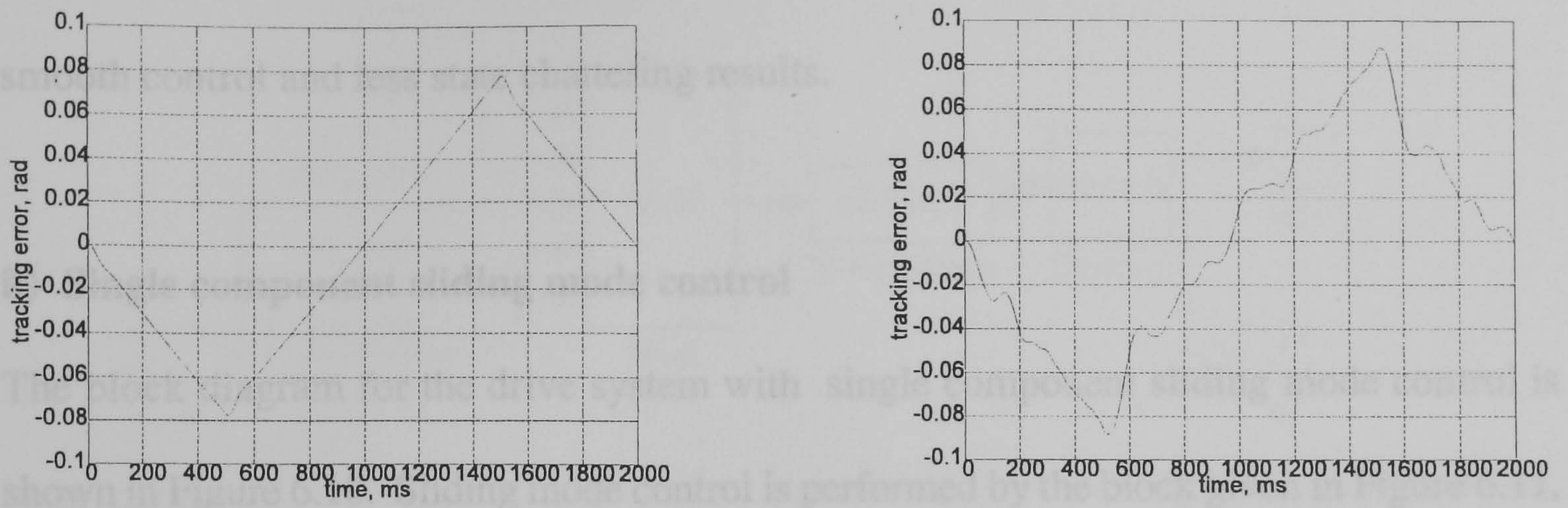

a without accounting for inductance ripple b when accounting for inductance ripple

Figure 6.9 Simulated tracking error for fixed gain controller

The simulation tracking error results for the fixed gain controller are shown in Figure 6.9 a and b. It is evident from the two figures that accounting for inductance ripple does not have a significant effect on the tracking error magnitude, implying torque ripple compensation would have little effect on the tracking error in this particular circumstance. The equivalent experimental result is shown in Figure 5.8 c. Good agreement between the simulated and practical results is seen.

The analysis and design of Slotine's approach to sliding mode is discussed in Chapter 5. Figures 5.8 and 5.9 show the practical results of this control technique. Theoretically, sliding motion is acheived by switching the control signal instantaneously between alternate values. Due to the discrete implementation, the switching rate is limited by the sampling rate. The control signal is kept constant for one sampling interval so the state of the system can move away from the switching line which leads to chattering. Slotine's approach reduces the problem of chattering, by the introduction of a boundary layer either side of the

switching surface. Having entered the boundary layer, the state trajectories are constrained to remain within it. The tracking accuracy of the system can be guaranteed to be $\epsilon=\phi/\lambda$. Within this boundary layer, the trajectory is not driven onto the switching line itself, so smooth control and less state chattering results.

ii) Single component sliding mode control

The block diagram for the drive system with single component sliding mode control is shown in Figure 6.10. Sliding mode control is performed by the block given in Figure 6.11, where the control algorithm is written in 'slidmb4', S-function, in Appendix H. The sliding mode design parameters are the same for experimentation.

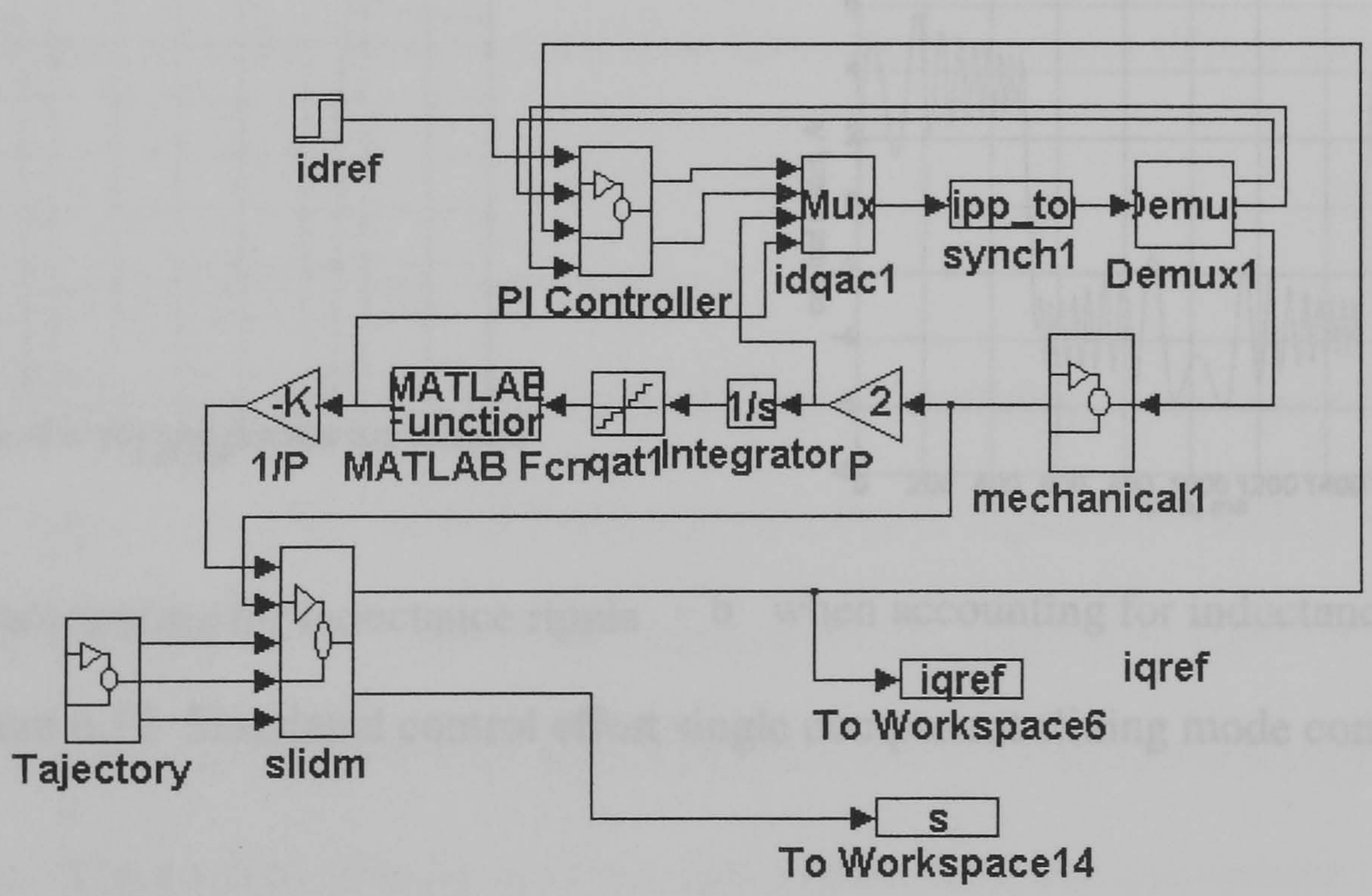

Figure 6.10 SIMULINK block diagram of single component sliding mode control for position control

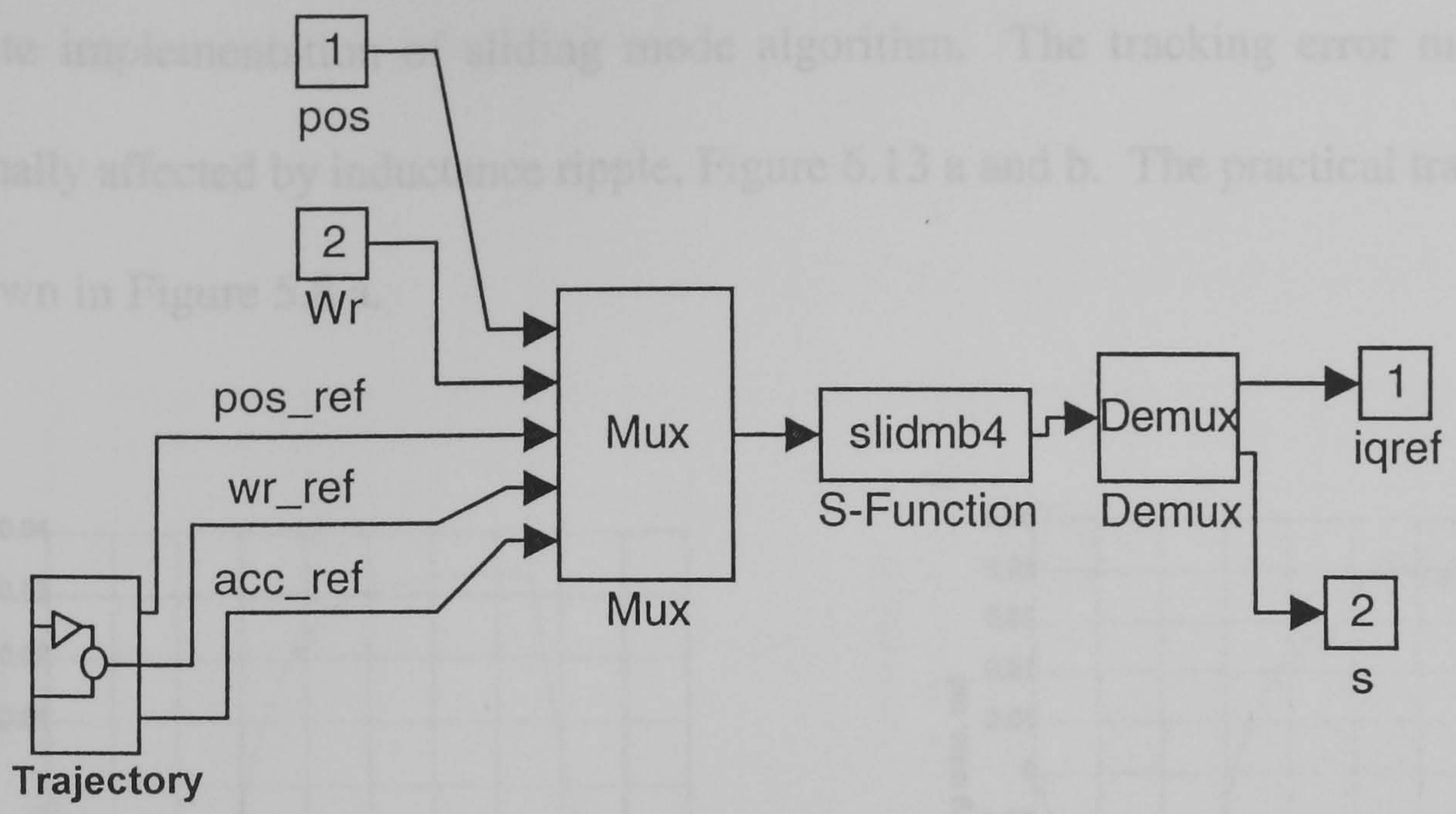

Figure 6.11 SIMULINK files,'slidm' and 'Trajectory'

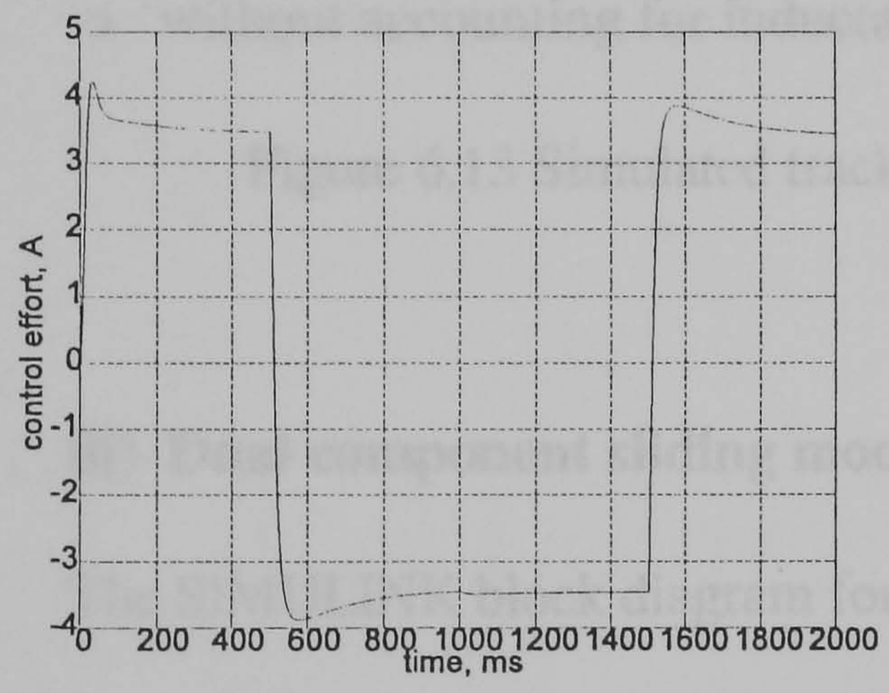

a without accounting for inductance ripple

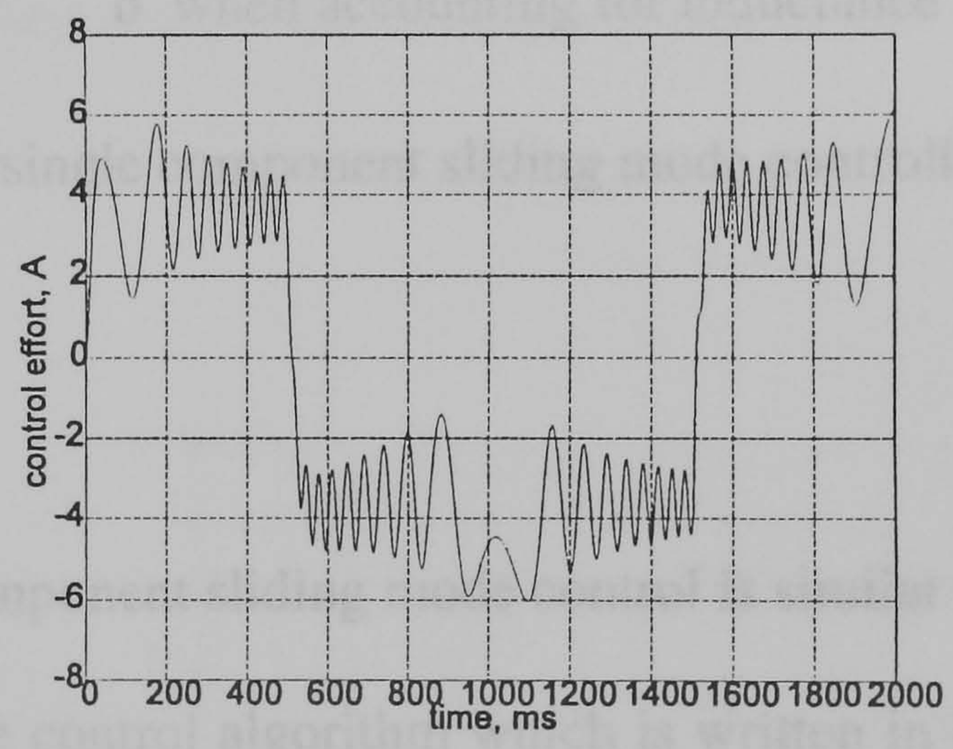

b when accounting for inductance ripple

Figure 6.12 Simulated control effort single component sliding mode controller

Figure 6.12 shows the simulated control effort of the single component sliding mode controller. The introduction of the boundary layer gives a smooth control signal in the simulation, Figure 6.12a. However the situation is different when accounting for inductance ripple, Figure 6.12 b. If a comparison is made between Figure 6.12 b and the equivalent practical control effort of Figure 5.12 a, high chattering is obvious in the

practical result. This could be due to noise on speed and position measurments and the discrete implementation of sliding mode algorithm. The tracking error magnitude is minimally affected by inductance ripple, Figure 6.13 a and b. The practical tracking error is shown in Figure 5.8 a.

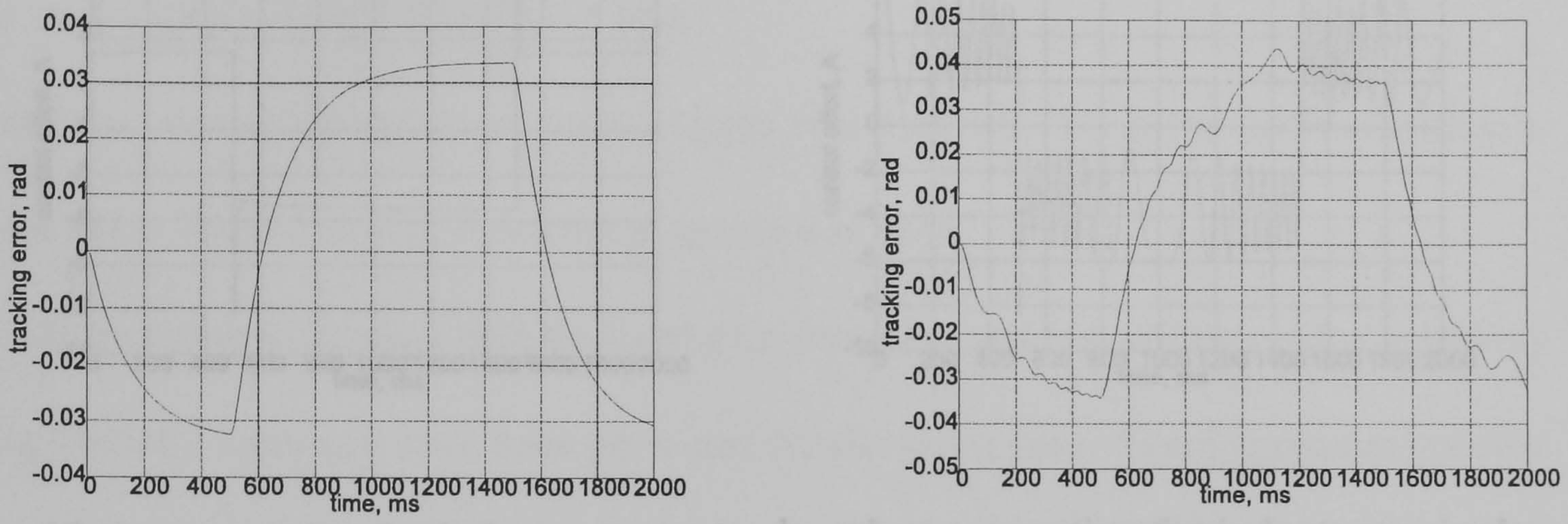

a without accounting for inductance ripple b when accounting for inductance ripple

Figure 6.13 Simulated tracking error forsingle component sliding mode controller

iii) Dual component sliding mode control

The SIMULINK block diagram for the dual component sliding mode control is similar to that in Figure 6.10. The only difference is the control algorithm which is written in S-function, 'slidma', given in Appendix H, replaces the file 'slidmb4' in Figure 6.11. The dual component sliding mode is termed Slotine's approach which attempts to solve the chattering problem. The control effort is split into two components, one continuous and the other switched. This amounts to smoothing the switching action across the switching line. The simulated results of the dual component sliding mode controller are shown in Figures 6.14 and 6.15. The dual component sliding mode design is the same as that used to obtain plots 5.12 b and 5.8 b respectively. The tracking error is much smaller than in the other two cases. However the simulated values obtained are different from the experimental results.

The main reason is noise on speed and position measurments, as sliding mode control assumes perfect state measurment.

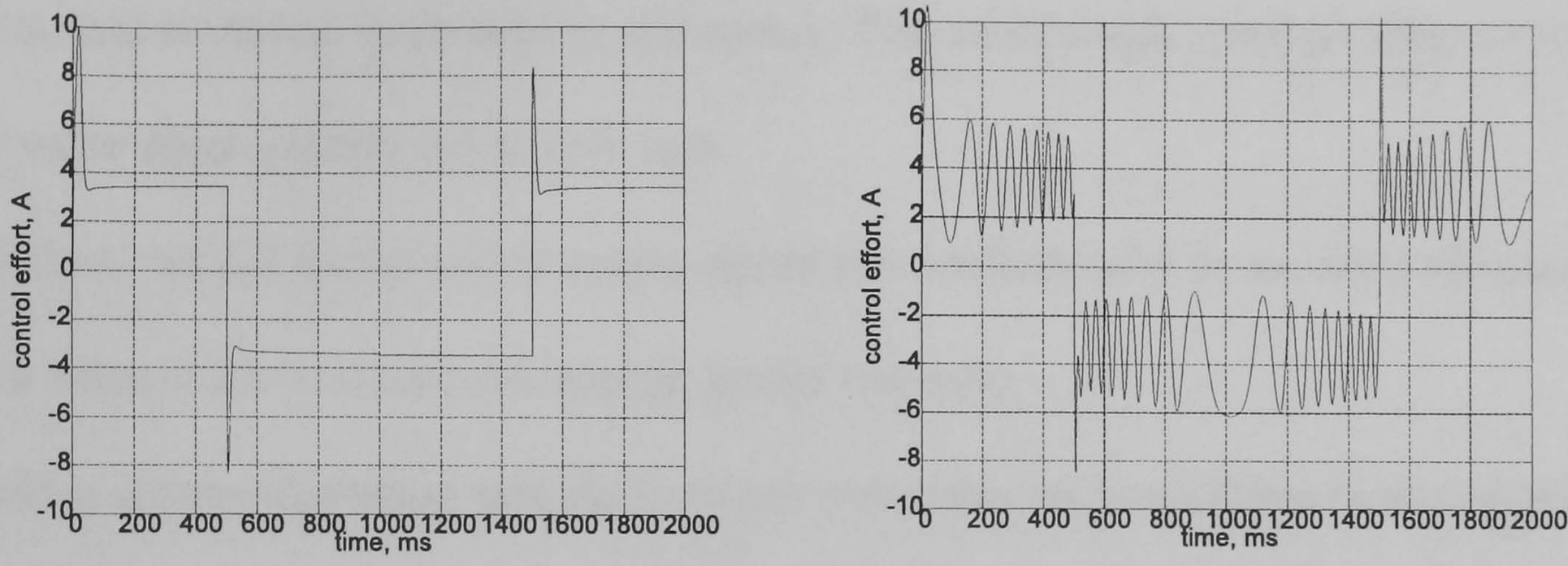

a without accounting for inductance ripple b when accounting for inductance ripple

Figure 6.14 Simulated control effort for dual component sliding mode controller

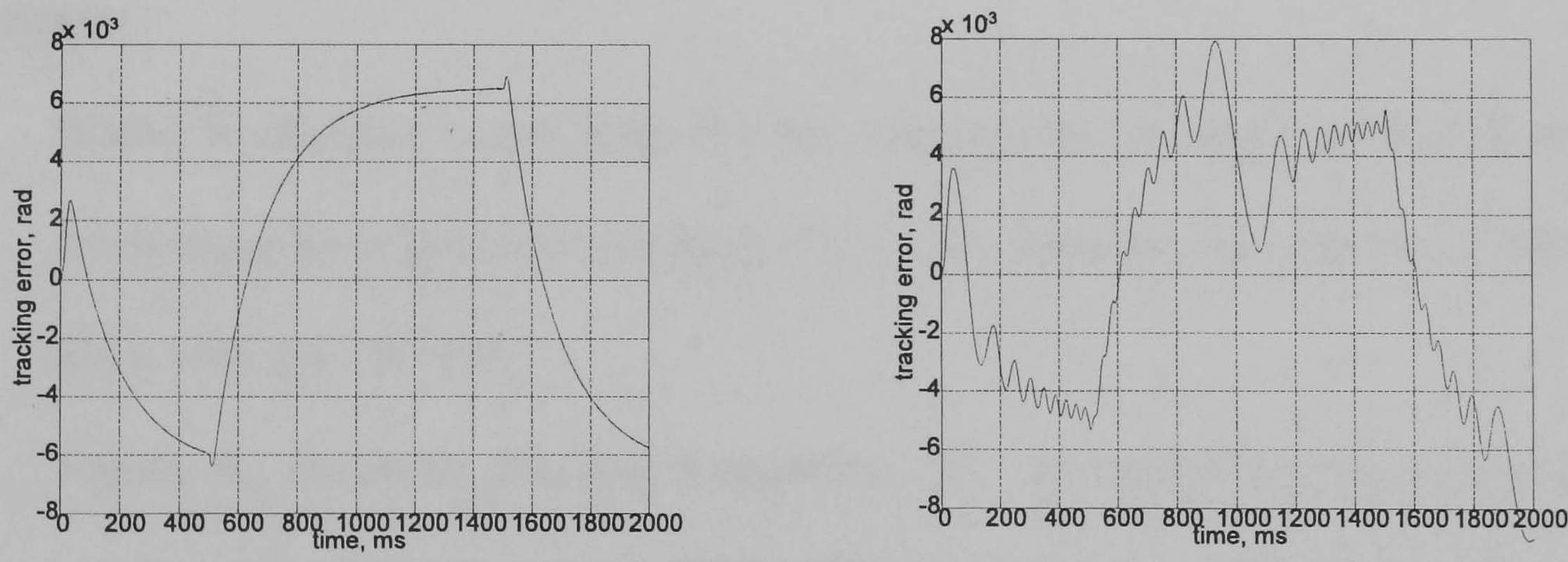

a without accounting for inductance ripple b when accounting for inductance ripple

Figure 6.15 Simulated tracking error for dual component sliding mode controller

6.8 Summary

In this chapter the effect of inductance ripple on the machine torque production has been addressed. Only the first harmonic components of the machine inductances were considered. A direct torque measurement method was used to determine the coefficients. The method involoves three steps at low speed. This avoids high speed problems such as flux vector displacement due to core loss.

A machine model incorporating torque ripple was implemented in the drive simulation, where a non linear machine mechanical model was used.

The drive system simulation with the fixed gain controller and two sliding mode controllers using Slotine's approach have been presented for the servo case. Good agreement occurs between the simulated results and practical results in section 6.5. It is concluded that there is no need to develop a control scheme for torque ripple compensation in some circumstances.

References

6.1 Matsui, N., Makino, T., and Satoh, H.: 'Auto compensation of torque ripple of direct drive motor by torque observer', IEEE Trans. Ind. Applicat., Vol. 29, No. 1, Jan. /Feb. 1993, pp. 187-194.

6.2 Vagati, A., Pastorelli, M., and Franceschini, G.: 'Design of low-torque-ripple synchronous reluctance motors', IEEE IAS Ann. Meet., Oct. 1997, pp. 286-293.

6.3 Zuncheng, Z., and Spooner, E.: 'High-speed reluctance machines with mixed-pole windings', IEE Proc. B, Vol. 138, No.5, Sep. 1991, pp 257-263.

Chapter 7

Conclusion

7.1 General Conclusions

The analysis and design of an axially laminated synchronous reluctance machine has been assessed in this thesis. Experimental results on the machine have validated the finite element analysis method used for the rotor design.

This thesis has highlighted the methods by which the Synchrel machine parameters were measured. Two control strategies for vector control were considered. Maximum torque per ampere control (MTC) and constant current in the inductive axis control (CCIAC) were experimentally assessed. The maximum torque obtained from the machine with both methods is similar to that of the induction motor with the same stator. The machine was tested on load at low speeds, where the effects of inductance ripple are obvious in the voltage and current waveforms. The inductance ripple has serious effects on controller performance and limits the ability to maintain a controlled stator current vector at higher speeds.

The torque ripple problem remains because it is difficult to skew an axially laminated rotor. The axially laminated synchronous reluctance machine is not suitable for mass production due to its rotor complexity, when compared with the equivalent induction machine rotor.

7.2 Author's Contribution

The finite element analysis method has been used to determine the optimum number of magnetic laminations. With this number the machine can develop the rated output torque of the equivalent induction machine (120 Nm), while maintaining a reasonable power factor. The thickness of the magnetic laminations with respect to insulation thickness has

been investigated in an effort to reduce inductance ripple.

Slotine's approach of sliding mode control for position control has been applied to a vector controlled synchronous reluctance machine, for both the regulator and servo cases. A comparison has been made between sliding mode control and a fixed-gain control method. Experimental results were presented showing greater robustness to variation of moment of inertia, compared to a fixed gain controller for the regulator and servo applications. Superior performance is exhibited over a fixed-gain position control method in terms of invariant regulator response and reduced tracking errors in a servo application. Also Slotine's approach allows torque ripple parameters to be incorporated and ripple reduction is afforded due to the high system gain.

Slotine's methodology, in this application, produces a control law that is computationally simple to implement, even with load dynamics incorporated. The technique allows the design of a control law that is both robust and stable, as long as parameter variation bounds are known.

The system bandwidth can be set to any desired realistic value. Introducing a boundary layer allows accurate prediction of the magnitude of the error in a servo application and alleviates the problem of chattering in this form of control. However the apparent "chattering" in the control effort of the fixed-gain controller is due to inductance ripple.

The effect of inductance ripple with increased inertia is more significant on the performance of the fixed gain controller. However the dual component sliding mode controller provides robustness even to this effect.

A machine model incorporating torque ripple was implemented in the drive simulation, where a non linear machine mechanical model was used. The drive system simulations

with the fixed gain controller and two sliding mode controllers using Slotine approach, with the standard inertial load have been carried out for the servo case. Good agreement occurs between the simulated and practical results.

7.3 Suggestions for Further Work and Investigation

It is suggested that the axially laminated design be replaced with a transverse laminated design. With the latter type, skewing and stagger might be used to reduce the level of torque ripple.

Inductance ripple has serious effects on the machine output performance, producing torque ripple. This work has investigated these effects on tracking error transient performance in the servo case. It was concluded that a control scheme for inductance ripple compensation might not be needed. However the situation is different in steady state applications where an appreciable torque ripple problem arises. This problem could be alleviated by a suitable current control scheme. It is thought that the direct axis current may be kept constant and to maintain a constant torque, the current in the quadrature axis would be varried in a way to achieve zero torque ripple. This can be deduced from the torque equation that accounts for torque ripple.

Appendix A

Finite element constraints

These constraints (binary and unary) are applied to reduce the overall modelled area.

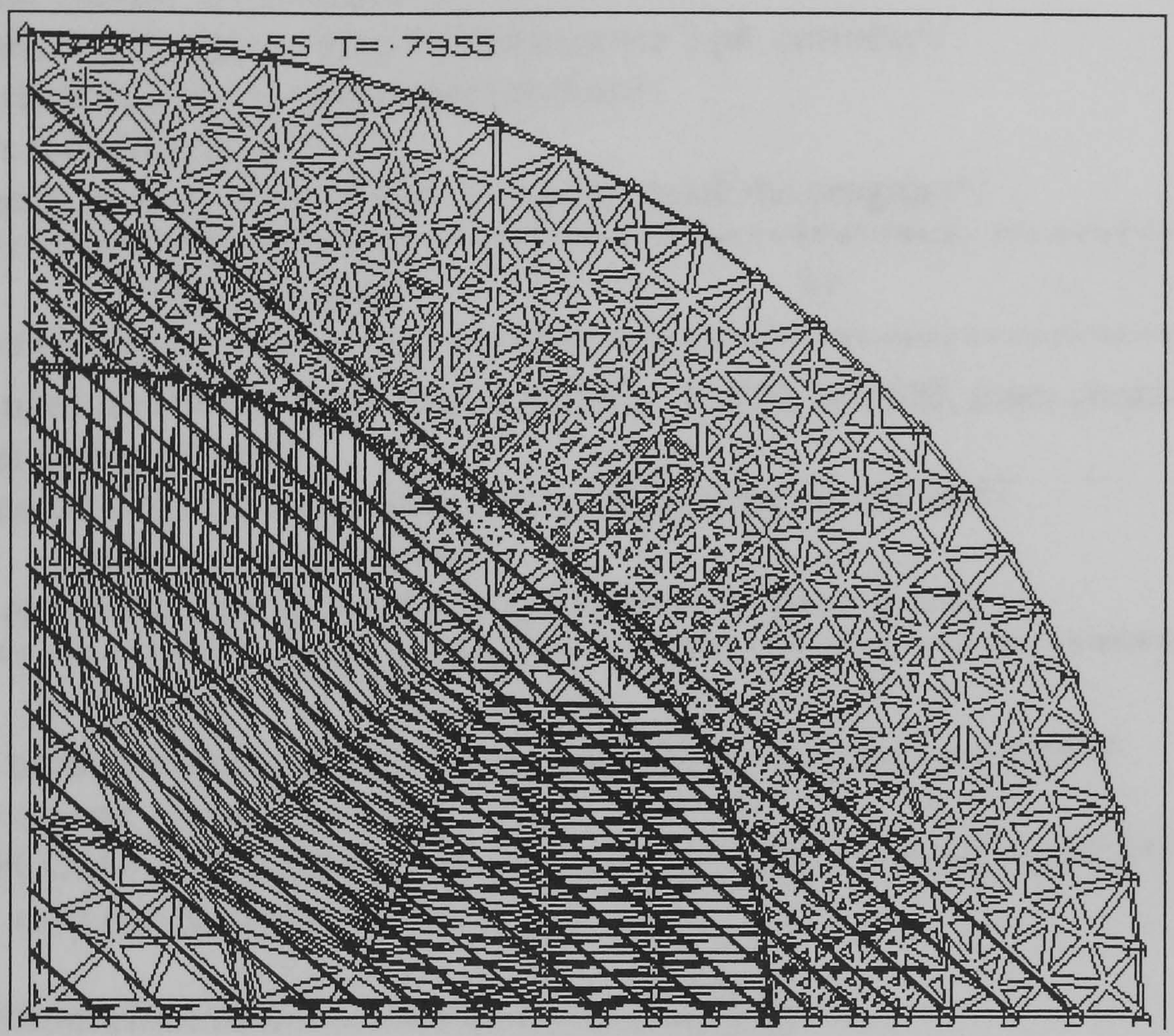

Binary constraints are configured such that

$$A_{(r,0)} = A_{(r,\pi/2)}$$

where $A_{(r,0)}$ represents the magnetic vector potential value of node at distance r from origin along the horizontal radial boundary

$A_{(r,\pi/2)}$ represents the magnetic vector potential value at the binary connected node (vertical boundary)

The unary constraints are set such that

$A = 0$ at the peripheral boundaries.

Appendix B

Vector Control Code

```
/*****************************************************************/
//10/97
/* Vector control of synchREl */
/* Monitoring ct vector using 2 C.Ts to sense 2 ph. currents*/
/* and shaft encoder to sense rotor position*/
/*park's transformation*/
/*integer scaling to all quantities is used to quick the program*/
/*****************************************************************/
/*          C166 comments                                        */
/*****************************************************************/
/* T1  used for PWM , timer freq. 4.88 KHz, T1REL =0xfdff, timer count=512*/
/* timer period 204 us*/
/* T6 used to control the execution time of the prog   0.408 ms*/
// ===       ==============
// The execution time should be integer number of pwm period
/*********************shaft encoder*****************************/

/* T3  used as counter, is clocked by -transition at ext. input pin p3.6*/
// === orange    =========
/*CAPCOM7 used to generate IR at the -ve ext. trans. on input pin p2.7*/
//===  save pos & time======
////////////////////////////////////////////////////////////////////////
#pragma SMALL                    /*memory model*/
#pragma CODE                     /* control directive */
#pragma DEBUG
#pragma PECDEF (0,1,2,3,4,5,6,7)   /* define PEC channel numbers */
#include <stdio.h>               /* standard I/O .h-file          */
#include <math.h>
#include <reg166.h>              /* special function register 80C166  */
#include <intrins.h>             /* generate pec transfer*/
#define pi 3.141592653589793
#define kp 836
#define R3 37837
#define b  8355944
#define kgd  327
#define kgq  327
#define kid  3211
#define kiq  8029
#define r2   724
#define a    208
#define dt    2
#define r    572
#define h  400
```

```
#define oo   15708160
#define b2 127
#define g 32767
/*****************************************************************************/
/* Globals */
void delay(int count);
int  sign(int  v);
long sin_tab[1024];
long idata sinm,cosm,sin120,cos120,sin240,cos240;

long idata ch,i,m,va1,va2,vb1,vb2,kpd,kpq,kk=0;
long idata kid1,iderr1,kqp,kdp,ch1,ch2,ch3,ch4,id,iq,id1,iq1,kdi, kqi,iderr,iqerr,ic;
long idata vd, vq,va,vb,vc;
long  idata idi=0,iqi=0;

long idata idref=10981,iqref=4758;   // current(Ampere)=  integer value/668

long idata  pos,posn1,posn;

signed int  sdata  ADDAT2[2];
signed int sdata ia, ib;

unsigned int sdata CC0_image,CC4_image,CC12_image;
unsigned int sdata CC8_image;
unsigned int sdata CC1_image, CC5_image, CC13_image;
unsigned int sdata CC9_image;
unsigned int sdata CC2_image, CC6_image, CC14_image;
unsigned int sdata CC10_image;
unsigned int idata pwm_period = 0xFDFF;
unsigned int idata under_lap=0x0003;    //1.2 us...underlap

signed int far *buf1;
unsigned int idata dat16;
signed int far *bufa;
signed int far *bufb;
signed int far *bufc;
signed int far *bufd;

int idata start_prog=0;
/*****************************************************************************/
void main (void)
{
 SYSCON |=0xf;        // zero wait states, NONMUX from the setting of the
                      // jumbers

/* Initialize A/D array*/
 ADDAT2[0]=1;
```

```
ADDAT2[1]=2;
ia=ADDAT2[0];
ib=ADDAT2[1];

/* initialize the serial interface    */
P3  |= 0x0400;       /* SET PORT 3.10 OUTPUT LATCH (TXD)          */
DP3 |= 0x0400;       /* SET PORT 3.10 DIRECTION CONTROL (TXD OUTPUT)  */
DP3 &= 0xF7FF;       /* RESET PORT 3.11 DIRECTION CONTROL (RXD INPUT) */
S0TIC = 0x80;        /* SET TRANSMIT INTERRUPT FLAG               */
S0RIC = 0x00;        /* DELETE RECEIVE INTERRUPT FLAG             */
S0BG  = 0x40;        /* SET BAUDRATE TO 9600 BAUD                 */
S0CON = 0x8011;      /* SET SERIAL MODE                           */

/***************** A/D conveter*********************************/
 IEN=0;      //disable all the interrupts

 /* p5.0, p5.1*/


 SRCP1  = _sof_(&ADDAT);  //ADDAT: source pointer
 DSTP1  = _sof_(ADDAT2);  // ADDAT2: destination pointer
 PECC1  = 0x0202;         // move results using PEC channel No. 1
                  // count=2; decreases by 1 after each transfer
                  //inc=01; increase destination pointer by 1
                  // when the count=0, cpu interrup...highest pr.
 ADCON = 0x0021;         /*start conversion with ch.1, auto scan conversion*/
                 /* mode 3*/
 ADCIC  = 0x39;          /*pr. 14 (PEC service), gr. 1, ch. 1  */
 ADCIR  =0;
 ADCIE  =1;



//sampling interval same as pwm_period


/*************************************************************/
/******************** Shaft Encoder interface*****************/
DP3 &= 0xFFAF;     // p3.4 and p3.6; inputs
              /* p3.4:T3EUD,  p3.6 is -ve transtion input for T3*/
DP2 &= 0x7F77;     /* p2.3(z-pulse to rest T3): external interruput input to CC3*/
              // P2.7(pos&time): ext. int. input to CC7*/


/**********counter setting*********************************/
```

```
T3CON = 0x01CA;    /*counter mode , -ve ext. transition, T3EUD controls */
                    /* count up or down P3.4(yel)... P3.6(ora) input clock*/
T3IC  =    0x34;   /* pr. 13 gr. 0*/
T3IR  =    0;      //+ve 1, -ve 2
T3IE  =    0;


/******** save position &work out the speed***********/
//cc7 &p2_7
CCM1    = 0x2000;     /* generates IR at -ve ext. transition on p2.7(dar blue)*/
CC7IC   = 0x37;       /*pr. 13 gr. 2 : cpu interruput*/
CC7IR   = 0;
CC7IE   = 1;


/************Z pulse: to reset timer every 360 degree*********/

CC3IC = 0x38;       /* pr.14 gr. 0, channel 0  PEC service*/
CCM0  = 0x1000;     /* capture on +ve ext. transition of CC3IO p2.3 /red */
PECC0 = 0x00FF;
SRCP0 =_sof_(&zeros); /*source pointer*/
DSTP0 =_sof_(&T3);    /* destination pointer*/
CC3IE =1;


/******************PWM generation*********************************/
/*initialise CCx double compare register mode cap_com unit on timer 1*/

P2    = 0x0007;         /* p2.0,p2.1,p2.2,p2.7 =1 as initial value*/
                        /*p2.4,p2.5,p2.6=0 complementary output*/
DP2   |= 0x0077;        /*p2.0,p2.1,p2.2,p2.4,p2.5,p2.6 as output*/
CCM0  |= 0x0DDD;        /* compare mode 1 for cc0,cc1,cc2 all of them*/
                        /*use timer 1 */
CCM1  |=0x0DDD;         /*compare mode 1 for cc4, cc5, cc6 (complementary)*/
CCM2  = 0x0CCC;         /* compare mode 0 for cc8,cc9,cc10*/
                        /* cc8,cc9,cc10 use timer 1*/
CCM3 |=0x0CCC;          /* compare mode 0 for cc12, cc13, cc14(complementary)*/

/*for double compare mode cc0 operates on mode 1 and cc8 on mode 0*/
/*interrupt mode only, and both of them uses T1*/

/*************************************************************/
/* setup for pec update of cc0 by cc8*/
/*output 1 p2.0*/
                        /*pec service, level pr.15, gr.pr. 3*/
CC8IC=0x3F;
```

```
CC0_image=0xFF00;          /*set initial duty ratio*/
CC8_image=0xFF01;
CC0   = CC0_image;
CC8   = CC8_image;

PECC7=0x00FF;
SRCP7 = _sof_(&CC0_image);  /* PEC7 source */
DSTP7 = _sof_(&CC0);        /* PEC7 destination */
CC8IE=1;
/*************************************************************/
/* setup for pec update of cc1 by cc9*/
/*output 2 p2.1*/

CC9IC=0x3E;                /*pec service,level pr.15, gr. pr. 2*/
CC1_image=0xFF00;          /*set initial duty ratio*/
CC9_image=0xFF01;
CC1   = CC1_image;
CC9   = CC9_image;

PECC6=0x00FF;
SRCP6 = _sof_(&CC1_image);  /* PEC6 source */
DSTP6 = _sof_(&CC1);        /* PEC6 destination */
CC9IE=1;
/*************************************************************/
/* setup for pec update of cc2 by cc10*/
/*output 3 p2.2*/

CC10IC=0x3D;               /*pec service,level pr.15, gr. pr. 1*/
CC2_image=0xFF00;          /*set initial duty ratio*/
CC10_image=0xFF01;
CC2   = CC2_image;
CC10   = CC10_image;

PECC5=0x00FF;
SRCP5 = _sof_(&CC2_image);  /* PEC5 source */
DSTP5 = _sof_(&CC2);        /* PEC5 destination */
CC10IE=1;
/*************************************************************/
/********complementary output*****************************/
/*************************************************************/
/* setup for pec update of cc4 by cc12*/
/*complentary output 1 p2.4*/

CC12IC=0x3C;               /*pec service,level pr.15, gr. pr. 0*/
CC4_image=0xFF00;          /*set initial duty ratio*/
CC12_image=0xFF01;
```

```
CC4   = CC4_image;
CC12  = CC12_image;

PECC4=0x00FF;
SRCP4 = _sof_(&CC4_image);  /* PEC3 source */
DSTP4 = _sof_(&CC4);        /* PEC3 destination */
CC12IE=1;


/*****************************************************************/
/* setup for pec update of cc5 by cc13*/
/*complementary output 2 p2.5*/

CC13IC=0x3B;                /*pec service,level pr.14, gr. pr. 2*/
CC5_image =0xFF00;          /*set initial duty ratio*/
CC13_image=0xFF01;
CC5    = CC5_image;
CC13   = CC13_image;

PECC3=0x00FF;
SRCP3 = _sof_(&CC5_image);  /* PEC2 source */
DSTP3 = _sof_(&CC5);        /* PEC2 destination */
CC13IE=1;


/*****************************************************************/
/* setup for pec update of cc6 by cc14*/
/*complementary output 3  p2.6*/
                    /*pec service,level pr.14, gr. pr. 1*/
CC14IC=0x3A;
CC6_image=0xFF00;           /*set initial duty ratio*/
CC14_image=0xFF01;
CC6    = CC6_image;
CC14   = CC14_image;

PECC2=0x00FF;
SRCP2 = _sof_(&CC6_image);  /* PEC2 source */
DSTP2 = _sof_(&CC6);        /* PEC2 destination */
CC14IE=1;
/*****************************************************************/


/** overflow interrupt to define pwm period**/
/*timer 1 =204 us*/
T1IC  = 0;
//timer 6 to define execution time
//0.408  ms
```

```
 CAPREL=63495;       // fs=1/((65535-x)*0.2 us) fs = prog. freq   408 us
                  // configure timer T6, count up, reload &output otl on p3.1
 T6CON=0x8040;      /* run only in timer mode , 5 MHz input freq.*/
 T6IR   =0;
 T6IC   = 0x28;     /* pr. 3, group 3 */
 T6IE   = 1;        /* timer overflow int enable */


T1REL =pwm_period;       /*set reload value  (0xffff-0x0200)*/
T1    =T1REL;            /* fc=1/(512*.4)= 4.88 khz*/
T1IC  = 0x35;            /*set priority 13, group 3 in T1IC (for PEC4) */
T1IR  = 0;               /*clear any spurious interrupts*/
T1IE  =1;                /* enable timer overflow PECs */
T01CON   = 0x4000;       /* start timer 1 & 0 timer mode */


IEN =1;                  // enable all interrupts

for (i=0;i< 1024;i++)

sin_tab[i]=16383*sin(i*pi/512.0);   /*14 bits*/


/****************main program*********************************/
printf("start");
while (1)
{

while(!start_prog);    // wait until start_prog =1
start_prog=0;

 ic=-(ia+ib);
 posn=posn1&0x3ff;

 sinm     =sin_tab[posn];
 cosm     =sin_tab[(posn+256)&0x3ff];
 sin120   =sin_tab[(posn+682)&0x3ff];
 cos120   =sin_tab[(posn+682+256)&0x3ff];
 sin240   =sin_tab[(posn+341)&0x3ff];
  cos240   =sin_tab[(posn+341+256)&0x3ff];


 id     = ((( ia* cosm+ ib*cos120+ ic*cos240) >>8)*kp)>>10; // 15act /16
 iq     = ((( ia*sinm + ib*sin120+ ic*sin240) >>8)*kp)>>10;

/*************** P controller*********************************/
```

```
iderr  = idref + id;
iqerr  = iqref + iq ;
kpd    =(iderr*dt)>>5;
kpq    =(iqerr*dt)>>5;
idi    = idi + kpd;
iqi    = iqi + kpq;
     if(idi>131040)  idi=131040;
     if(idi<-131040) idi=-131040;
```

```
    if(iqi>65520)   iqi=65520;      //vqi max=125
    if(iqi<-65520)  iqi=-65520;
```

```
kdi    = (kid*idi)>>15;
kdp    = (kgd*iderr)>>15;
vd     = (kdi)>>7;
vd     = vd+ kdp;
kqi    =(kiq*iqi)>>15;
kqp    =(kgq*iqerr)>>15;
vq     = (kqi)>>7;
vq     =  vq + kqp;
```

```
/****************** inverse park's transformation*************************/

va1= (vd* cosm )>>14;
va2= (vq*sinm  )>>14;

vb1   =(vd* cos120)>>14;
vb2    =(vq*sin120)>>14;
T1IE=0;
va     =((va1+va2)*kp)>>10;
vb     =(( vb1+vb2)*kp)>>10;
vc     = -(va+vb);

if (abs(va) > 125)
   va= sign(va) * 125;

if (abs(vb) > 125)
   vb= sign(vb) * 125;   // -125 < a,b,c<+125

if (abs(vc) > 125)
   vc= sign(vc) * 125;
```

```
 T1IE=1;
// DAC channels

ch1=(va*g+b)>>16;
ch2=(ia+510)>>2;
ch3=(iderr*a+b)>>16;
ch4=(iqerr*a+b)>>16;

/*****************************************************************************/
//////////////////////DACs selection ////////////////////////////////////
/*****************************************************************************/


//Address lines A0, A1 of the DAC connected to BA1, BA2 respectively
// output the data in the first 8 bits
//writing to address 0x3f800 will activate the data buffers(/CEEXT signal) only


bufa=0x3f000;        // data buffer is active, /CE1 signal is active as well
dat16=ch1;           // select channel A...BA2, BA1 BA0  0 0  0     c166
                  //  CHA address is  0              ----        DAC
*bufa=dat16;

bufb=0x3f002;        // data buffer is active, /CE1 signal is active as well
dat16=ch2;           // select channel B   ...2              0 1  0   c166
                  // CHB address is  1                 ----      DAC
*bufb=dat16;

bufc=0x3f004;        // data buffer is active, /CE1 signal is active as well
dat16=ch3;           // select channel C   ...4              1 0  0   c166
                  // CHC address is  2                 ----      DAC
*bufc=dat16;

bufd=0x3f006;        // data buffer is active, /CE1 signal is active as well
dat16=ch4;           // select channel D   ...6              1 1  0   c166
                  // CHD address is  3                 ----      DAC
*bufd=dat16;


// the address of the dac should be valid before WR goes low
// /CE2 3f400...CE3 3f800..CEEXT 3fc00



}

printf("done");
```

```
}/*main program*/


/**********************************************************************/


/**********************************************************************/
/* Interrupt service routines PWM */
/**********************************************************************/
void timer1_int(void) interrupt 0x21 using r_bank0 {

 ia =(ADDAT2[0]&0x3ff)-512;      // read ia, ib
 ib =(ADDAT2[1]&0x3ff)-512;      //yel p5.1=ia=yell    p5.0=ib=red
 if (!ADBSY)                    // if the conversion is not in progress then
                          // start conversion adst=1
 ADST=1;


  CC0_image=pwm_period+va+128;
  CC8_image=0xFFFF-va-128;
  CC4_image =CC0_image+under_lap;   // red phase
  CC12_image=CC8_image;
  CC8_image+= under_lap;

  CC1_image=pwm_period+vb+128;
  CC9_image=0xFFFF-vb-128;          // yellow
  CC5_image= CC1_image+under_lap;
  CC13_image=CC9_image;
  CC9_image+=under_lap;

  CC2_image=pwm_period+vc+128;      // blue
  CC10_image=0xFFFF-vc-128;
  CC6_image=CC2_image+under_lap;
  CC14_image=CC10_image;
  CC10_image+=under_lap;

  CC8=CC8_image;
    CC9=CC9_image;
    CC10= CC10_image;
    CC12= CC12_image;
    CC13= CC13_image;
    CC14= CC14_image;


}
```

```
/*************************************************************************/
/* Interrupt service routines */
/*************************************************************************/
void CAPCOM7_int(void) interrupt 0x17 using r_banka
{

/* save position and time*/
pos = T3;
posn1=(pos)&0x7ff;

}


/*************************************************************************/
/* Interrupt service routines A/D */
/*************************************************************************/
void addat_int(void) interrupt 0x28 using r_bank2
{
      DSTP1  = _sof_(ADDAT2);              //3?????
      PECC1 = 0x0202;
}


/**********************timer6  interrupt  routine**************/
void timer6_int(void) interrupt 0x26 using r_bank5 {
start_prog=1;
}


void delay(int count)
{
int x,y;
       for(x=0;x<count;x++);
         for(y=0;y<0xffff;y++);
}


int  sign(int  v)
{
 if (v >= 0)
    return(1);
 else
    return(-1);
}
```

Appendix C

Sliding Mode Control Code

```
/*************************************************************************/
//16/3/98
// Servo case with double component sliding mode control
// speed trajectory ad=12 rad/s/s, reverse from 6 to -6 rad/s, duration 2s
//Actual execution time 560 us,T6 is set to 1.63 kH,612 us
//////////////////////////////////////////////////////////////////////////
#pragma SMALL                    /*memory model*/
#pragma CODE                     /* control directive */
#pragma DEBUG
#pragma PECDEF (0,1,2,3,4,5,6,7)   /* define PEC channel numbers */
#include <stdio.h>               /* standard I/O .h-file          */
#include <math.h>
#include <reg166.h>               /* special function register 80C166  */
#include <intrins.h>             /* generate pec transfer*/
#define pi 3.141592653589793
#define kp 836
#define R3 37837
#define h  500
#define h3  500
#define ee 100000
#define b  8355944
#define kgd  327
#define kgq  327
#define kid  3211
#define kiq  8029
#define r2   724
#define h1    1000
#define dt    3
#define a1    1638
#define a2    51
#define a     208
#define lamda  6
#define lamda1 38
#define n   61440
#define k1    6
#define fai  1433
//#define f1   -54
//#define f2   -1038
#define F1   34
#define F2   1294
#define bi   758
#define beta 5005
#define g    500
#define kk  3430
```

```
#define a3  1000
#define b3  9830400
#define a4  1457
#define oo   15708160
#define r    6
#define qq   668
#define ti   0          // 0.5 s
#define t1   817          // 1 s
#define t2   2451          // 2 s
#define t3   3267          // 2.5 s
#define wa   12288        // 11 bits    6 rad/s*2048
#define wi   0
#define mag 22
/*****************************************************************************/
/* Globals */
void delay(int count);
int  sign(int  v);
int sat(int phi);
long sin_tab[1024];
long idata ch,i,m,pos,posn1,va1,va2,vb1,vb2,posn,kpd,kpq,posd,timed,t0;
long  idata  kid1,iderr1,tt,kqp,kdp,ch1,ch2,ch3,ch4,id,iq,id1,iq1,kdi,  kqi,iderr,iqerr,ic,  speed,
speedr;
long idata vd, vq,va,vb,vc;
long  idata idi=0,iqi=0,vrail=125, id0,ab, idref1,accd1,accd2,possd1,possd2;      /*80.85*4096
130*4096   125*sqrt(3/2)*/
long          idata          idref=10985,iqref,iqref2,s,iqref1,wd,err,possd=0,accd=0,k,f,F,wr,wr1,wd1,wb=-12288,f1=-55;
 //-0.0016/26 in 26 bits
long          idata          sinm,dd,dd1,cosm,zeros=0,sin120,cos120,sin240,cos240,vlimit,
posn0,time0,f2=-2077;   //-0.0634 in 14 bits

unsigned int sdata time=0;
signed int  sdata  ADDAT2[2];
signed int sdata ia, ib;     //yel trans=ia red trans=ib

unsigned int sdata CC0_image,CC4_image,CC12_image;
unsigned int sdata CC8_image;
unsigned int sdata CC1_image, CC5_image, CC13_image;
unsigned int sdata CC9_image;
unsigned int sdata CC2_image, CC6_image, CC14_image;
unsigned int sdata CC10_image;
unsigned int idata pwm_period = 0xFDFF;
unsigned int idata under_lap=0x0003;    //1.2 us...underlap

signed int far *buf1;
unsigned int idata dat16;
signed int far *bufa;
```

```
signed int far *bufb;
signed int far *bufc;
signed int far *bufd;
int idata start_prog=0;
/*****************************************************************************/
void main (void)
{
 SYSCON |=0xf;        // zero wait states, NONMUX from the setting of the
                      // jumbers
/* Initialize the array*/
 ADDAT2[0]=1;
 ADDAT2[1]=2;
 ia=ADDAT2[0];
 ib=ADDAT2[1];

 /* initialize the serial interface     */
 P3  |= 0x0400;       /* SET PORT 3.10 OUTPUT LATCH (TXD)          */
 DP3 |= 0x0400;       /* SET PORT 3.10 DIRECTION CONTROL (TXD OUTPUT)  */
 DP3 &= 0xF7FF;       /* RESET PORT 3.11 DIRECTION CONTROL (RXD INPUT) */
 S0TIC = 0x80;        /* SET TRANSMIT INTERRUPT FLAG               */
 S0RIC = 0x00;        /* DELETE RECEIVE INTERRUPT FLAG             */
 S0BG  = 0x40;        /* SET BAUDRATE TO 9600 BAUD                 */
 S0CON = 0x8011;      /* SET SERIAL MODE                           */

/*************** A/D conveter*********************************/
 IEN=0;
 // the values of the offset change from time to time
 // re-adjust the potentiameter to get 2.5 volts at 0 curent

 /* p5.0, p5.1*/

 DP3 |=0x0002;        // DP3.1  this pin is output
 P3  |=0x0002;        // p3.1=1 set alternate output function of T6

 SRCP1  = _sof_(&ADDAT);  /* count value decrement after each transfer*/
 DSTP1  = _sof_(ADDAT2);  //2???
 PECC1  = 0x0202;     /* inc=01 increase destination pointer, count=2*/

 ADCON = 0x0021;      /*start conversion with ch.1, auto scan */
                      /* mode 3, enable ADST?*/
 ADCIC  = 0x39;       /*pr. 14 (PEC service), gr. 1, ch. 1  */
 ADCIR  =0;           // when the count=0, cpu interrup...highest pr.
 ADCIE  =1;
// ADST=1;            /* start conversion */
 ADEIC= 0x04;
 ADEIR=0;
```

```
 ADEIE=0;            //1.2 ms


//control the sampling every pwm_period

/*****************************************************************/

/*****************************************************************/
/******************** Shaft Encoder interface*********************/
DP3 &= 0xFFAF;
              /* p3.4:T3EUD,  p3.6 is -ve transtion input for T3*/
DP2 &= 0x7F77;     /* p2.3(z-pulse res. coun): external interruput input to CC3*/
              // P2.7(pos): ext. int. input to CC7*/
               //p2.15 ext int input to cc15 (time)

/***********counter setting*********************************/


T3CON = 0x01CA;   /*counter mode , -ve ext. transition, T3EUD controls */
              /* count up or down P3.4(yel)... P3.6(ora) input clock*/
T3IC  =    0x34;     /* pr. 13 gr. 0*/
T3IR  =    0;       //+ve 1, -ve 2
 T3IE  =    0;

 /******* save time with every change in position ************/
//LATCH for TIME

 CCM3    = 0x2000;      /* generates IR at -ve ext. transition on p2.15(green)*/
 CC15IC   = 0x38;       /*pr. 13 gr. 2 : cpu interruput*/
 SRCP0 =_sof_(&T5);     /*source pointer*/
 DSTP0 =_sof_(&time);   /* destination pointer*/
 PECC0=0x00ff;
 CC15IR   = 0;
 CC15IE   = 1;


/******* save position &work out the speed************/

CCM1    = 0x2000;     /* generates IR at -ve ext. transition on p2.7(dar blue)*/
CC7IC   = 0x37;       /*pr. 13 gr. 2 : cpu interruput*/
CC7IR   = 0;
CC7IE   = 1;
```

```
/************Z pulse: to reset timer every 360 degree*********/

CC3IC = 0x33;       /* cpu interrup to reset T3 just once*/
CCM0  = 0x1000;    /* capture on +ve ext. transition of CC3IO p2.3 /red */
CC3IE =1;

/************timing?*********************************************/
//monitor terminal count at each timer overflow

T5CON  =0x0041;      /* input freq. 2.5 Mhz, timer mode, count up*/
 T5IC   =0x36;       //gr. 1 , pr.13  check the time...done  ?
 T5IR   =0;          //period 26 ms,.4 us resolution
 T5IE   =1;

/*******************pwm generation*******************************/
/*initialise CCx double compare register mode cap_com unit on timer 1*/

P2    = 0x0007;       /* p2.0,p2.1,p2.2,p2.7 =1 as initial value*/
                  /*p2.4,p2.5,p2.6=0 complementary output*/
DP2   |= 0x0077;       /*p2.0,p2.1,p2.2,p2.4,p2.5,p2.6 as output*/
CCM0  |= 0x0DDD;       /* compare mode 1 for cc0,cc1,cc2 all of them*/
                  /*use timer 1 */
CCM1  |=0x0DDD;        /*compare mode 1 for cc4, cc5, cc6 (complementary)*/
CCM2  = 0x0CCC;       /* compare mode 0 for cc8,cc9,cc10*/
                  /* cc8,cc9,cc10 use timer 1*/
CCM3  |=0x0CCC;        /* compare mode 0 for cc12, cc13, cc14(complementary)*/

/*for double combp mode cc0 operates on mode 1 and cc8 on mode 0*/
/*interrupt mode only, and both of them uses T1*/

/*****************************************************************/
/* setup for pec update of cc0 by cc8*/
/*output 1 p2.0*/
                     /*pec service, level pr.15, gr.pr. 3*/
CC8IC=0x3F;
CC0_image=0xFF00;          /*set initial duty ratio*/
CC8_image=0xFF01;
CC0   = CC0_image;
CC8   = CC8_image;

PECC7=0x00FF;
SRCP7 = _sof_(&CC0_image);  /* PEC7 source */
DSTP7 = _sof_(&CC0);        /* PEC7 destination */
CC8IE=1;

/*****************************************************************/
/* setup for pec update of cc1 by cc9*/
```

```
/*output 2 p2.1*/

CC9IC=0x3E;              /*pec service,level pr.15, gr. pr. 2*/
CC1_image=0xFF00;        /*set initial duty ratio*/
CC9_image=0xFF01;
CC1   = CC1_image;
CC9   = CC9_image;

PECC6=0x00FF;
SRCP6 = _sof_(&CC1_image);  /* PEC6 source */
DSTP6 = _sof_(&CC1);        /* PEC6 destination */
CC9IE=1;
/*************************************************************/
/* setup for pec update of cc2 by cc10*/
/*output 3 p2.2*/

CC10IC=0x3D;             /*pec service,level pr.15, gr. pr. 1*/
CC2_image=0xFF00;        /*set initial duty ratio*/
CC10_image=0xFF01;
CC2   = CC2_image;
CC10   = CC10_image;

PECC5=0x00FF;
SRCP5 = _sof_(&CC2_image);  /* PEC5 source */
DSTP5 = _sof_(&CC2);        /* PEC5 destination */
CC10IE=1;
/*************************************************************/
/*********complementary output*****************************/
/*************************************************************/
/* setup for pec update of cc4 by cc12*/
/*complentary output 1 p2.4*/

CC12IC=0x3C;             /*pec service,level pr.15, gr. pr. 0*/
CC4_image=0xFF00;        /*set initial duty ratio*/
CC12_image=0xFF01;
CC4   = CC4_image;
CC12  = CC12_image;

PECC4=0x00FF;
SRCP4 = _sof_(&CC4_image);  /* PEC3 source */
DSTP4 = _sof_(&CC4);        /* PEC3 destination */
CC12IE=1;


/*************************************************************/
/* setup for pec update of cc5 by cc13*/
/*complementary output 2 p2.5*/
```

```
CC13IC=0x3B;                /*pec service,level pr.14, gr. pr. 2*/
CC5_image =0xFF00;          /*set initial duty ratio*/
CC13_image=0xFF01;
CC5    = CC5_image;
CC13   = CC13_image;

PECC3=0x00FF;
SRCP3 = _sof_(&CC5_image);  /* PEC2 source */
DSTP3 = _sof_(&CC5);        /* PEC2 destination */
CC13IE=1;
```

```
/*************************************************************/
/* setup for pec update of cc6 by cc14*/
/*complementary output 3  p2.6*/
                    /*pec service,level pr.14, gr. pr. 1*/
CC14IC=0x3A;
CC6_image=0xFF00;           /*set initial duty ratio*/
CC14_image=0xFF01;
CC6    = CC6_image;
CC14   = CC14_image;

PECC2=0x00FF;
SRCP2 = _sof_(&CC6_image);  /* PEC2 source */
DSTP2 = _sof_(&CC6);        /* PEC2 destination */
CC14IE=1;
/*************************************************************/


/** overflow interrupt to define pwm period**/
/*timer 1 =204 us*/
T1IC  = 0;
//timer 6 to define execution time

 CAPREL=62475;         //ts=612 us 3*pwm_period, fs=1.63 kh
 T6CON=0x8040;       /* run only in timer mode , 5 MHz input freq.*/
 T6IR   =0;
 T6IC   = 0x28;      /* pr. 3, group 3 */
 T6IE   = 1;         /* timer overflow int enable */

/*T1 resolution: .4us, input freq=2.5Mhz*/

T1REL =pwm_period;        /*set reload value  (0xffff-0x0200)*/
T1    =T1REL;
T1IC  = 0x35;             /*set priority 13, group 3 in T1IC (for PEC4) */
T1IR  = 0;                /*clear any spurious interrupts*/
T1IE  =1;                 /* enable timer overflow PECs */
```

```
T01CON   = 0x4000;        /* start timer 1 & 0 timer mode */


IEN =1;                          /* fc=1/(512*.4)= 4.88 khz*/
for (i=0;i< 1024;i++)
sin_tab[i]=16383*sin(i*pi/512.0);   /*14 bits*/


/****************main program*********************************/
printf("start");
while (1)
{
while(!start_prog);    // wait until start_prog =1
start_prog=0;
m+=1;

  ic=-(ia+ib);
  posn    =  posn1&0x3ff ;   /*from mech. angle to elect. angle*/
                    /*and from 11bits to 10 bits to be the size of sin*/

 sinm     =sin_tab[posn];
 cosm     =sin_tab[(posn+256)&0x3ff];
 sin120   =sin_tab[(posn+682)&0x3ff];
 cos120   =sin_tab[(posn+682+256)&0x3ff];
 sin240   =sin_tab[(posn+341)&0x3ff];
 cos240   =sin_tab[(posn+341+256)&0x3ff];


//*********************speed trajectory generation*************************//

  if (( m>ti) && (m<=t1))         //100<t<300 ms
    {                             //163>m>490
     wd=(wa-wi)*(m-ti);
     wd=wd/(t1-ti);
     possd=(possd+wd);
     accd =(wa-wi)/(t1-ti);

    }                             //1
 else if((m>t1) && (m<=t2))           // 300<t<700 ms
 {//2                              //  490<t<816
 //wd=((wb-wa)/(t2-t1))*(m-t1)+wa;
 wd=wb-wa;
 wd*=(m-t1);
 wd=wd/(t2-t1);
 wd+=wa;
 possd=(possd+wd);
 accd=(wb-wa)/(t2-t1);
```

```
        }//2

else if((m>t2)&&(m<=t3))              //816<t<1143 ms
        {//3
    wd=(wa-wi)*(m-t2);
    wd=wd/(t3-t2);
    wd+=wb;
    possd=(possd+wd);
    accd =(wa-wi)/(t3-t2);

        }


    if (m==t3)
    {
    m=0;
    possd=0;
    }

                        // acc=45....51128
accd1=accd*a1;              //acc in 11 bits ..prog 31*(45/31*2047/1.8) or *1650
possd1=(possd*a2)>>19;                  // posd in 11 bits..1.8 rad...2047//correc. fac.=
2047/3362862=0.000608
                        //a2 =637 in 20 bits

//******************* sliding mode code ****************************//


f=(f1*wr);

f>>=15;

f+=(f2*sign(wr))>>4;
iqref1=-f+accd1-lamda*(wr-wd);
err=posn1-possd1;

if (err>980)  err-=2047;
s=(wr-wd)+lamda1*(err);

F=F1*wr;
F>>=15;
F+=(F2*sign(wr))>>4;
if (iqref1<0)  iqref2=-iqref1;
```

```
else        iqref2=iqref1;

k=(beta*(F+n))>>11;

k+=((beta-2048)*iqref2)>>11;

k*=k1;

tt=(s*2048)/fai;

dd1=k*sat(tt);

if ((tt> 2048)||(tt< -2048))  dd=dd1;
else dd=dd1>>11;
//printf("dd1=%ld dd=%ld\n\r",dd1,dd);

iqref=iqref2-dd;

iqref*=bi;
iqref>>=11;

iqref=(iqref*qq)>>15;

if(iqref>12931)  iqref=12931;
if(iqref<-12931) iqref=-12931;

/******************* park's transformation*****************/

 id    =  ia* cosm+ ib*cos120+ ic*cos240;
 id>>=8;
 id*=kp;
 id>>=10;
 iq    =  ia*sinm + ib*sin120+ ic*sin240;
 iq>>=8;
 iq*=kp;
 iq>>=10;

/*************** P controller*********************************/
 iderr  = idref + id;       /*15 bits + sign fact. 2 to get the real rep*/
 iqerr  = -iqref + iq ;     /*iqref from 11 bits to 15 bits */

// there is a level of inversion, maybe from A/D or A/D board

 kpd    =iderr*dt;
 kpd >>=5;
 kpq    =iqerr*dt;
 kpq >>=5;
```

```
idi    = idi + kpd;
iqi    = iqi + kpq;

//Limit integral terms idi and iqi
      if(idi>131040)  idi=131040;  // vdi max=100
      if(idi<-131040) idi=-131040;



     if(iqi>65520)   iqi=65520;       //vqi max=125   check again
      if(iqi<-65520)  iqi=-65520;

kdi    = kid*idi;
kdi  >>=15;
kdp    = kgd*iderr;
kdp  >>=15;
vd     = (kdi)>>7;
vd     = vd+ kdp;

kqi    =(kiq*iqi)>>15;
kqp    =(kgq*iqerr)>>15;
vq     = (kqi)>>7;
vq     =  vq + kqp;

/***************** inverse park's transformation*****************************/

 va1= (vd* cosm )>>14;
 va2= (vq*sinm  )>>14;

 vb1   =(vd* cos120)>>14;
 vb2    =(vq*sin120)>>14;
 T1IE=0;
 va     =((va1+va2)*kp)>>10;
 vb     =(( vb1+vb2)*kp)>>10;
 vc     = -(va+vb);

if (abs(va) > 125)
   va= sign(va) * 125;

if (abs(vb) > 125)
   vb= sign(vb) * 125;   // -125 < a,b,c<+125

if (abs(vc) > 125)
   vc= sign(vc) * 125;

 T1IE=1;
```

```
//ch1=(wr*h+b)>>16;
ch4=(possd1+1023)>>3;
ch1=(posn1+1023)>>3;
ch3=((err)*ee+b)>>16;

//ch3=(iqref*g+b)>>16 ;
ch2=(s*a3+b)>>16;
```

```
/*************************************************************************/
////////////////////DACs selection ////////////////////////////////
/*************************************************************************/


//Address lines A0, A1 of the DAC connected to BA1, BA2 respectively
// output the data in the first 8 bits
//writing to address 0x3f800 will activate the data buffers(/CEEXT signal) only


bufa=0x3f000;       // data buffer is active, /CE1 signal is active as well
//buf1=0x3f800;     // is not important now?
dat16=ch1;          // select channel A...BA2, BA1 BA0  0 0  0    c166
                    //  CHA address is  0          ----      DAC
*bufa=dat16;

bufb=0x3f002;       // data buffer is active, /CE1 signal is active as well
dat16=ch2;          // select channel B   ...2          0 1  0   c166
                    // CHB address is  1               ----     DAC
*bufb=dat16;

bufc=0x3f004;       // data buffer is active, /CE1 signal is active as well
dat16=ch3;          // select channel C   ...4          1 0  0   c166
                    // CHC address is  2               ----     DAC
*bufc=dat16;

bufd=0x3f006;       // data buffer is active, /CE1 signal is active as well
dat16=ch4;          // select channel D   ...6          1 1  0   c166
                    // CHD address is  3               ----     DAC
*bufd=dat16;


// the address of the dac should be valid before WR goes low
// /CE2 3f400...CE3 3f800..CEEXT 3fc00
```

```
}

printf("done");
}/*main program*/



/*****************************************************************/
/*****************************************************************/
/* Interrupt service routines PWM */
/*****************************************************************/

void timer1_int(void) interrupt 0x21 using r_bank0 {

 ia =(ADDAT2[0]&0x3ff)-512;      // read ia, ib
 ib =(ADDAT2[1]&0x3ff)-512;      //yel p5.1=ia=yell    p5.0=ib=red
 if (!ADBSY)              // if the conversion is not in progress then
                     // start conversion adst=1
 ADST=1;


   CC0_image=pwm_period+va+128;
   CC8_image=0xFFFF-va-128;
   CC4_image =CC0_image+under_lap;
   CC12_image=CC8_image;
   CC8_image+= under_lap;

   CC1_image=pwm_period+vb+128;
   CC9_image=0xFFFF-vb-128;
   CC5_image= CC1_image+under_lap;
   CC13_image=CC9_image;
   CC9_image+=under_lap;

   CC2_image=pwm_period+vc+128;
   CC10_image=0xFFFF-vc-128;
   CC6_image=CC2_image+under_lap;
   CC14_image=CC10_image;
   CC10_image+=under_lap;

   CC8=CC8_image;
   CC9=CC9_image;
   CC10= CC10_image;
   CC12= CC12_image;
   CC13= CC13_image;
   CC14= CC14_image;
```

```
}

/*********************************************************************/
/* Interrupt service routines  SHAFT ENCODER*/
/*********************************************************************/

/*********************************************************************/
/* Interrupt service routines */
/*********************************************************************/
void CAPCOM7_int(void) interrupt 0x17 using r_banka
{
/* save position and time*/

pos = T3;
posn1=(pos+21)&0x7ff;

timed=time-time0+t0;

wr=oo/timed;

if(!P3_4)  wr=-wr;

t0=0;
time0=time;
}

/*********************************************************************/
/* Interrupt service routines A/D */
/*********************************************************************/
void addat_int(void) interrupt 0x28 using r_bank2
{
      DSTP1  = _sof_(ADDAT2);              //3?????
      PECC1 = 0x0202;
}


/**********************timer6  interrupt  routine**************/
void timer6_int(void) interrupt 0x26 using r_bank5 {
start_prog=1;
}

void timer5_int(void) interrupt 0x25 using r_bankf
{
t0=0xffff;
}
```

```
void CAPCOM3_int(void) interrupt 0x13 using r_bankz
{
T3=zeros;     // rest T3 just once
CC3IE=0;
}

int  sign(int  v)
{
 if (v >= 0)
    return(1);
 else
    return(-1);
}

int  sat(int phi)

{ int gg;
    if ((phi> 2048)||(phi< -2048))
     gg=sign(phi);
    else
       gg=(phi);

    return(gg);
}
```

```
void delay(int count)
{
int x,y;
       for(x=0;x<count;x++);
         for(y=0;y<0xffff;y++);
}
```

Appendix D

Synchronous reluctance machine

Rating

No. phases 3

Connection star

No. poles 4

No. slots 36

n_s 18

Power 18 kW

Line voltage 415 V rms

Line current 18.6 A rms

Rated speed 1500 rpm

Rated torque 115 Nm

Rotor structure: axially laminated design

Stator : a standard IM stator

k_{pd} (proportional gain in the direct axis) 20

K_{pq} k_{pd} (proportional gain in the quadrature axis) 20

k_{id} (integral gain in the direct axis) 200

K_{iq} k_{id} (integral gain in the quadrature axis) 500

Fixed gain parameters	Regulator	Servo
k_{PP} (proportional gain in the position loop)	20	400
k_{PS} (proportional gain in the speed loop)	5	5
k_{IS} (integral gain in the speed loop)	200	200

Appendix E

Derivation of Sliding Mode Control Law

The vector controlled Synchrel machine drive system can be written as

$$\ddot{\theta}_r = \frac{1}{J}[K_T i_{qs}^* - B_1 \dot{\theta}_r - B_2 \ sgn(\dot{\theta}_r)] \tag{1}$$

The best approximation of a control law that would achieve $\dot{s}=0$ is

$$\hat{u}^* = \frac{1}{\hat{b}}[-\hat{f} + \ddot{\theta}_d - \lambda \dot{\theta}_e] \tag{2}$$

where

$$\hat{b} = \frac{\hat{K}_T}{\hat{J}} \tag{3}$$

$$\hat{f} = -\frac{\hat{B}_1}{\hat{J}} \dot{\theta}_r - \frac{\hat{B}_2}{\hat{J}} sgn(\dot{\theta}_r) \qquad \hat{f} = \frac{f_{\min} + f_{\max}}{2} \tag{4}$$

$$f_{\min} = -\frac{B_1}{J_{\max}} \dot{\theta}_r - \frac{B_2}{J_{\max}} sgn(\dot{\theta}_r)$$
$$f_{\max} = -\frac{B_1}{J_{\min}} \dot{\theta}_r - \frac{B_2}{J_{\min}} sgn(\dot{\theta}_r) \tag{5}$$

Using the values given in Table 2 gives, $\hat{f} = -0.003\dot{\theta}_r - 0.206 sgn(\dot{\theta}_r)$. A discontinuity must be added to ensure sliding occurs and the control law is then

$$i_{qs}^* = \frac{(\hat{u}^* - ksat(s/\phi))}{\hat{b}} \tag{6}$$

where k is taken as the equality condition of Eq. 18, and

Appendix F

Machine Model

```
%modling the Synchrel machine accounting for the inductance ripple
function[sys,x0]=ripp_tor(t,x,u,flag)
%continous time simulation of synchrel
%Input vd , vq,we,theta
%output iqm,idm,iqs,ids,te
%varaiables rs,ls,ld,lq,rm
rs=0.753;
ls=0.0077;
ld0 =0.1;
lq0 =0.0152;
dldq=0.0007;
dlq =0.0003;
dld= 0.0011;
n=18;                    %No. of slots per pole pair

if abs(flag)== 1
 % return state derivatives
rd=ld0-dld*cos(n*u(4));
sq=lq0+dlq*cos(n*u(4));
sd=-dldq*sin(n*u(4));
rq=sd;
den=rd*sq-sd*rq;
aa=rs+u(3)*(dldq+n*dld)*sin(n*u(4));
bb=u(3)*(-ld0+(dld+n*dldq)*cos(n*u(4)));
cc=u(3)*(lq0+(dlq+n*dldq)*cos(n*u(4)));
dd=rs-u(3)*(dldq-n*dlq)*sin(n*u(4));
piq=(x(2)*(rq*aa+rd*bb) -x(1)*(rq*cc+rd*dd) - rq*u(1) +rd*u(2))/den;
pid=(-x(2)*(sq*aa+sd*bb)+ x(1)*(sq*cc+sd*dd)+ sq*u(1) -sd*u(2))/den;

sys=[piq,pid];

elseif flag==3   %return system output
%te=0.21*x(1)*x(2);
te=3*(x(1)*x(2)*(ld0-lq0)-x(1)*x(2)*(dld+dlq+n*dldq)*cos(n*u(4))+x(2)*x(2)*(n*dld/2+dld
q)*sin(n*u(4))-x(1)*x(1)*(n*dlq/2+dldq)*sin(n*u(4)));
 sys=[x(1);x(2);te];


elseif flag==0
sys=[2,0,3,4,0,0];


% number of continous states   2
```

```
%number of discrete states     0
%number of outputs             3
%number of inputs              4
%number of discontinous roots  0
%dirct feedthrough between inputs and outputs 0
x0=zeros(2,1);       %initial state vector
else sys=[];
end
 %don`t return anything
```

Appendix G

Generating reference speed, position and acceleration

```
%generating reference speed, position and acceleration
function [sys,x0] = trajectory(t,x,u,flag)

ti=0;              % time in second
t1=0.5;
t2=1.5;
t3=2;


Wi=0;              % speed in rad/s
Wa=6;
Wb=-6;
Wc=0;

if flag == 3
  %Return system outputs

   if t <= t1&t>=ti
      Wd= (Wa-Wi)/(t1-ti)*(t-ti)+Wi;
      thd=thd+Wd*(t-ti);
      ad=(Wa-Wi)/(t1-ti);

   elseif t<=t2&t>t1
      Wd=(Wb-Wa)/(t2-t1)*(t-t1)+Wa;
      thd = thd+Wd*(t-t1);
      ad=(Wb-Wa)/(t2-t1);

   elseif (t<=t3)&(t>t2)
      Wd=(Wc-Wb)/(t3-t2)*(t-t2)+Wb;
      thd=thd+Wd*(t-t2);
      ad=(Wc-Wb)/(t3-t2);

   end

 sys = [Wd, thd,ad];

  elseif flag == 0
   %Return initial conditions
   sys = [0,0,3,0,0,1];

else
   sys =[];
end
```

Appendix H

Single component sliding mode control algorithm

```
%single component sliding mode control algorithm
%load dynamics are not included in single component
function [sys,x0]=slidmb4(t,x,u,flag)
%discrete-time sliding mode controller
%outputs: s,iqref
%inputs:pos, wr, pos_ref, wr_ref and acc_ref
ts=1e-3;          % sampling interval
offset=0;         % starting point of sampling
Lamda=6;          %Lamda=4.32 for regulator case
K=12;
%calculating the coefficients of the function f,F,
Phir=0.7;         %Phir= 0.8 for regulator
if abs(flag)==2
        sys(2)=x(2);
        sys(4)=x(4);
if abs(round((t-offset)/ts)-(t-offset)/ts)<=1e-8
                    %calculate the equivalent control iqse

                        s=(u(2)-u(4))+Lamda*(u(1)-u(3));

                        % with relaylike added ammount
                         Iqse=-K*sat(s/Phir);
                    sys(1)=Iqse;
                    sys(2)=Iqse;
                    sys(3)=s;
                sys(4)=s;
        else

                    sys(1)=x(2);
                    sys(3)=x(4);
        end

elseif abs(flag)==3

        sys(1)=x(1);
        sys(2)=x(3);
elseif abs(flag)==0
        x0=[0,0,0,0];
        sys=[0,4,2,5,0,0];

elseif abs(flag)==4
        ns=(t-offset)/ts;
        if round(ns)-ns>0
```

```
            sys=offset+round(ns)*ts;
        else
            sys=offset+(round(ns)+1)*ts;
        end

else
        sys=[];
end
```

Dual component sliding mode algorithm

```
% slidma; dual component sliding mode algorithm
%load dynamics are incorporated
function [sys,x0]=slidma(t,x,u,flag)
% discrete-time sliding mode controller
% using equivalent control law with relaylike added ammount -K*sat(s/Phir)
%output s,iqref
B1=0.0012;
B2=0.08;
ts=1e-3;        % sampling interval
offset=0;       % starting point of sampling
Jmin=0.289;
Jmax=0.638;
Ktmin=2.778;
Ktmax=3.88;
Lamda=6;        %Lamda=4.32 for regulator case
K1=6;
%calculating the coefficients of the function f,F,
fcoe1=-(B1/Jmin+B1/Jmax)/2;
fcoe2=-(B2/Jmin+B2/Jmax)/2;
Fcoe1=abs(B1/Jmin+fcoe1);
Fcoe2=abs(B2/Jmin+fcoe2);

b=sqrt((Ktmax/Jmin)*(Ktmin/Jmax));
beta=sqrt((Ktmax/Jmin)/(Ktmin/Jmax));
n=30;
Phir=0.7;    %Phir =0.8 for regulator case

if abs(flag)==2
        %calculate the equivalent control iqse
            f=fcoe1*u(2)+fcoe2*sign(u(2));
            iqse=-f+u(5)-Lamda*(u(2)-u(4));

             s=(u(2)-u(4))+Lamda*(u(1)-u(3));
```

```
            % with relaylike added ammount
             F=Fcoe1*u(2)+Fcoe2*sign(u(2));
             K=K1*(beta*(F+n)+(beta-1)*abs(iqse));
             dd=-K*sat(s/Phir)/b;
             Iqse=(iqse/b+dd);

sys(1)=Iqse;
sys(2)=s;
sys(3)=K;
sys(4)=dd;
elseif abs(flag)==3

            sys(1)=x(1);
            sys(2)=x(2);
            sys(3)=x(3);
            sys(4)=x(4);
elseif abs(flag)==0
            x0=[0,0,0,0];
            sys=[0,4,4,5,0,0];

elseif abs(flag)==4
            ns=(t-offset)/ts;
            if round(ns)-ns>0
                        sys=offset+round(ns)*ts;
            else
                        sys=offset+(round(ns)+1)*ts;
            end

else
            sys=[];
end
```

Appendix I

List of figures and Tables

Figures

Chapter 1

Chapter 2

Chapter 3

a without accounting for inductance ripple

b when accounting for inductance ripple

Tables